A search for neutrino-induced single photons and measurement of oscillation analysis systematic errors with electron and anti-electron neutrino selections, using the off-axis near detector of the Tokai to Kamioka experiment

Pierre Lasorak

March 29, 2018

Submitted in partial fulfillment of the requirements of the Degree of Doctor of Philosophy

Particle Physics Research Center, School of Physics and Astronomy
Queen Mary, University of London
United Kingdom

I, Pierre Jean Joseph Lasorak, confirm that the research included within this thesis is my own work or that where it has been carried out in collaboration with, or supported by others, that this is duly acknowledged below and my contribution indicated. Previously published material is also acknowledged below.

I attest that I have exercised reasonable care to ensure that the work is original, and does not to the best of my knowledge break any UK law, infringe any third party's copyright or other Intellectual Property Right, or contain any confidential material.

I accept that the College has the right to use plagiarism detection software to check the electronic version of the thesis.

I confirm that this thesis has not been previously submitted for the award of a degree by this or any other university.

Signature:

Date: March 29, 2018

Abstract

This thesis describes the search for neutrino-production of single photons using the off-axis near detector at 280 metres (ND280) of the T2K experiment. A photon selection is used to perform the searches using the first Fine Grained Detector (FGD1) of the ND280. The thesis also highlights the importance of systematic uncertainties in the analysis, since the selection is background dominated. After careful characterisation of the systematic uncertainties and estimation of the efficiency, it is concluded that, with the selected 39 data events and the expected background of 45 events, the limit for neutrino-induced single photons, at T2K energies, is $0.0903 \times 10^{-38}\text{cm}^2/\text{nucleon}$. This result can be compared with the expected limit of $0.1068 \times 10^{-38}\text{cm}^2/\text{nucleon}$. Using ND280's neutrino energy distribution (peaked at 600 MeV), NEUT predicts a flux-averaged cross section of $0.000239 \times 10^{-38}\text{cm}^2/\text{nucleon}$.

A fit to the muon and electron (anti-) neutrinos selections in the ND280 was performed. The aim of this analysis is to use a data-driven method to constrain the electron (anti-) neutrinos background events at SK, the far detector and electron neutrino cross section parameters for oscillation analyses. These are fundamental inputs in the context of the searches for Charge-Parity (CP) violation in the neutrino sector. After a fit to the nominal Monte Carlo was realised, the electron neutrino and anti-neutrino cross section normalisation uncertainties are found to be 7.6% and 19.3%, repectively. Although these numbers are much higher than the assumed 3% uncertainty of all the CP violation searches performed at T2K up to now, the difference in the δ_{CP} log-likelihood is found to be acceptable as the one sigma contours are not very different and the exclusion of the $\delta_{\text{CP}} = 0$ is roughly the same.

Acknowledgements

I first want to thank my supervisor, Teppei Katori. I think he got close to the what I consider is the best out of me over these three years. I learnt a lot in neutrino physics, but also in other related fields, such as neutrino cross sections, detector physics, exotic neutrino physics, “politics physics,” a bit of “gossip physics,” and “Ig physics.” I think all of these are very valuable for the future, and I certainly enjoyed learning all this and doing my PhD. Thank you Teppei for your support.

I also want to thank Francesca Di Lodovico, who gave me the opportunity to “have a go” in Queen Mary, University of London, over a long internship and try a mini-analysis, just before my PhD started. This conforted me in my choice for making a PhD here.

I am greateful to my fellow PhDs, Sophie (at the time), Nick, Paul, Tom, Andres, Shivesh, Eddie, Rodrigo, Thomas and Susanna. Thank you Queen Mary post docs and staff, Ryan, Sam, Sophie (again), Stéphane and Alex. Thank you all for your friendly support, advice, and of course the litres of beers, pubs and pool we have shared. Good luck for the ones who still have to graduate!

Thank you T2K UK students and post docs, Clarence, Raj, Callum, Patrick, Luke, Steve, Dave, Jon and Leon for showing me around in Tokai, for the ski in Mioko, and for the fun during Shin Shan and Pono Pono evenings.

Thanks Clarence, Callum and Patrick for the help with Nuisance.

Merci Simon pour les derniers plots de la thèse!

Thanks José, Xiaoyue, Ko, Yano-san for making SK shifts less boring.

Finally, thank you Jigmet, for your patience and perseverance, across the seas. Thanks for making the trip to London and France several times, and for the nice time during the layovers on the way to Japan. Thanks for sometimes reminding me how “*pagal*” this all has been, and thanks for pulling me out of work when it was too much, and taking me out. Thanks for letting me chopping the onions and veggies in your sacred sanctuary, the kitchen.

Merci Eliot, pour l’inconditionnel support, les cheeky bières du soir en rentrant du

labo, la musique, l'appartement et les petites tueries de pâtisseries.

Merci papa, maman pour votre support et encouragements, par Skype, par téléphone, sur un vélo ou sur les chemins boueux pyrénéens.

Merci Natacha d'avoir eu la patience de relire entièrement cette thèse!

Merci Alexis de m'avoir fait refaire de l'escalade!

Merci aux copains français, Olivier, Vivien, Claire, Pierre, Sarah, Quentin, Youmna pour les weekends et escapades, et surtout pour vos patiences; je n'ai pas été souvent en France pendant la thèse, j'en suis désolé.

Thanks "F*ckoffee" (excuse my French), in Bermondsey, for the long afternoons spend behind my laptop and double espressos.

To those who endure the ones doing a PhD.

Contents

List of Figures

List of Tables

List of Terms

$\bar{\nu}_e$ electron anti-neutrino.

$\bar{\nu}_\mu$ muon anti-neutrino.

ν_e electron neutrino.

ν_μ muon neutrino.

$\pi^\pm$ charged pion.

π^0 neutral pion.

2p2h 2 particles 2 holes nucleus excitation, a process where a boson interacts with a nucleon or a pair of nucleons, where, because of FSI, correlation or exchange of pion excitation, two nucleon get excited.

ADC Analog to Digital Converter.

anti-shadowing Enhancement of the electron DIS cross section for nuclear targets as a function of the Bjorken x variable in the middle range ($0.05 < x < 0.2$).

ArgoNeuT LArTPC neutrino experiment at Fermilab.

Asimov Asimov data set, the “best guess” Monte Carlo prediction.

BANFF Beam And ND280 Flux extrapolation task Force, the fitting framework that realise the near detector fit and constrain the cross section and flux systematic uncertainties before every oscillation analyses using the Super-Kamiokande data.

BeRPA Effective RPA, in the Bernstein polynial basis, the parametrisation used on T2K for RPA.

BLM Beam Loss Monitor, device containing gas which detects the charge particles escaping from the beam pipes at the J-PARC, it is used to stop the beam when the beam losses exceed a certain value.

BrECal Barrel ECal, side part of the ECal (around the FGDs and the TPCs).

CC Charged Current.

CCQE Charged Current Quasi Elastic.

CDHSW CERN-Dortmund-Heidelberg-Saclay-Warsaw experiment.

CHORUS CERN Hybrid Oscillation Research ApparatUS.

CL Confidence Level.

COH Coherent, a process where the boson interacts with the whole nucleus rather than single nucleon, sometimes defined as a process which leaves the nucleus in its ground state.

CP Charge Parity.

CT Current Transformer, a device in the secondary beam line at J-PARC which measures the intensity of the proton beam by measuring the induced current on a coil around the beam pipe.

DIS Deep Inelastic Scattering, a process where a boson interacts with a single quark.

DsECal Downstream ECal, the most downstream part of the ECal.

DUNE Deep Undergroud Neutrino Experiment, an planned neutrino experiment in Fermilab and Sanford Underground Research Facility aiming to discover ΔCP in the neutrino sector.

ECal Electromagnetic Calorimeter subdetector of the ND280, which aims at measuring the escaping EM objects from the tracker region.

EM Electro-Magnetic.

EMC European Muon Collaboration, the name of the experiment that discovered the "EMC effect," which is an unexpected reduction of the electron DIS cross section for nuclear targets as a function of the Bjorken x variable in the high range ($x > 0.3$).

EMFP Effective Mean Free Path, the mean effective distance the photons traverse before converting in the OOFV regions.

EMHIP ECal variable used for discrimination of Electro-Magnetic object and hadronic shower. It is the discriminator after running a boosted decision tree on electron and a proton particle guns.

ESM Electro-Static beam position Monitor, device which uses a capacitor to measure the beam center of in the secondary beamline.

FGD Fine Grain Detector, a subdetector of the ND280, which usually is used as target mass for most analysis.

FHC Forward Horn Current, neutrino enhanced beam mode.

FSI Final State Interactions, the interaction which a pion or a nucleon undergo before exiting the nucleus (i.e. sometime a charged pion created inside the nucleus will be reabsorbed by the nucleus and will not be visible in the detector).

FV Fiducial Volume of a particular detector (usually the FGD1 in this thesis).

GENIE General purpose neutrino event generator.

HERMES e-p experiment at the HERA collider.

Highland2 HIGH Level Analysis at ND280, version 2, used for event selection and analysis at the near detector.

HK Hyper-KamiokaNDE, a plananed neutrino experiment using an upgraded J-PARC facility and two 50 kTon water Cherenkov detectors as far detectors (sometime loosing referring to the far detector only), aims at discovering ΔCP in the neutrino sector.

HPD Highest Posterior Density. In this thesis, this is a method to assign an error in the case of asymmetrical errors.

INGRID Interactive Neutrino GRID, the neutrino detector at 280 m of the target at the near side which primarily serves to measure the beam center.

J-PARC Japan Proton Accelerator Research Complex, the facility that is used to create the T2K neutrino beam, in Tokai.

K2K Neutrino oscillation experiment in Japan, KEK to Kamioka.

LArTPC Liquid argon Time Projection Chamber.

LFG Local Fermi Gas, a parametrisation of the density of states in the nucleus, which depends on the local density in the nucleus.

LINAC LINear ACcelerator, the first accelerator which accelerates H^- up to 181 MeV at the J-PARC.

MaCh3 Markov-Chain 3 flavours neutrino oscillation parameter fitting software, used for T2K oscillation analyses, relying on the use of a MCMC method.

magnet Neutrino events happening in the volume enclosed by the magnet in the ND280.

MC Monte Carlo simulations.

MCMC Markov-Chain Monte Carlo, a method which is used by MaCh3 to sample the allowed parameter space and get a posterior likelihood distribution given observed data and a parametrisation.

MEC Meson Exchange Current, a process where a boson interacts with a pair of correlated nucleons in the nucleus (thus exchanging a pion in the chiral theory). Most often on T2K, MEC refers to any correction that has to be added to a standard CCQE in a nucleus (except the RPA correction), and no difference is made with 2p2h events..

MINERνA Fermilab neutrino scattering experiment, using the NUMI neutrino beam (on-axis).

MiniBooNE Fermilab sterile neutrino and neutrino scattering experiment, using the Booster neutrino beam (on-axis).

MIP Minimum Ionising Particle, the minimum energy a particle looses by unit distance (for a muon, this is typically 2MeV/cm in a matterial that has a density of 1 g/cm^3).

MIPEM ECal variable used for discrimination of Minimum Ionising Particle or Electro-Magnetic object. It is the discriminator after running a boosted decision tree on electron and muon particle guns.

MPPC Multi-Pixel Photon Counter, Photon counter used in the T2K experiment for all the scintillator detectors at the near site.

MR Main Ring at the J-PARC facility, accelerating protons to 30 GeV.

MT Main Track, the highest momemtum track with positive of negative charge, propagating from the FGD1 to the TPC2.

NC Neutral Current.

NCEl Neutral Current Elastic.

ND280 Near Detector at 280 metres, the off-axis neutrino detector of the target at the near site, which is used for near detector fits (BANFF), and cross section measurements.

NEUT Neutrino event generator (for T2K & SK).

NIWG Neutrino Interaction Working Group, the group in T2K which creates the cross section parametrisaton and assign errors to it.

NOνA NUMI Off-axis neutrino ν_e Appearance neutrino experiment, Fermilab experiment using NUMI neutrino beam (off-axis).

NOMAD Neutrino Oscillation Magnetized Detector, near detector of the OPERA experiment, at CERN.

NUANCE Neutrino interaction generator used in MiniBooNE.

NUISANCE NeUtrino Interaction Systematics ANalyser by Comparing Experiments, NeUtrino Interaction Synthesiser Aggregating Constraints from Experiments, or NeUtrino Interaction Systematics from A-Neutrino sCattering Experiments, ...

NuTEV Fermilab high energy neutrino scattering experiment, using the Tevatron beam dump.

OOAFV Out Of All the Fiducial Volumes of all the detectors.

OOFV Out Of Fiducial Volume of a particular detector (usually the FGD1 in this thesis).

OTR Optical Transition Radiation, device which measures the beam center centre 280 mm before it hits the target, it is composed of a fluorescent thin foil which is monitored by a camera.

P0D Pi-zero [sub]Detector of the ND280 which aims at measuring neutral pions.

P0DECal Electromagnetic Calorimeter surrounding the P0D, which aims at measuring escaping EM objects from the P0D.

pc1 partially calibrated processing of the ND280 data.

PDF Probability Density Function, or Parton Distribution Function.

PEU Pixel Equivalent Unit, pC value detected in a detector.

PID Particle IDentification.

PMNS Pontecorvo Maki Nakagawa Sakata, often attached to matrix for neutrino mass mixing.

PMT Photo-Multiplier Tube, the device that collect the Cherenkov light on the walls of Super-Kamiokande.

POPOP 1,4-bis(5-phenyloxazol-2-yl) benzene (wavelength shifter organic scintillator).

POT Proton On Target, measure of the total intensity that the experiment was exposed to.

PPO 5-Diphenyloxazole (wavelength shifter organic scintillator).

psyche Propagation of SYstematics and CHaracterization of Events, comes with highland2, applies all the detector systematic uncertainties to the event selections.

PT Pair Track, the second highest momentum track with an opposite charge to the one of the MT, propagating from the FGD1 to the TPC2.

p-theta Neutrino oscillation parameter fitting software taking into account the p-theta distribution of the electron neutrino appearance signal, used for T2K oscillation analyses.

RCS Rapid Cycling Synchrotron, the second stage of proton acceleration after the LINAC which accelerates the protons up to 3 GeV.

rdp real data processing of the ND280 data.

RES Resonant, a process where a boson interacts with a nucleon and creates a nuclear resonance.

RFG Relativistic Fermi Gas, a parametrisation of the density of states in the nucleus, which only depends on the number of nucleons in the nucleus.

RHC Reverse Horn Current, anti-neutrino enhanced beam mode.

RMM Readout Merger Module, merger for the TFB signals.

RPA Random Phase Approximation, a boson screening effect which usually depends on the Q^2 of the reaction. At low Q^2, the RPA correction leads to a damping of the cross section; at medium Q^2, the correction is an enhancement of the cross section; at high Q^2, the correction is 1.

sand Neutrino events happening in the sand around the ND280.

SBN Short Baseline Neutrino program at Fermilab, composed of the ICARUS, MicroBooNE and SBN detector, which are on-axis detector in the Booster neutrino beam.

SCC Second Class Currents, which depends on the mass of the outgoing lepton in neutrino scattering, hence could be responsible for difference between electron and muon neutrino cross sections.

SciBooNE Neutrino experiment at Fermilab using a scintillator detector in the Booster neutrino beam (on-axis).

SF Spectral Function, a parametrisation of density of states in the nucleus, taking into acount the interaction between the nucleons.

SiPM Silicon Photo-Mulitplier, on T2K they are MPPCs.

SIS Shallow Inelastic Scattering (also refered as "Transition region"), an intermediate process between resonant and DIS, which has no classical interpretation.

SK Super-Kamiokande, a 22 kTon water Cherenkov in Japan, used as the far detector of the T2K experiment.

SMRD Side Muon Range [sub]Detectors of the ND280, which aims at measuring the muon ranging out of the ND280, and serve as cosmic ray muon trigger.

SNO Sudbury Neutrino Observatory.

SSEM Segmented Secondary Emission Profile Monitors, "comb" which is placed in the secondary beam at the J-PARC to measure its profile by collecting the secondary electrons that are created when the protons interact with it.

T2K Tokai to Kamioka, neutrino oscillation experiment in Japan using the J-PARC beam (off-axis).

T2KReWeight A software package developped in T2K to change the cross section of an event via its weight according to "dials" (fundamental inputs to the calculations of the cross section).

TFB Trip-T Frontend Board, digitaliser for the MPPCs.

TPC Time Projection Chamber, a subdetector of the ND280, which realises precise PID, charge and momentum measurement for charged particles.

VaLOR Valencia-Lancaster-Oxford-RAL neutrino oscillation parameters fitting software.

WSF Wavelength Shifting Fiber, used in the scintillator detector, it carries the light from the center of the bar to the MPPC.

Introduction

The thesis covers two topics, a search for neutrino-induced single photons and the measurement of oscillation systematic uncertainties using (anti-) electron neutrino selections. Both the analyses were done with the Near Detector at 280 metres (ND280) of the Tokai to Kamioka experiment (T2K).

The first chapter covers the introduction to neutrino physics and includes a brief history of neutrinos and a description of the neutrino oscillation phenomenon which is being measured at T2K. It also covers the neutrino scattering physics landscape for T2K energies (few 0.5 to a few GeV).

The second chapter describes the T2K experiment, consisting of an accelerator, a near detector complex and a far detector called “Super Kamiokande” (SK).

An additional task of monitoring the data quality of the electromagnetic calorimeter (ECal) is described in Chapter 3.

Chapter 4 covers the models leading to neutrino-production of single photon.

The first topic of the thesis, a search for neutrino-induced single photons is presented in Chapters 5, 6 and 7. It highlights the rationale for conducting the search, methodology for event selection, evaluation of systematic uncertainties and limit calculation of the cross section.

Finally, Chapter 8 describes the ND280 fits done to reduce systematic errors for oscillation analysis, including (anti-) electron neutrino samples.

Chapter 1

Neutrino Physics

Neutrinos were postulated in 1930 by W. Pauli to explain missing energy in the beta decays of nitrogen and lithium, in a famous letter to the "*radioactive ladies and gentlemen* [1]." At the time, postulating a new, undetected, particle was quite controversial; it is now considered a breakthrough. These particles were later experimentally discovered by Reines and Cowan in 1953 [2]. They measured the inverse beta decays, $\bar{\nu}_e + p \rightarrow e^+ + n$, initiated by the Savannah nuclear reactor anti-neutrinos on cadmium-doped water.

Since then, the observation of neutrinos is still a challenge for physicists, but there are a wide number of experiments that observe neutrinos from very different sources [3–6], such as the Sun, cosmic ray interacting with the atmosphere, nuclear reactors or accelerated protons impinging a target.

This section is dedicated to the description of neutrino properties; the first section of this chapter describes the oscillatory behaviour of the neutrinos. Precise and reliable measurements of this phenomenon are the main purpose of the T2K experiment [3], which measures muon electron (anti-) neutrinos appearance in a muon (anti-) neutrino beam of 600 MeV, in Japan[2].

The second section of this chapter is about the phenomenology of neutrino cross sections. This is a fundamental input to the oscillation measurements made at T2K and the subject of this thesis. The section will only cover the "mid-range" energies (0.5 to few GeV) cross sections, which are relevant to in the T2K case. The section starts with a common description of the processes that happen when a neutrino interacts with matter, with an emphasis on the measurements within and outside of T2K that are the most sensitive

---

[2] Muon (anti-) neutrinos of energy 600 MeV are created at Tokai in the J-PARC facility. The Super-Kamiokande detector (SK), in Kamioka (295 km away) detects the oscillated neutrino signal. The Near Detector (ND280) at 280 m, in Tokai of this experiment is used for the analyses develeped in this thesis.

to these channels.

1.1 Oscillation physics

An interesting behaviour of the neutrinos is that they change flavour changes when they propagate. The simplest way to explain this phenomenon is via neutrino oscillations, which leads to the conclusion that they have mass. This behaviour is not unique in particle physics as it has been observed for kaons and B-mesons. The oscillations of neutrinos had been postulated a long time before by Pontecorvo in 1958 [7] and later by Maki, Nakagawa and Sakata [8]. The evidences that neutrinos oscillate is fairly recent; it dates from 1998 with the Super-Kamiokande detector [9]. The evidence was confirmed later by the SNO experiment in 2002 [10]. The spokespersons of these experiments were awarded the Nobel Prize of physics for the discovery of neutrino oscillation and the implication that had on neutrino mass [11].

This section introduces an approximated mathematical formalism to the phenomenon of neutrino oscillations. The main approximation is that the formalism is not Lorentz invariant. To have a Lorentz invariant equation, a full Quantum Field Theory (QFT) approach is required, which is beyond the scope of this introduction [12]. In broad terms, it consists of calculating amplitudes of Feynman diagrams such as the one in Figure 1.1, where the neutrino is considered as a propagator.

The oscillation relies on the hypothesis that the neutrino mass and flavour states have the same momentum. These equations are developed in the case of relativistic neutrino, which is true for all detectable neutrinos[1]. It is worth noting that although this derivation lacks physical motivation and robustness compared to a full rigorous QFT approach, it leads to the exact same answer.

To show that neutrinos oscillate, one can start with the common expressions of the flavours state as a function of the mass state via the PMNS (Pontecorvo-Maki-Nakagawa-Sakata) matrix [8, 16–18]:

$$\begin{pmatrix}\nu_e\\ \nu_\mu\\ \nu_\tau\end{pmatrix} = \begin{pmatrix}U_{e1} & U_{e2} & U_{e3}\\ U_{\mu1} & U_{\mu2} & U_{\mu3}\\ U_{\tau1} & U_{\tau2} & U_{\tau3}\end{pmatrix}\begin{pmatrix}\nu_1\\ \nu_2\\ \nu_3\end{pmatrix} \tag{1.1}$$

$$= \begin{pmatrix}1 & 0 & 0\\ 0 & c_{23} & s_{23}\\ 0 & -s_{23} & c_{23}\end{pmatrix}\begin{pmatrix}c_{13} & 0 & s_{13}e^{-i\delta_{\mathrm{CP}}}\\ 0 & 1 & 0\\ -s_{13}e^{i\delta_{\mathrm{CP}}} & 0 & c_{13}\end{pmatrix}\begin{pmatrix}c_{12} & s_{12} & 0\\ -s_{12} & c_{12} & 0\\ 0 & 0 & 1\end{pmatrix}\begin{pmatrix}1 & & \\ & e^{-i\frac{\alpha_{21}}{2}} & \\ & & e^{-i\frac{\alpha_{31}}{2}}\end{pmatrix}\begin{pmatrix}\nu_1\\ \nu_2\\ \nu_3\end{pmatrix}, \tag{1.2}$$

---

[1] The neutrinos have a mass smaller than few eVs [14], and detectable neutrinos have energy greater than few hundreds of keVs [15]

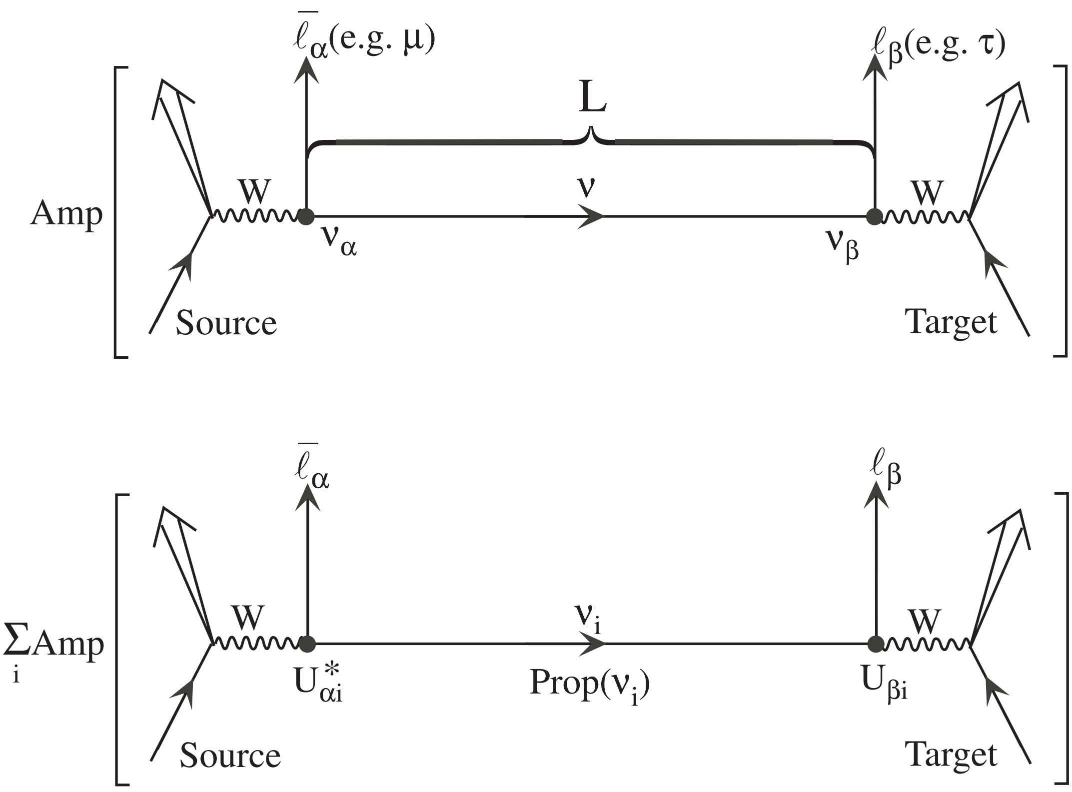

Figure 1.1: Neutrino flavour change (oscillation) in vacuum. "Amp" denotes an amplitude. Taken from [13].

which quantifies the massive content of the flavour neutrino ν_e, ν_μ and ν_τ according to their mass eigenstates ν_1, ν_2 and ν_3. Each c_{ij} and s_{ij} reads $\cos(\theta_{ij})$ and $\sin(\theta_{ij})$ respectively, where θ_{ij} are the mixing angles. δ_{CP} (α_{21}, α_{31}) are the Dirac (Majorana) phases indicating CP (Charge Parity) violation. Equation 1.1 is the general form for the PMNS matrix, and Equation 1.2 is a more elegant way to parametrise it. Note that, in the absence of oscillations of the active neutrinos to sterile neutrinos. Since there is no experimental observations of oscillations to sterile neutrinos, these matrices considered are unitary.

With Equation 1.2, one factorises in "sectors" the oscillations according to the type of neutrino oscillation which are observed. Hence, the first matrix relates to the "atmospheric sector," which, at first order, describes the oscillation of $\nu_\mu \to \nu_\tau$. The third matrix describes the "solar sector" that quantifies the oscillation of $\nu_e \to \nu_\mu$. Finally, the second matrix is the "cross mixing" matrix, which depends on the Dirac phase in its off-diagonal terms. This phase encloses the difference in the oscillatory behaviour between neutrinos and anti-neutrinos.

The calculation which leads to the conclusion that the neutrino of a certain flavour oscillates to another during its propagation is now quickly developed.

Supposing a neutrino of a defined flavour is created in space-time, one can write:

$$|\nu_\alpha\rangle = \sum_k U^*_{\alpha k} |\nu_k\rangle \, (\alpha = e, \mu, \tau), \tag{1.3}$$

where ν_α are the flavour eigenstates and ν_k are the mass eigenstates. This is just another way of writing Equation 1.1. The term $U^*_{\alpha k}$ is an element of the mixing matrix. Next, the neutrino mass states are orthogonal, so this leads to

$$\langle \nu_k | \nu_j \rangle = \delta_{kj} \tag{1.4}$$

and similarly for the flavour states:

$$\langle \nu_\alpha | \nu_\beta \rangle = \delta_{\alpha\beta}. \tag{1.5}$$

The massive states $|\nu_k\rangle$ are eigenstates of the Hamiltonian operator $\mathscr{H}$:

$$\mathscr{H} |\nu_k\rangle = E_k |\nu_k\rangle, \tag{1.6}$$

and, solving this equation, one reaches:

$$|\nu_k(t)\rangle = \exp(-iE_k t) |\nu_k\rangle. \tag{1.7}$$

Consider now a neutrino of flavour α, that was created at $t = 0$, $|\nu_\alpha(t = 0)\rangle$. This neutrino propagates in space-time, using Equation 1.7 and 1.3, one can write:

$$|\nu_\alpha(t)\rangle = \sum_k U_{\alpha k} \exp(-iE_k t) |\nu_k\rangle, \tag{1.8}$$

for which, if $t = 0$, $|\nu_\alpha(t = 0)\rangle = |\nu_\alpha\rangle$.

Note that it is possible to invert Equation 1.3:

$$|\nu_k\rangle = \sum_\alpha U_{\alpha k} |\nu_\alpha\rangle, \tag{1.9}$$

and that can be inserted into Equation 1.8:

$$|\nu_\alpha(t)\rangle = \sum_{\beta=e,\mu,\tau} \left(\sum_k U^*_{\alpha k} \exp\left(-iE_k t\right) U_{\beta k} \right) |\nu_\beta\rangle \,. \tag{1.10}$$

Hence, for an arbitrary time t, one can see that the $|\nu_\alpha(t)\rangle$ is a superposition of the states $|\nu_\beta\rangle$. This means the neutrino created at $t = 0$ is now a composite state of the different flavour neutrinos. Consider now the amplitude of the oscillation process $\nu_\alpha \to \nu_\beta$, $\mathscr{A}_{\nu_\alpha \to \nu_\beta}$:

$$\mathscr{A}_{\nu_\alpha\to\nu_\beta}(t) = \langle \nu_\beta | \nu_\alpha(t) \rangle \tag{1.11}$$

$$= \sum_k U^*_{\alpha k} U_{\beta k} \exp(-iE_k t), \tag{1.12}$$

which can be squared to get the probability of oscillation:

$$\begin{aligned} \mathscr{P}_{\nu_\alpha\to\nu_\beta} &= \left|\mathscr{A}_{\nu_\alpha\to\nu_\beta}\right|^2 \\ &= \sum_{k,j} U^*_{\alpha k} U_{\beta k} U_{\alpha j} U^*_{\beta j} \exp\left(-i(E_k - E_j)t\right). \end{aligned} \tag{1.13}$$

Further simplification can be made to reach a simple equation. First, the energy for any particle is given by:

$$E_k = \sqrt{m_k^2 + \vec{p}^2} \tag{1.14}$$

and that can be simplified with a simple Taylor expansion for the case of large momentum (i.e. relativistic particle):

$$E_k \simeq |p| + \frac{m_k^2}{2|p|}, \tag{1.15}$$

which can be reinserted in the exponential term of Equation (1.13):

$$E_k - E_j \simeq \frac{m_k^2 - m_j^2}{2|p|}. \tag{1.16}$$

In this equation, it is assumed that the momentum of the mass states during the creation of the neutrino is the same, p. One can then define $\Delta m^2_{kj} = m_k^2 - m_j^2$, and replace $|p|$ by E since the neutrinos are ultra-relativistic. Substituing everything in Equation (1.13) leads to:

$$\mathscr{P}_{\nu_\alpha\to\nu_\beta} = \sum_{k,j} U^*_{\alpha k} U_{\beta k} U_{\alpha j} U^*_{\beta j} \exp\left(-i(\Delta m^2_{kj})t/(2E)\right). \tag{1.17}$$

One further simplification comes from the fact that the neutrino are propagating at almost the speed of light, c, which equates 1 in natural units. So $t = L$, where L is the distance of propagation of the neutrino:

$$\mathscr{P}_{\nu_\alpha \to \nu_\beta} = \sum_{k,j} U^*_{\alpha k} U_{\beta k} U_{\alpha j} U^*_{\beta j} \exp\left(-i(\Delta m^2_{kj}) L/(2E)\right). \tag{1.18}$$

Finally, this probability can be simplified to:

$$\begin{aligned} \mathscr{P}_{\nu_\alpha \to \nu_\beta} = \delta_{\alpha\beta} &- 4 \sum_{k>j} \mathscr{Re}\left[U^*_{\alpha k} U_{\beta k} U_{\alpha j} U^*_{\beta j}\right] \sin^2\left(\frac{\Delta m^2_{kj} L}{4E}\right) \\ &+ 2 \sum_{k>j} \mathscr{Im}\left[U^*_{\alpha k} U_{\beta k} U_{\alpha j} U^*_{\beta j}\right] \sin\left(\frac{\Delta m^2_{kj} L}{2E}\right). \end{aligned} \tag{1.19}$$

Note that the oscillation probability depends on terms of the form $U^*_{\alpha k} U_{\beta k} U_{\alpha j} U^*_{\beta j}$ for which the Majorana phases systematically cancel, which is why neutrino oscillation experiments cannot detect these phases. These Majorana phases can be determined via the detection of neutrinoless double beta decay processes [19].

In the case of T2K, which measures electron neutrinos in a muon neutrino beam of 600 MeV at a distance of 295 km, the oscillation probability, Equation 1.19, becomes [20]:

$$\begin{aligned} \mathscr{P}_{\nu_\mu \to \nu_\mu} &= \mathscr{P}_{\bar{\nu}_\mu \to \bar{\nu}_\mu} \\ &\simeq 1 - 4\cos^2\theta_{13}\sin^2\theta_{23}\left[1 - \cos^2\theta_{13}\sin^2\theta_{23}\right]\sin^2\left(\frac{\Delta m^2_{32} L}{4E}\right), \end{aligned} \tag{1.20}$$

for the muon neutrino survival probability and

$$\begin{aligned} \mathscr{P}(\overset{(-)}{\nu}_\mu \to \overset{(-)}{\nu}_e) &\simeq \sin^2\theta_{23}\sin^2 2\theta_{13}\sin^2\left(\frac{\Delta m^2_{31} L}{4E}\right) \\ &\overset{(+)}{-} \frac{\sin 2\theta_{12}\sin 2\theta_{23}}{2\sin\theta_{13}}\sin\left(\frac{\Delta m^2_{21} L}{4E}\right) \times \sin^2 2\theta_{13}\sin^2\left(\frac{\Delta m^2_{31} L}{4E}\right)\sin\delta_{CP}, \end{aligned} \tag{1.21}$$

for the electron (anti-) neutrino appearance probability. Figure 1.2 shows these oscillation probabilities in the case of T2K for typical values of the parameters measured at T2K (and reported in Table 1.1).

The Dirac phase, δ_{CP}, is the last of parameter of the matrix that remains to be measured. All the PMNS angles value are given in Table 1.1, along with the differences

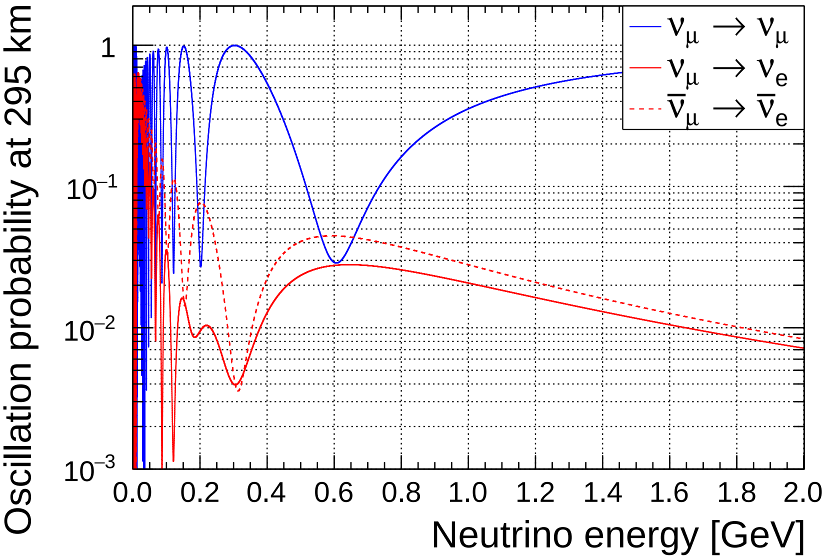

Figure 1.2: Neutrino oscillation probability at T2K, for normal ordering, $\delta_{CP} = \pi/2$ and using the values given in Table 1.1. Produced with Prob3++ [21].

of mass squared, $|\Delta m^2_{jk}|$. Note that this table differentiates the normal and inverted ordering: this is because neutrino oscillations are yet insensitive to the sign of the mass of the atmospheric mass squared splitting. This can be seen in both Equation (1.20) and (1.21): the first, dominant, term always appears squared ($\sin^2\left(\frac{\Delta m^2_{32}L}{4E}\right)$, for example), hence experiments still do not have access to signs of Δm_{31} and Δm_{32}. Both hypotheses for the mass ordering are illustrated in Figure 1.3. In the normal ordering case (left of the figure), the mass states are ordered by increasing order: $m_{\nu_1} < m_{\nu_2} < m_{\nu_3}$; in the inverted case (right of the figure), the mass states are ordered in a different way: $m_{\nu_3} < m_{\nu_1} < m_{\nu_2}$.

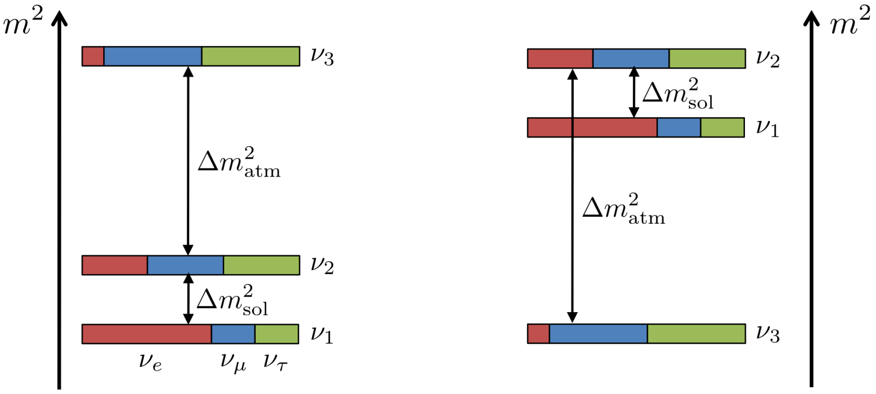

Figure 1.3: Possible neutrino mass ordering. ***Left:*** Normal ordering case. ***Right:*** Inverted ordering case. Reproduced from [22]

Parameter	Ordering	Best fit value	3σ range
$\Delta m^2_{21}/10^{-5}$ eV^2	NO, IO, Any	7.37	6.93 – 7.96
$\sin^2\theta_{12}/10^{-1}$	NO, IO, Any	2.97	2.50 – 3.54
$\lvert\Delta m^2\rvert/10^{-3}$ eV^2	NO	2.525	2.411 – 2.646
	IO	2.505	2.390 – 2.624
	Any	2.525	2.411 – 2.646
$\sin^2\theta_{13}/10^{-2}$	NO	2.15	1.90 – 2.40
	IO	2.16	1.90 – 2.42
	Any	2.15	1.90 – 2.40
$\sin^2\theta_{23}/10^{-1}$	NO	4.25	3.81 – 6.15
	IO	5.89	3.84 – 6.36
	Any	4.25	3.81 – 6.26
δ_{CP}/π	NO	1.38	0 – 0.17 $\oplus$ 0.76 – 2
	IO	1.31	0 – 0.15 $\oplus$ 0.69 – 2
	Any	1.38	0 – 0.17 $\oplus$ 0.76 – 2

Table 1.1: Neutrino oscillation parameters as described in the text, with their current best fit value and their 3σ range. This is shown for each mass ordering ("NO": Normal Ordering ; "IO": Inverted Ordering), and for the absolute minimum with the mass ordering marginalised ("Any" in the table). $\Delta m^2_{21}/10^{-5}$ eV^2 The first two parameters ($\Delta m^2_{21}/10^{-5}$ eV^2 and $\sin^2\theta_{12}/10^{-1}$) are insensitive to mass ordering. Δm^2 is defined as $m^2_3 - (m^2_1 + m^2_2)/2$, and $\Delta m^2_{21} = m^2_2 - m^2_1$. Reproduced from [23].

1.2 Medium energy neutrino scattering physics

This section describes the current state of the neutrino cross sections for energies of order of 1 GeV. Good knowledge of the neutrino cross section is fundamental in neutrino accelerator experiment, the introduction of this paragraph explains why. Then, a summary of the knowledge is made for the nuclear model and the following processes: charged-current quasi-elastic, resonant, coherent pion production and deep inelastic scattering. Finally the known differences between muon and electron (anti-) neutrino scattering are explained.

1.2.1 Introduction

Neutrino cross section predictions are one of the major inputs for any oscillation experiment; a way to see this is to analyse the equation that leads to the number of events that are seen in a detector. In the case of neutrinos, this is:

$$N(l_{\mathrm{rec}}) = \Phi(E_{\mathrm{true}}) \times (1 - P(E_{\mathrm{true}})) \times \sigma(E_{\mathrm{true}}, l_{\mathrm{true}}, A) \times \epsilon(l_{\mathrm{true}})_{\mathrm{det}} \times R(l_{\mathrm{true}}, l_{\mathrm{rec}}) \quad (1.22)$$

where:

- $N(l_{\mathrm{rec}})$ refers to the number of events reconstructed in a detector in a particular differential bin of a reconstructed quantity l_{rec} (usually lepton momentum or angle),
- $\Phi(E_{\mathrm{true}})$ is the flux (which depends on the true energy of the neutrino, E_{true}),
- $P(E_{\mathrm{true}})$ is the oscillation probability (that also depends on the baseline and the oscillation parameters, as seen in the Section 1.1),
- $\sigma(E_{\mathrm{true}}, l_{\mathrm{true}}, A)$ is the cross section, where A is the target nucleus,
- $\epsilon(l_{\mathrm{true}})_{\mathrm{det}}$ is the detector efficiency,
- and $R(l_{\mathrm{true}}, l_{\mathrm{rec}})$ is the migration matrix (or "smearing matrix") containing the detector effects to go from l_{true} to l_{rec}.

Note that this is an approximated equation, since all these quantities are generally convoluted, rather than simply multiplied.

In most accelerator neutrino oscillation experiments, two detectors are used; one is next to the neutrino source and measures $N(l_{\mathrm{rec}})$ in the special case where the oscillation probability is zero and the second detector, far from the neutrino source, measures the same quantity with a non-trivial oscillation probability.

From the near detector measurement, one can extract a data-driven constraint on the flux and / or the cross section. There are different ways of doing this:

- via a direct fit to the flux and cross section as is done in T2K (as will be seen in Chapter 8),

- or by directly correcting the true neutrino energy and thus modifying the flux (*à la* NOνA [24]).

Whichever method is used, the neutrino flux is then extrapolated to the far detector, which has access to the oscillation probability that one wants to measure. In the case of T2K, the flux and cross section parameters become "nuisance" parameters and errors will be constrained by the fit with data from the near detector. In the case of NOνA, the flux has a reduced error based on what was observed at the near detector.

Most of the time, the targets at the near and far detectors are chosen to be the same or similar. Complications generally appear in the case where acceptances are different between the near and the far detectors. This leads to selecting events from different phase spaces of the cross section in the two detectors, and it is generally not trivial to extrapolate the cross section for the different phase spaces. Similarly, the cross section depends on the neutrino energy, therefore if the neutrino energy distribution changes due to the baseline or the oscillations, the importance of the different processes will change. To be able to make the extrapolation (near to far) as described, one needs to precisely know the cross section and create shape and normalisation systematic errors that encapsulate the flux, acceptance and target differences between the near and the far detector. The risk is to underestimate the cross section errors at the far detector after over-constraining the cross section with the near detector data. This is a constant source of challenges within the T2K experiment, which forces us to understand and use recent cross section calculations.

In this context, precise knowledge of cross section is required to reach acceptable fits of the near detector data. In the next sections, the main processes for neutrino scattering are described in the context of neutrinos energy from 500 MeV to a few GeV. Although not explicitly described here, all the neutral current equivalent reactions do exist, however, due to the complexity of detection (absence of lepton) and lesser interest for oscillation analysis, data is more sparse, and models are generally under constrained. The analysis in this thesis is a good example of the challenges one faces for measuring these cross sections.

1.2.2 Nuclear Model

The nuclear model is purely related to the description of the nucleus, it can be accessed via experiments such as electron scattering. One of the most fundamental input to the nuclear model is the distribution of momentum of the nucleons in the nucleus. There are several ways to simulate this. The simplest of which is the Global Relativistic Fermi Gas (RFG). In this model, the nucleons momentum simply follow a Fermi distribution (the momentum of the nucleons is a quadratic distribution up to the Fermi momentum, p_F),

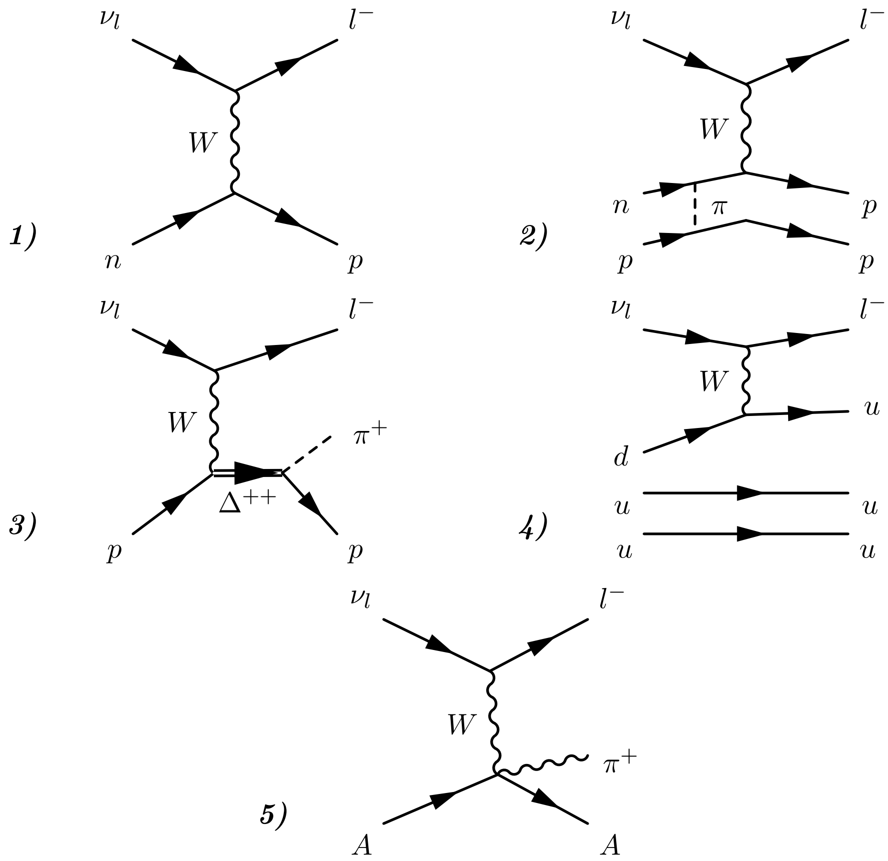

Figure 1.4: Main Feynman diagrams contributing to the total cross section of neutrinos from 500 MeV to a few GeV: ***1)*** charged-current quasi-elastic (CCQE) ***2)*** charged-current multi-nucleons (charged-current 2 particles-2 holes, 2p2h); ***3)*** charged-current resonant pion production; ***4)*** charged-current deep inelastic scattering (DIS); ***5)*** charged-current coherent pion production.

where the nuclear matter is assumed to have a constant density, this is the default model in NEUT, which is the neutrino interaction generator used at T2K.

The other model that was included in the T2K simulations is the Spectral Function (SF) model [28]. In this model, all the nucleon-nucleon interactions are factorised-out to produce a more realistic distribution of the nucleon momentum in the nucleus. Note that this model was significantly improved since its implementation in the NEUT generator [29].

The NEUT SF models has proven to be insufficient to predict MINERνA and MiniBooNE data [30], so the RFG model is used.

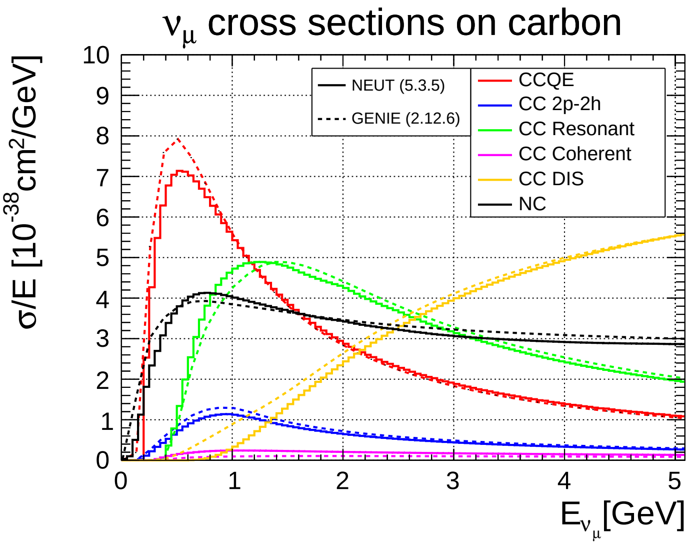

Figure 1.5: Muon neutrino cross sections on carbon from GENIE [25,26] and NEUT [27].

1.2.3 Charged-Current Quasi-Elastic process

A Charged-Current Quasi-Elastic (CCQE) interaction is depicted on the top left of Figure 1.4. In this process, a (anti-) neutrino of a given flavour interacts with a single neutron (proton) to create a negatively (positively) charged lepton of the same flavour. These interactions can happen on free nucleon (hydrogen) or nuclear target (carbon, oxygen), if the neutrino has enough energy to create a charged lepton. The neutrino interacts via W-boson exchange.

Since this is a two body process, momentum and energy conservation laws can be used to reconstruct the energy of the neutrino. In the case of a free nucleon, the reconstructed neutrino energy, E_{rec}, is [31]:

$$E_{\text{rec}} = \frac{E_l - m_l^2/(2M)}{1 - (E_l - P_l \cos(\theta_l))/M} \tag{1.23}$$

where E_l is the energy of the lepton (muon or electron), m_l is the lepton mass, P_l its momentum, $\cos(\theta_l)$ is the cosine of the lepton scattering angle, and M is the mass of the struck nucleon (neutron for neutrino and proton for anti-neutrino).

As can be seen in Figure 1.5, which shows the neutrino cross section against its energy, the CCQE cross section is largely dominant around 600 MeV, which is also the T2K peak energy. As will be described later, this is not a coincidence.

The formalism to calculate the value of the cross section [32] in the context of bubble chamber experiments [33–35]. Most of the parameters involved in the calculation of the cross section can be accessed via electron scattering, however the cross section also depends on a fundamental parameter which can only by accessed via neutrino measurements, called the axial mass (M_A^{QE}).

The CCQE cross section is proportional to the following form factor (so-called dipole form factor):

$$F_A(Q^2) = \frac{g_A}{\left(1 + \frac{Q^2}{M_A^{\mathrm{QE}\ 2}}\right)^2} \tag{1.24}$$

This form factor and M_A^{QE} parameter are related to the spacial extension of the nucleon for neutrino interactions by a inverse Fourier transform. This has recently come into more focus as a dipole form facbintor may not be justified for the neutrino case [36, 37].

The description of the cross section quickly becomes more complicated in the case of nuclear targets or even for deuteron [38]. In this case, corrections of various kinds have to be applied [39, 40]. Some of these corrections are listed here:

- The nucleons have a binding energy in the nucleus, the consequence is that the excited nucleon after neutrino interaction has to have a over the Fermi energy to happen. If the excited nucleon does not go over this threshold, the event said to be Pauli blocked.

- As was seen in the previous section, the nucleons move in the nucleus, the descriptions of the distribution of the nucleon momentum range from simple Global Relativistic Fermi Gas (RFG) to more complex Spectral Functions [28] or Local Fermi Gas (LFG).

  It is clear that depending on the nuclear model used, one will get different energy distributions for the initial state of the system just before the neutrino interaction. These models will produce different kinematics for the outgoing particle and "Pauli block" different events.

- The long range correlations has effect on Q^2 (which is the absolute value of the 4-momentum transfer squared): at low Q^2 the cross section is expected to be reduced; whereas it is enhanced at intermediate Q^2 and goes back to unity for $Q^2 \to \infty$. This correction, also refered as "Random Phase Approximation" (RPA) [40] is due to the fact that the W-boson creates virtual particle-holes in the nuclear medium in which it is propagating.

It should be noted that most of our knowledge in the CCQE cross section stems from bubble chamber data [33–35]. Nuclear targets experiments such as MINERνA [41], MiniBooNE [42] and, in a lesser extent, T2K [43] and K2K [44] near detectors data are still challenging to interpret. One of the reasons being that these measurements cannot disentangle the multi-nucleon processes from the pure CCQE contributions [30]. Indeed, all the CC0π[1] measurements on nuclear targets show that the data is higher than the one would get by only considering the CCQE cross section. This hints towards the presence of another contribution.

1.2.4 Multi-nucleon processes

Multi-nucleon processes, also called "np-nh" for n-particles n-holes (or even sometimes loosely referred as Meson Exchange Current (MEC)) are those processes where the neutrino interacts with a correlated pair of nucleons. The cross section for these events to happen is smaller than one for CCQE processes as can be seen in Figure 1.5. They also are largely more complex to calculate and to measure. This makes them one of the primary focuses in the neutrino cross section community.

Due to their similarity with pure CCQE events, these events lead to an enhancement to the total number of expected CC0π events as explained earlier. An example of one of the many contributing Feynman diagrams for this cross section is shown in top right of Figure 1.4, where the similarity with CCQE processes is clearer. Three main calculations for the multi-nucleon cross section were done recently in [45, 46], [47, 48] and [49, 50].

Note that despite the similarity in topology with the pure CCQE processes, the reconstructed energy in Equation 1.23 [31] does not hold for these events since this is no longer a two body process.

np-nh events are by definition nuclear processes which can only be accessed by modern neutrino experiments using a nuclear target, and the corrections listed in the previous section need to be applied to reliably calculate its cross section. Most of the knowledge on these processes originates from experiments such as K2K [44] and MiniBooNE [42, 51], which were the first to see the effect of these processes (enhancement of the CC0π cross section); these were followed a few years later by T2K [43]. More recently, the MINERνA experiment released data which proves that our understanding of this cross section is still very limited [52]. This measurement shows that one needs to multiply the np-nh cross section by a factor of two to fit the data. This is still a puzzle, which no nuclear theorist

---

[1] CC with no pion in the final state measurements, as opposed to direct measurements of the CCQE measurements, includes events where pions are created in the nucleus but do not exit the nucleus, or events where several nucleons escape the nucleus.

has been able to explain yet.

The way to shed light on these processes will probably come from the observation of the protons exiting the nucleus, with use of the precise detectors in the Fermilab Short Baseline Neutrino program [53, 54], although the theoretical calculations of proton kinematics are still at their early stage [55] (for example they are only available for carbon and do not include interactions of the exiting protons with the nuclear medium).

1.2.5 Resonant processes

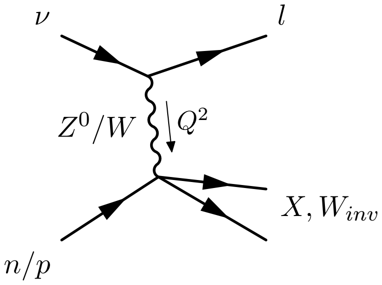

Figure 1.6: Illustration of the Q^2 and W_{inv} quantities for a generic neutrino reaction. l denotes a charged lepton or a neutrino of the same flavour as the incoming one (ν), depending on whether the interaction is Charged-Current (W) or Neutral-Current (Z^0). The X denotes any particle(s) of total energy W_{inv} that has been generated by the boson interaction on a nucleon. In the case of a resonant interaction, the X would be a nuclear resonance that decays into a pion or a photon, and a nucleon.

A Charged-Current Resonant (CCRES) process is illustrated in the middle left of the Figure 1.4. In the case of a resonant interaction, rather than interacting "elastically" with a nucleon, the W-boson has enough energy to create a "nuclear resonance," which, in simple terms, can be seen as equivalent to flipping the spin of a valence quark in the proton, and changing the isospin of one or several of the quarks. The resonance usually undergoes a strong decay by emitting of a pion and a nucleon. The resonance created is a much more complex object than a simple Dirac spinor and the calculation of the amplitudes of this cross section is more involved mathematically than in the case of CCQE [56, 57].

These RES cross sections are usually parametrised by a double differential cross section of the form $\frac{d^2\sigma}{dQ^2 dW_{inv}}$, where Q^2 is the absolute value of the 4-momentum transfer squared and W_{inv} is the invariant mass of the outgoing hadron system. These quantities are illustrated in Figure 1.6.

Some additional corrections due to the nuclear environment have to be taken into account for reliable cross section predictions. The main of which are the Final State Interactions (FSI). These affect the exiting pions and can change the topology of the events if a pion is absorbed, for example. Another correction can be applied on the resonance, since it can also scatter with a nucleon during its very short life-time. This leads to processes such as pion-less delta decays or a change in the decay width of the resonance [58, 59].

Also, note that there exist several resonances (Δ_{1232} having the lowest mass of them, and contributing the most to the amplitude) and a non-resonant "background" [60] (where the nucleon is used as a propagator between the interacting boson and the decay to pion and nucleon). These different contributions produce the same final states and the amplitudes for each of them needs to be added coherently to correctly take into account interferences. These interferences can significantly modify the topology of the single pion events [61].

As it was the case for CCQE, most of the models are constrained by the bubble chamber experiments [62–64], although there is still some confusion in the compatibility between these data sets [65]. The MINERνA [66], MiniBooNE [67–69], K2K [70] and T2K data are still a long way from being understood within an unique framework.

1.2.6 Deep Inelastic Scattering processes

The Deep Inelastic Scattering (DIS) processes occur at higher energies when the W-boson interacts with a single quark. The process is illustrated in Figure 1.4 (bottom right). In DIS events, many pions are usually created.

This process can be calculated from first principles but relies on the precise knowledge of the parton distribution functions, at low Q^2 and relatively high x[1] regions, for which scaling violations occurs and DGLAP equations, which are used to extrapolate PDF across Q^2, do not hold [71–74].

Most of the data used for the PDF (Parton Distribution Functions) fits come from NuTEV [75], CHORUS [76] and CDHSW [77]. From these, it is still unclear whether coupled DIS / nuclear effects such as the EMC effect or the anti-shadowing happen for neutrino interactions. These phenomena are observed in DIS electron scattering: it was shown that the nuclear cross section is enhanced in certain regions of x compared to the one of the free nucleon. They have unclear theoretical explanations.

Some more recent data from MINERνA [78] is hinting towards the same conclusion (absence of anti-shadowing effect).

For the hadronisation physics, it was recently noted that the HERMES data [79] could

---

[1] Q^2 is the momentum transfer of the probe to the target, and x is defined as $\frac{Q^2}{2M\omega}$, where M is the target mass (if at rest) and ω is the energy transfer.

used to better predict some basic quantities related to hadron multiplicities [80].

These processes need to be carefully studied in the context of higher energy beams, such as the DUNE [81–84] one, or NOνA [85] and atmospheric neutrino experiments [86].

1.2.7 Shallow Inelastic Scattering processes

Between the RES and DIS, other processes called Shallow Ineslastic Scattering processes can happen. This is refered theoretically as the "transition region." These processes are added because the regions of validity of the RES and DIS cross sections are disjoint. In practice, the problem is overcome by using the continuum (background term) of the RES cross section and ensuring continuity in the W variable [25].

Although these channels are very important in the context of NOνA (because the neutrino energy distribution peaks at 2 GeV), there are still little theoretical calculations. A last notable reference is a two pions neutrino production calculation in [87].

1.2.8 Coherent pion production processes

The coherent processes happen when the W-boson from the neutrino has a very low momentum and cannot resolve individual nucleons inside the nucleus [88, 89]. In that case, the boson interacts with the whole nucleus. A pion is created from de-excitation of the nucleus and critically, this pion does not undergo final state interactions. Only recent nuclear data is sensitive to the coherent pion production processes, historical measurements date from 1988 with the experiments SKAT, BEBC, CHARM-II and E632 [90–93], that measured neutrino coherent pion production on neon. More modern experiments also tried to measure the coherent interaction on plastic scintillator, at the beginning unsuccessfully (K2K [94] and SciBooNE [95]). The first charged-current measurement on plastic scintillator was made by MINERνA [96], and was followed by T2K [97]. ArgoNeuT [98] also measured these interactions on liquid argon.

1.2.9 Electron neutrino cross sections

Electron neutrino cross sections have the same contributing Feynman diagrams as the ones shown in Figure 1.4. There are further differences expected since the fact that electrons have a smaller mass than muons opens phase space when one compares muon neutrino to electron neutrino cross sections. Further complications arise for the so-called Second Class Current (SCC) and radiative corrections [99]. The electron neutrino cross section in these energies always suffers from having very low statistical power (few events), since it is simpler to create an muon neutrino beam as will be seen later (Section 2.1). The current knowledge stems from bubble chamber experiments (Gargamelle [100]), T2K [101] and MINERνA [102]. There has not been an exclusive measurement of electron anti-neutrino cross section made on its own yet.

1.2.10 Anti-neutrino cross sections

Anti-neutrino cross sections are also a challenge because their cross section is about half of the neutrino ones. This happens because a cancellation appears in the matrix element of the anti-neutrino cross section due to the presence of the anti-neutrino.

Some experiments, such as MiniBooNE and MINERνA have been exposed to anti neutrino beams and have made measurement of the CCQE and CC1π cross sections [103–105].

1.2.11 Neutral-Current processes

All the cross sections described earlier have their equivalent in the Neutral Current (NC) channel. However, it is much harder to detect these processes due to the absence of a high energy lepton.

1.2.11.1 Neutral-Current elastic process

The CCQE equivalent is the NC elastic process (sometime referred as NCEl), which only produces a single proton (or a neutron) after neutrino interaction. As for CCQE, the nucleon-level information mostly comes from bubble chamber experiments [106–108].

1.2.11.2 Neutral-Current neutral pion processes

Another channel of interest is the NC1π^0, which leads to production of two photons via the π^0 decay. In the case when one of the photon has a low energy, it is very common to interpret these events as electron neutrino interaction, since both of them create electromagnetic (EM) showers in the Cherenkov detectors. Indeed, the photons, in the energy range of 100 MeV to 5 GeV interact via Compton scattering and create electron / positron pairs. At similar energies, electron loose energy by Cherenkov and bremsstrahlung [109] processes. All these interactions involve creation and excitation of electrons and positrons and therefore create the same signal.

This was already a problem at K2K which used the water Cherenkov Kamiokande detector as far detector. To overcome this problem, the collaboration use its near 1 ton Cherenkov detector was used to measure this channel [110]. MiniBooNE later measured this same channel for neutrino and anti-neutrino [111]. The equivalent coherent process were also measured by the MiniBooNE [112] and by the NOMAD [113] collaborations.

1.2.11.3 Neutral-Current single photon processes

The channel of interest of this thesis is the "NC gamma," or neutrino-induced single photons. In this process, a single photon is created after the neutrino interaction. The phenomenology will be described in greater details in a subsequent chapter (Chapter 4). Note that there is currently no observation of this process. The only search that was ever done was conducted in the NOMAD detector [114]. For the same reason as the one described in the previous paragraph (similar photon and electron topology in detectors), the interest in this channel is increasing.

1.2.11.4 Neutral-Current diffractive processes

Very recently, MINERνA reported an unexplained excess of neutral pion-like events. Observations seem to hint towards the presence of a diffractive channel on hydrogen atom [115]. They have the same topology as the coherent events (i.e. very forward). However, a clear theoretical interpretation is still lacking. The observed cross section is small ($0.26 \pm 0.02(\text{stat}) \pm 0.08(\text{syst}) \times 10^{39}$ on hydrocarbon target [115]). It should be noted that these events are not in the neutrino interaction generators NEUT [27] and GENIE [25, 26] used for T2K analyses.

Chapter 2

The T2K Experiment

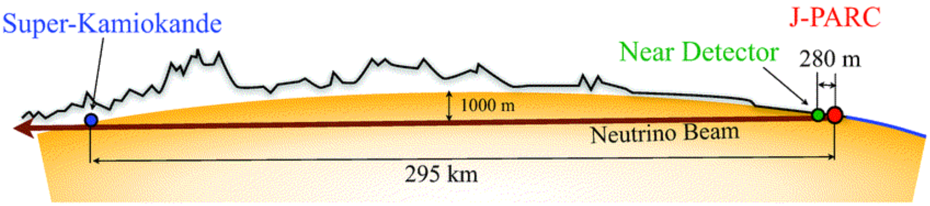

Figure 2.1: Overview of the T2K experiment (not to scale). Taken from [3].

The Tokai to Kamioka (T2K) experiment [3], represented in Figure 2.1, was designed to measure $\sin^2(2\theta_{13})$ via electron (anti-) neutrino (ν_e and $\bar{\nu}_e$) appearance in a muon (anti-) neutrino (ν_μ and $\bar{\nu}_\mu$) beam [3]. Neutrino and anti-neutrino measurements can lead to hints of a possible non-zero $\sin(\Delta\delta_{\mathrm{CP}})$ which would indicate violation of Charge Parity (CP) in the lepton sector. This is one of the remaining parameters of particle physics that has not been measured yet. T2K also measures $\sin^2(\theta_{23})$ via muon (anti-) neutrino disappearance [116].

To do this, it uses an off-axis neutrino beam and a far detector, Super-Kamiokande (SK), placed off-axis at 295 km from the Japan Proton Accelerator Research Complex (J-PARC) and a beam energy of 600 MeV, such that the ν_μ to ν_μ disappearance probability is maximum; the peak energy also coincides with the energy where the CCQE processes are the most likely to happen.

Two other detectors (the Interactive Neutrino GRID, INGRID and the off-axis Near Detector, ND280) are located 280 m away from the target and are used for beam and cross section measurements.

In all this thesis, unless stated otherwise, the Z direction refers to the direction between the target and the far detector (with the positive direction being towards the far detector), the X direction is the horizontal direction and Y is the vertical direction (positive Y being upwards).

2.1 T2K Beamline

The neutrino beam is created by impinging 30 GeV protons on a carbon target at the J-PARC facility in Tokai, Japan [117]. This produces pions and kaons that mainly decay into muons and neutrinos, as can be seen in the listing in Table 2.1. In Figure 2.2, the beam spectrum for different off-axis angles of the neutrino beam is shown. This technique was developed in 1995 at BNL [118]. The main idea is to use the 2 body decay kinematics of the hadron to predict the neutrino energy, which comes from considering the energy and momentum conservations equation of a pion decaying to a neutrino and a charged lepton:

$$E_\nu = \frac{m_\pi^2 - m_\mu^2}{2(E_\pi - p_\pi \cos\theta_\nu)}. \tag{2.1}$$

Assuming that the parents of the neutrino are mainly pions of mass m_π, energy E_π and momentum p_π; they decay into a muon of mass m_μ and a neutrino of energy E_ν and angle θ_ν with respect to the pion trajectory.

When one integrates the pion kinematics from the pion energy distribution, it can be found that the energy distribution of the neutrinos also becomes more peaked (smaller width of the distribution) for increasing off-axis. This effect is visible in Figure 2.2: increasing the off-axis angle of the neutrinos reduces the peak energy of the neutrino flux and the width of the neutrino energy distribution. At T2K, the ν_μ beam whose energy is centred at 600 MeV when viewed from an off-axis angle of 2.5° as seen on Figure 2.2. This angle was optimised to maximise the disappearance probability of the muon neutrino as can be seen in top of Figure 2.2.

At J-PARC, the production of the neutrino beam is realised in 3 stages:

- first, protons are accelerated in the J-PARC accelerator;
- then, they are monitored and transported to the target in the primary beamline;
- finally, once the protons hit the target, the hadrons produced are propagated in the secondary beamline.

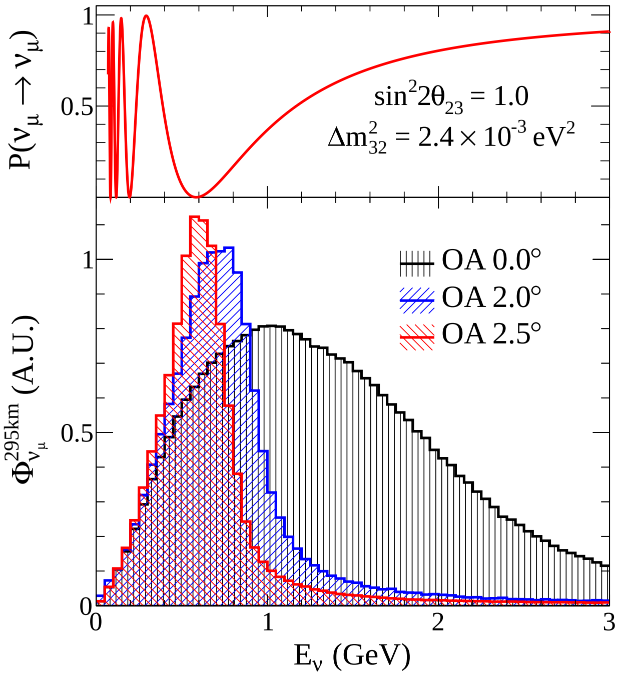

Figure 2.2: ***Top:*** Muon (anti-) neutrino survival probability at SK (295 km), against neutrino energy assuming maximal mixing ($\sin^2 2\theta_{23} = 1$) and $\Delta m^2_{32} = 2.4 \times 10^{-3}$ eV^2. ***Bottom:*** T2K neutrino flux energy distributions for different off-axis angles. Taken from [117].

The three parts leading to the creation of the neutrino beam are now described.

2.1.1 J-PARC accelerator

The J-PARC accelerator consists of one linear accelerator (LINAC) and two synchrotrons (RCS for Rapid Cycling Synchrotron and MR for Main Ring). The LINAC is 300 m long and accelerates H^- up to 181 MeV. These H^- are converted to protons by charge-stripping foils while entering the RCS. The protons are then accelerated to 3 GeV, and then injected in the MR to be accelerated to 30 GeV. At this point, 8 bunches are circulating in the MR, and each of these contains roughly 3×10^{14} protons. These 8 bunches are then "kicked" (i.e. deviated) by magnets to go into the primary beamline. This process is repeated every $2 \sim 3$ seconds to create spills. The time between two bunches in the same spill is ~ 600 ns. Short spills allow efficient rejection of cosmogenic particles at the ND280 and SK.

Particle	Decay products	Branching fraction (%)
π^+	$\rightarrow \mu^+\nu_\mu$	99.9877
	$\rightarrow e^+\nu_e$	1.23×10^{-4}
K^+	$\rightarrow \mu^+\nu_\mu$	63.55
	$\rightarrow \pi^0\mu^+\nu_\mu$	3.353
	$\rightarrow \pi^0 e^+\nu_e$	5.07
K^0_L	$\rightarrow \pi^-\mu^+\nu_\mu$	27.04
	$\rightarrow \pi^- e^+\nu_e$	40.55
μ^+	$\rightarrow e^+\bar{\nu}_\mu\nu_e$	100

Table 2.1: Neutrino-producing decay modes considered in T2K's flux simulation and their branching ratio in percentage. Decay modes for $\bar{\nu}_\mu$ and $\bar{\nu}_e$ are omitted in this table, but can be derived by taking the charge conjugate of the π^-, K^- and μ^- modes. Reproduced from [117].

2.1.2 Primary beamline

The whole beamline is represented on the left of Figure 2.3. The primary beamline consists of a preparation section of 54 m which contains eleven magnets (four steering magnets, two dipole magnets, and five quadrupole magnets to focus the beam), an arc-section of 147 m composed of fourteen superconducting magnets to bend the beam by $\sim 80°$, and a final focusing section (37 m). This last section directs the beam downwards and focuses the beam on the target; it contains ten magnets (four steering magnets, two dipole magnets and four quadrupole magnets).

The primary beamline is instrumented to monitor the proton intensity, position, profile and losses.

The proton intensity stability measurement is done by five current transformers (CTs) around the beam. Schematic representation of a CT is given on the left of Figure 2.4.

There are fourty Beam Loss Monitors (BLMs), which are gaseous detectors around the beamline. They are able to detect protons escaping from the beam which ionise the gas. The BLMs can trigger an interlock which stops the operations of the beam if the losses exceed a certain threshold value.

Nineteen SSEMs (Segmented Secondary Emission Profile Monitors) are located in the beam pipe. They consist of strips oriented in the X and Y directions placed in front of an anode foil; a bias voltage is then applied between the strips and the anode. When the beam goes through, it creates electrons on the strips that are accelerated to the anode. This process generates a current on each strip directly proportional to the number of protons crossing it. An illustration of the device is given on the right of Figure 2.4. Because the SSEMs are destructive of the proton beam and lead to unacceptable beam loss, they are movable and are only used at specific times, during the so-called “beam tuning” runs. In normal physics runs, only the last SSEM is used.

Finally, twenty-one ESMs (Electro-Static Beam Position Monitor) are located near the SSEM to measure the electrostatic shape of the beam; these are capacitors which give access to the position of the beam in the beam pipe.

2.1.3 Secondary beamline

The most upstream components of the secondary beamline are in the target station. It contains the OTR (Optical Transition Radiation Monitor), which is a device composed of a foil that produces radiation and fluorescent light when the beam crosses it. This is imaged using mirrors and a camera. This device has access to the beam position and size before it hits the target, 280 mm downstream of it.

The target is a graphite cylinder. Its length is 91.4 cm and its diameter 2.6 cm. The size and material have been carefully designed to resist the heat wave generated by the high intensity proton bunches impinging it. The target is surrounded by an inert helium vessel (15 m in length, 4 m in width and 11 m in height).

The other parts of secondary beamline are downstream of the carbon target, i.e. they manipulate and monitor the hadrons produced by the proton collision on the target. This part is represented on the right hand side of Figure 2.3.

Downstream of the target station, one finds a decay volume for the hadrons. It is an empty 96 m long steel tunnel, which measures 1.4 m wide upstream and 3.0 m wide downstream, whereas the height is increased from 1.7 m to 5.0 m between the upstream and the downstream part.

Finally, the beam dump is downstream of the decay tunnel. It is used to stop the muons and the hadrons that have not decayed in the tunnel. The MUon MONitor (MUMON) is placed just after the beam dump to detect the muons going through.

Three magnetic horns are placed around the secondary beamline. The first one is around the target station and serves to collect the pions. The second and third ones focus the pions. In neutrino mode, these horns operate at 250 kA and produce a magnetic field of up to 1.7 T (so-called Forward Horn Current, FHC). The current can be reversed to focus negative pions and produce an anti-neutrino beam (Reverse Horn Current, RHC). The effect of the horns is to increase 17-fold the neutrino flux at the far detector. They also provide better rejection of wrong sign hadrons which produce background neutrinos for oscillation analysis, making them fundamental parts of the T2K experiment. The beam composition at the off-axis near detector is shown in Table 2.2.

Energy Range [GeV]		0 to 1.5	1.5 to 3.0	greater than 3.0	all
Beam mode	Flavour	Proportion: relative (total)			
Neutrino	ν_μ	93.8%(84.9%)	81.7%(4.55%)	88.6%(3.49%)	92.9%
	$\bar{\nu}_\mu$	5.23%(4.74%)	14.1%(0.784%)	7.97%(0.314%)	5.83%
	ν_e	0.869%(0.786%)	3.44%(0.192%)	2.8%(0.11%)	1.09%
	$\bar{\nu}_e$	0.0852%(0.0771%)	0.787%(0.0439%)	0.66%(0.026%)	0.147%
Anti-neutrino	ν_μ	7.07%(6.53%)	32.7%(1.68%)	42.4%(1.09%)	9.3%
	$\bar{\nu}_\mu$	92%(84.9%)	63.8%(3.29%)	53.5%(1.37%)	89.5%
	ν_e	0.131%(0.121%)	1.37%(0.0705%)	2.07%(0.0529%)	0.244%
	$\bar{\nu}_e$	0.83%(0.766%)	2.17%(0.112%)	1.97%(0.0505%)	0.929%

Table 2.2: Fraction of the total flux by flavour in bins of the neutrino energy when running in neutrino mode (run 4) and anti-neutrino mode (run 5) at the off-axis near detector (ND280). The fractions in parentheses are relative to the total flux over all neutrino energies. Extracted from the neutrino flux prediction from the T2K beam group [120].

After simulation and including the constraints from the replica target measurements at the NA61 / SHINE experiments [121–123], the flux uncertainty reaches $\sim 8\%$ at the energy peak and the different components of the flux can be estimated as a function of the neutrino energy for neutrino and anti-neutrino modes, as can be seen in Figures 2.5 and 2.6. This uncertainty is expected to decrease as more data from NA61 / SHINE are analysed.

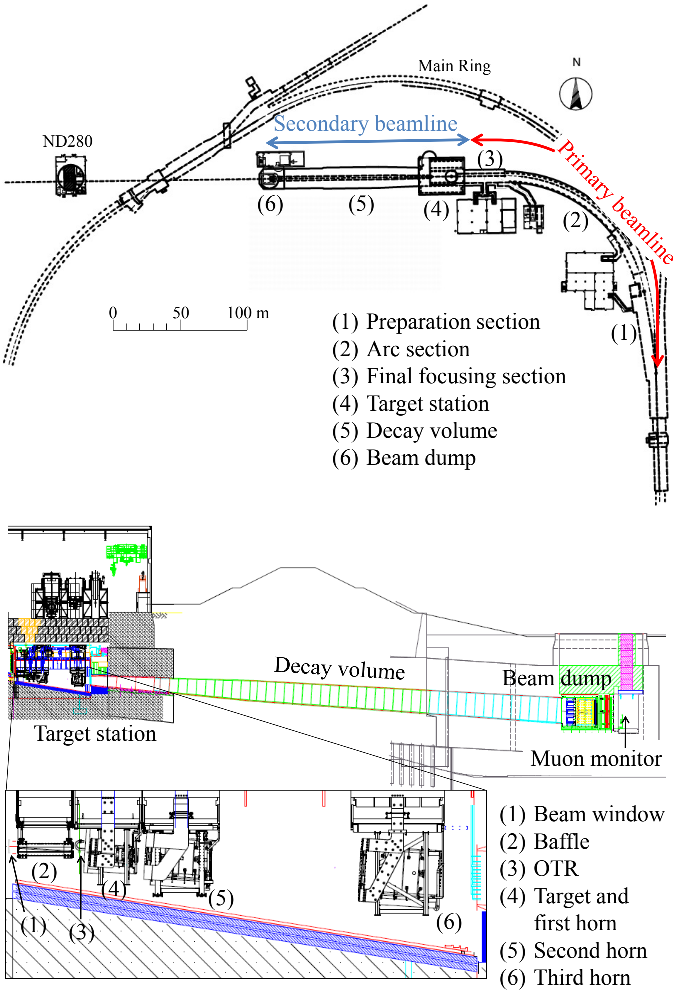

Figure 2.3: ***Top:*** Beamline at J-PARC. ***Bottom:*** Secondary beamline. Taken from [117].

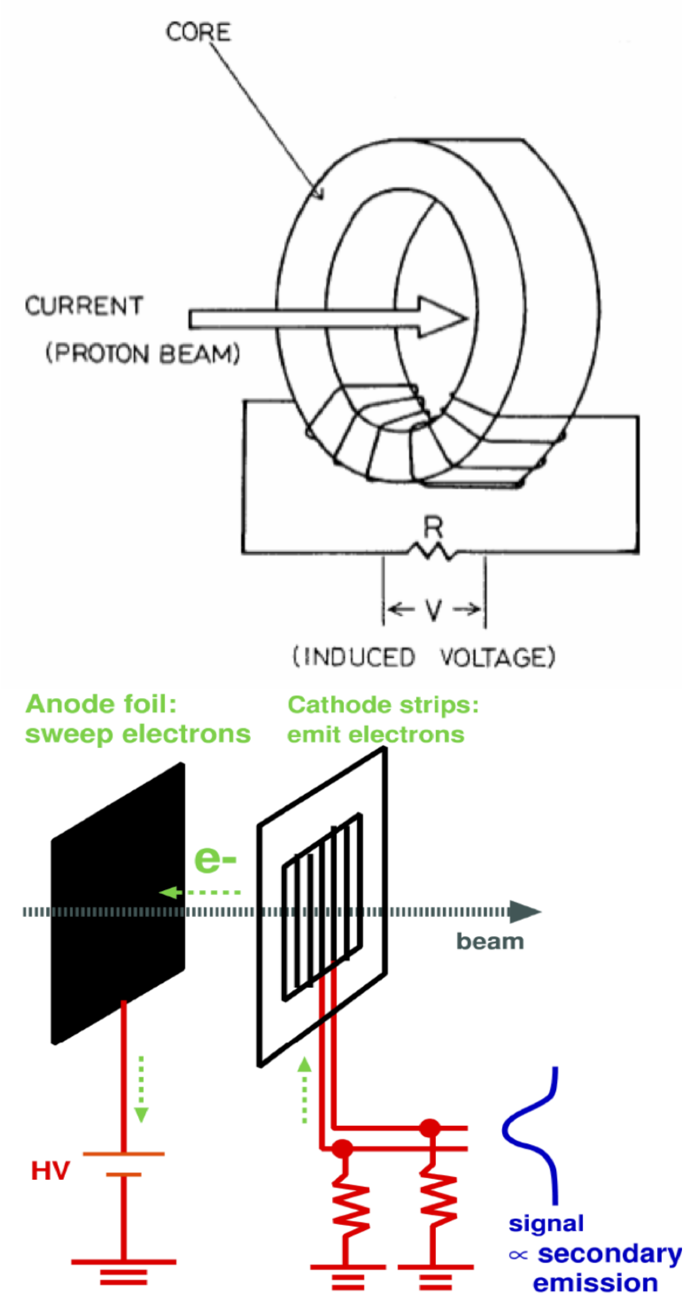

Figure 2.4: ***Top:*** Illustration of a CT. ***Bottom:*** A SSEM. Taken from [119].

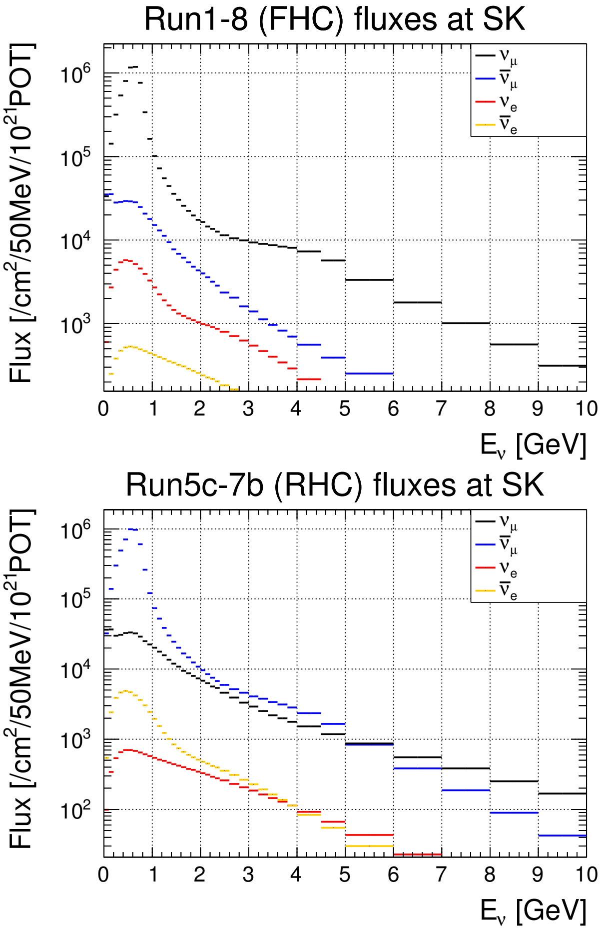

Figure 2.5: ***Top:*** Neutrino flux prediction in neutrino mode. ***Bottom:*** Neutrino flux in anti-neutrino mode. Extracted from the neutrino flux prediction and errors from the T2K beam group [120, 124].

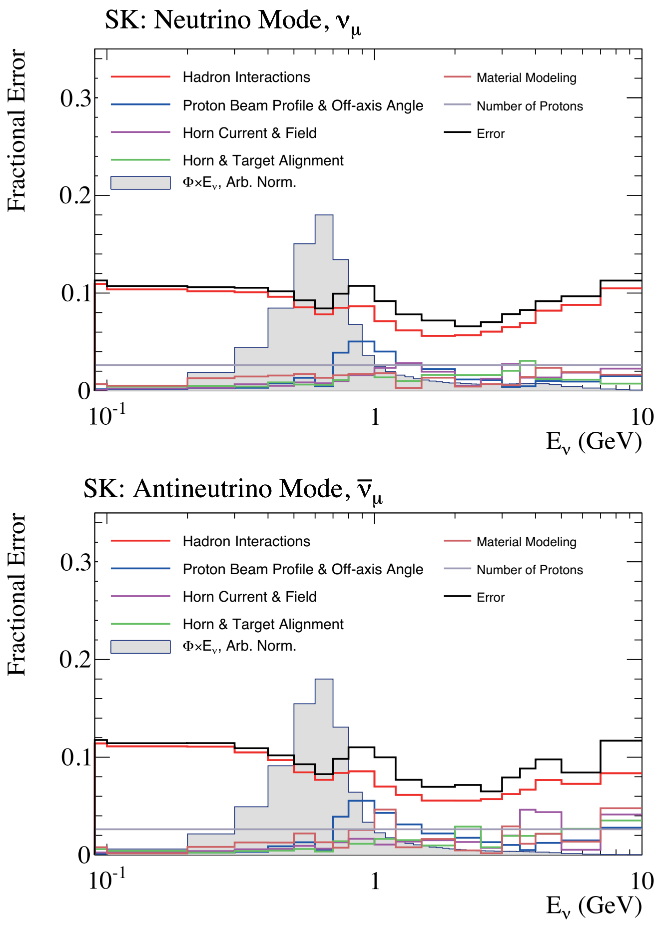

Figure 2.6: Top: Diagonal uncertainties on the ν_μ flux in neutrino mode at SK, overlaid with the neutrino rate (cross section times flux) ***Bottom:*** Diagonal uncertainties on the $\bar{\nu}_\mu$ flux in anti-neutrino mode at SK, overlaid with the neutrino rate. Extracted from the neutrino flux prediction and errors from the T2K beam group [120, 124].

2.2 Near detectors

The near detector suite is composed of 2 detectors, INGRID and ND280. Both of them are in the so-called "pit" (Figure 2.7). Their designs are described here.

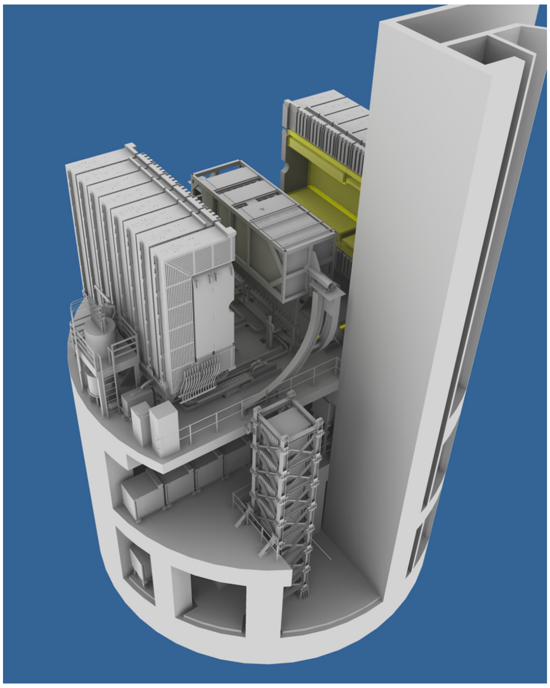

Figure 2.7: Near detector complex of the T2K experiment. On the top, the off-axis near detector at 280 metres (ND280) can be seen in open configuration; in the bottom, the Interactive Neutrino GRID (INGRID) cross structure can be seen. Taken from [3].

2.2.1 Interactive Neutrino GRID

The INGRID (Interactive Neutrino GRID) detector is composed of sixteen modules. They are placed in a cross structure as shown in Figure 2.8. The centre of the cross corresponds to the centre of the beam. INGRID's primary purpose is to monitor the beam centre. A 10 cm precision is required to get a 0.4 mRad precision in the direction of the beam which is an important input to know the peak energy as shown earlier in Equation 2.1.

All the modules have the same design. They consist of nine iron layers of $124 \times 124 \times 6.5\ \text{cm}^3$ providing a total target mass of 7.1 t for each module. These iron layers are alternated with eleven scintillator layers. Each one of these layers is made with forty-eight bars oriented both in X and Y directions (perpendicular to the beam axis). This cube is surrounded by a veto region made of twenty-two scintillator bars oriented in the

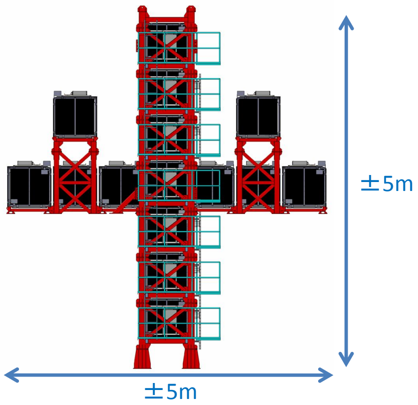

Figure 2.8: INGRID detector of the T2K experiment. Taken from [3].

Z direction. All the scintillators have a wavelength shifting fibre (WSF) going through the centre to collect the light produced by the particles. The scintillators are made of polystyrene doped with PPO and POPOP (which emits UV light from charged particle and shifts the light frequency to enhance the light absorption on the fibre, respectively). They have a rectangular cross section of 1.0×5.0 cm and are co-extruded with reflective material (TiO_2) to reflect escaping photons, thus reducing cross-talk between bars and enhancing the photon collection yield on the fibre.

In addition, a "proton module" was designed to study the protons from ν_μ interactions. The difference with the other module is that it has finer scintillator bars and no iron layer, which improves the tracking capabilities for short proton tracks. It is located between the two central modules.

The readouts were provided by the Hamamatsu company. They are Multi-Pixel Photon Counters (MPPCs). These photosensors are connected to the WSF which collects the light inside the scintillators. This set-up provides the timing and the detected light which are used to reconstruct the particles' trajectories, charge and momentum.

2.2.2 Multi-Pixel Photon Counter

The Mutli-Pixel Photon Counters (MPPCs[1], also referred as Silicon photo-multiplier, SiPM) are elementary parts of the near detectors at T2K. They are used in all the scintillator detectors and are the readout for the photons from the WSF[2]. A single MPPC measures $1.3{\times}1.3$ mm^2 and contains 667 individual pixels. The MPPC pixels are avalanche

---

[1] MPPC is a trademark of Hamamatsu Photonics, the MPPCs used at the T2K are the model S10362-13-050C [125].

[2] of reference: Kuraray Y11 (200) S-35 J-type [3].

photodiodes.

In the Geiger regime, which is the one the MPPC are opperated at, the output charge of the diode does not depend on the number of the photoelectrons that have fired the pixel, and the output charge is given by the simple relation:

$$Q = C(V - V_{\mathrm{BD}}), \tag{2.2}$$

where Q is the output charge, C ($\simeq$ 60pF) is the internal capacity of the diode and V is the applied bias voltage and V_{BD}, the breakdown voltage, which is around 70V. This set-up gives a gain of about $10^5 \sim 10^6$ (nominally 7.5×10^5). Note that the breakdown voltage is dependent on the ambient temperature (typically 50 mV/°C), so a change of few degrees can significantly modify the gains. The value of the gain has to be calibrated for each period of roughly constant temperature.

Since the pixels have a binary response (0 or 1 depending if the pixel was hit), this allows to count photo-electrons depending on the number of fired pixels. The charge deposited in the scintillator bar is roughly proportional to the number of pixels hit.

2.2.3 Off-Axis Near Detector at 280 meters

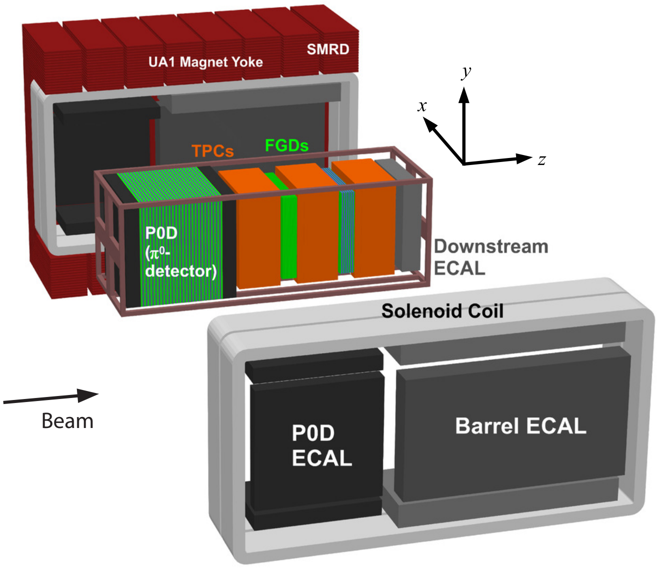

Figure 2.9: Exploded view of the ND280 of the T2K experiment, with its coordinate system and beam direction. Taken from [3].

The off-axis Near Detector at 280 metres (ND280), which is used in the analyses described in this thesis, is a composite detector enclosed in a magnet. The ND280 is illustrated on Figure 2.9. It is placed at a 2.5° off-axis angle to have the closest neutrino energy distribution to the one in the far detector. The description of the detector is made from the most outward to inward regions and upstream to downstream, where upstream refers to closest position to the target (left of Figure 2.9).

2.2.3.1 UA1 Magnet

The magnet consists of aluminium coils circulating around the ND280 as can be seen in light grey on Figure 2.9. They create a horizontal dipole field of 0.2 T. The return yoke (in red) and coils were reused from the UA1 and the NOMAD experiments at CERN. The yoke is composed of 2 C-shaped half yokes, that provide magnetic insulation for the surrounding of the detector. The yoke is used as a muon spectrometer and contain the magnetic field inside the inner region of the detector due to their low saturation field. Both halves are placed on rails that open to allow reach of the inner region. This is visible in Figure 2.7.

The magnetic field is a central part in the particle identification with the Time Projection Chambers as will be shown later, so the field was carefully calibrated in the whole detector before the inner parts of the detector were placed inside it.

2.2.3.2 Side Muon Range Detector

The Side Muon Range Detector (SMRD) [126] is placed inside the yoke and can identify escaping muons from neutrino interactions inside the inner detector. It also serves as veto (or trigger) for cosmic muons. It is composed of 2008 scintillator bars with coarse granularity ($7 \times 175 \times 875\text{mm}^3$) oriented horizontally and vertically.

2.2.3.3 Pi Zero Detector

The Pi Zero detector (P0D) [127] is a scintillator detector that was designed to measure the neutrino cross section of neutral pion (π^0) production on water. As scintillator offers better resolution than water, the idea is to have bags that can be filled with water between the scintillator bars. One can make two measurements: one with water in the bag and another one without water. Both measurements can be used simultaneously to get a cross section on water only.

The P0D is made of fourty modules each containing 134 vertical and 126 horizontal scintillator bars, alternating with brass as depicted on Figure 2.10. This set-up is realised to damp the EM showers. The scintillator bars have very similar design to the ones in the

INGRID detector (PPO and POPOP doped, coated with TiO_2, using a WSF and MPPC readout), except their triangular cross section as can be seen in the insert of Figure 2.10. Their sizes are 33 mm at the base of the triangle, 17 mm for the height, similarly to what was done for the MINERνA neutrino experiment.

In the upstream and downstream parts of the P0D, the water is replaced by iron to contain the Electro-Magnetic (EM) showers.

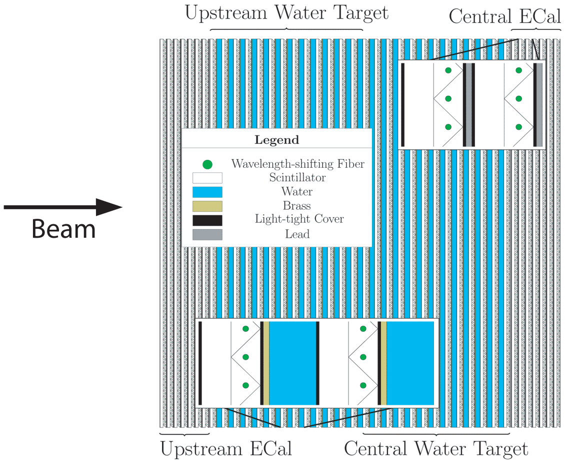

Figure 2.10: P0D of the ND280 at the T2K experiment. The neutrino beam is directed from the left to the right. Taken from [127].

2.2.3.4 Time Projection Chambers

Going downstream from the P0D, one finds the first Time Projection Chambers (TPCs) [128]. There are three TPCs in what is loosely called the tracker region (composed of the Fine Grained Detectors (FGDs) and TPCs region) of the ND280.

In the central part of the TPC, a cathode is polarised with a strong negative voltage (-25 kV) which provides a drift field of 275 V/cm across the inner box.

The TPCs are filled with a mix of argon, CF_4 and iC_4H_{10} gas (where the i stands for the “iso” isomer, which means the molecule has a pyramidal configuration) at atmospheric pressure. This choice of pressure is to reduce the strains and deflections on the side panels of the TPCs, as this would distort the drift electric field in the chamber. When a charged particle enters the detector, it ionises the gas and the electrons, typically a hundred electrons per cm are created in the gaseous argon at atmospheric pressure. These ionisation electrons are drifted to a charge detector (MicroMegas). The drift time depends on the density of the gas and is typically between $10 - 100$ μs.

The MicroMegas on the walls opposite to the cathode, record the delayed pattern of the ionisation. A schematic view of a TPC is shown in Figure 2.11. On each wall of the TPC, MicroMegas are aligned in 2 columns of 6 MicroMegas with a vertical offset to avoid dead zones. Each MicroMegas is composed of a Micro Mesh Gaseous detector that amplifies the charge of the drifted electron by applying a strong electric field ($\sim$ 40 kV/cm) causing an electron avalanche (similar to an avalanche diode). The MicroMegas amplifies the signal by a factor of about 2000. This gain is inversely proportional to the pressure of the gas and thus the current atmospheric pressure. The electrons from the cascade are then read in the MicroMegas Pads, which is later called a hit. The size of a MicroMegas is 342×359 mm^2 and each of them is meshed in a 36×48 array of pads, that have sizes of 6.85×9.65 mm^2. This is the typical spatial resolution for a charged particle crossing the detector.

The argon chamber is surrounded by another gas chamber filled with carbon dioxide (CO_2) to insulate it electrically.

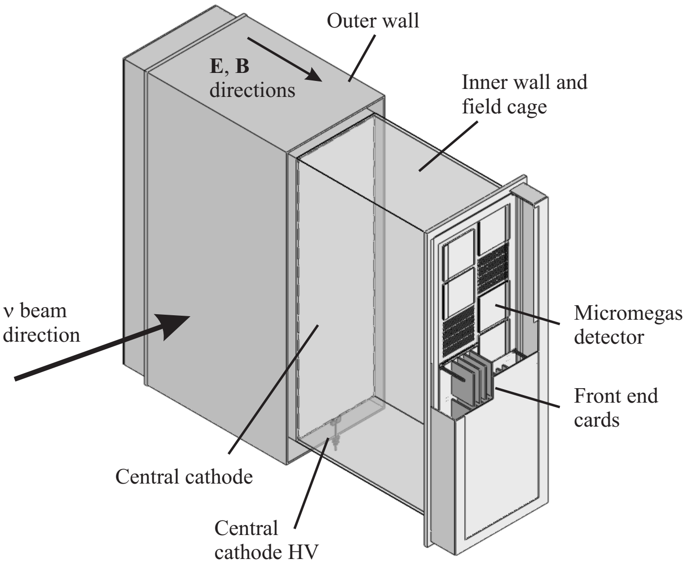

Figure 2.11: Schematic view of the TPC in the ND280. Taken from [128].

The TPC is a very precise detector that can be used for pointing the particles and measuring their momentum in the magnetic field and Particle IDentification (PID) by measuring the energy loss along the trajectory (dE/dx) of the particle from the local curvature of the trajectory in the magnetic field. This is visible in Figure 2.12, which shows the dE/dx of the several particles (positrons, anti-muons, positively charged pion and proton) as measured in the TPC against their momentum.

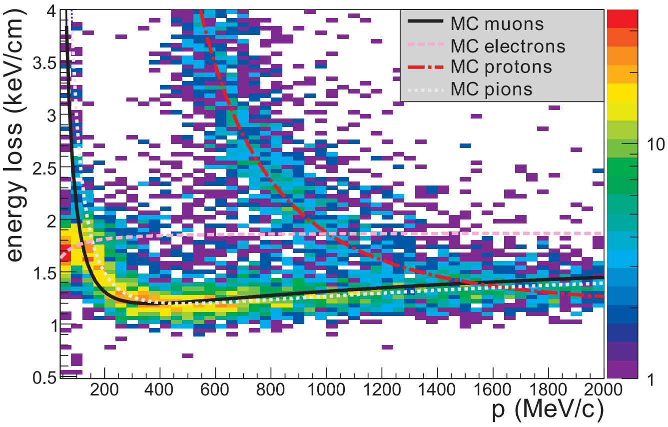

Figure 2.12: TPC dE/dx for different ionising particles of positive charge in the TPC. Taken from [128].

2.2.3.5 Fine Grained Detectors

There are two Fine Grained Detectors (FGDs) [129] in the ND280; they are placed in between the TPCs. Each FGD is composed of scintillator bars which have small cross sections ($9.61 \times 9.61 \times 1864.3$ mm^3). They are oriented in the X and Y directions, alternately. Each scintillator bar has a WSF in it and a MPPC associated at one end. It has the same characteristics as those of the INGRID or P0D.

When a Minimum Ionising Particle (MIP) enters one bar of the FGD, it produces generally between ten to thirty photons. Most of these enter the WSF and reach the MPPC. The MPPCs amplifies the signal with a gain of about 5×10^5 to create a detectable charge.

Each of the thirty layers is composed of 192 bars, providing active carbon target of 1.1 t. For the second FGD, six layers were removed and filled with water to allow neutrino water cross section measurement similar to what was described in P0D section.

2.2.3.6 Electromagnetic Calorimeter

The whole ND280 tracker region (composed of the three Time Projection Chambers and two Fine Grained Detectors) is surrounded by an Electromagnetic Calorimeter (ECal) [130]. This detector was designed to measure π^0 coming from neutrino interaction inside the tracker region.

The ECal is composed of six modules surrounding the tracker (BrECal, for barrel ECal) parallel to the Z direction, six modules surrounding the P0D (P0DECal) and another placed after the third TPC (Downstream ECal, DsECal). All the ECal modules are made of scintillator bars. These bars have a cross section of 4.0×1.0 cm^2 and have with similar specifications as the P0D, FGD and INGRID bars. The scintillator bars are alternated with lead layers to develop the showers.

The DsECal is composed of thirty-four layers of lead alternated with fifty layers of scintillator bars oriented in X and Y directions. A similar design was made for the BrECal, with thirty-one layers of lead.

The P0DECal is different because of the P0D size and the available space in the UA1 magnet. It only has five layers of lead and six active layers of scintillator, all of which are oriented in the same direction.

The BrECal and DsECal have an interaction length allowing containment of all the showers ($\sim 10\text{X}_0$[1]) whereas the P0DECal cannot contain some of the showers due to its reduced size (3.6X_0). The P0DECal was designed to veto external particles.

Note that the BrECal and the P0DECal were placed in the detector at the start of the run 2 of T2K, over the summer 2011.

2.3 The far detector: Super-Kamiokande

The far detector (SuperKamiokande, SK) is located at 285 km away from the graphite target at J-PARC, in the Kamioka mine, on the western cost of Japan [4]. The mine is 1,000 m deep, under the mount Ikenoyama, which is equivalent to roughly 2,700 m.w.e. (metre equivalent water).

The geometry of the detector is cylindrical (vertically), and the vessel is made of stainless steel. A diagram of the detector is shown in Figure 2.13. SK is composed of two coaxial cylinders that define the inner volume and the outer volume. The inner detector has a diameter of 33.8 m and the outer detector is 2 m wide. Its height is 36.2 m. This provides a fiducial volume of 22.5 kton of ultra-pure water.

The inner detector is surrounded by 11,129 PMTs pointing inwards of the detector, providing a 40% photocoverage. The PMTs detect the Cherenkov lights from charged particle after neutrino interactions. There are also 1,885 PMTs pointing outwards in the outer detector volume to veto events that happen outside the detector. Each PMT can detect single photons. They are sensitive to photons of wavelengths in the $350 - 500$ nm

---

[1] X_0 is defined as the length for which an electron / photon has $sim63\%$ chance to interact. This length is normalised by the density of the material its units are g/cm^2.

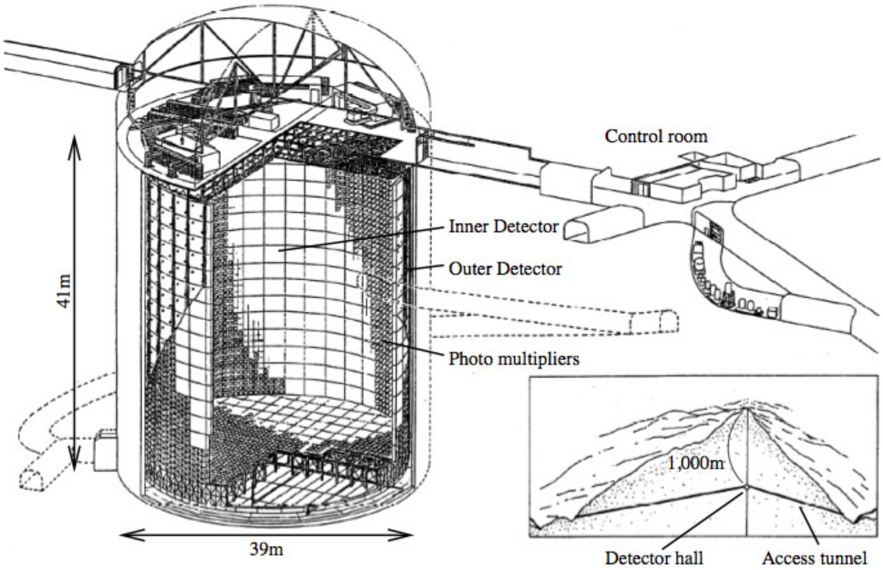

Figure 2.13: Schematic view of the SK detector. Taken from [4].

range and the maximum quantum efficiency is reached for photons of wavelength ~ 400 nm (21 % efficiency). The number of photo-electrons is multiplied by a system of eleven dynodes of Venetian blind type which are providing a gain of about 10^7 when operated at around 2 kV, as is the case in SK [131].

Note that to produce Cherenkov light, a charged particle must propagate at a velocity faster than the speed of light in the medium it traverses. This means there is a threshold of energy for a particle to be detected, which is given by $p > m/\sqrt{n^2-1} = m/1.27$, where p and m are the momentum and mass of the charged particle, and n is the refractive index of the medium, (1.3 in water).

In Figure 2.14, the signal produced by electrons and muons from T2K is shown. The somewhat simple design of the detector allows a very efficient separation between muons and electrons. Indeed, muons have a large mass (105.6 MeV) and therefore propagate relatively straight in water. This is the reason muons produce a clear Cherenkov ring on the SK wall. Electrons on the other hand, because of their small mass, change direction and produce EM showers when propagating (bremsstrahlung photons, Compton scattering, pair production). They will produce a more poorly defined (or "fuzzier") Cherenkov ring on the wall.

The detector can also detect delayed signals from Michel electrons and detect charged current interaction with one charged pion in the final state. In this case, if at least 30 hits are detected 100 ns after the primary trigger, a decay electron is tagged. The electron neutrino CC1$\pi^{\pm}$ sample was introduced for 2017 analyses [132]. It gives a higher statistical power to the appearance signal and thus makes the T2K experiment more senstive to CP violation in the neutrion sector.

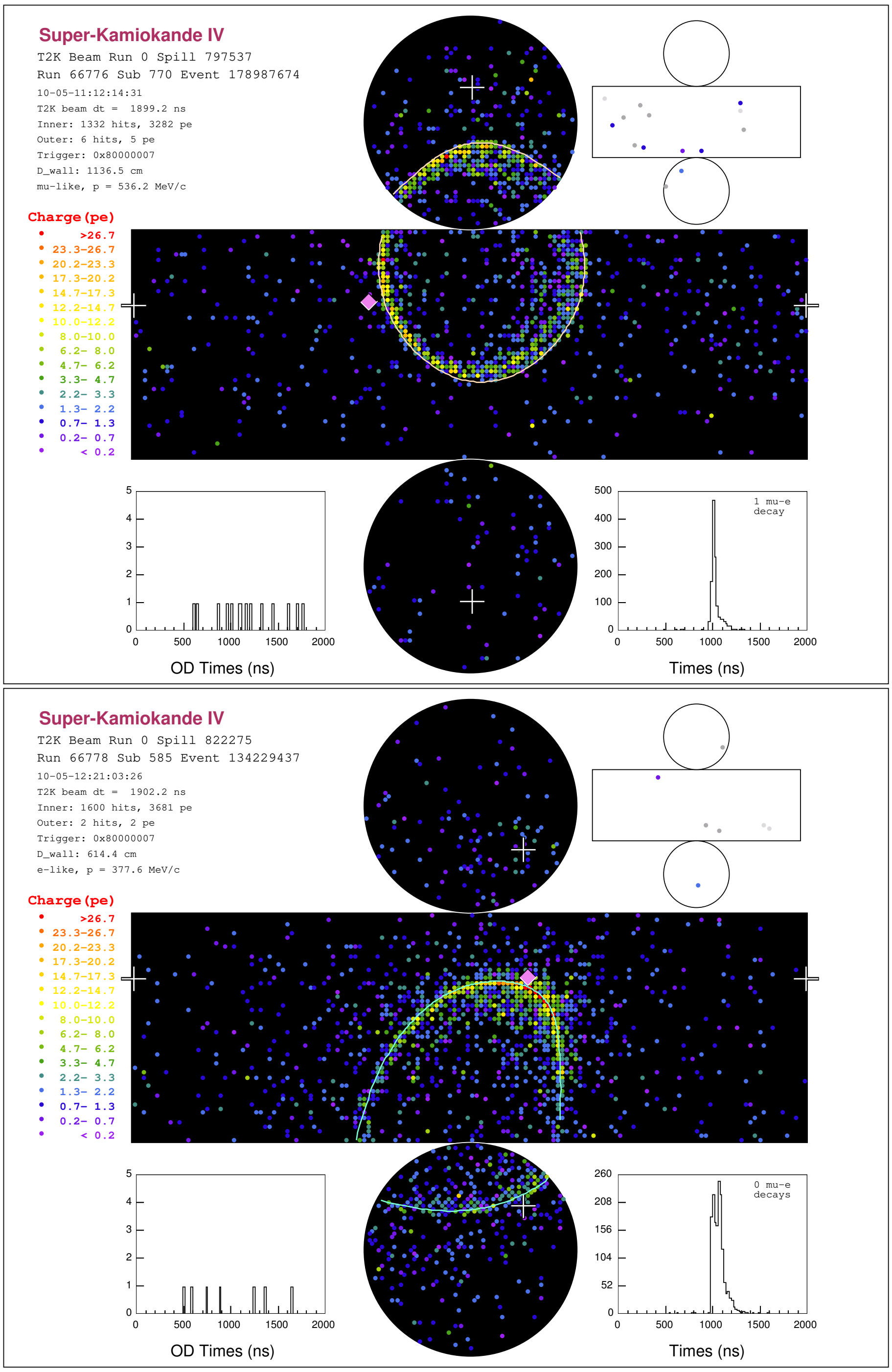

Figure 2.14: Events observed at SK. ***Top:*** ν_μ candidate. ***Bottom:*** ν_e candidate. The Cherenkov light ring is "fuzzier" in the case of ν_e due to multiple scatter of the electron. Both taken from [3].

Chapter 3

Electromagnetic Calorimeter data quality

An additional task of monitoring the data quality of the electromagnetic calorimeter was conducted during the PhD, this task is described here. A good quality of data for the ECal is required for the both analyses described in this thesis, as will be described later. Both the analyses (Neutral Current single photon search and ND280 electron (anti-) neutrino selection) use the ECal for vetoing events and the ND280 electron (anti-) neutrino selections uses the ECal for particle identification.

To ensure that the quality of the data is good for all the components of the experiment, checks are realised by the beam, ND280 and SK groups. For the ND280, each sub-detector is checked individually by a data quality expert who produces monitoring plots every week during the period of data taking and when the detector is powered on. In the case of the ECal, the main quantities that are checked are the timing, the gains, the pedestals and the event rates, which are checked at the end of each run.

As shown in Section 2.2.3.6, the ECal encompasses different detectors in the ND280. The readouts for these are all separated into 12 Read-out Merger Modules (RMM) which are collecting data from a total of 366 Trip-T Front-end Boards (TFB). These TFBs are directly connected to each channels (Multi-Pixel Photon counter, MPPC). Typically, the checks are divided for each RMM and each of them is checked individually.

Once the normal operation has been established for all the RMMs, a flag is uploaded to a SQL database which is later used for processing the data. Each RMM is treated independently. The flag is a 12 bit field translated to decimal number which is assigned between two timestamps. During the normal running of the ECal, the flag will be 0 (or 000 000 000 000 in the binary basis), whilst if a RMM is not working normally the flag will be equal to 2^{RMM}. If several RMMs are not working properly then the sum of these numbers will be the flag[1]

This task has been carried out for the 12 RMMs of the ECal during two years. For the purpose of clarity, only the run 7 RMM0 data (which is the 2016 data of half of the DsECal), is shown in this section, unless stated otherwise.

In the first section, the beam timing monitoring is explained; then the monitoring of gain and pedestal are described. Finally, the stability of event rates is demonstrated in the last section. This section shows that the RMM0 of the ECal (and more generally the whole ECal) has produced good and usable data for run 7 data-taking period.

3.1 Beam timing

The reconstruction good timing of the hits in the detector are required to be able to match the track between the ND280 sub-detectors. Knowledge of the beam timing in the ECal relies on the offsets introduced by the electronics, which can be simulated.

In Figure 3.1, one can see some examples of timing distributions. In this figure, one clearly sees the bunch structure of the beam.

The blue bands are the ECal reset windows between each bunch. It can happen that the high voltage fluctuates and introduces some variations in the beam timing profile. For run 7, this has been very rare and it is believed that all the fluctuations in these histograms are due to changes in the configuration of the beam itself rather than in the ECal. For other runs, it was noted that fluctuations could happen if the power supply of a RMM changes, or if a mistake is introduced in the cabling of the RMM while maintaining the detector.

The check consists of producing figures such as the one on the right of Figure 3.1 every week, and checking that all the points are aligned. Any deviation from constant beam timing has to be explained and flagged accordingly.

3.2 Gain and Pedestal of the MPPC

The ECal gains for each channel are also checked every week. Fast and large gain variations are not desirable as they make the calibration more complex, and can be indicative of a problem with the ECal or its power supply. The ADC[2] counts of each channel can be used

---

[1] For example, if RMM2, 3 and 11 were not working normally the bit field will be: 100 000 001 100, which translates to $2^{11} + 2^3 + 2^2 = 2060$ in the decimal basis.

[2] ADC: Analog to Digital Converter

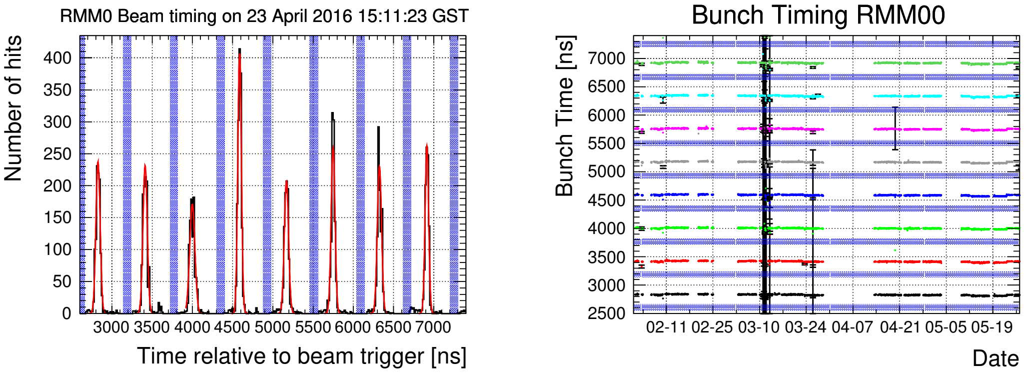

Figure 3.1: ***Left:*** Beam timing data (black) for RMM0 fitted by 8 Gaussian curves (red). ***Right:*** Mean of the Gaussian fits over extended period for the run 7. Note that all the points with a large error are points for which the Gaussian fit did not converge properly as there were too few points to fit. The ECal reset window are in blue on both figures.

to calculate the pedestal and gain values. To do that, the ADC counts are stored in a histogram over a period which corresponds to about 20 minutes (usually 500 events). An example of the histogram is shown in Figure 3.2 for a longer period. In this histogram, the first peak corresponds to having no hit in the MPPC and is called the pedestal. The pedestal is the ADC value when nothing happens in the detector. One could manually set the pedestal value to be read 0 in the ADC, however this is not preferable because the ADC is not linear in this region. The second peak corresponds to the ADC output when one photo-electron fires one pixel. The difference between the first two peaks provides a direct measurement of the single photo-electon response, i.e. the number of ADC counts for each detected photo-electron. This single photo-electron response can be use to calculate the gain.

Every week, the value of the pedestal and gain are checked. Note that on top of the built-in MPPC gain (of about 10^6 as shown in Subsection 2.2.2), there are two electronic gain channels:

- a high gain channel, where 1 PEU[1] is encoded in ∼ 10 ADC counts. This value can be seen in the difference between the two first peaks of Figure 3.2,
- and a low gain channel, where a 1 PEU is encoded in ∼ 1 ADC counts.

This provides two sets of measurements relevant for many detected photo-electrons, for the low gain channel; and few photo-electrons for the high gain channel. For the low gain, the pedestal and the first photo-electron peak are superimposed, and hence the equivalent

---

[1] PEU: Pixel Equivalent Unit, is the raw value in pC of the charge detected by the MPPC.

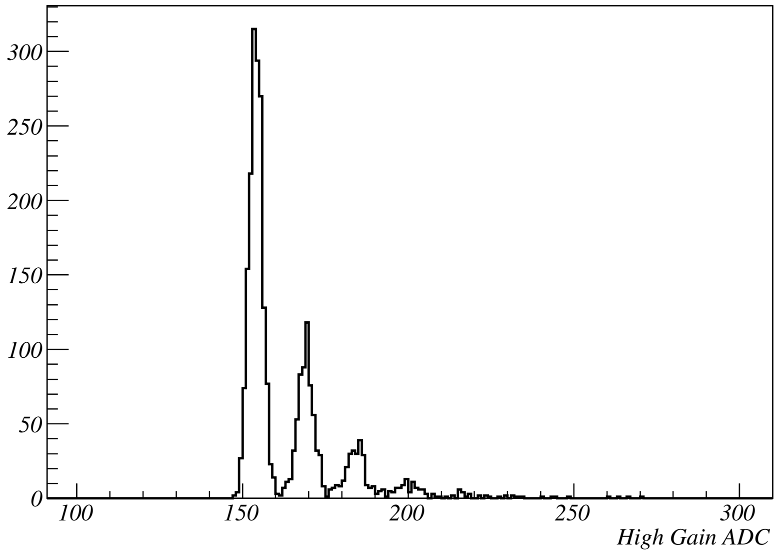

Figure 3.2: Few ECal ADC readings for the high gain channel, this figure is called a DPT (Data Processing Task) histogram. The histograms are realised by the processing nodes (TFB) by using the data from all the Trip-T detectors connected to the TFB during a period of around 20 min (500 events). On this figure, the first, second, third and fourth photo-electron peaks are visible from left to right. Such histograms are used during the calibration of the detectors. Taken from [133].

of Figure 3.2 for the low gain channel would only have one peak. This means the only gain that can be easily monitored is the high gain. It is also the most sensitive one.

To produce the weekly plots used for the monitoring, on Figures 3.3 and 3.4, a reference value of the gain is taken every time calibration is done (typically once every week). Then, the difference between the gain and the reference is "histgrammed" over the week for all the channels. The same procedure is applied for the high and low pedestal. The differences should be under 0.5 in absolute value (red line).

As for the beam timing, any deviation from the allowed regions should be understood and flagged accordingly. Since the gain are dependant on the temperature (see Section 2.2.2), it is very common that abrupt changes of temperature cause the gain to change to unacceptable values. This generally happens after a long shutdown, when the RMMs boards are cold, when the magnet is being closed or when the magnetic field is turned off of on. Additionally, extreme weather variations can cause unwanted gain variations. "Turn-on" effects are visible on Figures 3.3 and 3.4, where the gain and pedestal value change abruptly in the beginning of the run or after the winter shutdown.

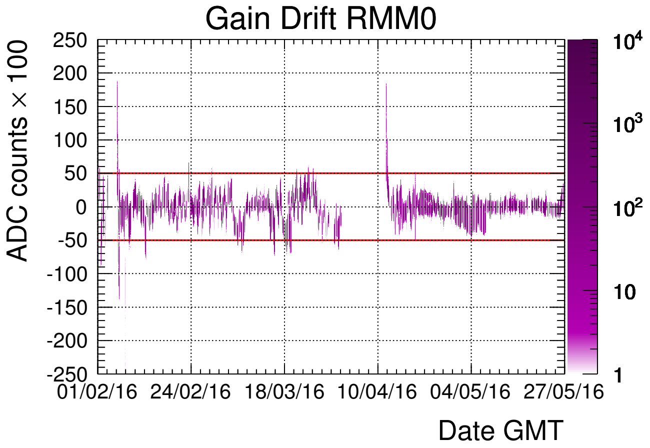

Figure 3.3: ECal RMM0 gain drifts over run 7.

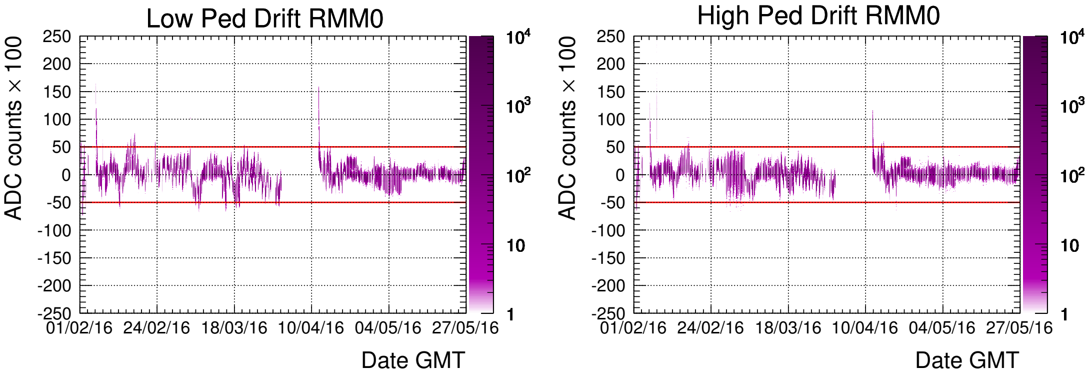

Figure 3.4: ECal RMM0 pedestal drifts over run 7. ***Left:*** Low pedestal. ***Right:*** High pedestal.

3.3 Event rates

Another final check that is realised consists in checking the event rate of the ECal. This is done once at the end of the run. To do this, a simple cluster algorithm is run on the data. One can then normalise the number of reconstructed clusters by the number of POT (Protons on Target). If the ECal runs normally, this number should be constant over time. Some changes can happen if the horn current is modified (if the horn current increases, for example, more neutrinos are going to be focused and reach the ECal thus increasing the event rate). Similarly, if the horn polarity is reversed, the fraction of neutrinos and anti-neutrinos reaching the ECal will be different and will lead to different event rates.

The result for run 7 is shown in Figure 3.5 (in this figure, all the RMMs cluster[1] rates are summed). One can see that the event rate for anti-neutrino mode is smaller than in neutrino mode. This happens because the both the anti-neutrino flux and cross section are much smaller than the in the neutrino case. As can be seen, some problems happened around mid-April, when the part of the BrECal was turned off due to a cooling issue.

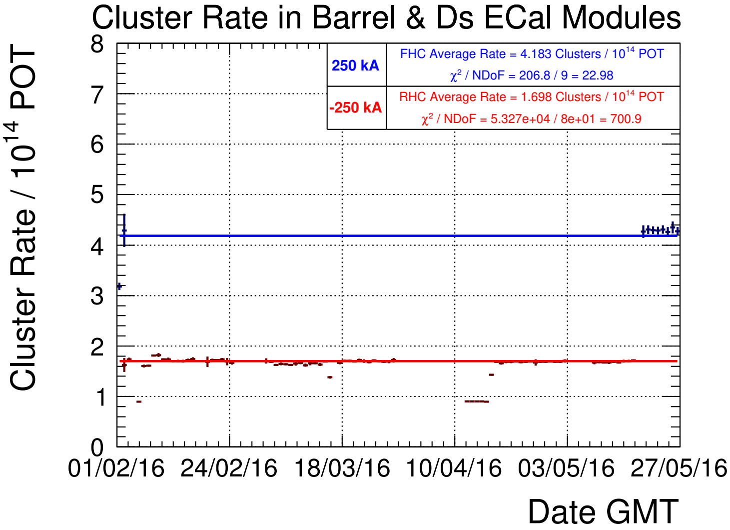

Figure 3.5: Cluster rate for all the ECal during run 7, during which the horn polarity was positive (FHC, in blue) and negative (RHC, in red).

3.4 Summary

From the three sections developed in this chapter, it is clear that the ECal of the ND280 delivers good and usable data. Monitoring the data quality is a fundamental step during the data-taking periods which ensures fast feedback and diagnostic of the problem to the expert in charge of the maintenance of the detector. This is critical as the T2K collaboration has to make sure that all the allocated beam time of the experiment can be used for physics analysis and thus address any hardware issue as fast as possible. The ECal data has found many use for ND280 analyses (high angles [134, 135], ECal as target analyses [136]) which includes the two analyses described in this thesis (NCγ and electron (anti-) neutrino selections).

---

[1] A cluster is defined here as at least three hits (i.e. at least one detected photo-electron for three different bars), in adjancent bars, in a time window of 30 ns. The cluster is expanded from the highest detected charge to neighboring bars. Note that for physics purpose, the number of required hits is seven, which is an additional security to noise clusters.

Chapter 4

Neutrino Neutral Current single photon phenomenology

This section covers the description of the "NC gamma", or single photon neutrino-production processes in more details. There is no data that can constrain the cross section calculations that have been made up to now, however some models are more theoretically motivated than others. There are two main reasons why the NCγ interactions have an importance in the accelerator neutrino physics:

- The background in the so-called MiniBooNE low-energy excess [137,138]: This excess was discovered in the electron (anti-) neutrino samples of the MiniBooNE Cherenkov detector. NCγ processes are one of the background for the electron (anti-) neutrino samples. The presence of these processes with cross section enhanced by a factor of 2.7 could explain this excess [137].
- The background for search for CP violation at T2K or NOνA: Similarly to the MiniBooNE analyses, NCγ events are one of the background for electron (anti-) neutrinos. From the last T2K result [132], it is clear that this background is already a problem.

The reason NCγ events systematically are present in the electron (anti-) neutrino samples was developed earlier, it is because the photons and electrons produce the same signal in Cherenkov detectors (see Section 1.2.11.3).

Firstly, the models leading to these events are described, then the generator implementation of the models are explained. Accurate modeling of the NCγ processes becomes increasingly important as statistics in the electron sample increase and therefore the statistical uncertainty on these becomes smaller. All the available predictions (from generators and different theories) are summarised in Figure 4.1 for the integrated cross sections and

Figure 4.2 for simple one-dimensional differential cross sections.

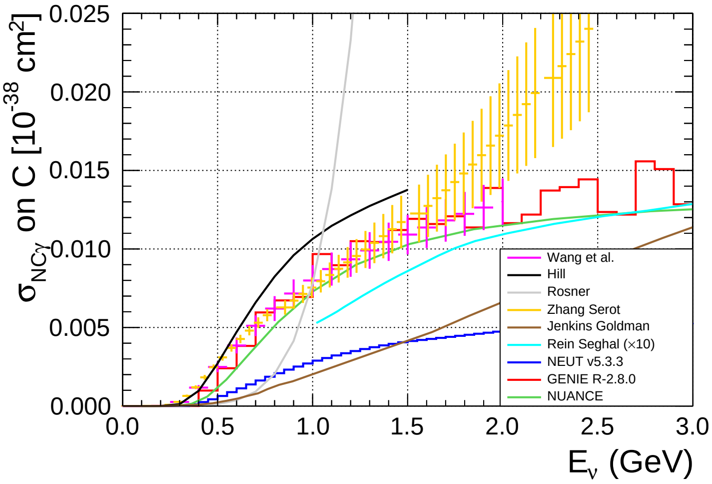

Figure 4.1: Integrated cross section for neutrino single photon production on carbon, based on the theoretical work from: Wang et al. [139], Hill [140], Rosner [141], Zhang et al. [142], Jenkins Goldman [143], Rein Seghal [144]. The following are neutrino interaction generators: NEUT [27], GENIE [25, 26] and NUANCE [145]. Figure based on [146] (Figure 43).

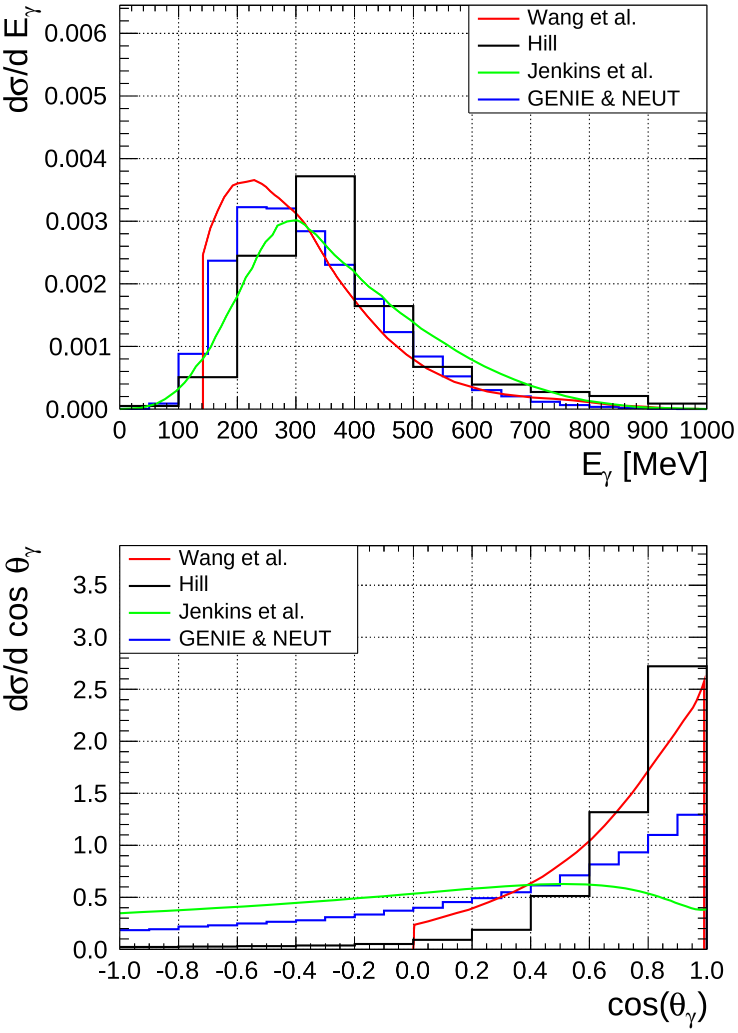

Figure 4.2: Differential cross sections for a 1 GeV neutrino single photon production on carbon. ***Top:*** Differential cross section in photon energy. ***Bottom:*** Differential cross section in photon angle (right), based on the theoretical work from: Wang et al. [139], Hill [140], Jenkins Goldman [143], NEUT [27]. The following are neutrino interaction generators: GENIE [25, 26]. All the distributions have been normalised to unit area. The NEUT and GENIE distributions are almost identical, so only the NEUT distribution was kept for clarity.

4.1 Models

Figure 4.3 shows the Feynman diagrams that are used in recent calculations [139–144]. All the models use a resonant production model based on the chiral description of the nucleus, except the Rein and Sehgal model which only has the coherent contribution. Note that this is a different model to the one that is implemented in the generators.

The model in [139] carefully estimates the background / Δ / higher resonances interferences by adding coherently all the amplitudes of the Feynman diagrams in Figure 4.3 (contribution 1 to 6). The model in [140] takes into account a the Δ contribution (1 in the figure), and an additional anomalous countribution (9 in the figure) All the known effects due to the nuclear medium are also taken into account. Figure 4.2 shows the differential one dimensional cross section available for the NCγ.

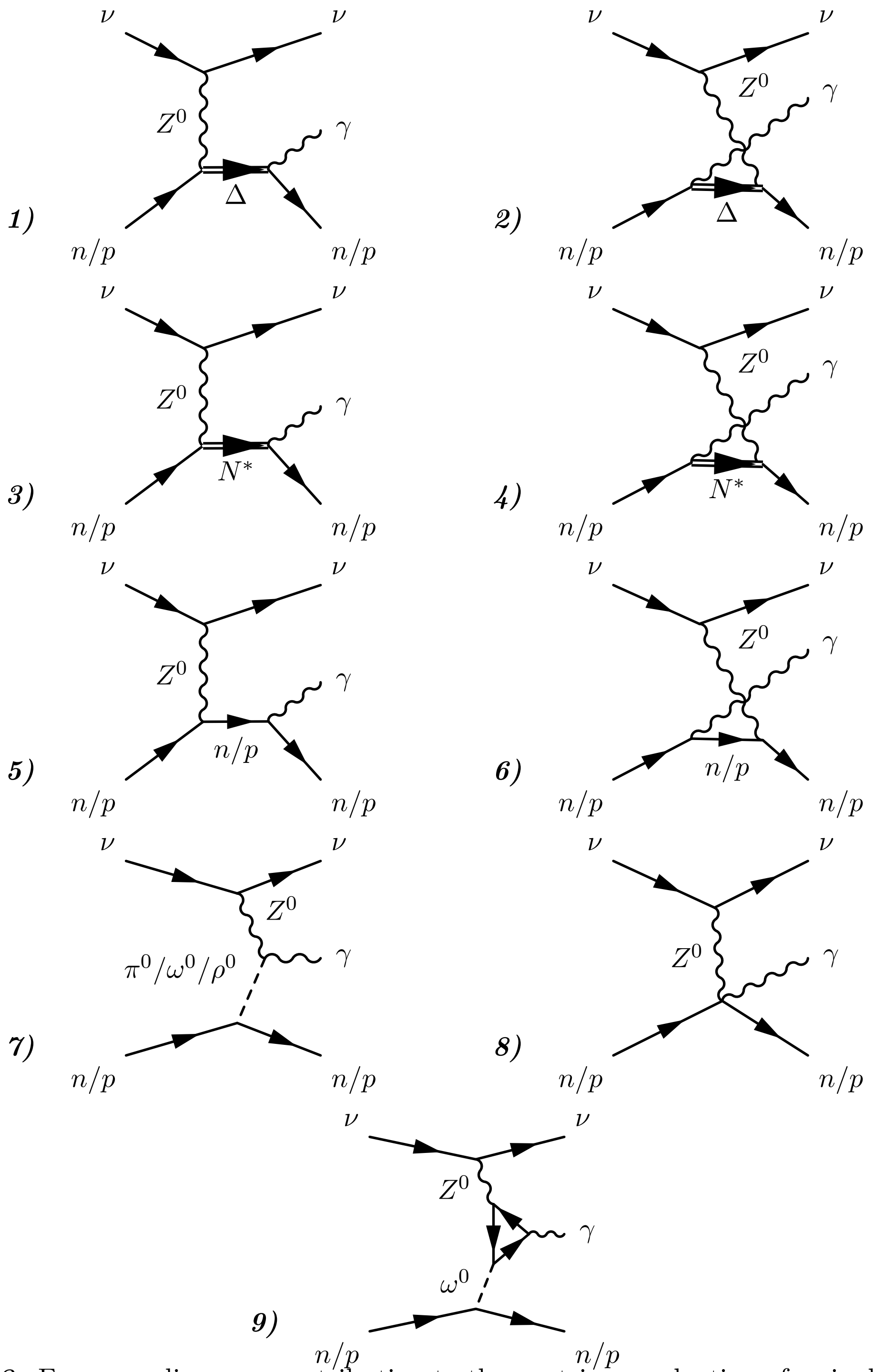

Figure 4.3: Feynman diagrams contributing to the neutrino production of a single photon: ***1)*** Direct Δ excitation. ***2)*** Crossed Δ excitation. ***3)*** Direct heavy resonance excitation. ***4)*** Crossed heavy resonant excitation. ***5)*** Direct nucleon excitation (or "background"). ***6)*** Crossed nucleon excitation. ***7)*** Meson exchange. ***8)*** Contact. ***9)*** Anomaly mediated.

4.2 Generators

The two main generators (NEUT [27] and GENIE [25, 26]) used for accelerator and atmospheric neutrino experiments use a similar way to treat the NCγ processes. They rely on the "standard" Rein and Seghal resonance production from neutrino interaction [56]. As was the case in the RES section (1.2.5), the cross sections are computed via a differential $\frac{d^2\sigma}{dQ^2 dW_{inv}}$ calculation. Note that these are free nucleon calculations. The only nuclear effects taken into account are the Fermi momentum of the struck nucleon and the Pauli blocking, and the final state effects for the outgoing nucleons. The photon does not undergo final state interactions, unlike a typical pion production. One of the main differences between NEUT and GENIE is the fact that the NEUT adds all the resonance contributions at the amplitude level, thus considering all the interferences between them. GENIE adds all the contributions incoherently.

The main problem with GENIE and NEUT's approach is that the invariant mass has no effect on the decays branching ratios of the resonance. This is quite counter-intuitive since there is, a priori, no restriction on the lower limit for the invariant mass, which could be smaller than the mass of a pion and a nucleon, and would therefore lead to an enhancement of the "NC gamma" cross section in this region of phase space. This problem was overcome in NUANCE [145], the generator used for the MiniBooNE experiment, where the branching ratio was manually changed for small W.

The other main problem is the absence of coherent effects in the generators, which is a contribution of around 10 % to the total cross section that has been neglected.

Finally, it was noted that a bug was present in NEUT: the branching ratios were wrong and producing 1/2 of the expected cross section [147]. This is visible in Figure 4.1. Note that this bug marginally impacts the differential cross section and therefore has a no effect on the result discussed in this thesis. This is because NEUT is only used to calculate the efficiency of the NCγ events as will be discussed in a subsequent chapter.

4.3 Summary

In this chapter, the predictions of the models leading to the neutrino-production of single photons are shown and explained. The conclusion is that the cross section for such events is much smaller than the cross section of dominant processes in T2K (CCQE). The NCγ cross section is roughly three orders of magnitude smaller than the one of CCQE at 1 GeV.

The absence of any measurement for NCγ processes leads to high uncertainties in the theoretical predictions and it is impossible to conclude which model is more suitable.

Chapter 5

Single photon selection

5.1 Introduction

This chapter details the selection of the NCγ events. First, the data sets are described. This section broadly explains how the triggers, calibration, reconstruction work and show which samples were used for the analysis. Then, the second section details the selection cuts. Finally, the performance of selection is shown.

The NCγ selection is largely based on the so-called "gamma selection", developed as a control sample for the ν_e CC inclusive cross section as was used in [101].

In short, it relies on identifying two electron tracks of opposite charges in the TPC that come from the FGD1. To be sure that these tracks come from a photon conversion, some simple requirements are made on the reconstructed invariant mass and the distance between the two tracks. Some vetoes are also added to reduce the contamination coming from outside the fiducial volume (OOFV) and from ν_μ CC interactions.

5.2 Data sets

This section covers three topics: how to process the recorded data, the software used for the selection and finally the data sets POT that are used in the analyses.

5.2.1 Data processing

In this subsection, the data processing steps are explained. In summary, the data has to trigger the detector to be recorded, it is then calibrated. A reconstruction software is run on the calibrated data and the data is put in a light weight format to be used in the selections and analyses.

5.2.1.1 Triggering

Each readout (such as the RMMs in the case of the ECal) is connected to a Slave Clock Module (SCM) which instructs to record the data of the subdetector each time they receive a trigger word. All the subdetectors are equipped with their own SCMs so that each one can be operated alone for debugging and calibration without the need to have the whole ND280 running.

Since the triggering is related to the timing of the neutrino, a Master Clock Module (MCM) which controls all the SCMs is synchronised to a GPS-based clock that indicates when the neutrino spills are created (so-called “beam triggers”). There are also two cosmic triggers that allow to record data from cosmic muon that happen outside the beam timing window. The cosmic trigger records the event when:

- the two FGDs trigger,
- or two opposite side subdetectors (such as top and bottom SMRD modules, left and right side BrECal, P0D and DsECal) are triggered in the same time.

More information about the Data Acquisition at the ND280 and triggers can be found in [3].

5.2.1.2 Calibration

Broadly, there are two types of calibrations. The ones that are done on scintillator subdetectors (FGDs, ECal, P0D and SMRD), and the calibration that is done on the TPCs. The calibration is made from constants that are in a MySQL database and is done by a package called “`oaCalib`” that gets called during the data processing.

Scintillator subdetectors calibration The aim is to correct the detector effects on the energy recorded by the detector and on the timing of the event. It involves precise knowledge of the subdetector and can change over time during the run or the day.

Common effects that get corrected are electronic noise, bar-to-bar corrections and ADC corrections, attenuation of scintillation photon with to the MPPC and the ageing of the scintillator.

To calibrate these detectors, LEDs are placed in the detector and can be used to measure the response of the subdetector to the known LED pulses. DPT histograms such as the ones in Figure 3.2 are also used for the gain calibration.

TPCs calibration The aim is to correct the drift electron trajectories due to electric and magnetic fields inhomogeneities. To achieve this, a laser system illuminates some "dots" on the cathode that create photo-electrons at a known place on the cathode. The pattern they create on the MicroMegas can be used for calibration. This method can also be used to calculate the gain of the MicroMegas.

5.2.1.3 Reconstruction

Time Projection Chamber To reconstruct charged particles creating ionisation electrons in the TPCs, the following steps are applied to the waveforms. These are the recorded ADC against time for all the channels) [148]:

1. Each time the waveform goes over a certain treshold, it is considered that an ionisation electron reached the MicroMega.
2. The MicroMegas which triggered at a similar time are then clustered horizontally and vertically to create straight lines in the Y and Z directions.
3. These clusters are then merged if they are close together in space and time. It can happen that the charged particle creates another particle (such as a δ-ray) and thus the merging of the cluster branches in two clusters. In this case, the algorthm chooses the path that creates the longest path. The merging of the clusters can also happen if they are not exactly adjacent.
4. Next, particle trajectories are adjusted on the merged clusters via a likelihood fit. The particle is assumed to move in a modified helix trajectory, due to the fact that particle looses energy in the gas by ionisation. The transverse drift diffusion (i.e. the fact that drift electron may not move in a straight line in the TPC) is also taken into account.
5. The determination of the t_0 (time at which the track enters the TPC) is important to reconstruct the X position of the particle. This is done by joining the particle

with the surrounding detector hits (note these are not reconstructed objects), which have much better timing resolution, via a Kalman fit.

Once the above steps are done, the momentum of the particle (in MeV) can be calculated at all the points of the reconstructed trajectory by applying the following equation:

$$|p| = 0.3 \times q \times B \times R, \tag{5.1}$$

where q is the charge of the particle in unit of e, B is the magnetic field in Tesla and R is the curvature radius in m.

Fine Grain Detector The FGD reconstruction [148] provides precise timing and vertex information for the charged particle and matching to the TPC reconstructed trajectories. The FGD can also be used for PID, however, this feature is not used in this analysis and therefore it will be omitted here (see [148] for its complete description). The following steps lead to the reconstruction of the FGD tracks:

1. The hits recorded in the FGD are sorted according to their timestamp and "time bins" of 100 ns are created. The hits that are clustered together.
2. Next, the time between a time bin and the TPC t_0 (which comes from individual hits rather than time bins) are compared. If the time is similar, the track is extrapolated from the TPC-FGD by computing a χ^2 between the extrapolated TPC track and the FGD hits in all the layer of the FGD (Kalman fit).
3. The TPC track trajectory is then refitted with this improved seed and t_0.

Electromagnetic Calorimeter The ECal reconstruction [148] aims to reconstruct charged and neutral particles entering the ECal. The algorithm is able to differentiate between shower-like and track-like events and reconstruct their position, timing and energy. The following steps are applied on calibrated hit-level data [136]:

1. The hits are sorted according to their timing and a time bins of 100 ns are created in a similar way as the FGD, for each bar orientation (thus the clusters will be two-dimentional).
2. The highest energy hit is selected as the seed for a potential cluster. This cluster is expanded by adding candidate hits that are close in time (30 ns) and space (adjacent bar and nearby layer). To be considered as a cluster, it must have at least three hits.
3. The clusters are then combined together. This is realised after the PCA (Principal Component Analysis) has been run and was able to identify the main axis of the elipsoid formed by the cluster. The clusters are merged if they are close together

(80 mm) along the direction of the main axis of the cluster that has the largest number of hits, they have consistent timing (40 ns) and the charge weighted average of the two clusters should be close together (40 cm).

4. Three-dimentional clusters are created using both the orientations. The matching is done only if the total charge of cluster is similar. The exact cut is tabulated from MC particle guns and varies with the distance from the tracker region.

The energy reconstruction and the PID are not used in the analysis so it will be omitted here.

Pi-zero Detector The P0D reconstruction is quite similar to the ECal for what interests this analysis (the presence of an object or not). More detailed information can be found in [148].

5.2.2 Selection software

The event selection and detector systematic error are done within one common software framework on T2K, called Highland2, for HIGH Level Analysis and the ND280 version 2 [149]. The error propagation of the detector systematic uncertainties is made with a package called Psyche, for Parametrisation of SYstematics and CHaracterisation of Event, which gets called by Highland2 (see [149] and references therein).

Highland2 provides a framework to analyse the data events from the Monte Carlo simulations (MC) or data productions. The reconstructed objects can be used in the selections and one has to write the event selection based on the characteristics of the reconstructed objects.

It is also possible to use the “systematics mode:” in this case, a loop is created over “toy experiments,” when running over the MC. They are sets of variations of the detector systematic parameters around their nominal values within their errors. Each toy experiment leads to a slightly different outcome for the selection and thus the set of all the toy experiments encloses the effect of all the detector systematic uncertainties.

5.2.3 Data sets statistics

For this analysis, the data used is the neutrino mode (FHC) data collected by the ND280 between November 2010 to May 2013. This corresponds to 5.80×10^{20} Protons On Target (POT) as shown in Table 5.1. In the table, the MC column includes all the interaction types simulated by the neutrino interaction simulator NEUT which happen in all the parts of the detectors enclosed in the Magnet (this includes the magnet itself which is the most massive part of the detector and which constitutes the most part of the T2K MC). An additional sample is generated for those neutrino interactions from outside the ND280 (thus in the sand) and create particles that go inside the ND280 [150]. Both the sample are denoted “magnet” and “sand” in this section and throughout this thesis.

As will be shown later, this is very important in this particular analysis. In this table, the run is indicated with the P0D status. If the P0D was operating with or without water (Water or Air). The beam configuration is indicated by letters: B is for 120 kW and C for 178 kW.

Runs	POT				
	data	magnet MC	(ratio)	sand MC	(ratio)
2 Air B	3.59×10^{19}	9.24×10^{20}	(0.0389)	4.65×10^{19}	(0.772)
2 Water B	4.34×10^{19}	1.2×10^{21}	(0.036)	4.75×10^{19}	(0.914)
3 Air B	2.17×10^{19}	4.45×10^{20}	(0.0488)	2.35×10^{19}	(0.923)
3 Air C	1.36×10^{20}	2.63×10^{21}	(0.0519)	1.64×10^{20}	(0.946)
4 Air C	1.78×10^{20}	3.5×10^{21}	(0.0509)	2.12×10^{20}	(0.842)
4 Water C	1.64×10^{20}	1.89×10^{21}	(0.0868)	2.11×10^{20}	(0.777)
Total data sets	5.80×10^{20}	1.17×10^{21}	(0.0496)	70.45	0.823
NCγ signal sample (beam C)		6.5×10^{23}			

Table 5.1: POT of the data, Monte Carlo (magnet, sand and signal) samples used for the NCγ searches, where magnet refers to MC events that happen in the volume enclosed by the magnet, sand refers to MC events that happen in the surrounding sand of the ND280. The ratio denotes the data POT / MC POT. The total nominal data sets denotes, in the case of the MC, what is used for prediction of the background and, in the case, of data the recorded real ND280 data that is used in the analysis. The NCγ signal sample denotes the MC sample that was generated with only FGD1 NCγ events.

However, this MC sample does not have enough events to calculate any meaningful quantity regarding NCγ, such as the efficiency or a smearing matrix. This is because the NCγ cross section is very small compared to other neutrino cross sections. This is visible in Figures 1.5 and 4.1: the ratio of the total NCγ to the total cross section at 1 GeV for a ν_μ on carbon as given by the NEUT generator is 3.06×10^{-4}.

To overcome this problem, an additional MC sample was locally generated. It corresponds to a very high exposure of the FGD1 to neutrino NCγ events as can be seen in Table 5.1, and is being used to calculate efficiency or when needed.

5.3 Event selection cuts

In this section, the details and motivations for each of the cuts of the analysis are given and explained.

5.3.1 Photon selection

Cut 1 Main Track selection Figure 5.1 depicts the Main Track (MT) momentum distribution before any cut. The MT is the highest momentum track crossing the TPC2 and starting in the fiducial volume of FGD1 (as defined in Table 5.2). Note the excess corresponding to electrons and positrons for tracks below 200 MeV. This excess disappears after the Pair Track (PT) is required.

Direction	Dimension of the FGD1 [mm]	Fiducial volume trim [mm]
+x	932.17	57.66
-x	-932.17	57.66
+y	987.17	57.66
-y	-877.17	57.66
+z	447.375	0
-z	115.625	21.25

Table 5.2: Cut 1: Fiducial volume used in the analysis for the signal sample, given in the standard ND280 coordinate system (see beginning of Chapter 2), these numbers are in Psyche and comes from [151] (Section 6).

Cut 2 Main Track quality To achieve reliable TPC PID, momentum and direction reconstruction, the track must leave enough hits (or nodes, this is the number of triggered MicroMegas) in the TPC. The standard number at which is this done in most ND280 analysis is 18, following a recommendation from the ν_μ group [152] and from the ν_e group [153]. Figure 5.2 shows the distribution of TPC hits, below the cut line; the next PID cut is not reliable any more. This is because the charged particle does not leave a trace which is long enough in the detector. Indeed, it is required to have several measurements of the curvature of the trace with good accuracy to perform the PID.

The two peaks correspond to the tracks crossing one MicroMegas (thirty-six pads horizontally) and two MicroMegas (a whole TPC horizontally, seventy-two pads). The track can also curve back in the TPC and leave more than seventy-two nodes.

Cut 3 Main Track electron particle identification Next, the particle identification is realised using the energy loss per unit length as a function of the trajectory and the momentum of the track. The reconstruction algorithm computes $\mathrm{dEdx}_{\mathrm{Measured}} = dE/dx$[1] of the track seen in the TPC (using Equation 5.1 and assuming the track is an electron) and similarly the $\mathrm{dEdx}_{\mathrm{Expected}}$ under a particle PID hypothesis. The “pull” ratio, $\pi_{l,\mathrm{PID}}$, is the computed as following, for a certain particle l:

$$\pi_{l,\mathrm{PID}} = \frac{\mathrm{dEdx}_{\mathrm{Measured}} - \mathrm{dEdx}_{\mathrm{Expected}}}{\epsilon} \tag{5.2}$$

Where ϵ is the fit error of the difference $\mathrm{dEdx}_{\mathrm{Expected}} - \mathrm{dEdx}_{\mathrm{Measured}}$. The distribution one gets under the assumption of the MT to be electron is shown in Figure 5.3. The cut value is 3 in absolute value to remove most of the muon background; this was also chosen to keep all the electrons and positrons in the selection to get the best efficiency possible.

Note the data excess on this plot is consistent with low energy electrons (the excess disappear for tracks of momentum over 200 MeV). This is thought to be due to a possible mismodelling of the neutron background orginated from the BrECal.

Cut 4 Pair Track selection The second track from the photon conversion (Pair Track, PT) is selected from the remaining tracks in the events. The following requirements are made upon selecting this track:

- The charge of the track is opposite to the one of MT.
- The track goes into a TPC.
- The track starts at a distance smaller than 10 cm from the MT starting point.
- Amongst the tracks satisfying these conditions, the highest momentum is identified as the PT.

In Figure 5.4, which is the distribution of nodes before the cut 5 one can see that the excess disappears after this track is selected.

Cut 5 Pair Track quality The PT undergoes the similar PID selection as the MT, so the number of nodes also has a threshold for reliable PID. The cut is realised at 18, as can be seen on the Figure 5.4.

Cut 6 Pair Track electron particle identification As for the MT, the same “pull” quantities, Equation (5.2), are computed and the events where the PT has a pull greater than 3 in absolute value are rejected. This is illustrated in Figure 5.5.

---

[1] where $dEdx$ denotes the first spatial derivative of the measured energy of the particle.

Cut 7 Invariant mass Then, the events are rejected if the reconstructed invariant mass according to Equation 5.3 is greater than 50 MeV.

$$M^2_{\text{Invariant}} = 2 \times m^2_{\text{electron}} + 2(E_{\text{electron}} \times E_{\text{positron}} - \vec{p}_{\text{electron}} \cdot \vec{p}_{\text{positron}}). \tag{5.3}$$

In this equation, m_{electron} is the mass of the electron (or positron), E_{electron} (E_{positron}) and p_{electron} (p_{positron}) are respectively the energy and the momentum vector of the electron (positron). The effect of this cut is illustrated in Figure 5.6.

5.3.2 Single photon selection

Cut 8 TPC muon rejection cut After the "Photon Selection" described in the previous subsection (5.3.1), the selection is very pure in photon conversions (94.5%); however the events selected can still be from a CC interaction, especially if the neutrino reaction happened far from the FGD1 and the muon was not the MT. To remove this background, a muon rejection cut was designed. It consists in checking each TPC track with reasonable quality (greater than 18 nodes) and TPC PID consistent with a muon hypothesis, as opposed to the selection of the MT and PT which use the electron PID. The pull, in Equation (5.2), should be smaller than 1 in absolute value). If a track is found in any TPC satisfying both these conditions and is not the MT or the PT, the event is tagged as CC and rejected. The effect of the cut is illustrated in Figure 5.7, where the number of tracks satisfying this veto is represented, and the pull distributions for the tracks considered are also depicted in this figure.

Cut 9 P0D veto This cut was designed to remove the events in which the neutrino interaction point is in the P0D. Some of these events can create neutral pions and photons, muons, or protons which can deposit energy in the P0D and a photon which propagates until the FGD1. Therefore, the events where an object[1] is seen in the P0D are rejected. Note that sometimes the electron / positron pair can be in the fiducial volume of the FGD1 and there is still a different object present in the P0D. The effect of this cut is shown on Figure 5.8.

Cut 10 TPC1 veto Similar to the P0D veto described earlier, the TPC1 veto was designed to remove events where the neutrino vertex is on the TPC support structure and the outgoing particle deposits energy in the TPC. This leads to having a zero efficiency

---

[1] Here, a P0D object can be track-like (i.e. a MIP-like) or a shower-like object. There is no PID requirement.

for backwards events. Note that the efficiency for backward track is anyway very low at the ND280. The effect of this cut is shown on Figure 5.9.

Cut 11 ECal veto This cut removes neutral pions from the selection by vetoing any event which has a reconstructed object in the BrECal (MIP-like or shower-like). It also removes high angle CC interactions and OOFV. The idea is that the secondary photon from π^0 will leave an isolated cluster of energy in the ECal. The number of times this happens is compared to how often the photon is converting in another part of the ND280 as shown in Figure 5.10. For example, if a neutral pion decays in the FV of the FGD1, if the highest energy photon converts in the FGD1, there is a probability of 10.71 % that the second photon went in the BrECal, which is exaclty the events this cut is aimed at removing. The effect of the cut is shown in Figure 5.11.

Also, a high angle CC interaction could produce a muon that does not go inside the TPC and goes directly in the BrECal.

Finally, this cut removes quite a lot of OOFV events that create a photon which converts in the FGD1.

Cut 12 φ_{photon} cut After computing the detector error, it was found opportune to add an additional cut that remove photon coming from below the FGD1. This cut was optimised on the expected limit result directly, therefore the motivation will be shown later. The value of the cut are shown below and apply on the φ_{photon} (azimuthal angle of the photon):

$$-90^\circ - \varphi_{\text{cut}}/2 < \varphi_{\text{photon}} < -90^\circ + \varphi_{\text{cut}}/2 \tag{5.4}$$

$$-108^\circ < \varphi_{\text{photon}} < -72^\circ. \tag{5.5}$$

Note that, unless specified otherwise, none of the next figures or tables include this cut.

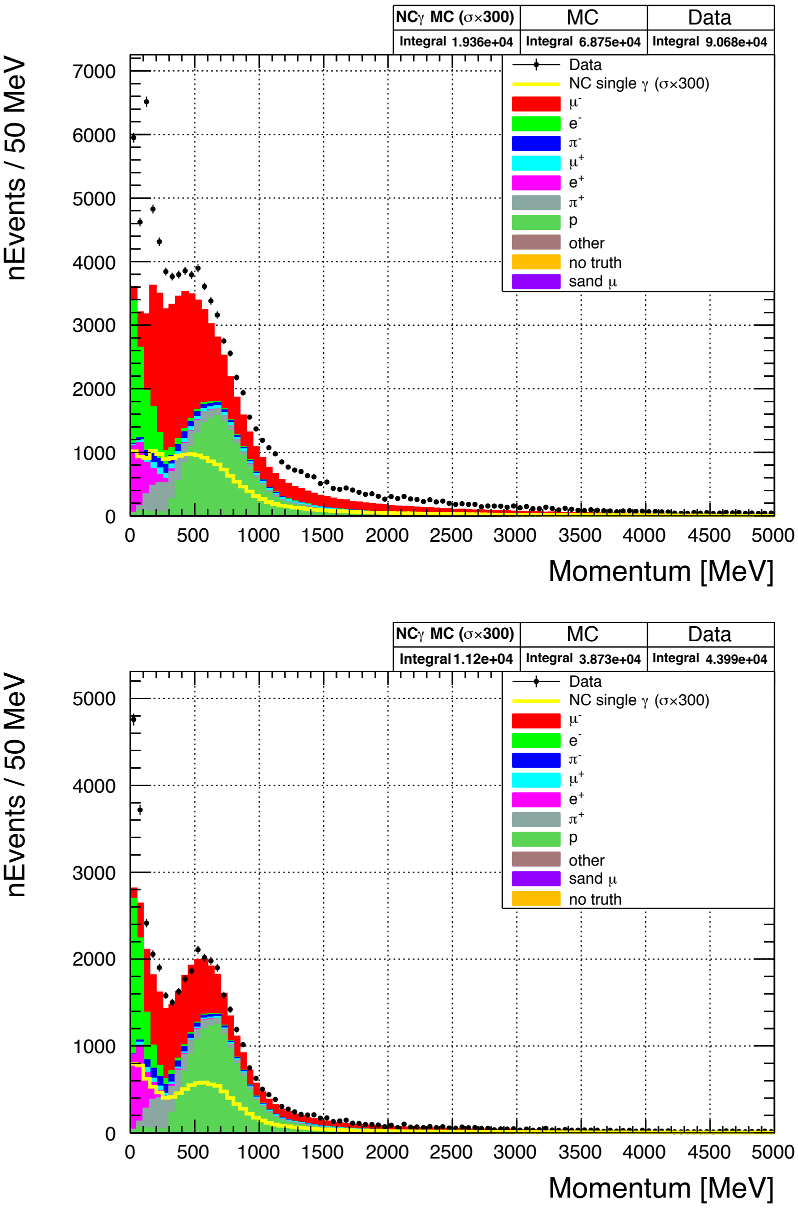

Figure 5.1: Cut 1: Top: TPC momentum distribution of the MT after the pre-selection (no cut applied other than data quality, triggering and the track is required to go inside a TPC), most of the particles starting in FGD1 are muons. The signal is contained in the electron and positron categories. ***Bottom:*** Same with the fiducial volume requirement from Table 5.2.

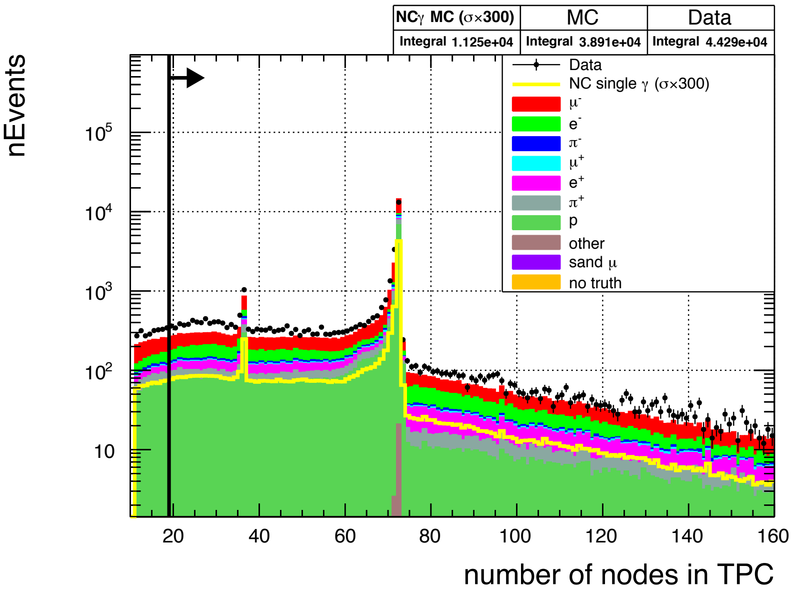

Figure 5.2: Cut 2: Number of TPC nodes for the MT. The cut value is depicted by the black line.

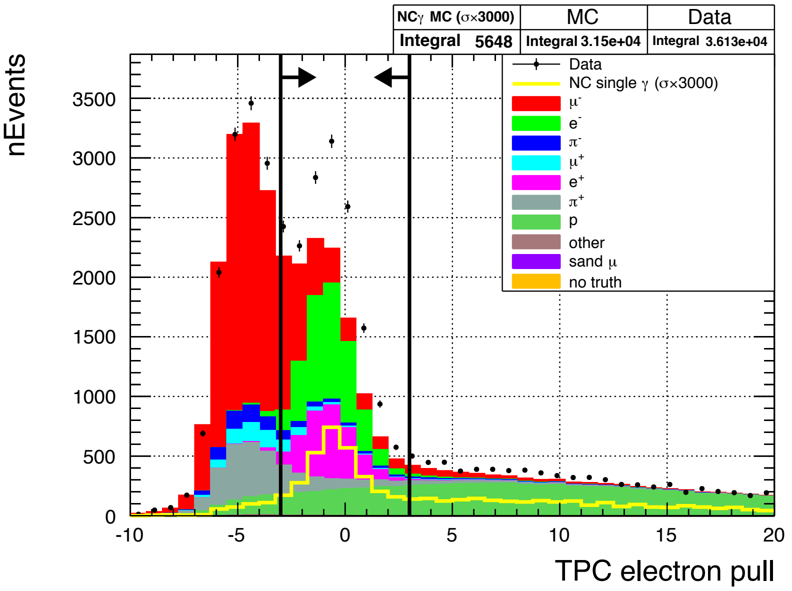

Figure 5.3: Cut 3: TPC pull for the MT. The cut values are depicted by the black lines.

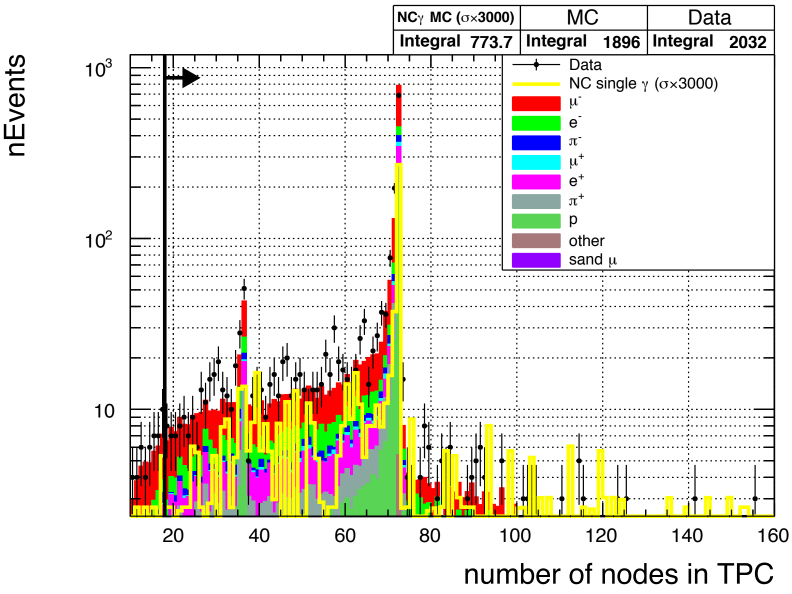

Figure 5.4: Cut 5: Number of TPC nodes for the PT. The cut value is depicted by the black line.

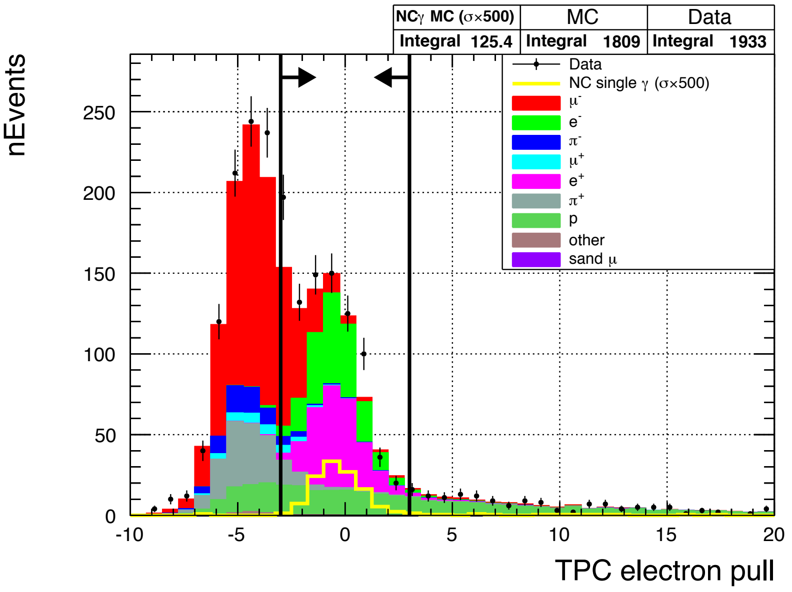

Figure 5.5: Cut 6: TPC pull for the PT. The cut values are depicted by the black lines.

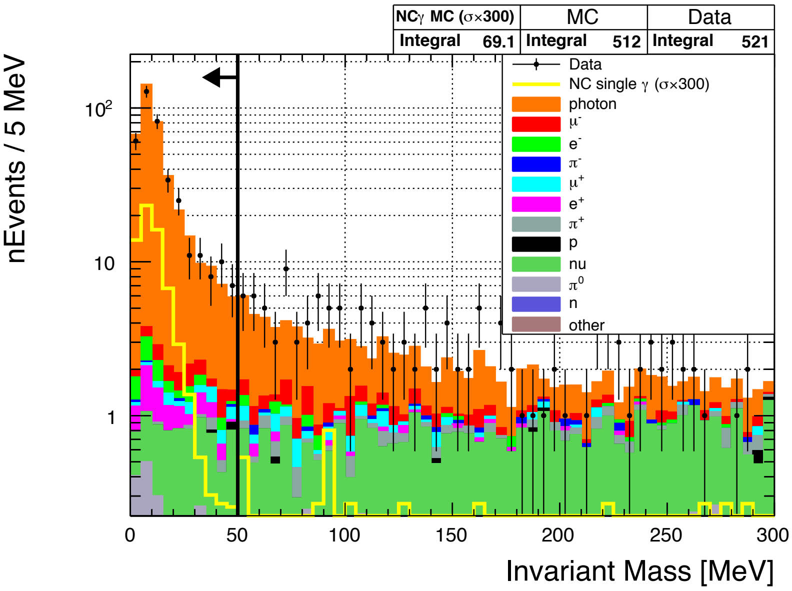

Figure 5.6: Cut 7: Invariant mass of the two tracks system, assuming both of them have a mass of electrons, in MeV/c. The colour coding is the parent of the main track. When the parent is a photon, one can see that the invariant is usually smaller than 50 MeV/c. When the main track does not have a parent, (as in the case of a ν_e CC interaction), the colour coding applied is the "nu" category. The cut value is depicted by the black line.

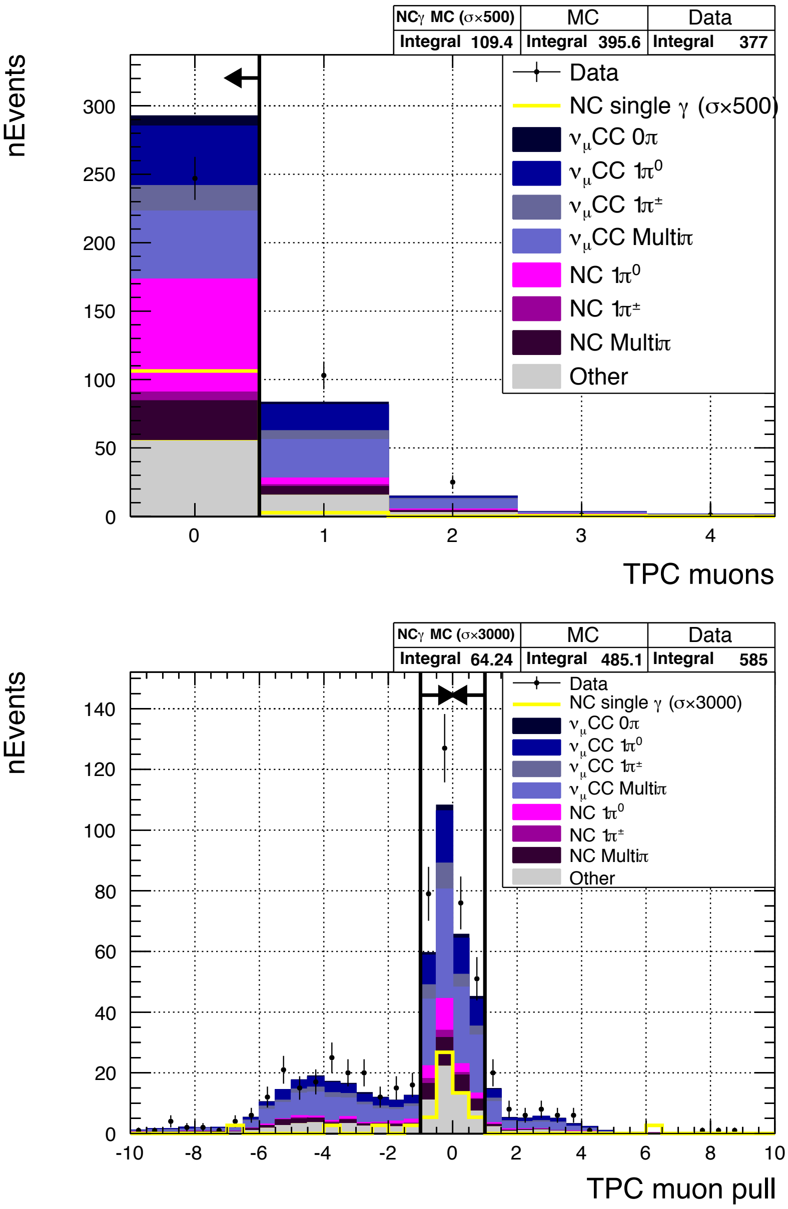

Figure 5.7: Cut 8: Top: Number of TPC muon tracks; the events that are not in the first bin are rejected. ***Bottom:*** Pull of tracks in the TPC.

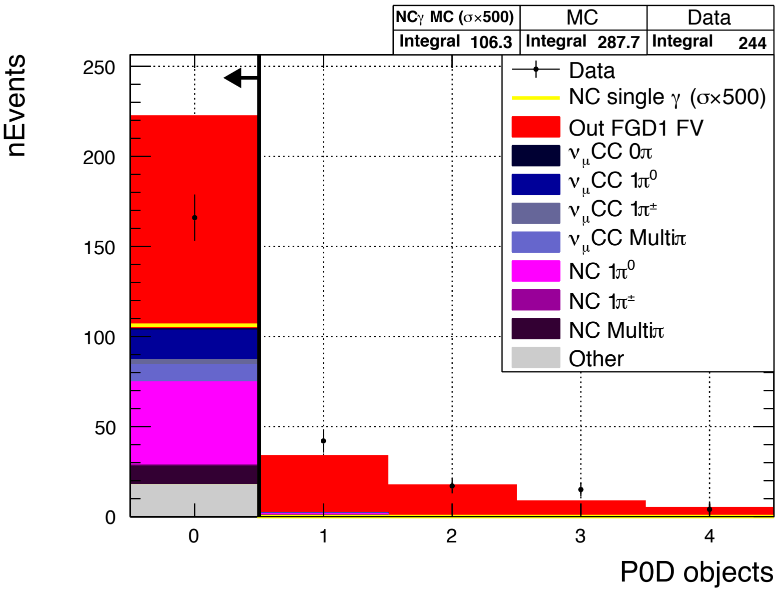

Figure 5.8: Cut 9: Number of P0D objects. The events that are not in the first bin are rejected.

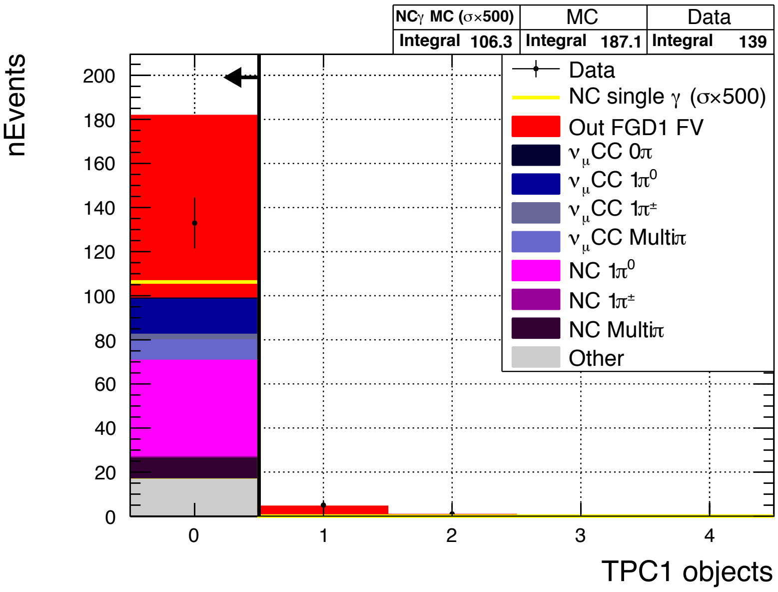

Figure 5.9: Cut 10: Number of TPC1 objects. The events that are not in the first bin are rejected.

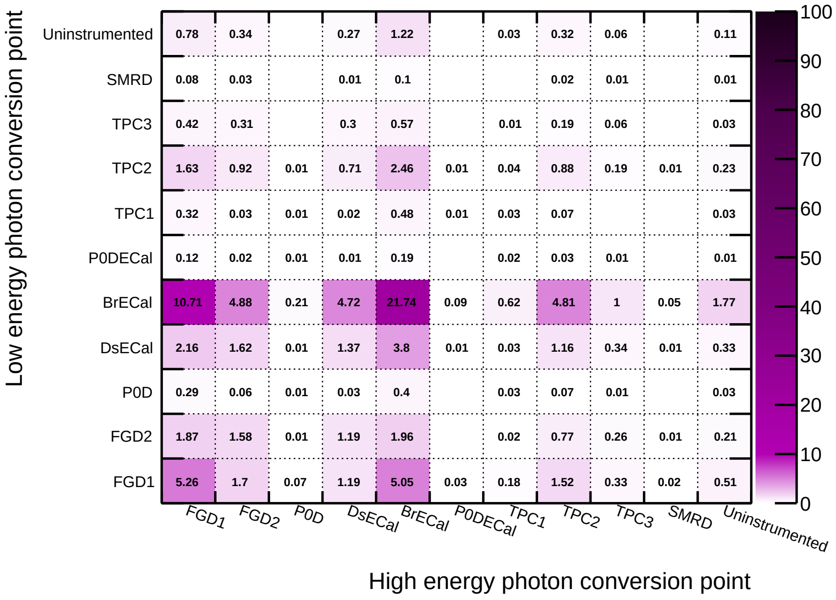

	FGD1	FGD2	P0D	DsECal	BrECal	P0DECal	TPC1	TPC2	TPC3	SMRD	Uninstrumented
Uninstrumented	0.78	0.34		0.27	1.22		0.03	0.32	0.06		0.11
SMRD	0.08	0.03		0.01	0.1			0.02	0.01		0.01
TPC3	0.42	0.31		0.3	0.57		0.01	0.19	0.06		0.03
TPC2	1.63	0.92	0.01	0.71	2.46	0.01	0.04	0.88	0.19	0.01	0.23
TPC1	0.32	0.03	0.01	0.02	0.48	0.01	0.03	0.07			0.03
P0DECal	0.12	0.02	0.01	0.01	0.19		0.02	0.03	0.01		0.01
BrECal	10.71	4.88	0.21	4.72	21.74	0.09	0.62	4.81	1	0.05	1.77
DsECal	2.16	1.62	0.01	1.37	3.8	0.01	0.03	1.16	0.34	0.01	0.33
P0D	0.29	0.06	0.01	0.03	0.4		0.03	0.07	0.01		0.03
FGD2	1.87	1.58	0.01	1.19	1.96		0.02	0.77	0.26	0.01	0.21
FGD1	5.26	1.7	0.07	1.19	5.05	0.03	0.18	1.52	0.33	0.02	0.51

Figure 5.10: The photon conversion points for neutral pions originated in the FGD1; the values reported are percentages. Reproduced from [154].

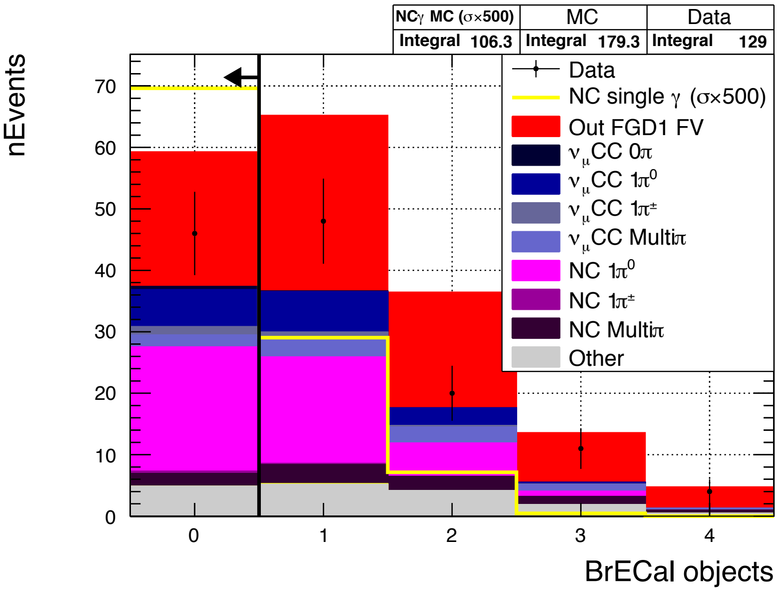

Figure 5.11: Cut 11: Number of ECal objects. The events that are not in the first bin are rejected.

5.4 Overview of the cuts for the events selection

The events are first preselected to be in the beam timing window and to have a good data quality over all the ND280 detectors. This selection has been applied within the Highland2 and psyche framework[1]. The selection is divided in two stages: the first stage selects a very high purity photon sample, the second is designed to reduce the background from photons produced in interactions other than NCγ (mostly: CC, interactions with vertex out of fiducial volume and photons from neutral pion (π^0) decay).

The cut flow for the first part of the selection is as follows (referred as "photon selection" later in the text):

1. The highest momentum track starting in FGD1 propagating in the TPC is selected and is called the Main Track (MT).

2. The MT is required to leave more than 18 nodes in the TPC2. This allows reliable Particle IDentification (PID) and good momentum resolution.

3. A $dEdx$-based electron PID is performed on the MT, and pulls are constructed using the TPC2. The pull of the track must be smaller than 3 in absolute value.

4. The track which has opposite charge, starts from a distance smaller than 10 cm from the starting point of the MT and has the highest momentum is selected. Throughout this note, it will be called the Pair Track (PT).

5. The PT is required to have more than 18 nodes in the TPC2.

6. The TPC2 PID for electron is realised by requiring the pull to be less than 3 in absolute value.

7. The photon invariant mass is calculated assuming the tracks are electron and positron. The maximum allowed value is 50 MeV.

The cut flow for the second section of the selection is the following (later referred as "single photon selection"):

8. The "muon veto" is applied by looping over all the tracks that have more than 18 TPC nodes and checking that none of the tracks have a muon pull smaller than 1 (absolute value). If any track satisfies this, the event is rejected.

---

[1] To get the code, use the ND280 CMT environment, and type in a shell `cmt co -R highland2/gammaNCAnalysis`. This will download the analysis package, and recursively Highland2 and psyche.

9. In order to remove neutrino events from outside the FGD1, the P0D, the P0DECal and the TPC1 must have no reconstructed object for the event to be kept.
10. To further reduce this background, remove high angle CC interactions and π^0 events; the tracks in the BrECal that are not associated with the tracks are vetoed.
11. The photon coming from under the FGD1 are removed from the selection.

5.5 Selection performance

Final sample In Figures 5.12, 5.13 and 5.14, one can see the photon energy and angular distribution of the selected events, respectively. On the same one-dimensionnal figures (Figures 5.12 and 5.13), the NCγ true events from NEUT distribution is also overlayed (note that this is done with the version of NEUT which has a bug in it which results in smaller cross section). This illustrates the sensitivity of the selection to such processes. One can see from Figures 5.12 and 5.13 that the selection is dominated by backgrounds and thus the focus of this analysis is to set a limit on the NCγ.

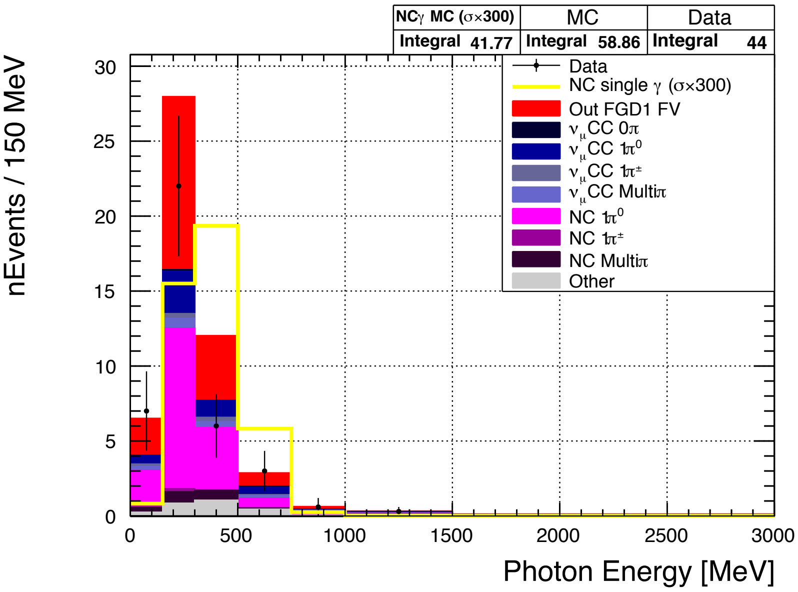

Figure 5.12: Photon reconstructed energy after the selection with the NEUT (5.3.3) NCγ cross section and normal magnet MC simulations.

To further clarify the content of the selection, breakdowns by target, reaction and topology are realised in Tables 5.3, 5.4 and 5.5, respectively. Note that the FGD1 external photon events have been separated from the internal ones. These tables highlight the difficulties to perform such a measurement: even after essentially blocking all the upstream activity, the selection still contains around 35% of OOFV events. This comes from the dead material regions which are not instrumented and for which it is not possible to veto the event. Table 5.3 shows the breakdown by target, from which it can be concluded that most of these events happen on the support structure (aluminium) or on the case of the TPC (carbon), or in regions close to the edge of the detector where no object has

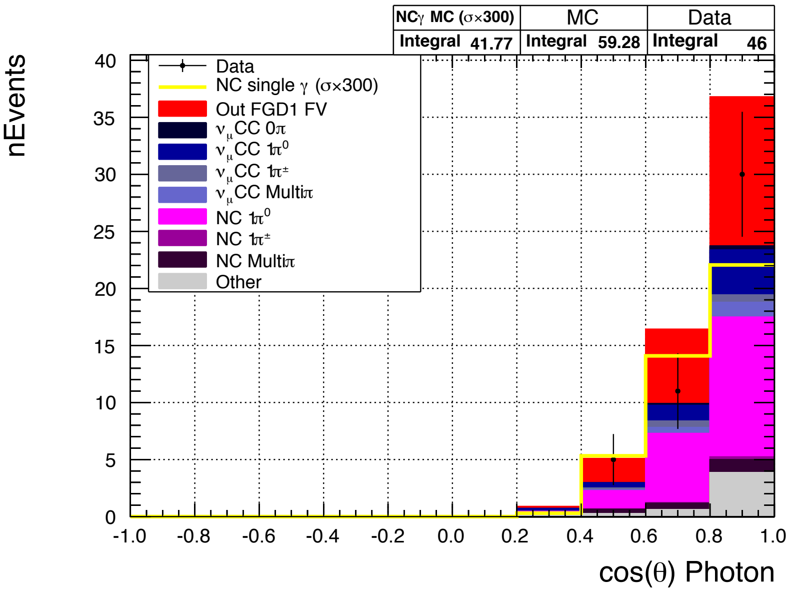

Figure 5.13: Photon reconstructed $\cos(\theta)$ after the selection with the NEUT (5.3.3) NCγ cross section and normal magnet MC.

been reconstructed (for example, lead events come from the ECal, but these events do not create any object in the ECal). The spatial distributions of these events are shown in Appendix A.

Similarly, one can see on Table 5.4 that some CC events do survive the CC veto; these events probably have a low momentum muon which makes them go below a number of node threshold to be identified as muon.

Finally, the Table 5.5 highlights the difficulties to detect and reconstruct the secondary photon from neutral pion decay. Most of the time, the photon that creates the electron / positron pair in the FGD1 is the most energetic one, and, since the neutral pion has a relatively small kinetic energy, the secondary photon has quite low energy and is not detected.

Based on the Table 5.5, and the fact that the analysis is dominated by backgrounds, it should be concluded that the final result of this analysis will be a limit on the NCγ processes. Therefore, the uncertainties on the background are the main drive of the limit.

With this number of events, the statistical uncertainty on the limit is roughly less than 15 %. This is already smaller than the expected error for OOFV events as will be detailed later. It was concluded that the error on this sample is already largely limited by systematic errors and therefore it makes sense to conduct this analysis now.

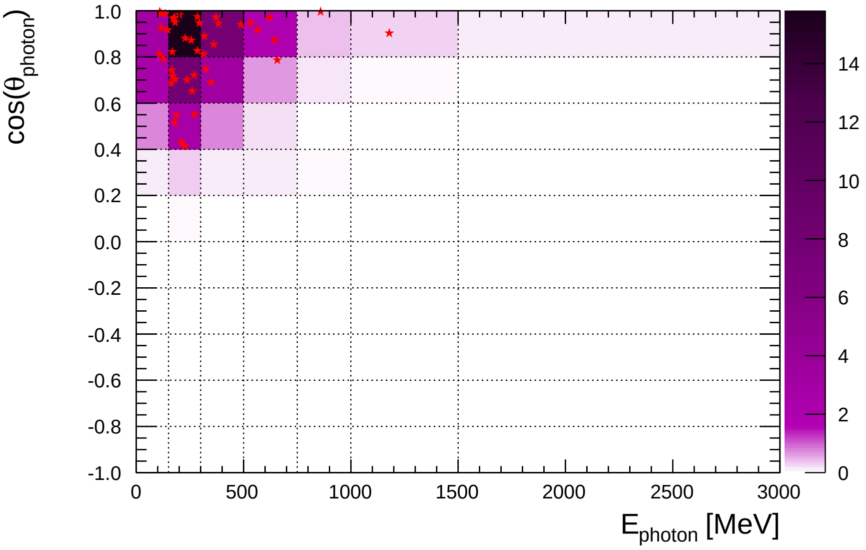

Figure 5.14: Photon reconstructed $\cos(\theta)$ and energy after the selection, the stars indicate the data points.

Target	NEvents	Percentage
carbon	32.18	55.32
oxygen	1.20	2.06
hydrogen	2.36	4.05
other	0.88	1.51
Total inside FGD1 FV	36.61	62.94
carbon	8.85	15.21
oxygen	1.34	2.30
hydrogen	0.49	0.84
aluminium	4.79	8.24
iron	2.59	4.45
copper	0.10	0.17
lead	2.57	4.41
other	0.84	1.45
Total outside FGD1 FV	21.56	37.06

Table 5.3: Neutrino target for the selected events, separated for external photons and for FGD1 FV photons

Reaction	NEvents	Percentage
ν_μ CCQE	0.41	0.70
ν_μ CC RES π^0	4.81	8.24
ν_μ CC RES $\pi^\pm$	4.18	7.16
ν_μ CC SIS / DIS	0.73	1.25
NC RES π^0	11.71	20.05
NC RES $\pi^\pm$	9.63	16.49
NC SIS / DIS	0.84	1.44
NC single γ	0.14	0.24
other	4.30	7.36
Total inside FGD1 FV	36.75	62.94
ν_μ CCQE	1.52	2.60
ν_μ CC RES π^0	2.54	4.35
ν_μ CC RES $\pi^\pm$	2.84	4.86
ν_μ CC SIS / DIS	0.61	1.04
NC RES π^0	5.39	9.23
NC RES $\pi^\pm$	5.85	10.02
NC SIS / DIS	0.86	1.47
NC single γ	0.10	0.17
other	1.93	3.31
Total outside FGD1 FV	21.56	37.06

Table 5.4: Neutrino true interaction modes for the selected events, separated for external photons and for FGD1 FV photons. Note that the NCγ component was derived with a high statistic sample generated independently.

Topology	NEvents	Percentage
ν_μ CC0π	0.51	0.87
ν_μ CC1π^0	5.93	10.17
ν_μ CC1$\pi^\pm$	1.40	2.40
ν_μ CC multi-π	2.00	3.43
NC 1π^0	19.50	33.44
NC 1$\pi^\pm$	0.35	0.60
NC multi-π	2.02	3.46
NC single γ	0.14	0.24
other	4.89	8.38
Total inside FGD1 FV	36.75	62.94
ν_μ CC0π	1.92	3.29
ν_μ CC1π^0	3.53	6.05
ν_μ CC1$\pi^\pm$	0.68	1.17
ν_μ CC multi-π	0.94	1.61
NC 1π^0	10.15	17.40
NC 1$\pi^\pm$	0.40	0.69
NC multi-π	1.96	3.36
NC single γ	0.10	0.17
other	1.90	3.26
Total outside FGD1 FV	21.56	37.06

Table 5.5: Topology of the selected events, separated for external photons and for FGD1 FV photons. Note that the NCγ component was derived with a high statistic sample generated independently.

Efficiencies Upon deciding the cut values; one is interested whether the cuts are actually the best way of selecting the NCγ events; the effect of all the cuts on the efficiency[1] to select the NCγ events is shown Figure 5.15. On this plot, one notices the relative low impact of the vetoes on the selections and that one of the largest drop in efficiency comes from requiring track propagating in the TPC. This is probably because of the high angle photons that get cut away from the selection (this is also visible in bottom of Figure 5.17).

Another concern is the PID cuts: in Figure 5.3, one sees that all the electrons and positrons are within the cut lines, so one could wonder why the efficiency is impacted by these cuts as can be seen in Figure 5.15. The reason why this cut removes half of the events is because the protons coming out of the vertex can sometimes be the MT or the PT. As can be seen in Figure 5.16, if the PID cuts were made looser, the efficiency would become higher after both the PID cut, but the invariant mass will reject the events, since they have different kinematics.

Another interesting feature is the ECal veto, which halves the efficiency. This is because the MT and PT can lose energy via bremsstrahlung and eventually create an unmatched object in the ECal, however it is quite complicated to differentiate these from a secondary photon coming from a π^0, so it was chosen to leave the cut as it is.

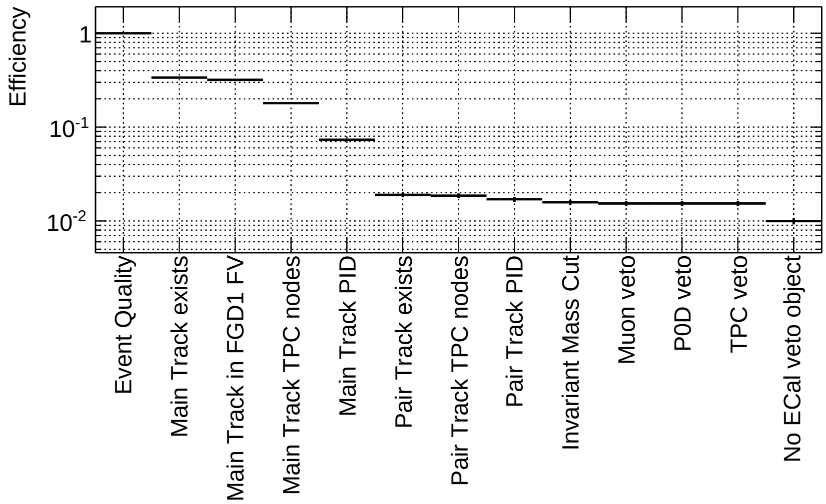

Figure 5.15: Efficiency against selection cut for NEUT NCγ events happening in the FGD1 (errors are statistical).

---

[1] The efficiency is defined here as the following ratio: $\frac{\text{Number of selected NC}\gamma\text{ events}}{\text{Total number of NC}\gamma\text{ events generated}}$

Using the selection as described, and the NCγ enhanced MC, the one-dimensionnal photon efficiencies were computed for signal and background photons, as can be seen in Figures 5.17 and 5.18. Note that a background event for the calculation of the efficiency is defined as “any event that creates a photon in the FGD1 or that creates a photon entering the FGD1”.

Similarly, since the π^0 are the major background of the analysis, the efficiency of the different processes creating π^0 in terms of the π^0 kinematics in Figures 5.19 and 5.20 were calculated. In this case, this is shown before and after the vetoes, since they are expected to have a significant effect on the π^0 efficiency.

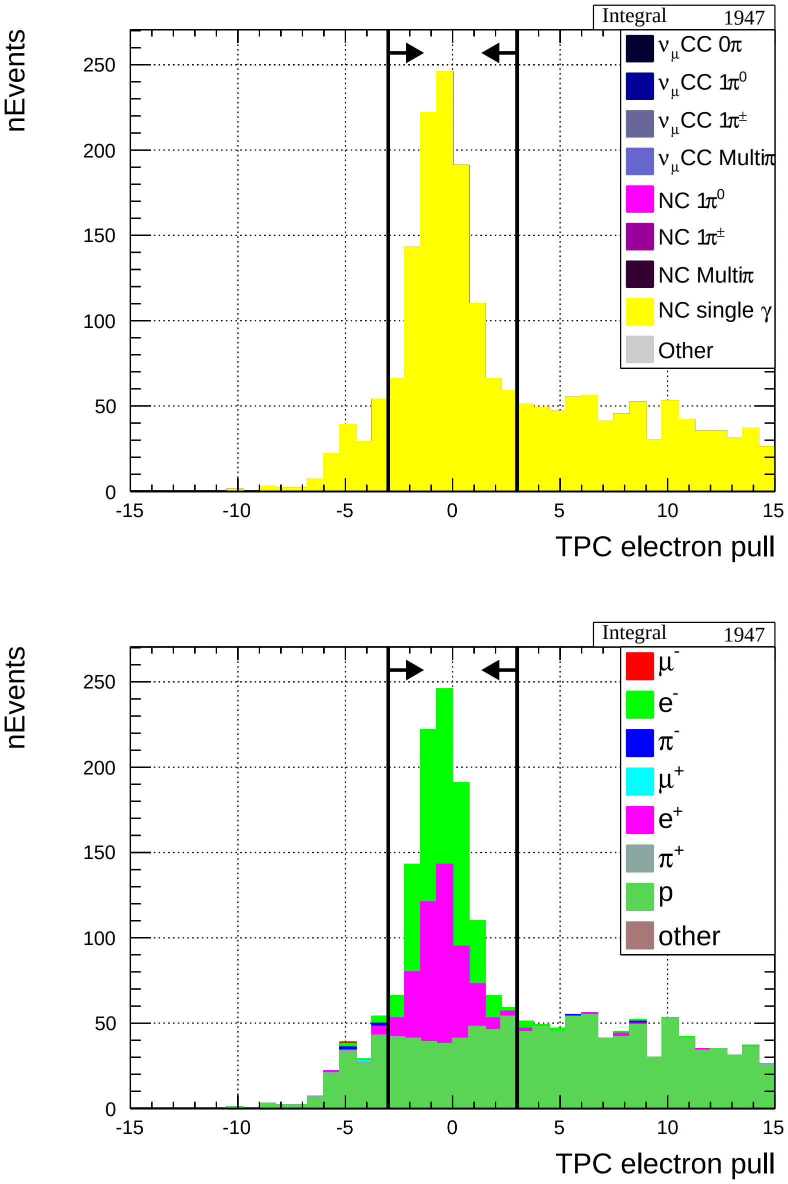

Figure 5.16: TPC pull cut for MT if the interaction was a true NCγ event happening in the FGD. ***Top:*** For each interaction channel. ***Bottom:*** For each the particle type. All the excluded events are protons. The cut values are depicted by the black lines.

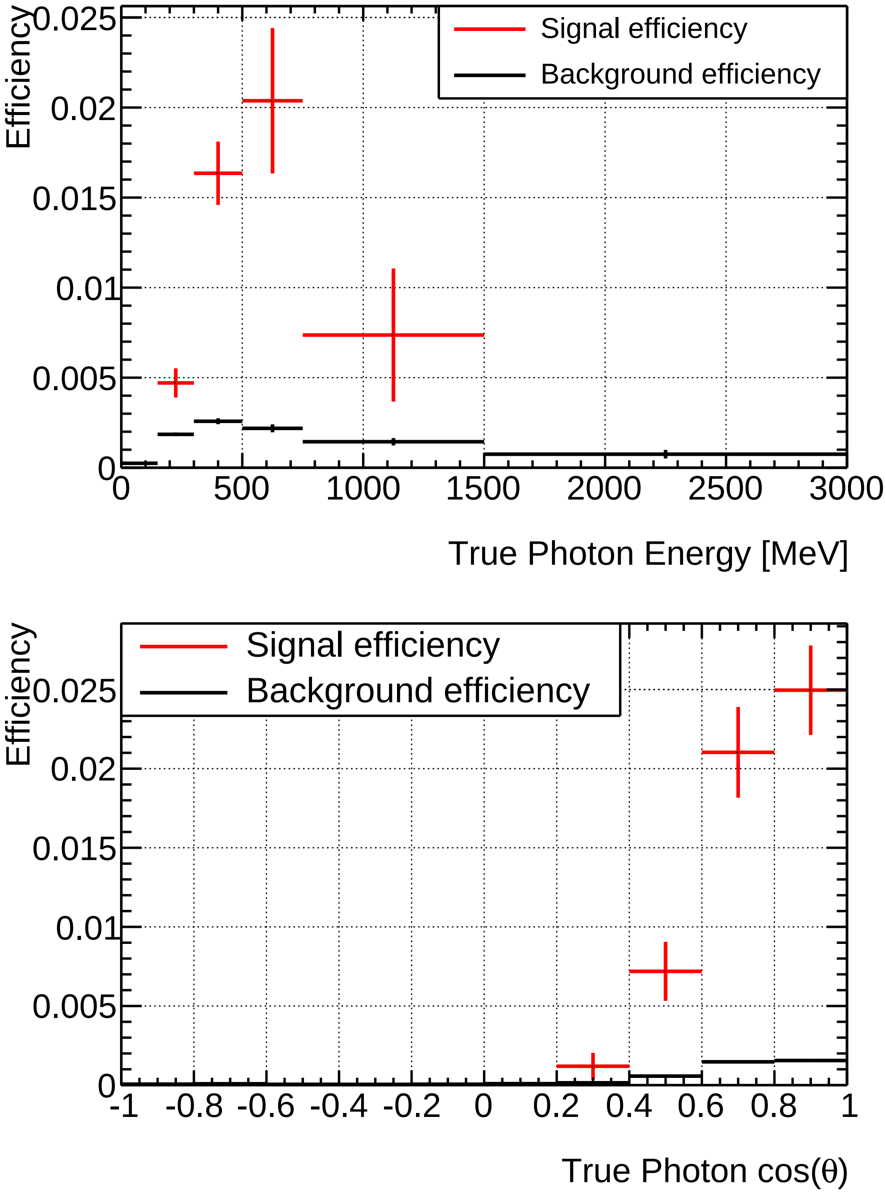

Figure 5.17: Photon selection efficiency for signal events and for background events (errors are statistical. ***Top:*** Efficiency against the photon energy. ***Bottom:*** Efficiency against the photon angle ($\cos(\theta)$).

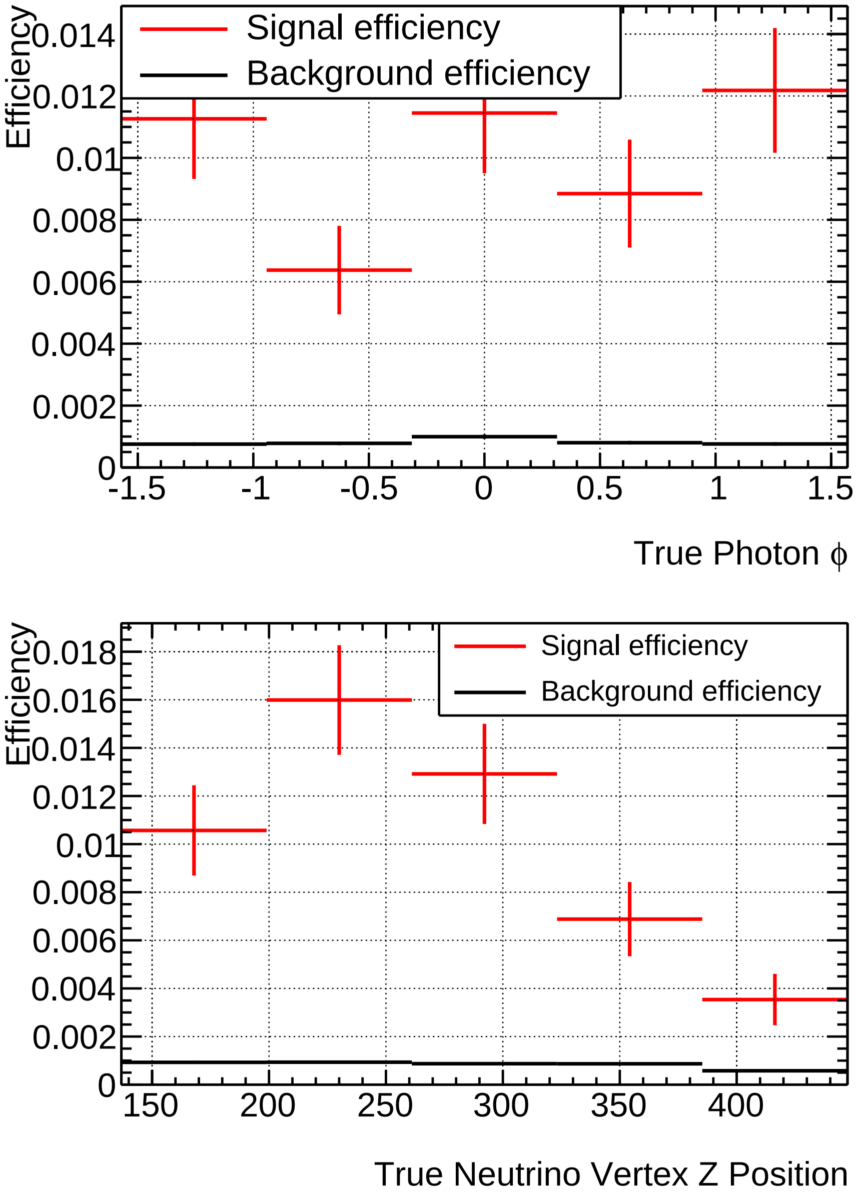

Figure 5.18: Photon selection efficiency for signal events and for background events (errors are statistical). ***Top:*** Efficiency against the photon azimuthal angle. ***Bottom:*** Efficiency against the photon Z starting point in the FGD1.

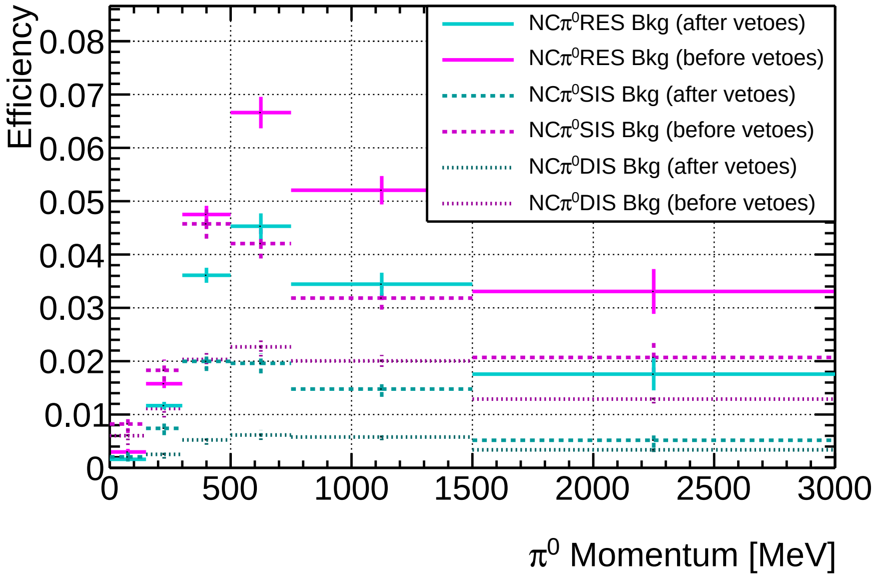

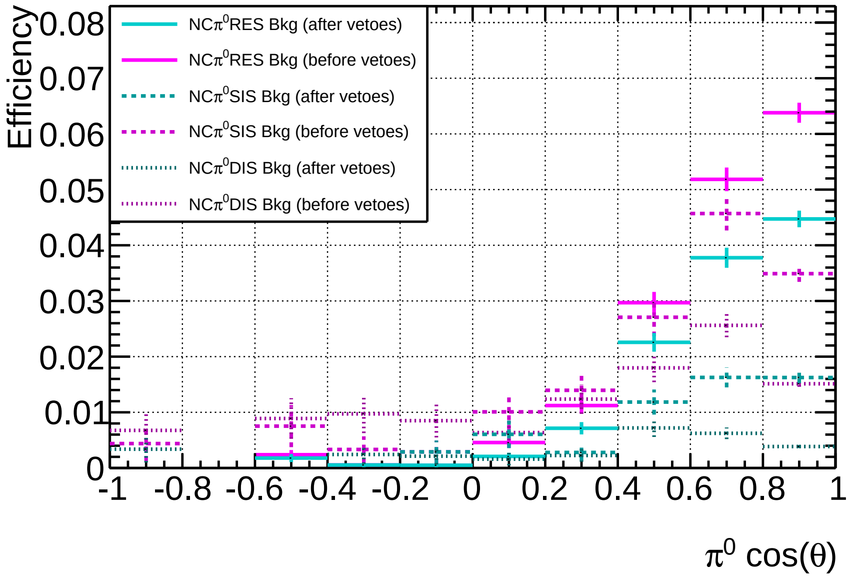

Figure 5.19: Background selection efficiency for neutral pions before and after the vetoes (errors are statistical). ***Top:*** Efficiency against the in pion momentum for NC interactions. ***Bottom:*** Efficiency against the in pion angle for NC interactions. The signal definition is any neutral pion creating a photon in the FGD1.

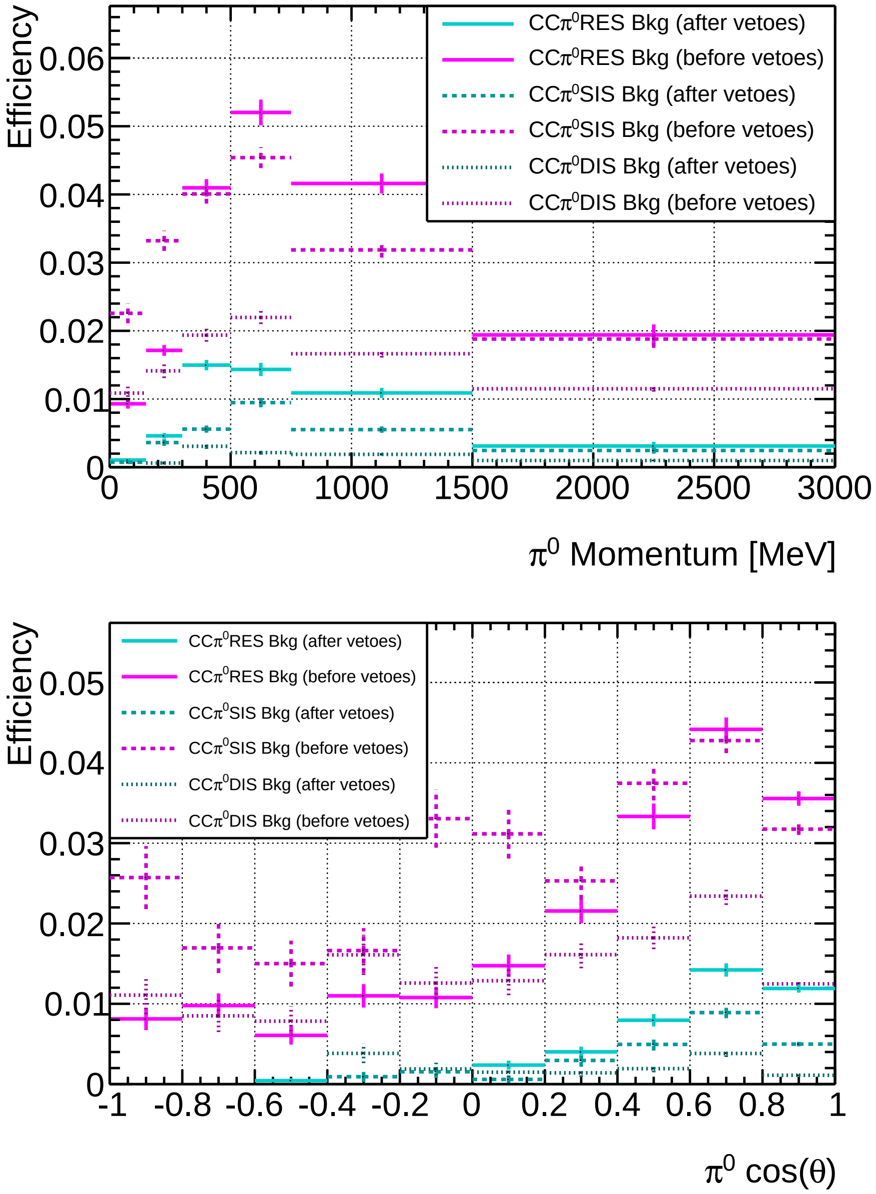

Figure 5.20: Background selection efficiency for neutral pions before and after the vetoes (errors are statistical). ***Top:*** Efficiency against the in pion momentum for CC interactions. ***Bottom:*** Efficiency against the in pion angle for CC interactions. The signal definition is any neutral pion creating a photon in the FGD1.

5.6 Conclusion

In this section, the NCγ events selection was detailed. The selection relies on the identification of a photon which decays into a pair of electron / positron in the FGD1. Both these tracks have to propagate in the TPC2, where a electron PID is realised. The two tracks system should also be consistent with a photon. This is realised by requiring that the reconstructed invariant mass should be small (< 50 MeV). After this selection, it is found that the efficiency is (1.04 ± 0.07) %. The selection is largely dominated by backgrounds (58.86 events) and the expected number of NCγ events in the selection is 0.14, for a number of data events equal to 44. These numbers allow us to conclude that:

- The analysis will lead to a limit on the NCγ cross section rather a NCγ cross section,
- The data limit will be lower than the expected result which comes from MC. This is due to the fact that the number of observed data event is less that the number of MC events.

Chapter 6

Systematic uncertainties

In this chapter, the systematic uncertainties relevant for neutrino induced single photon production are detailed.

The systematic uncertainties are divided according to their sources. Similarly to most of the ND280 cross section analysis, they reduce to flux (Section 6.1), cross section (Section 6.2) and detector (Section 6.3) systematic errors. Additionally, the statistical uncertainty and the efficiency uncertainty are also taken into account.

However, given the scale of the contamination of events that happened outside the Fiducial Volume (OOFV) of the FGD1 and the expected differences which arise for the systematic uncertainty when considering neutrino interaction happening in the FGD1 and the rest of the detector, the two backgrounds systematic uncertainties are independently motivated.

Finally, all the systematic uncertainties are combined and summarised in Section 6.4.

6.1 Flux systematic uncertainties

The flux systematic error accounts for the uncertainty one has in predicting the flux of neutrinos. The uncertainty was propagated using a code called `JReWeight` (see instructions and references in [155]), which changes the relative importance of the selected events based on the neutrino energy and according to the relative uncertainty as shown in Figure 6.1. Note that these errors are very correlated; although there are 100 bins of energy for the neutrino, after decomposition of the covariance matrix, only seven parameter eigenvalues are greater than 1%, which indicates that the flux error can been parametrised by only few parameters. These are, by decreasing order of importance:

- the proton interaction error, which are constrained by the NA61 / SHINE experiments [121–123],
- the beam characteristic (profile, intensity, direction) which are characterised *in situ*, as shown in Section 2.1,
- the survey of material around the target station,
- the horn current and positions.

As can be seen in Figure 6.1, the flux uncertainty is expected to be around 10%.

Note that the flux uncertainty was constructed for FGD neutrino interactions. The photons, on the other hand, can come from regions far from the FGD central region. Following what was done in [156], the conclusion was that the error should not be increased by more than 5% for ECal interactions. The increase of the error is considered negligible compared to other effects taken into account here.

Another motivation for not inflating the flux error is that the photons do not come from very far from the tracker region, as can be seen in Appendix A. The conversion length of the photons in the ECal (10.4 cm) is much shorter than for a standard scintillator (41.1 cm), so it is not expected that the OOFV neutrino interactions come from far regions such as the SMRD.

The PDF (for Probability Density Function) of the number of selected events is shown in Figure 6.2.

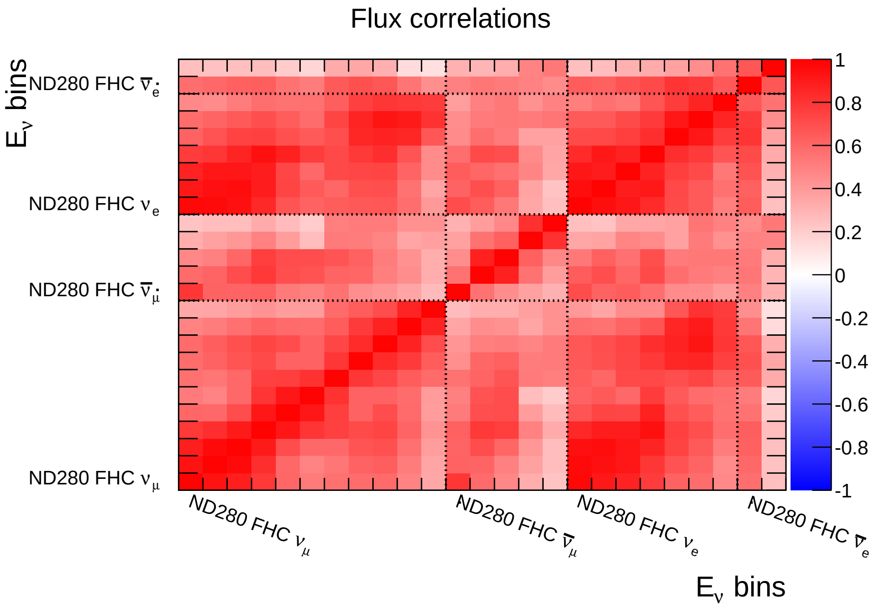

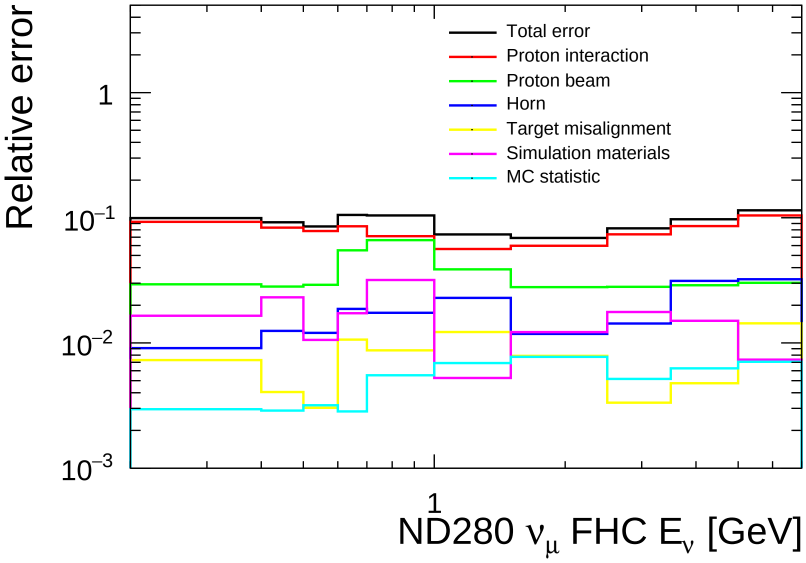

Figure 6.1: ***Top:*** The T2K flux uncertainty correlations across true energy bins in for ND280 and SK, while running in FHC and RHC modes, for ν_μ, $\bar{\nu}_\mu$, ν_e and $\bar{\nu}_e$. ***Bottom:*** The diagonal uncertainty for ν_μ neutrinos in FHC at the ND280. Both extracted from T2K beam working group inputs [120, 124].

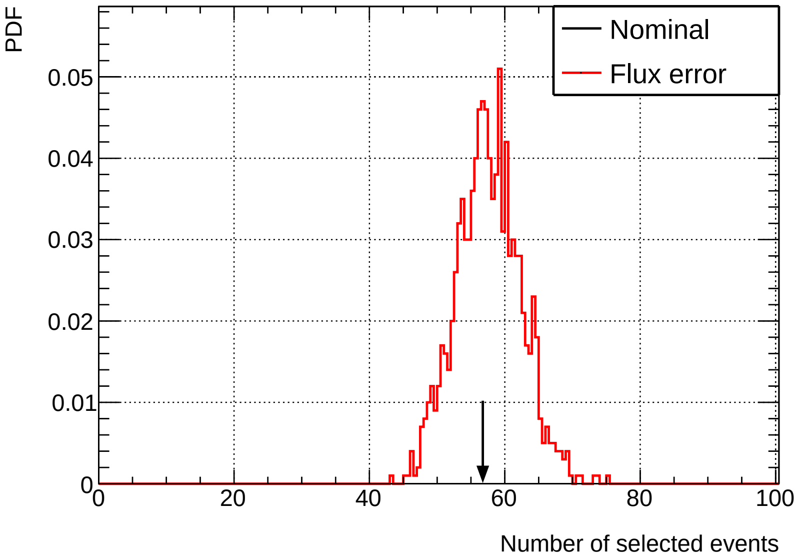

Figure 6.2: Effect of the flux uncertainty on the number of selected events. The nominal central value for MC is indicated by the arrow.

6.2 Cross section systematic uncertainties

The cross section uncertainties were propagated using the `T2KReWeight` package [155], which modifies the relative importance of the neutrino events based on a change of the underlying cross section model.

6.2.1 Cross section uncertainty on primary processes

In this section, the cross section uncertainties on primary processes are explained. The main background of the analysis comes from π^0 NC RES (resonant) interactions. There are a lot of vetoes in the selection which remove muons from charged current interactions and the second decay photons from the π^0. All the cross section systematic errors propagated are the same as those that were recently used for the near detector fits supporting the oscillation analysis in [116] and in Chapter 8.

Even if the CCQE processes are dominant at T2K energies, their impact on the analysis is minimal, since they only contribute marginally to the selection of events as can be seen in Table 5.4, standard cross section errors were nevertheless propagated and will be explained here.

6.2.1.1 Free nucleon resonant interaction uncertainties

There are three uncertainties related to the RES interactions. All of them are parameters of the Rein and Sehgal model [56, 57].

Resonant axial mass This parameter controls the axial mass (M_A^{RES}). This is one of the fundamental inputs for the cross section calculation related to the form factor. T2K now uses a new form factor compared to the original one from Rein and Sehgal, which has the form [157]:

$$\sigma_{\text{RES}} \propto C_5^A(Q^2) = \frac{C_5^A(0)}{\left(1 + \frac{Q^2}{M_A^{\text{RES}\,2}}\right)^2}. \tag{6.1}$$

Where the linear dependence of the neutrino cross section (σ_{RES}) to the axial form factor (C_5^A) is made explicit. In this equation, M_A^{RES} is the axial mass (which is the equivalent for RES cross section to the CCQE M_A^{QE} described in Section 1.2.3), and Q^2 (see Footnote 1 on page 41) is the momentum transfer.

Resonant axial form factor at $Q^2 = 0$ In Equation 6.1, the parameter $C_5^A(0)$ is also an uncertainty, which acts on the total normalisation of the RES events.

Isospin 1/2 background The background component refers to the non-resonant component contribution of the cross section as described in Section 1.2.5.

Tuning and uncertainty Several tunings of these parameters are done using different combinations of the available data (bubble chamber), and using channels that are sensitive or not to the background term [158].

The errors used are listed in Table 6.1.

Parameter	Value	Error	Correlation		
			M_A	C_5^A	$I_{1/2}$
M_A	1.07	0.15	1	-0.83	-0.01
C_5^A	0.96	0.15	-0.83	1	-0.31
$I_{1/2}$	0.96	0.40	-0.01	-0.31	1

Table 6.1: Neutrino RES errors used in the analysis, reproduced from [158].

6.2.1.2 Nuclear resonant interaction uncertainty, the MiniBooNE $NC1\pi^0$ fits

Due to the relative importance of π^0 in the analysis, it was decided to add additional parameters to properly deal with the uncertainties coming from these events where a π^0 was created. It should be noted that most of these backgrounds are from resonant interactions and single π^0 production as can be seen in the previous section (Tables 5.4 and 5.5). Furthermore, in Figures 5.19 and 5.20, one can see that the efficiency in selecting these π^0 from resonant interactions is not flat. Therefore, any uncertainty on the π^0 background that creates a shape difference in the pion kinetic space is expected to have a significant importance in the overall systematic error budget. These parameters are relevant since none of the previously described parameters has the ability to change the pion momentum distribution. This can be seen in Figure 6.3, where the neutral pion (π^0) measurement was from MiniBooNE [111] and compared to the NEUT prediction and errors.

Based on this study, two parameters were re-introduced from cross section parametrisation (identical to the ones used in Section B.3 of [159]). The reason is that the errors on the pion kinematics produced by the cross section parameter described earlier do not cover all the data points and a shape discrepancy can be seen. Note that all the plots and studies were realised with the newly-released NUISANCE [160].

The T2K pion model (which is the Rein and Sehgal model [56,57] with the parameters: axial mass, normalisation of the form factor and isoscalar background free) is fitted using the bubble chamber data, and the reasons why this under-coverage could happen are multiple: for example a problem with FSI, but also the Pion-less Delta decay or any other nuclear effects (such as the one discussed in the Section 1.2.5) that makes the extrapolation from a single nucleon to nuclear target wrong. Note that all the parameters described above are designed to act on the leading muon kinematics in the Charged Current resonant channels.

In most of the extended models that deal with resonant interactions in nuclear media, the modifications that arise are dependent on the momentum of the resonance (Delta width), so a parameter that modifies the shape of the W distribution is a fairly natural way to account for differences arising from nuclear correction. The parameters as function of Q^2 have more impact on the leading lepton. If one looks at the pion momentum, these parameters are acting as normalisation and cannot change the shape of the pion momentum.

For the purpose of the analysis, the MiniBooNE NCπ^0 momentum distribution [111] was fitted using the Delta width and position of the Breit-Wigner distribution.

In the MiniBooNE fits, the normalisation of the data is left free as most of the existing bubble chamber data are already constraining the normalisation of the nucleon level resonant processes and were explicitly tuned to accommodate other MiniBooNE CC and NC measurement normalisations [158].

Similarly, the FSI (for which the systematic error effects are not displayed in any of the plots in this section) can also change the normalisation (but not the shape of the pion momentum). This is because it is not simple to code a reweighting scheme which changes the shape of the kinematics of the pions when they undergo the FSI. Therefore, given that the normalisation of the data is a convolution of a number of non trivial parameters, it was chosen to leave the normalisation free, and the aim of this fit is solely to be able to reproduce MiniBooNE pion kinetical shape with sensible errors.

After doing the fit, one gets the result for the parameters listed in Table 6.2. In this case, only the two Delta parameters were fitted, while the other parameters were fixed at their initial tuned values.

The plots in Figure 6.4 show the error coverage one gets after generating toy with the errors from Table 6.2 and the all the standard errors from [161]. The Figure 6.5 shows the same distribution with an increased NC coherent uncertainty from 30% to 100%. This was done to try to accommodate data / MC differences in the forward region, which is expected to be purer in coherent interactions as illustrated on Figure 6.6.

Parameter	Prior	Uncertainty
Δ mass mean	-0.002	0.004
Δ mass width	-0.26	0.14

Table 6.2: MiniBooNE $p_{NC\pi^0}$ shape-only fit result.

In the case of the OOFV background interactions, they mostly are from RES interactions, as can be seen in Tables 5.4 and 5.3. The same effects as described before are also valid so one could wonder if having a carbon measurement is enough. However, given that there is no NCπ^0 measurement on target other than carbon (and Argon with ArgoNeuT [162]) where the π^0 kinematics are available, and the size of the detector error, it was considered that the differences in uncertainty between carbon and other nuclear targets should be negligible and thus the uncertainties described above were applied to the OOFV interactions.

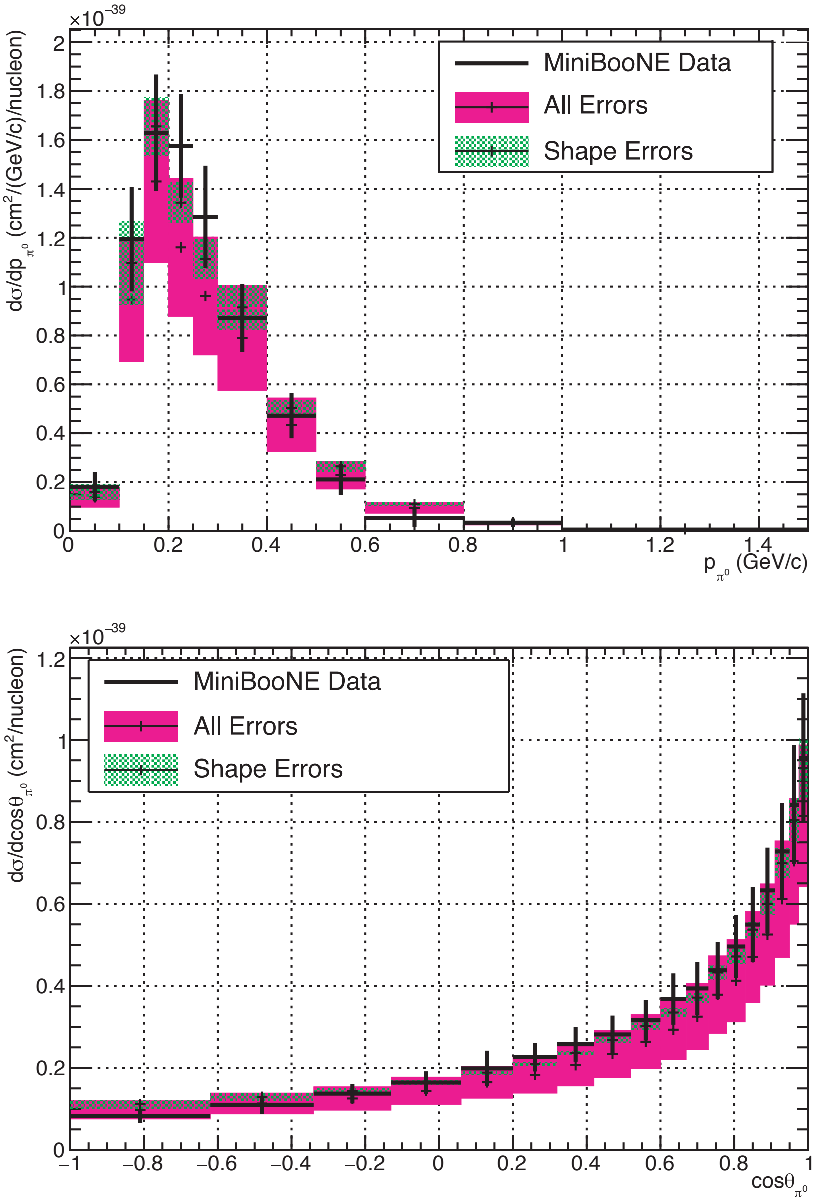

Figure 6.3: MiniBooNE error coverage from standard parametrisation [158] (Table 6.1). The black line shows the MiniBooNE neutrino mode NCπ^0 data [111], magenta boxes NEUT predictions with errors, overlayed green boxes are shape only variations from NEUT. ***Top:*** Pion momentum distribution. ***Bottom:*** Pion angular distribution.

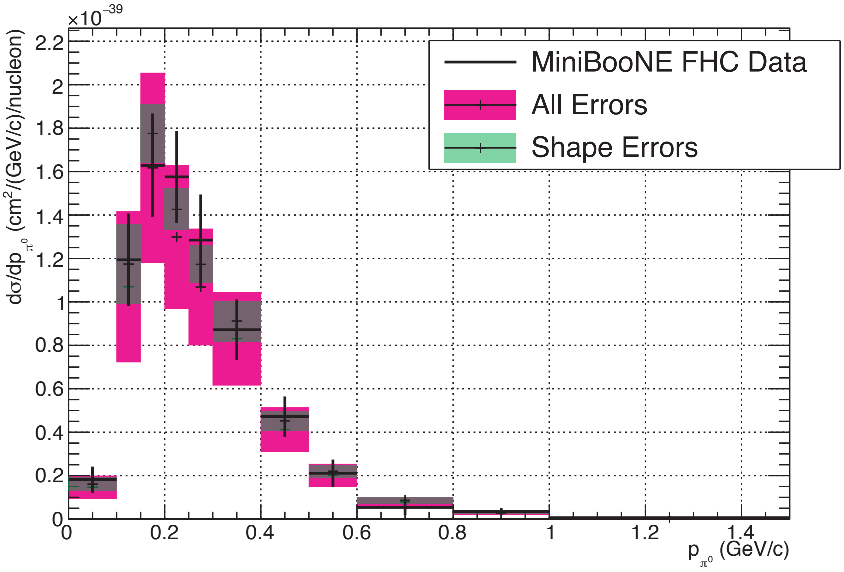

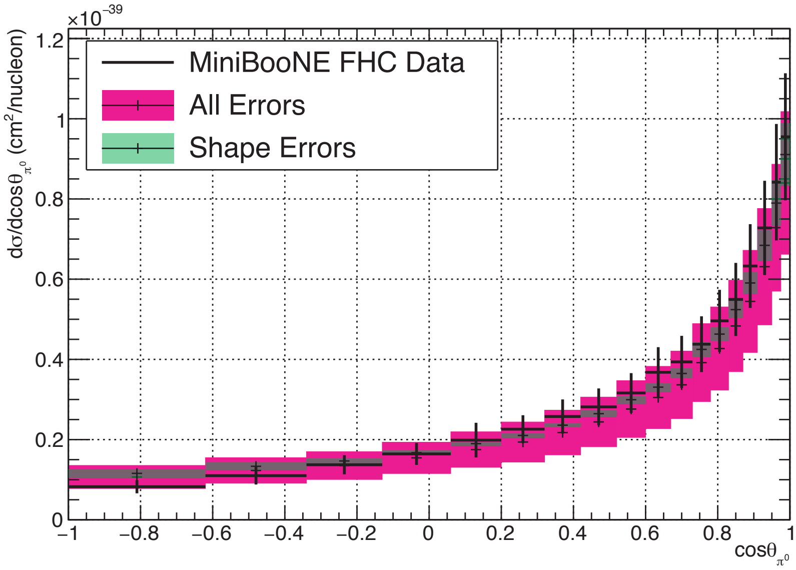

Figure 6.4: MiniBooNE error coverage using the fitted errors from standard parametrisation [158] (Table 6.1) and W-shape error (Table 6.2). The black line shows the MiniBooNE neutrino mode NCπ^0 data [111], magenta boxes NEUT predictions with errors, overlayed green boxes are shape only variations from NEUT. ***Top:*** Pion momentum distribution. ***Bottom:*** Pion angular distribution.

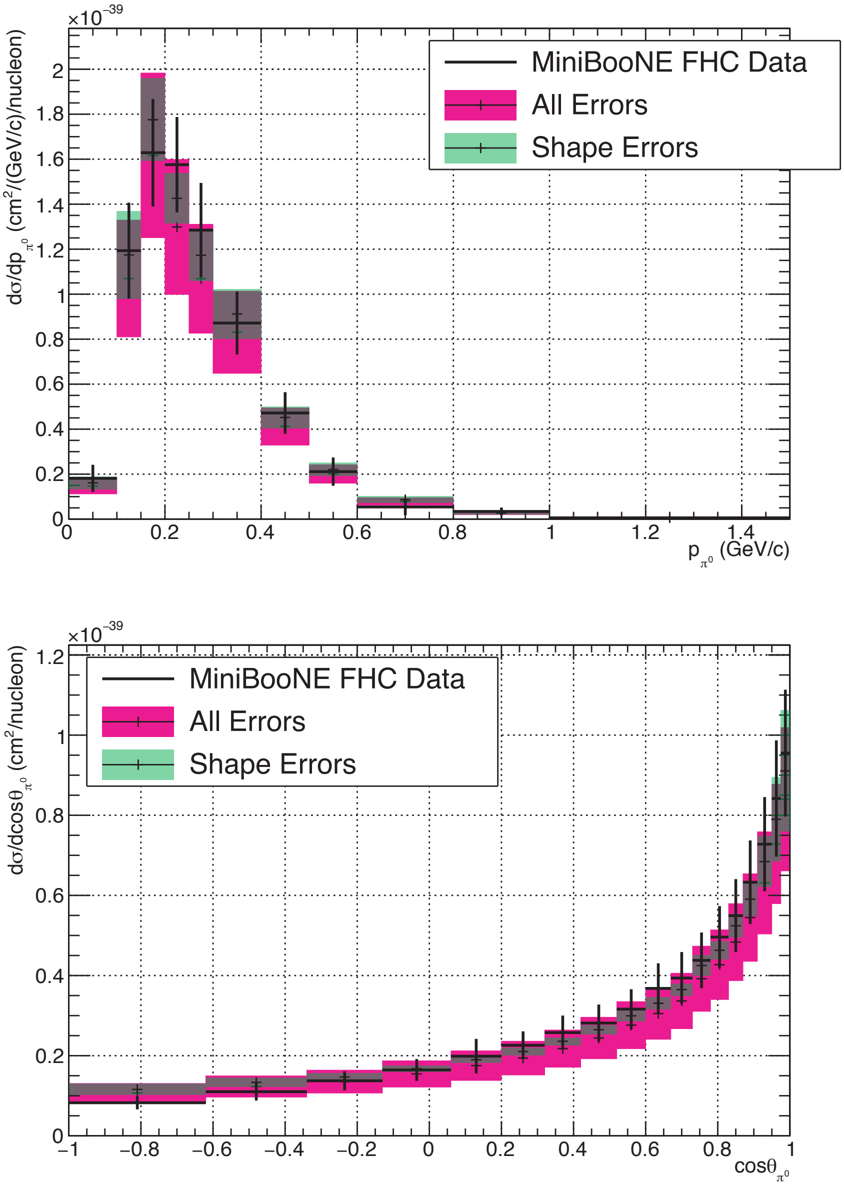

Figure 6.5: MiniBooNE error coverage using the fitted errors from standard parametrisation [158] (Table 6.1) and from W-shape error (Table 6.2) with a 100% error on NC coherent interaction The black line shows the MiniBooNE neutrino mode NCπ^0 data [111], magenta boxes NEUT predictions with errors, overlayed green boxes are shape only variations from NEUT. ***Top:*** Pion momentum distribution. ***Bottom:*** Pion angular distribution.

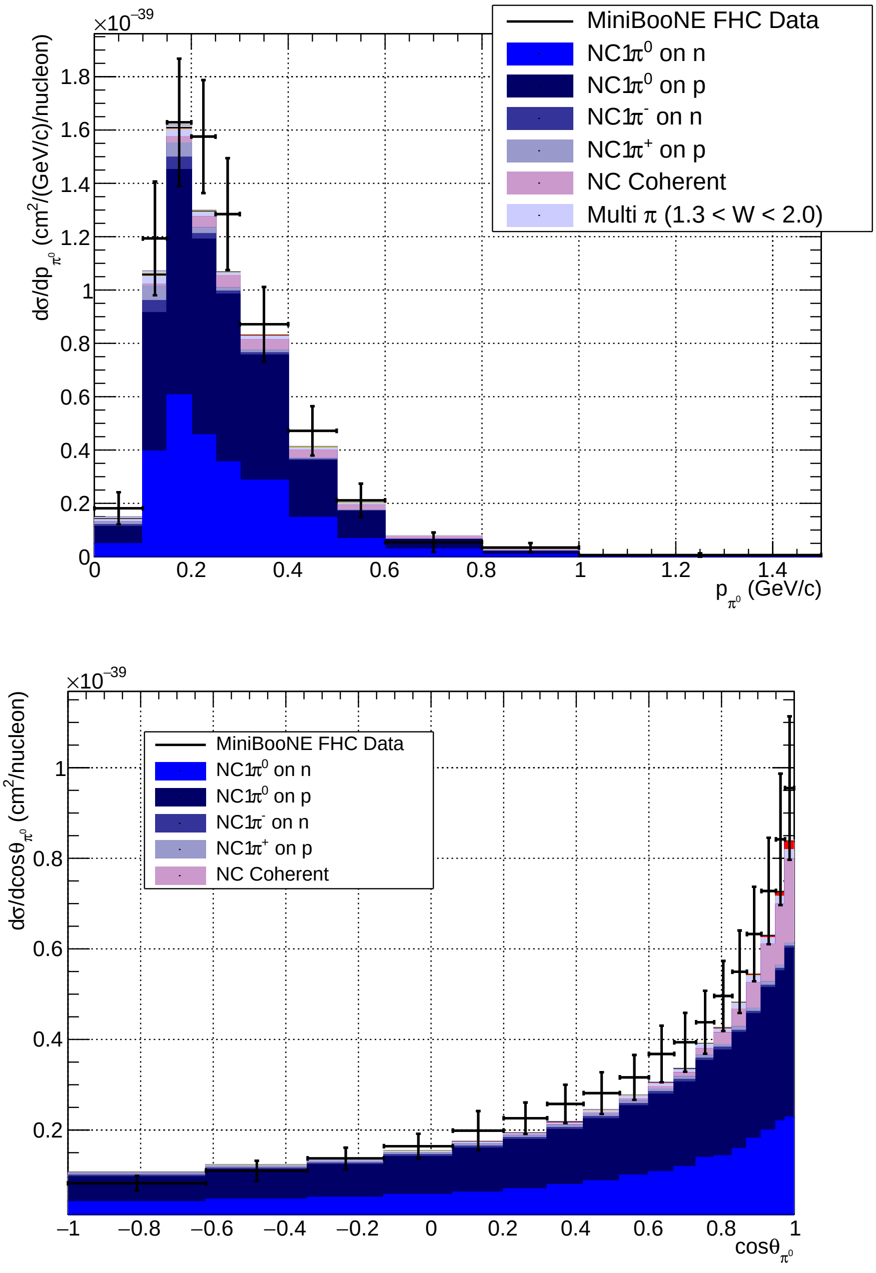

Figure 6.6: MiniBooNE NCπ^0 differential distribution, top: p_{π^0}, bottom: $\cos(\theta_{\pi^0})$, broken down by NEUT reaction modes, the central values and are the same as for 6.5.

6.2.1.3 Relativistic Fermi Gas parameters

The RFG model is dependent on two fundamental parameters. Both of them can be determined via electron scattering [163].

The first parameter is the Fermi momentum, this quantity is determined by the width of the elastic peak. The second parameter is the binding energy, which is determined by the position of the elastic peak. This quantity corresponds to the energy needed to extract a nucleon from the Fermi sea.

Unfortunately, even with very accurate electron scattering measurements, it is hard to find values for these two parameters which can explain all the electron scattering data [158], indicating a deficiency in the model.

The values and uncertainties that are used at T2K are listed in Table 6.3

Parameter	Value (carbon)	Value (oxygen)	Error
Fermi momentum p_F	217 MeV	225 MeV	31 MeV (flat prior)
Binding energy E_B	25 MeV	27 MeV	9 MeV (flat prior)

Table 6.3: Neutrino RFG errors used in the oscillation analysis, reproduced from [158]

Note that decreasing the E_B parameter “opens up” parameter space (as more events are allowed), and creating a reweighting scheme for these parameters is not a trivial problem and can lead to significant bias [158].

6.2.1.4 CCQE Form factor

Based on bubble chamber data [33–35], the CCQE form factor error that is used for the propagation is 5.8 %.

6.2.1.5 Multi nucleons

A 29.5 % normalisation uncertainties is assumed for multi-nucleons events, this comes from analysis from the MINERνA [41] and MiniBooNE [42] experiments.

6.2.2 Electron neutrino error

The traditional error for the electron neutrino cross section error is parametrised as an error on the ratio $\frac{\sigma_{\text{CC inc } \nu_e}}{\sigma_{\text{CC inc } \nu_\mu}}$ and similarly for anti-neutrinos. This is admitted to be of the order of 3%, with a 50% correlation for neutrino and anti-neutrino based on studies in [99].

6.2.3 Other cross section uncertainty

Other uncertainties were propagated on the DIS and COH events. In the case of DIS and SIS events, the scheme is to reweight the normalisation of the events with an error of the form:

$$\delta_\sigma = \frac{0.4}{E_\nu} \tag{6.2}$$

Which gives an error of 10% at 4 GeV as was observed in [164].

The NC and CC COH events have a normalisation error of 100% as explained in the previous section.

6.2.4 Final State Interactions

Final state interactions denote all the hadron interactions in the nucleus that happen after the primary neutrino interaction. For example, if a resonant process happens and creates a pion, this pion is inside the nucleus and can reinteract in the nucleus. The effect of the FSI is to generally change the topology of the event (bias towards lower energy for the pion, absorption of the pion, charge exchange). However, as discussed earlier, these changes in the shape have no error (only a normalisation error). For each NEUT interaction channel of the pion inside the nucleon, an uncertainty is computed. All the parameters and errors are given in the Table 6.4.

Systematic	Relative uncertainty
Pion absorption	50%
Low energy charge exchange	50%
Low energy quasi elastic	50%
Inelastic scattering	50%
High energy charge exchange	30%
High energy quasi elastic	30%

Table 6.4: FSI parameters and uncertainties.

For this analysis, the "16 throws" method was used. The idea is that it is sufficient to use sixteen different parameter sets for the FSI parameters to estimate the systematic error from FSI. These parameter sets have been detailed in [165] and are reproduced in Table 6.5. The effect of applying this reweighting is shown in Figure 6.7.

Set	Parameters					
	Quasi elastic		Inelastic scattering	Pion absorption	Charge exchange	
	LowE	HighE			LowE	HighE
Nominal	1.0	1.8	1	1.1	1.0	1.8
15	0.6	1.1	1.5	0.7	0.5	2.3
16	0.6	1.1	1.5	0.7	1.6	2.3
17	0.7	1.1	1.5	1.6	0.4	2.3
18	0.7	1.1	1.5	1.6	1.6	2.3
19	1.4	1.1	1.5	0.6	0.6	2.3
20	1.3	1.1	1.5	0.7	1.6	2.3
21	1.5	1.1	1.5	1.5	0.4	2.3
22	1.6	1.1	1.5	1.6	1.6	2.3
23	0.6	2.3	0.5	0.7	0.5	1.3
24	0.6	2.3	0.5	0.7	1.6	1.3
25	0.7	2.3	0.5	1.6	0.4	1.3
26	0.7	2.3	0.5	1.6	1.6	1.3
27	1.4	2.3	0.5	0.6	0.6	1.3
28	1.3	2.3	0.5	0.7	1.6	1.3
29	1.5	2.3	0.5	1.5	0.4	1.3
30	1.6	2.3	0.5	1.6	1.6	1.3

Table 6.5: The “16 throws” parameter sets of the FSI parameters.

Some interactions creating these π^0 are on heavy elements, such as the one on the aluminium of the support structure or the lead of the ECal. Additionally, some interactions on the brass in the P0D can occur.

For the FSI, the NEUT program is used to predict the pion-nuclear cross section on heavy targets and compared with the available pion scattering data. A subset of these comparisons is shown in Figure 6.8, which comes from [166], where all of them are available. Most of the data points lie within the current error budget, so the errors were not inflated. There is currently no shape uncertainty for the FSI, and since the π^0 momentum efficiency is not flat (as can be seen in Figures 5.19 and 5.20), this could lead to an effect similar to the one described earlier with the Delta mass parameter. However, FSI shape reweighting will not be done on an acceptable timescale for the scope of this work; it was therefore assumed that the normalisation error is sufficient to cover the error.

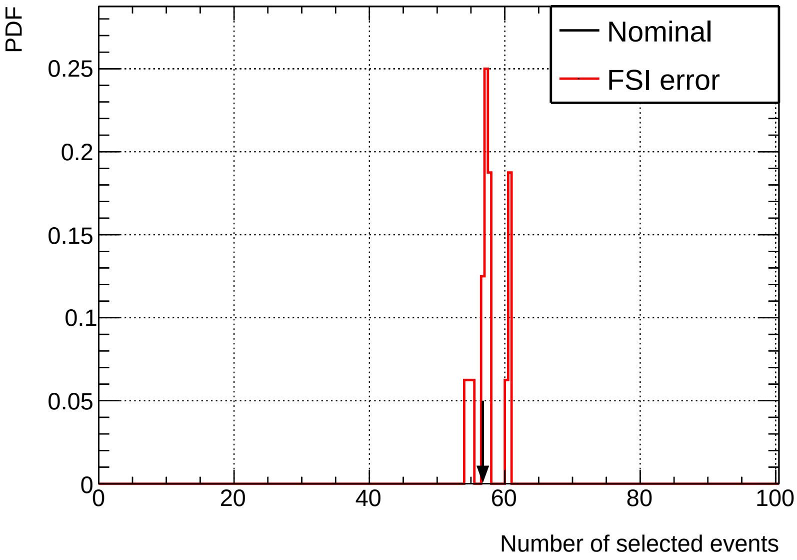

Figure 6.7: Effect of the pion FSI uncertainty on the number of selected events, using the "16 throws method". The nominal central value is indicated by the arrow.

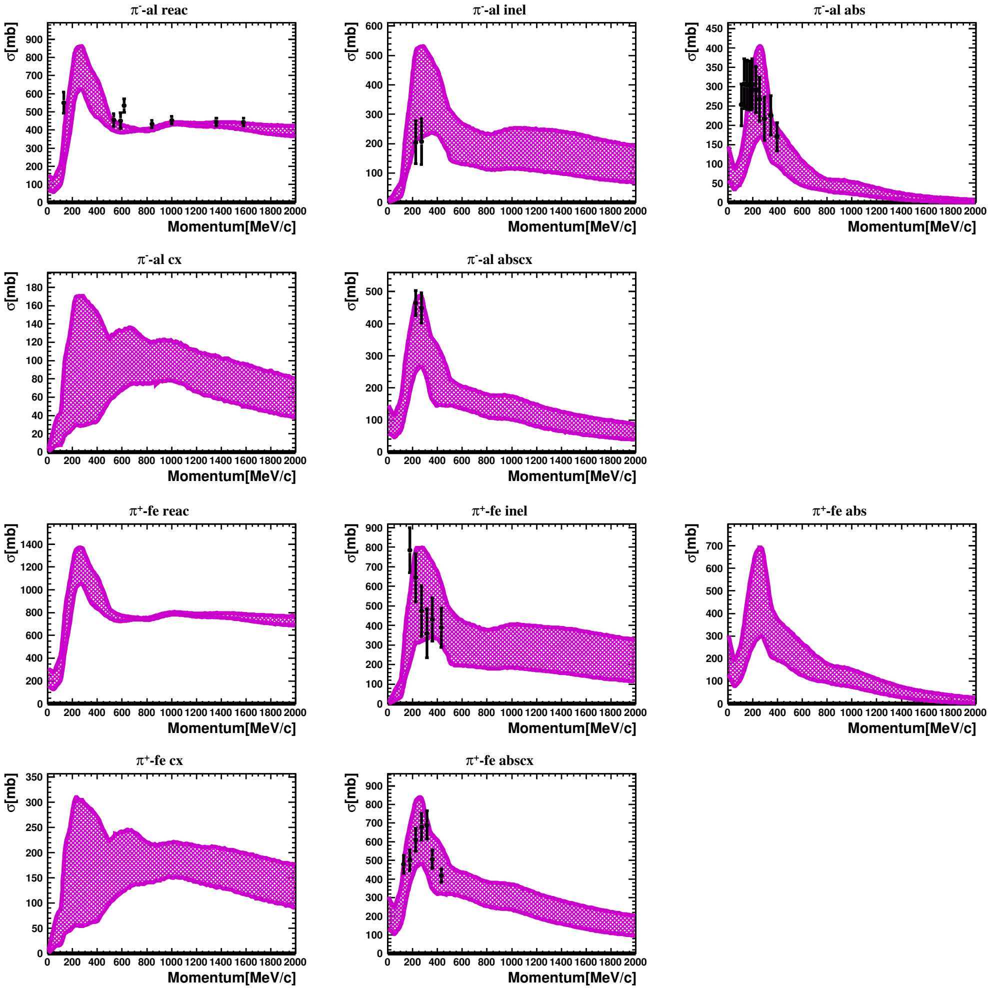

Figure 6.8: Comparison of pion scattering data to NEUT prediction and uncertainty. ***Top five:*** Negatively charged pion on aluminium. ***Bottom five:*** Positively charged pion on iron. From [166], for references, see in Table (5.1) of [167].

6.2.5 Effects on the selection

The effects from the nucleon level pion production uncertainties are shown in Figure 6.9, which shows the effects on the number of selected events for FGD1 FV events only. Note that the NC coherent weight distribution shows a spike at 45 events which corresponds to no coherent events in the selection. Since the uncertainty is a Gaussian function centred at one with an error of one; this is expected to happen 16% of the time.

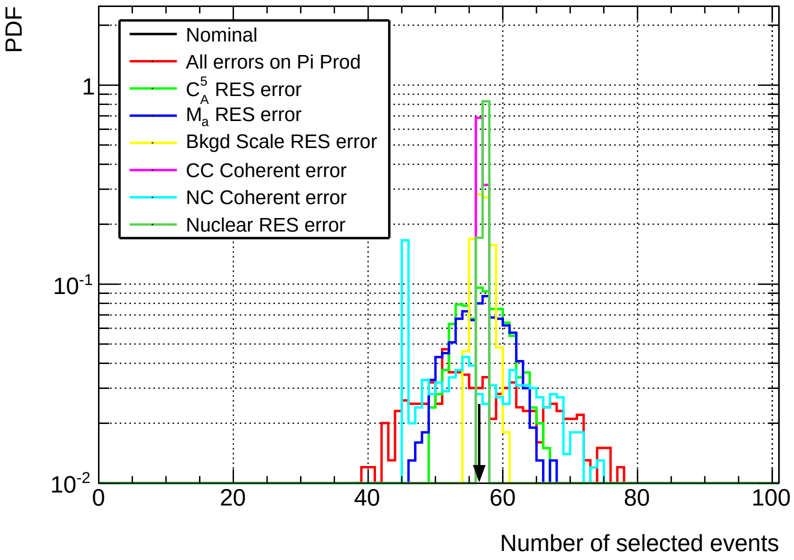

Figure 6.9: Effects of the pion resonant cross section uncertainties on the number of selected events. The nominal central value is indicated by the black arrow.

The other CCQE and ν_e cross section errors effects are shown in Figure 6.10.

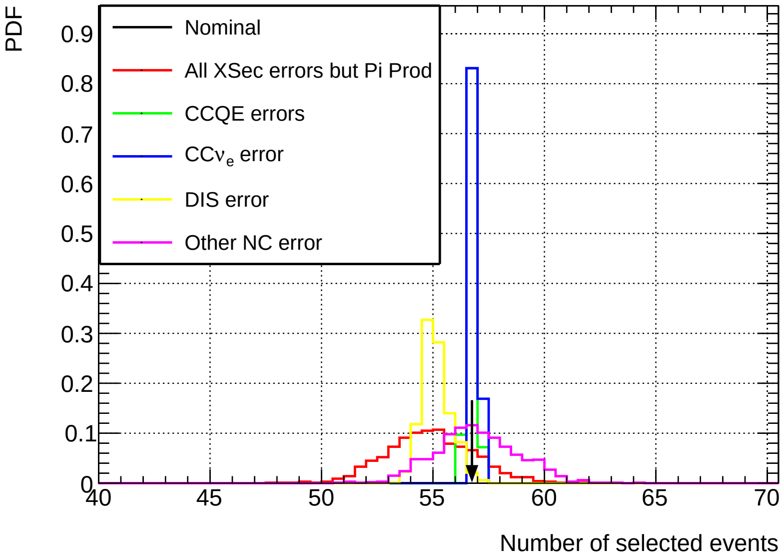

Figure 6.10: Effects of the DIS (CC and NC), CCQE, CC coherent and ν_e cross section uncertainty on the number of selected events. The nominal central value is indicated by the arrow.

6.3 Detector systematic uncertainties

The motivation for each of the detector uncertainty is detailed here. There are three ways of implementing the ND280 detector systematic uncertainties in T2K, the first ones are called "variation systematics", where the physical quantity (momentum and TPC PID pull) that is being measured is changed according to the effect of the systematic; another type controls the normalisation of a whole class of events (so-called "normalisation-like systematics") and finally, "efficiency-like systematics" which control, on an event by event basis the weight of an event. All the uncertainties that comes from detector effects are described here.

6.3.1 Variation systematic uncertainties

6.3.1.1 The momentum scale uncertainty

The magnetic field has an absolute error of 0.57% that gets directly propagated on the momentum of the particle [152].

6.3.1.2 The magnetic / electric field uncertainty

The magnetic and electric field uncertainty [152] comes from the fact that both the fields are not uniform in the TPC. This is due to the presence of various equipment around the TPC or the TPC case itself which produce fringe fields. In general, the magnetic field and these fringe fields make the drift electrons from the ionisation travel in a line which is not straight, which makes the reconstruction more complicated. Some corrections can be applied at the reconstruction level to take this effect into account, but there is still a systematic uncertainty which has applied to the reconstructed momentum.

On the cathode, some "dots" can be illuminated by lasers to produce photo-electrons. These electrons drift until the readout plane, and one can estimate the error on the corrections by calculating distance from the reconstructed position of the dots to their real position. This leads, at the analysis level, to an uncertainty on the momentum of the particle.

6.3.1.3 The momentum resolution uncertainty

The TPC momentum resolution [152] was computed with through going tracks that are reconstructed in multiple TPCs. This systematic uncertainty aims at characterising the intrinsic momentum resolution of the TPCs. The presence of intermediate FGDs complicates the error calculation, as one needs to correct for momentum loss in them. The uncertainty is propagated on $1/p_T$ where p_T is the transverse momentum of the particle (where transverse means orthogonal to the Z direction, in the ZY plane). The uncertainty is around 10^{-4} for a 500 MeV particle. This uncertainty is directly propagated on the momentum of the particle.

6.3.1.4 The TPC PID uncertainty

The PID quantities that are used are the pulls, defined from the $dEdx$ as shown in Equation (5.2). To get an uncertainty on these quantities, the pull is calculated for control samples on a subset of the data available. This is then compared to the expected MC distribution. In this case, the control sample is a photon sample (electron / positron pairs with an invariant mass and good TPC quality requirements). One obtains distributions similar to the one shown in Figure 6.11 and can compare the width and position of the Gaussian distributions which are used as systematic uncertainties. In Figure 6.11, on the right, each of the data and MC distributions (in blue and green histograms, respectively) are fitted with Gaussian functions (blue and green curves). The MC predictions are then shifted to overlap with the data by moving the mean of the Gaussian function for MC and its spread, thus producing a correction that has to be applied to the nominal MC.

The systematic uncertainty comes from the errors on the parameters of the Gaussian functions, which is retrieved from the fit.

This is repeated for different momentum bin, particle type and, if the statistics are sufficient, run period and TPC (in practice, this split can only be realised for muons) [152].

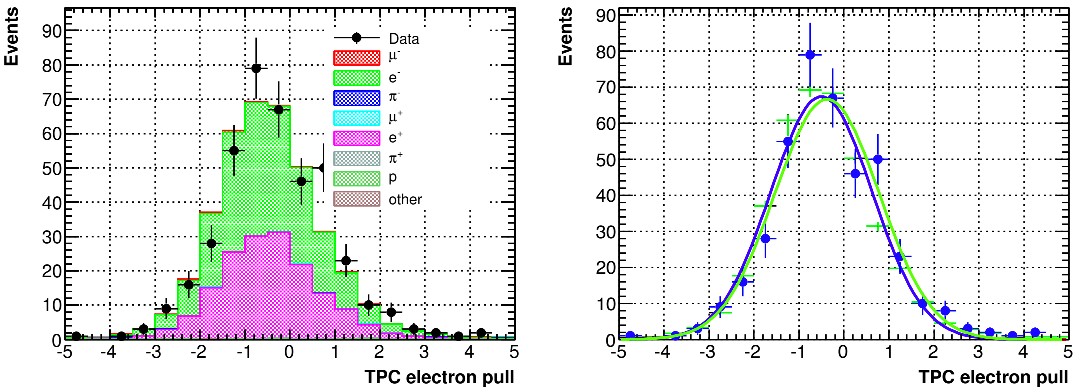

Figure 6.11: ***Left:*** PID pull for electrons (or positrons) of momentum smaller than 200 MeV. ***Right:*** PID pull Gaussian fits for data (blue) and MC (green).

6.3.2 Efficiency systematic uncertainties

The efficiency systematic errors are applied to the events and in general are applied to both the pair and main tracks, unless stated otherwise.

6.3.2.1 The TPC cluster efficiency uncertainty

The TPC cluster efficiency uncertainty [152] is applied because there is a cut on the number of nodes the tracks creates in the TPC (track quality cut). Note that clusters are horizontal or vertical hits that are joined together (see the step 2 in the TPC paragraph in Section 5.2.1.3). This was computed by comparing the number of nodes of muon data control samples to its equivalent in the MC. These control samples are a subset of a CC inclusive selection and cosmic muons triggers. The selections are run without the TPC track quality and the ratios

$$\frac{\epsilon_{\mathrm{Data}}}{\epsilon_{\mathrm{MC}}} \tag{6.3}$$

$$\text{and } \frac{\epsilon_{\mathrm{MC}} - \epsilon_{\mathrm{Data}}}{\epsilon_{\mathrm{MC}}} \tag{6.4}$$

are computed (in these equations, ϵ indicate the data and MC efficiency). It was then found that shifts one has to apply to the MC (first ratio) and error (second ratio) are both the order of one per mil.

6.3.2.2 The TPC track efficiency uncertainty

The TPC track efficiency uncertainty [152] characterises the error one gets by solely requiring the presence of a track in the TPC. Rather than cluster efficiency, this error is related to the presence of a full reconstructed object as explained in the TPC paragraph of Section 5.2.1.3 (step 3). The error is computed with through-going muons which cross several detectors. The data and MC comparison for such sample show that there is no unexpected behaviour in the all TPCs and that the uncertainty does not depend on the momentum, position and number of track crossing them. The error is around 0.5% for a single track entering the TPC2.

6.3.2.3 The TPC / FGD matching efficiency uncertainty

The TPC / FGD matching efficiency uncertainty [152] arises because the tracks in the selection have to be reconstructed as a single object. Note that, even though there is no explicit requirement for the Pair Track to be in the FGD (only a distance specification is made), there is a priori, no requirement to apply this error for cases where the Pair Track does not use the FGD. However this was considered to be a marginal effect that happens only if the Main Track is next to the TPC, on the edge of the FGD, so it was applied regardless of the topology of the Pair Track.

The efficiency was computed using through-going muons crossing different TPCs, and found to be exactly 100% (i.e. no track that enter the TPC from the FGD are missed, and vice versa). Recalling that the FGD1 FV extends to the last layer downstream, right next to the TPC2, and that only two bars are removed in the upstream direction, this is maybe not surprising. To assign the error, it was decided that the TPC / FGD matching could fail if a track leaves only two hits in the FGD (i.e. it is very close to its edge) and therefore the hit efficiency is used as the error, which in this case is equal to about 0.8%.

6.3.2.4 The TPC / ECal matching efficiency uncertainty

It was found recently that the ECal's representation in the MC was few millimetres away from its real position. Therefore there could be a mismatch between the probability in reconstructing a particle in the ECal which came from the TPC in data and MC. This could affect the ECal veto since there is a requirement for the selected veto object to not be one of the two tracks. An uncertainty is therefore applied on the MT of PT when they enter the ECal. The uncertainty which is propagated on these tracks is of the order of 5% [168].

6.3.2.5 Charge Identification uncertainty

The charge identification is a fundamental input to the analysis, since it relies on the selection of two tracks of opposite charge. The error that is used is determined from the control samples which have a muon traversing several TPCs [152]. One can then compare the probability to incorrectly swap the charge between data and MC. The error decreases with the number of TPC the particle traverses; in the worst case, when the track is reconstructed in two TPCs, and each one reconstructs a different charge, the uncertainty is of 2%. The error is propagated on the inverse transverse momentum as in the case of the momentum resolution.

6.3.3 Normalisation uncertainties

These uncertainties are applied to a whole class of events based on their topologies, it generally does not rely on the detector efficiencies themselves, but rather on other effects such as the cross section (for the pion and proton secondary interaction), the mass uncertainties (for the photon secondary interactions and the FGD mass), or the presence of additional events (pile up uncertainties).

6.3.3.1 FGD mass uncertainty

The FGD has a mass uncertainty of 0.6%, which comes from the uncertainty in size of its bars and the hole for the fibre [152].

6.3.3.2 The pile up and sand uncertainties

The pile up uncertainty comes from the fact that vetoes are present in the selection. Indeed, additional "sand" events that comes from the sand around the ND280 can reach the detector and trigger the veto of the selection. In the interest of time and space, these events are not included in the standard "magnet MC" (i.e. events that are in happening the volume enclosed by the ND280 magnet) that is used for the analysis, they are added separately. The problem is then, since these "sand" events are added separately on top of the simulation, how to see their effect on the vetoes? For example, if a "magnet" event is selected and passes the selection, and if there was a "sand" in the same time, one would expect to select fewer events. Hence the name, the magnet and sand events are "piled up."

The way to overcome this is by calculating a pile up correction and uncertainty. For that, the strategy is to run a selection which only has the vetoes, and comparing the data to the sum of the magnet MC and sand MC. The vetoes are added in the same order as in the selection.

Note that the sand events have an intrinsic uncertainty of 10%, which comes from the simulation of the surroundings of the ND280, the flux uncertainty and the cross section.

Upon assigning the pile up correction, the strategy is to modify the normalisation of the whole selection based on the sand trigger rate one gets. The error is either the data / MC difference, or the sand error if it is greater than the former. All the errors and corrections are listed in Table 6.6, note that the correction is dependent on the run, since the MR power increases and produces different yields in the vetoes due to the expected increase in sand interaction and thus pile up.

Finally, as no sand event enters the actual selection, they thus lead to no additional uncertainty.

Veto	Run	Correction	Systematic uncertainty
TPC muon rejection	2A	0.992	0.009
	2W	0.993	0.007
	3AB	0.994	0.009
	3AC	0.991	0.009
	4A	0.989	0.010
	4W	0.990	0.010
TPC Veto	2A	0.995	0.008
	2W	0.996	0.007
	3AB	0.996	0.008
	3AC	0.994	0.009
	4A	0.992	0.010
	4W	0.994	0.010
P0D Veto	2A	0.928	0.009
	2W	0.936	0.008
	3AB	0.937	0.009
	3AC	0.920	0.010
	4A	0.897	0.012
	4W	0.906	0.010
ECal Veto	2A	0.9989	0.0006
	2W	0.9983	0.0007
	3AB	0.9991	0.0007
	3AC	0.9979	0.0008
	4A	0.9974	0.0008
	4W	0.9967	0.0010

Table 6.6: Pile up corrections and systematic uncertainties used in the analysis.

6.3.3.3 The pion secondary interaction uncertainty

The pion secondary interaction uncertainty [152] is a weight error that is propagated on the events which have charged pions in them. A secondary interaction happens when this pion reinteracts with some of the detector material, rather than losing energy by ionisation in the detector.

There are a lot of channels in which a charged pion can interact, but the most important in the context of this analysis is the charge exchange channel, where a pion goes from being a charged pion to a neutral pion after interaction with a nucleus. Unfortunately, the MC model that was implemented in the ND280 simulations (Bertini model [169]) was found to very poorly describe the available data at T2K energies [170–172] (200 MeV); therefore a correction factor was included in the cross section for charged pions. The error on the above mentioned data [172] was also propagated to the weight to be able to get an uncertainty on the secondary pion interaction. Note that these are completely uncorrelated with the FSI errors as described earlier; correlating the pion secondary interaction and the FSI will constitute an improvement for the next generation of analyses at the ND280.

6.3.3.4 The proton secondary interaction uncertainty

The proton secondary interaction probability uncertainty [152] is propagated if the MT or PT is a proton. This happens if the PID did not work properly, for example. The low energy protons have a probability of interacting with the scintillator in the FGD and can reinteract in it. A very conservative error of 10% is applied for the proton interactions.

6.3.3.5 The photon secondary interaction uncertainty

As can be seen in Table 5.3, the selection has a substantial contamination with π^0 events happening outside the FV of the FGD1. Since photons propagate $\simeq 40$ cm in the plastic, which is roughly the size of the FGD1, this is not surprising. However, most of the detector errors described up to now are designed for tracker CC analyses, where the OOFV contamination is much smaller. It is important to check that these errors can be applied for the OOFV events in this analysis. The purpose of this section is to estimate the detector uncertainty due to OOFV gamma rays.

Firstly, the errors on the mass of each part of ND280 detector were derived (this can be found in Appendix B), then the photon is reweighted according to its path length in each detector, by effectively changing its survival probability according to fractional mass changes of the detector. The effect of the vetoes on this systematic error is not trivial, because if the photon is converts somewhere else, it may trigger a veto. Such effects are not taken into account.

Photon Propagation As well as the absolute normalisation of all the events coming from outside the fiducial volume, a more subtle effect is to take into account the case when the photons are traversing different materials with poorly known density.

The photon pair conversion length depends on the density of the material it traverses. Therefore, it makes sense to assign an uncertainty to the conversion length of the photons. This uncertainty is going to be propagated via a “reweighting” to the event, which modifies the normalisation of each photon coming from outside the FGD1 depending on the region of space in the ND280 it traverses. This weight depends on the assumed value of the mass of the region of space and therefore the uncertainties summarised in Table B.3 will propagate to the weight of the photon event. This section describes how this is realised.

The best way to do that is to use a stepping algorithm that calculates and reweights the interaction probability for every arbitrary small step of the photon trajectory. However, these are usually CPU intensive so an approximation of this method by using the "integrated" version of a stepping algorithm. The intensity of photons traversing material is given by the well known equation:

$$N(x) = N(\overrightarrow{x}_0)e^{-|\overrightarrow{x}-\overrightarrow{x}_0|/\lambda}, \tag{6.5}$$

where $\overrightarrow{x}$ and $\overrightarrow{x}_0$ are the spatial vectors for the conversion point of the photon and the creation of the photon, respectively and $N(\overrightarrow{x})$ is the number of photons at a position $\overrightarrow{x}$.

The mean free path, λ, that the photon traverses before creating a pair is given in the Born approximation by [109]:

$$1/\lambda = \frac{7}{9}4Z(Z+1)D_{\mathrm{atom}}r_e^2\alpha\left(\ln(183Z^{-\frac{1}{3}}) - f(Z)\right), \tag{6.6}$$

where Z is the atomic number of the material the photon traverses, D_{atom} the atom density, r_e is the radius of the electron $((e^2/mc^2)^2)$, α the EM constant, and $f(Z)$ a correction to the Born approximation, which has the form:

$$f(Z) = a^2\left(\frac{1}{1+a^2} + 0.20206 - 0.0369a^2 + 0.0083a^4 - 0.002a^6\right), \tag{6.7}$$

in which $a = Z/137$.

The first thing to notice is that the density dependence is inversely proportional to the mean free path, while the Z dependence is non-trivial. For an arbitrary change of density in the material the photon traverse, one would expect a change in the total number of events reaching the FGD to be of the form:

$$\begin{aligned}\frac{N_{\mathrm{toy}}(\overrightarrow{x})}{N_{\mathrm{nominal}}(\overrightarrow{x})} &= \frac{N_{\mathrm{toy}}(\overrightarrow{x}_0)e^{-|\overrightarrow{x}-\overrightarrow{x}_0|/\lambda_{\mathrm{toy}}}}{N_{\mathrm{nominal}}(\overrightarrow{x}_0)e^{-|\overrightarrow{x}-\overrightarrow{x}_0|/\lambda_{\mathrm{nominal}}}}\\ &= \frac{N_{\mathrm{toy}}}{N_{\mathrm{nominal}}} \times e^{-|\overrightarrow{x}-\overrightarrow{x}_0|\left(\frac{1}{\lambda_{\mathrm{toy}}}-\frac{1}{\lambda_{\mathrm{nominal}}}\right)},\end{aligned} \tag{6.8}$$

for a particular event crossing a single detector. In Equation 6.8, N_{toy} (N_{nominal}) is the number of photons in a world where the material density is such that it leads to a photon mean free path of λ_{toy} ($\lambda_{\mathrm{nominal}}$), respectively.

In this case, λ_{toy} and λ_{nominal} are effective parameters that describe the Mean Free Path (EMFP, for Effective Mean Free Path) of the photon for each dead region; the explanations for getting the EMFP numbers are given later. These are not retrieved from the simulations but rather calculated using simpler geometry and composition data, so that one can change those simple input values to calculate an event weight.

The labels nominal and toy indicate the number of photons for the nominal (best guess) MC and for a toy MC which represents a different "universe" where, due to a different mass of the detector, the λ_{toy} parameter was different.

The uncertainty that describes the number of neutrino interaction detected in FGD1, which corresponds to the ratio $N_{\text{toy}}/N_{\text{nominal}}$, follows a Gaussian distribution which has a width corresponding to the mass error. This means that the error on the number of neutrino interactions from the mass uncertainty is accounted for.

It is important to realise that a Gaussian error on the mass of the detector is unlikely to produce a Gaussian weight for the event, in Equation 6.8. *A priori*, the weights are going to be asymmetrical (increasing or decreasing λ will have a very different effect on this ratio). The next two paragraphs describe the procedures used to get these EMFP numbers.

The P0D and BrECal regions effective mean free paths In simple cases, for the P0D or the ECal regions, the EMFP can just be calculated using the mass proportion and Equation 6.6.

Note that the EMFP for a detector is retrieved using a mass weighted harmonic average of the EMFP (i.e. the inverse of the average is the weighted sum of the inverse of the EMFPs):

$$1/\lambda_{\text{mean detector}} = \sum \frac{p_{\text{material}}}{\lambda_{\text{material}}} \tag{6.9}$$

The average EMFP is $\lambda_{\text{mean detector}}$, and the proportion of material in the detector is $\lambda_{\text{material}}$, which is obtained from the density and atomic number of the material. Table 6.7 summarises the materials and densities used to get the values of $\lambda_{\text{mean detector}}$ and the volume limits.

Effective mean free paths and density parameters for other regions For all the other regions (which are called OOAFV, for Out Of All Fiducial Volumes), the complexity and composite nature of the materials means that one cannot access the density and the atomic number of the materials. For example, this happens when a photon traverses some cables, or the TPC case; it is quite complicated to have a simple density profile.

Region	Constituants (proporition)	Photon χ_0 $[mm]$
P0D with water	Brass (22.25 %) Water (8.54 %) Lead (21.84 %) Scinitillator (47.37 %)	16.4
P0D without water	Brass (10.98 %) Lead (28.08 %) Scinitillator (60.93 %)	20.8
ECal sides	Lead (50.08 %) Scinitillator (49.92 %)	10.5
ECal top / bottom	Lead (50.46 %) Scintialltor (49.54 %)	10.4

Table 6.7: OOFV detector regions constituants and EMFPs.

To estimate these densities, a special sample of the Monte Carlo was prepared. All the true photons of at least 5 MeV that started and ended in the OOAFV regions were saved and their path lengths were computed.

A decaying exponential function (Equation 6.5) was then fitted on the resulting distributions. In the case where the photon is contained between the P0D and the FGD1, the fit function was the sum of two decaying exponential functions. This was used because the distribution shows two different populations of photons, one travelling short distances and probably coming from very close to the FGD1, or in the end of the P0D and the other longer distances, probably when the photons traverse the whole TPC1. This can be seen in Figure 6.12 (e).

To avoid geometrical effects, which happen because the selection volumes are not infinite, the fits are performed within relatively short ranges (from 0 to 200 mm for all the regions between the BrECals and the FGD1 and from 0 to 600 mm for the TPC1 region); these ranges are smaller than the smallest distance in the defined volumes.

The fits of the path lengths are shown in Figure 6.12, and the results are in Table 6.9. In this table, the volume definitions, densities and materials used are also detailed.

To get the density, one needs to assume a particular material (Z), in this case, aluminium was used since it is the supporting structure of the ND280. An exception was made for the region in between the P0D FV and the TPC1: in this case, since the region is mostly composed of the Central ECal of the P0D, lead was used (the composition of this region is given in Table 6.8).

Finally, the density function in Figure 6.13 which comes from plotting Equation 6.6 against the density (D_{atom}) were intersected with the fit results from the path lengths (in Figure 6.12) which is a horizontal line on these plots to read off the density in the abscissa.

Material	Percentage
carbon	38.6%
oxygen	0%
hydrogen	4.6%
aluminium	0%
iron	5.5%
copper	0%
zinc	0%
lead	48.5%
other	2.9%

Table 6.8: OOFV region composition which corresponds to the Central ECal region in the P0D, the percentages are the number of true neutrino NC events, and give an idea of the mass composition. The volume is defined later in Table 6.9.

This is then used in the density reweighting.

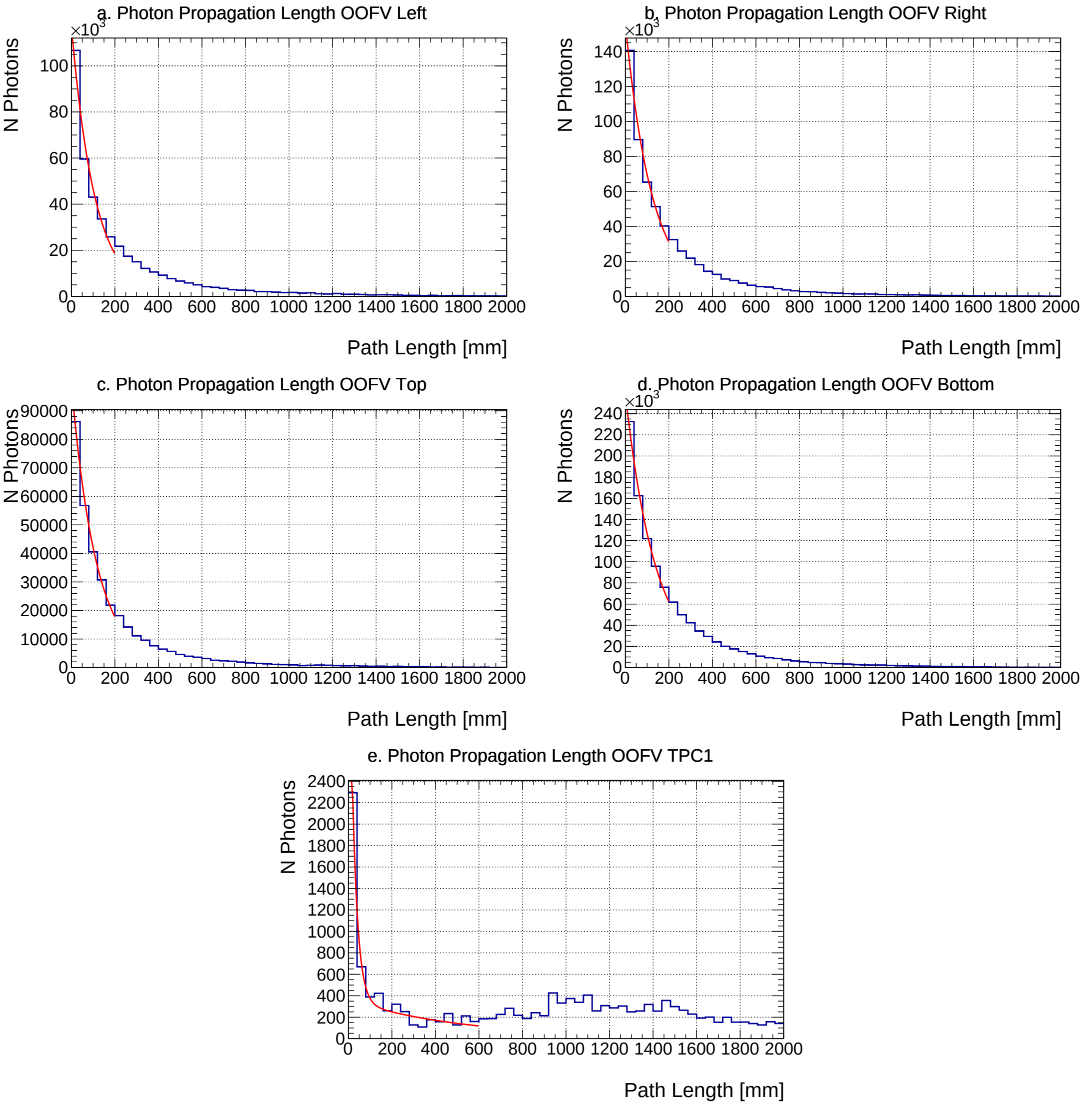

Figure 6.12: Blue histograms: Path length distributions of photons propagating in the OOFV regions. ***Red curve:*** Fits. ***Top four:*** Regions between FGD1 and BrECal (fitted with one exponential function). ***Bottom:*** Region between P0D and FGD1 (fitted with the sum of two exponential functions).

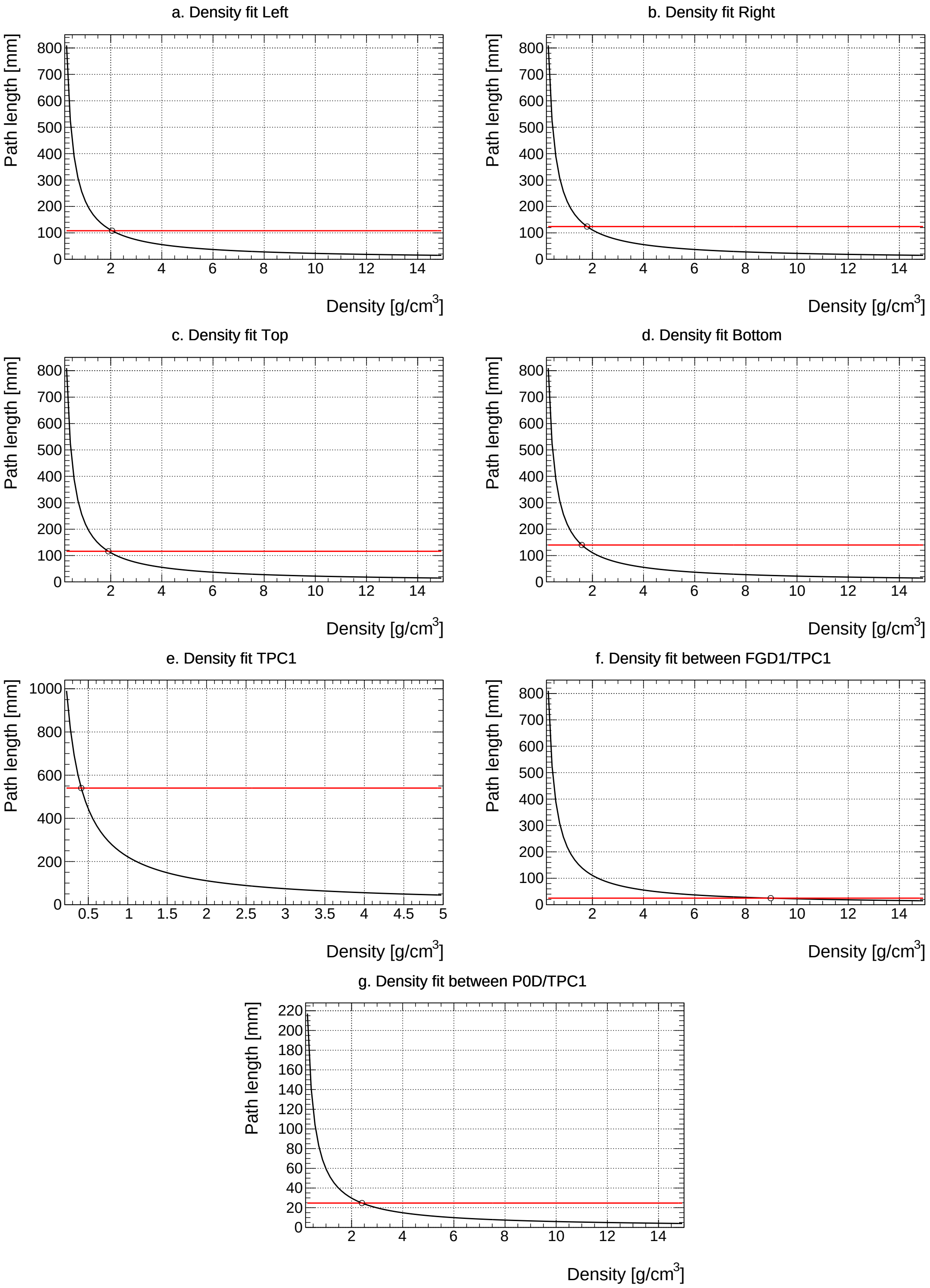

Figure 6.13: ***Black curves:*** Photon EMFP calculation from Equation 6.6 assuming aluminium material (except for the last bottom figure where lead was chosen) as function of D_{atom}, the density. ***Red line:*** Photon EMFP from the fit shown in Figure 6.12.

Summary Using the procedure mentioned in the two previous sections, one gets the EMFP in OOFV regions shown in Table 6.9.

Two reweightings are then applied to the λ_{nominal} to get the weight of event:

- For the density dependance, the path length can be reweighted with: $\lambda_{\text{toy}} = \lambda_{\text{nominal}}(1+\epsilon_{\text{mass}})$, where the overall mass uncertainty of the detector the photon traverses is used to change ϵ_{mass}.
- For the Z dependence, Equation 6.6 is used to recalculate the EMFP of the photon according to a flat variation of the mass number in the case of an isoscalar nucleus. This reduces to varying Z with half of the variation in the mass: $Z_{\text{toy}} = Z_{\text{nominal}}(1+\epsilon_{\text{mass}}/2)$

For the events that are entering the selection, the photon might propagate through several volumes of different densities before converting in the FGD1. To take this into account, Equation 6.8 can be extended:

$$w = \prod_{\text{area traversed}} \frac{N_{\text{toy}}(\overrightarrow{x}_{\text{area traversed}})}{N_{\text{nominal}}(\overrightarrow{x}_{\text{area traversed}})}, \tag{6.10}$$

where the conventions are the same as in Equation 6.8, and $\overrightarrow{x}_{\text{area traversed}}$ are the distances the photon travels in each area.

All the OOFV volumes and planes used for the reweighting and the nominal conversion lengths are shown in Table 6.9

Region	Volume limits $[mm]$	Density	Material	Photon χ_0 $[mm]$	Mass error
In TPC1	$x_{\text{min}} = -874.51$ $x_{\text{max}} = 874.51$ $y_{\text{min}} = -819.51$ $y_{\text{max}} = 929.51$ z_{min} No Cut z_{max} No Cut	0.41	^{26}Al	540	6.5380 %
between TPC1 and FGD1	$x_{\text{min}} = -874.51$ $x_{\text{max}} = 874.51$ $y_{\text{min}} = -819.51$ $y_{\text{max}} = 929.51$ $z_{\text{min}} = 89.00$ $z_{\text{max}} = 136.875$	8.97	^{26}Al	25	6.5380 %
between P0D and TPC1	$x_{\text{min}} = -836.00$ $x_{\text{max}} = 764.00$ $y_{\text{min}} = -871.00$ $y_{\text{max}} = 869.00$ $z_{\text{min}} = -1264.00$ $z_{\text{max}} = -1150.00$	2.41	^{208}Pb	25	6.5380 %
between TPC1/FGD1 and BrECal (left)	$x_{\text{min}} = 874.51$ x_{max} No Cut $y_{\text{min}} = -819.51$ y_{max} No Cut z_{min} No Cut z_{max} No Cut	2.05	^{26}Al	108	6.0402 %
between TPC1/FGD1 and BrECal (right)	x_{min} No Cut $x_{\text{max}} = -874.51$ y_{min} No Cut $y_{\text{max}} = 929.51$ z_{min} No Cut z_{max} No Cut	1.79	^{26}Al	123	6.6506 %
between TPC1/FGD1 and BrECal (top)	$x_{\text{min}} = -874.51$ x_{max} No Cut y_{min} No Cut $y_{\text{max}} = -819.51$ z_{min} No Cut z_{max} No Cut	1.91	^{26}Al	116	5.5572 %
between TPC1/FGD1 and BrECal (bottom)	x_{min} No Cut $x_{\text{max}} = 874.51$ $y_{\text{min}} = 929.51$ y_{max} No Cut z_{min} No Cut z_{max} No Cut	1.58	^{26}Al	140	38.2304 %

Table 6.9: OOFV regions characteristics, showing the volume definition, the density used for propagating the error, the material, and the photon EMFP and the mass error of the region.

6.3.3.6 Out of fiducial volume reconstruction uncertainty

This uncertainty is propagated because the MT and PT are selected inside the FV of the detector. This was based on work from [173]. It can happen that the tracks come from outside the fiducial volume but are reconstructed inside if for example there was a failure to detect a hit in the outer layers of the FGD, or a hard scatter in the FGD that somehow confuses the reconstruction. These can sometime have a large uncertainty (30 to 50%) depending on the topology of the track.

6.3.4 Summary of the detector uncertainties

Table 6.10 gives a summary of the overall effects of all the detector errors. Note that in this table, the positive and negative errors are determined using the HPD (Highest Posterior Density) method[1]. Note that this method is quite sensitive to the number of toy thrown and the binning chosen for the computation.

Figure 6.14 shows the PDF of the selected event after propagation of the detector errors.

---

[1] The following method was used to calculate the error of a distribution:

- Find the mode of the distribution, which is now referred as $N_{\text{event}}^{\text{mode}}$,
- Create an interval for which the PDF is constant and contain the 68% of the total distribution,
- Read off the values corresponding to the number of events (on the X axis) the positive and negative values are called $N_{\text{event}}^{\pm}$,
- Use the values $\frac{|N_{\text{event}}^{\text{mode}} - N_{\text{event}}^{\pm}|}{N_{\text{event}}^{\text{mode}}}$ as the positive and negative relative uncertainties.

Systematic	Relative uncertainty
Weight errors	
Charge identification efficiency	0.002
TPC cluster efficiency	0.000009
TPC track efficiency	0.011
TPC / FGD matching efficiency	0.006
TPC / ECal matching efficiency	< 0.00001
FGD mass	0.043
Secondary interaction pion	0.046
Secondary interaction proton	0.026
Secondary interaction photon	$\pm^{0.41}_{0.15}$
Reconstructed OOFV	0.061
ECal pile up	0.0004
Muon rejection pile up	0.0004
P0D pile up	0.006
TPC pile up	0.005
Variation errors	
Magnetic field	0.009
Momentum scale	0.022
Momentum resolution	0.025
TPC PID	0.019
Total	$\pm^{1.24}_{0.20}$

Table 6.10: Relative detector uncertainties for the events that pass the selection.

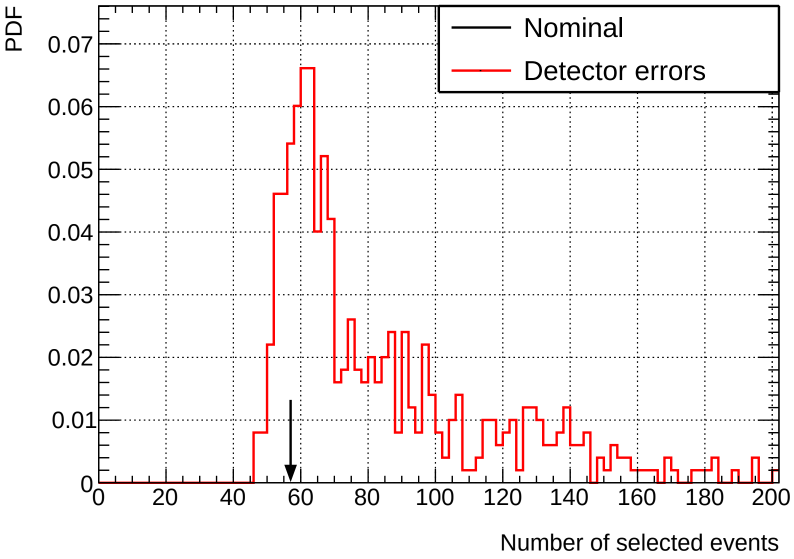

Figure 6.14: Effect of the detector uncertainty on the number of selected events. The nominal central value is indicated by the arrow.

6.4 Total uncertainty

6.4.1 Statistical uncertainty

To account for statistical uncertainty, the data normalisation was thrown according to a Poisson distribution of parameter the number events expected. Similarly, for the MC statistic uncertainty, same procedure was applied without any weight nor correction or tuning. Doing this, one finds that the relative statistical uncertainty is 14% for the data, and 3.2% for the MC. The effect on the selected events is shown in Figure 6.15.

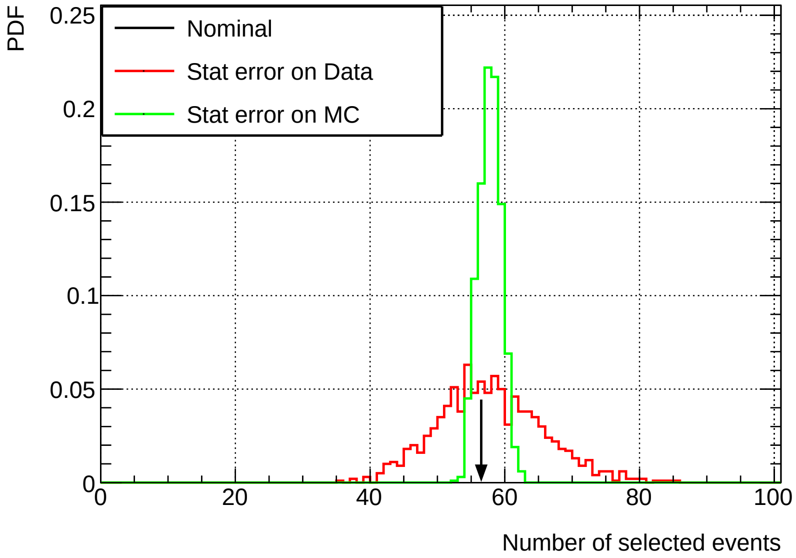

Figure 6.15: Effect of all the statistical uncertainties (data and MC) on the number of selected events. The nominal central value is indicated by the arrow.

6.4.2 Efficiency uncertainty

The efficiency also has an systematic error associated to it. To get it, the statistical uncertainty on the number of events selected after all the cuts is computed (simply the square root of the number of event divided by the number of event selected). To do this, a very high POT of NCγ events have been generated (6.5×10^{24} POT).

6.4.3 Combination of asymmetric error

To combine all the systematic errors and get a toy distribution allowing a proper treatment of the very asymmetric detector error that was discussed in the previous sections, a "discrete convolution method" was proposed, this method is now described.

All the independent errors were thrown, including the Poisson statistical uncertainty of the data and MC. In a standard cross section analysis where all the errors that are Gaussian, the errors are then added in quadrature and get the number of event at 90% CL, $N_{\text{events}}^{90\%CL}$, by integrating:

$$0.90 = \int_{-\infty}^{N_{\text{events}}^{90\%\text{CL}}} \text{Gauss}\left(\mu = N_{\text{events}}^{\text{nominal}}, \sigma\right) dN_{\text{events}}, \tag{6.11}$$

where $N_{\text{events}}^{\text{nominal}}$ is the nominal number of events after all the correction and tuning, and σ is the total uncertainty on this number after summing all the independent errors in quadrature.

Note that the assumption that one can add the errors in quadrature is central in this method. However, it cannot be applied for asymmetric errors as is the case in this analysis.

Rather than adding the errors in quadrature, the ratios $N_{\text{events}}^{\text{toy}}/N_{\text{event}}^{\text{nominal}}$ were computed for each toy and for each uncertainty source. To get the total PDF (Probability Distribution Function) of the number of selected events, one just has to multiply all these ratios with each other:

$$N_{\text{events}}^{\text{toy}} = N_{\text{event}}^{\text{nominal}} \times \prod_{i=\text{source}} \prod_{j=\text{toy}} \frac{N_{\text{events}}^{\text{toy}i,j}}{N_{\text{events}}^{\text{nominal}}}, \tag{6.12}$$

where i denotes the source of the uncertainty (it can be detector, flux, FSI, cross section, data or MC statistics), and j is the particular toy. In practice, the number of toy experiments grows exponentially with the number of source of systematic errors, therefore the systematic uncertainties with Gaussian behaviour (flux, cross section, FSI, data and MC statistics) were added in quadrature and used to generate 1000 toy experiments to combine with the asymmetric detector uncertainty as described earlier.

6.4.4 Effect of all uncertainties

When combining the uncertainties as described in the previous section, one obtains the distribution shown in Figure 6.16.

Note, that as can be seen in Figure 6.14, the detector systematic uncertainties introduce

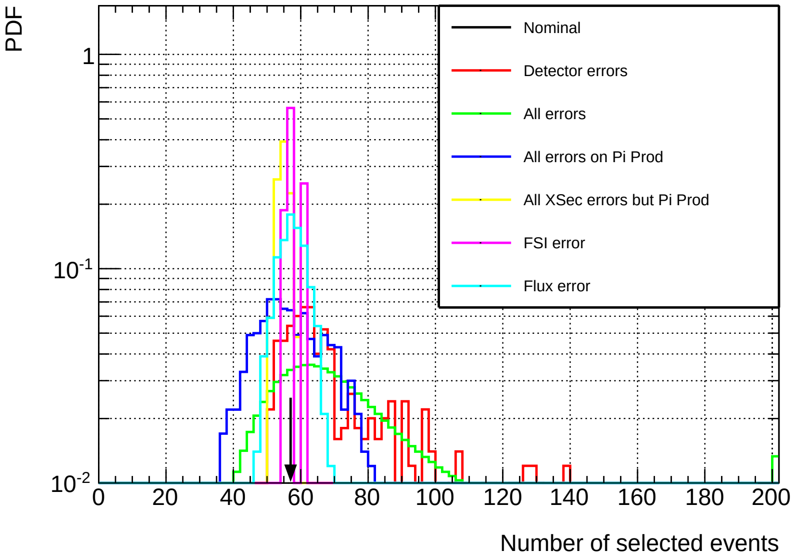

Figure 6.16: Effect of all the uncertainties in the total number of selected events.

a relatively large bias towards higher number of events. This bias gets propagated on the total systematic uncertainty distribution ("All errors" on Figure 6.16), but not on the other distributions (cross section errors, FSI, flux). This is why the error on pion production PDF seems to extend towards lower number of events than the one with all the errors. It was checked that appling the same bias to the pion production error gives shifts the pion production error PDF under the one with all the errors.

6.4.5 Motivation of the $\varphi_{\mathbf{photon}}$ cut

An interesting feature is exhibited in Appendix B, for bottom-originated events, there is a higher uncertainty than for the rest of the selection (Table B.3). Since the pointing capabilities of the FGD1 is reasonably good for event coming from all the directions (see Appendix C), one can restrict the phase space to events originated from the top and the side directions. This is done with a simple cut on the φ angle of the reconstructed photon direction. The effect of adding this phase space cut is shown in Figure 6.17.

However, such a cut would have an impact too drastic on the efficiency and on the statistics of the selected events. So, rather than removing all the events from the downward direction, the cut was optimised. To do that, the only uncertainties of interest are the detector systematic errors and the data statistical error. Similarly, the efficiency is going to decrease if one removes too many events from downward. The optimisation of this cut was performed by minimising its value by minimizing the value $N_{\text{Signal}}/\epsilon$

In this ratio, N_{Signal} is the difference between the 90% upper CL of the number of MC events and the nominal number of events (which essentially gives an idea of the uncertainty) and ϵ is the efficiency. The Figure 6.18 motivates the chosen value of $\varphi_{\text{cut}} = 36°$. This value is then translated for the excluded angles φ_{photon}:

$$-90° - \varphi_{\text{cut}}/2 < \varphi_{\text{photon}} < -90° + \varphi_{\text{cut}}/2 \tag{6.13}$$

$$-108° < \varphi_{\text{photon}} < -72°. \tag{6.14}$$

All the errors are depicted in Figure 6.19 and summarised in Table 6.11 after this cut (called φ_{photon} cut from now on). Note that in this table, the positive and negative errors are determined using the HPD (Highest Posterior Density) method (see Footnote 1 on page 144). As explained earlier, this method is quite sensitive to the number of toy thrown and the binning chosen for the computation. For example, it fails in giving a reasonable answer for the COH cross section error, since the highest probability is at the edge of its PDF. Therefore, only the detector and the total errors have been computed using this method.

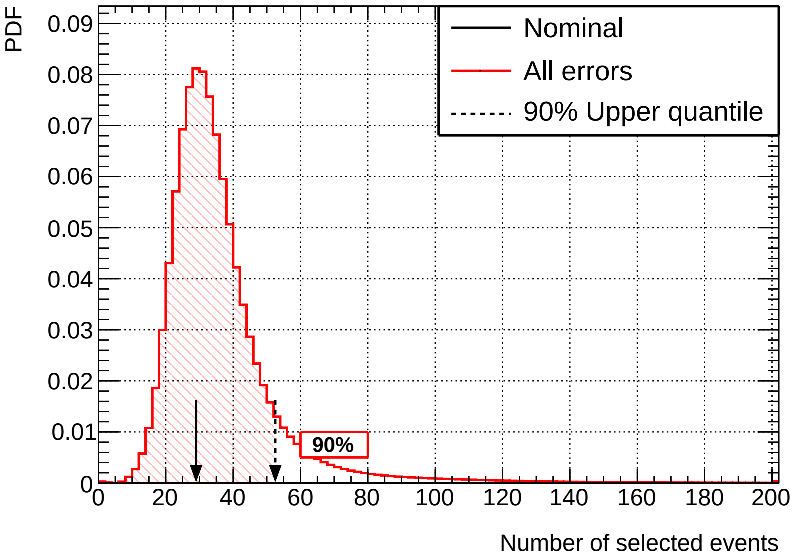

Figure 6.17: PDF of the selected number of events from detector uncertainties (including the OOFV one) after the azimuthal cut ($\varphi > 0$). The nominal central value is indicated by the arrow.

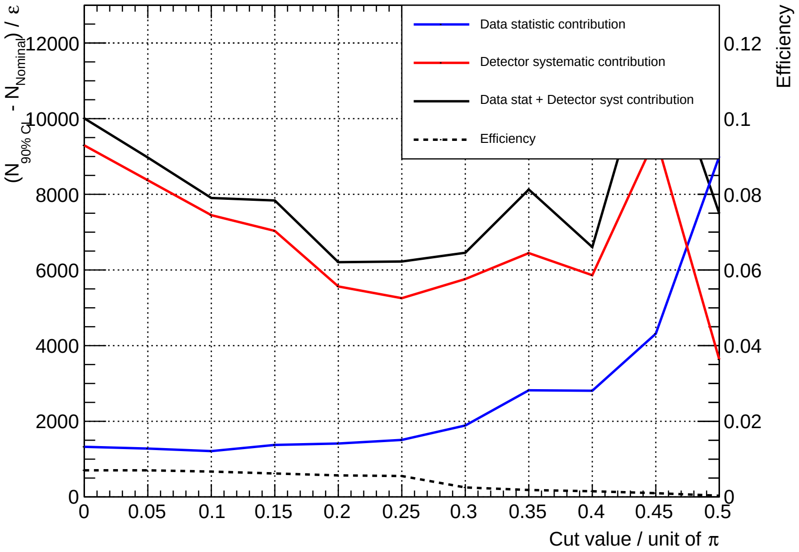

Figure 6.18: Optimisation of the φ cut, showing the contribution of the data statistic, detector systematic errors and efficiency on $N_{\text{Signal}}/\epsilon$, which is proportional to the cross section limit.

6.4.6 Conclusion

In this section, the importance of each systematic uncertainty and its effect on the number of selected events were shown. In the case of a analysis which aims to set a limit, careful characterisation of the systematic uncertainties is primoridial. This is because the limit is directly proportional to the total systematic errors (at least in the case of Gaussian errors). All the asymmetric errors were added coherently via the described method of discrete convolution. The main, dominant, error is the detector uncertainty. This error is mitigated by adding a cut on the reconstructed azimuthal angle of the photon and removing the photons that comes from under the ND280, which have a large propagation error.

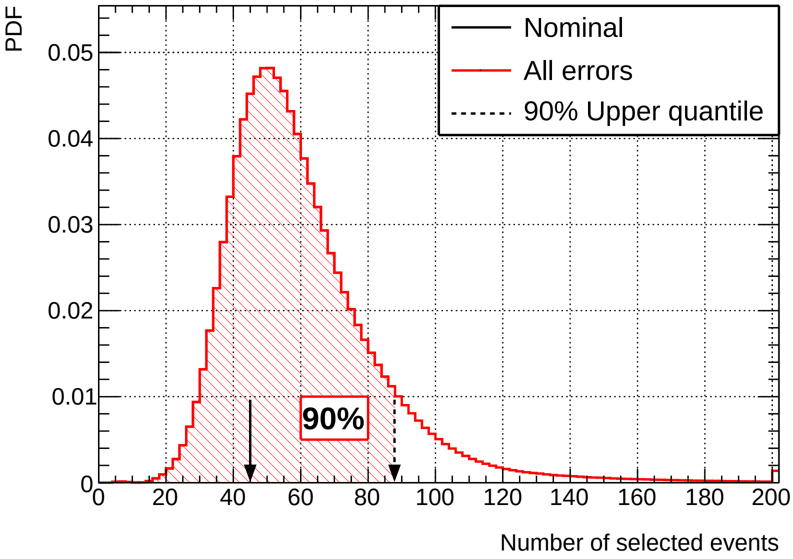

Figure 6.19: PDF of the selected number of events from the detector uncertainties after the optimised azimuthal cut (with events satisfying $-108^\circ < \varphi_{\text{photon}} < -72^\circ$ excluded). The nominal central value is indicated by the arrow. The 90% quantile of the MC is also shown.

Systematic error	Relative uncertainty
Statistical error on Data (expected)	± 0.14
Statistical error on Data (observed)	± 0.16
Statistical error on MC	± 0.032
Detector errors	$\pm^{0.27}_{0.17}$
C_A^5 RES error	± 0.078
M_a RES error	± 0.089
Background scale RES error	± 0.023
Nuclear RES (Δ mass) error	± 0.002
All errors on single pion production	± 0.20
CCQE errors	± 0.003
CCν_e error	± 0.006
DIS error	± 0.012
CC COH error	± 0.001
NC COH error	± 0.163
Other NC error	± 0.032
All cross section errors (except single pion production)	± 0.036
Flux error	± 0.082
FSI error	± 0.037
Efficiency error	± 0.0985
All errors (except efficiency)	$\pm^{0.33}_{0.23}$

Table 6.11: Summary of all the errors after the φ angle cut using the HPD method.

Chapter 7

Results

7.1 Monte Carlo sensitivity

For the extraction of the final result, all the systematic uncertainties were thrown and combined as described in Section 6.4.3, and the effect of all the errors on the final result was computed to generate toy experiments. This is shown on Figure 6.19, where the effect of the errors from cross section, detector, flux and data and MC statistics are shown.

7.1.1 Number of targets

For the number of targets, [174] and the fiducial volumes defined in Table 7.1 were used to get the total number of nucleons (neutrons and protons) in the FGD1. There are 14 XY modules in the FGD1 FV, the first one (most upstream) is removed for the fiducial volume. Table 7.1 summarises the FGD1 FV composition.

Element	Areal density[g/cm^2]	Number of nucleons $\rho_{\text{Areal density}} \times 14 \times A_{\text{XY module}} \times A_{\text{Avoagadro}}$
^{12}C	1.849	4.769×10^{29}
^{16}O	0.0794	2.048×10^{28}
^{1}H	0.1579	4.072×10^{28}
^{48}Ti	0.0355	9.156×10^{27}
^{28}Si	0.0218	5.622×10^{27}
^{14}N	0.0031	7.995×10^{26}
Total	2.1467	5.5364×10^{29}

Table 7.1: Elemental composition of the FGD1 FV. $A_{\text{XY module}}$ is the area of the FV and is equal to $30,590$ cm^2

7.1.2 Cross section limit calculation

To compute the cross section limit, the standard formula is used [175],

$$\sigma = \frac{N_{\text{Signal}}}{\epsilon \times \int_{0\text{GeV}}^{30\text{GeV}} \Phi_{E_\nu} dE_\nu \times N_{\text{Nucleon FV}}} \tag{7.1}$$

where the NCγ efficiency ϵ, is computed using the NCγ enhanced sample; N_{Signal} is the 90% upper CL of the number of MC events minus the nominal number of events from MC as illustrated in Figure 6.19 ($N_{\text{Signal}} = N_{90\%CL} - N_{\text{Nominal}}$); $\int_{0\text{GeV}}^{30\text{GeV}} \Phi_{E_\nu} dE_\nu$ is the flux integral and $N_{\text{Nucleon FV}}$ is the number target nucleons in the FGD1 FV.

Note that a phase space cut was applied, based on the $\cos(\theta)$ distribution in Figure 5.17, where it can be seen that the for values of $\cos(\theta) < 0.4$, the efficiency is zero. Therefore, the $\cos(\theta)$ of the photon is required to be higher than 0.4 for the efficiency calculation. This removes some of the dependency of the limit to the NEUT model of NCγ. The idea being that, without these cuts, the NEUT cross section model is used to extrapolate the forward photons to the backward region.

Say another nuclear calculation gave a much greater contribution in the backward region, and used the full phase space cross section limit described here (which is in fact only sensitive to the forward region), one would have a very optimistic limit on the cross section when comparing to that particular cross section. This is known to lead to some strong bias in the CC channels measurements, and somewhat relates to the same problem as extrapolating the ND280 CC -forward- events to the SK detector, as described in Section 1.2.1.

The double differential cross section from NEUT for NCγ events is shown in Figure 7.1.

The number of targets, $N_{\text{Nucleon FV}}$, in the FGD1 is 5.54×10^{29} nucleons (which is the same as what was found in Section 10.2 of [176]).

The flux integral, $\int_{0\text{GeV}}^{30\text{GeV}} \Phi_{E_\nu} dE_\nu$ is 1.71×10^{13} Neutrinos/cm^2, which again is the same as the number reported in previous results (Section 10.1 of [176]).

This is a single bin measurement, so only the total flux integrated cross section is reported. One gets the total cross section limit by subtracting the number of background events to detected number of events and taking the 90% upper quantile as the number of detected events.

Once this is done, the expected limit is 0.0460×10^{-38}cm^2/nucleon.

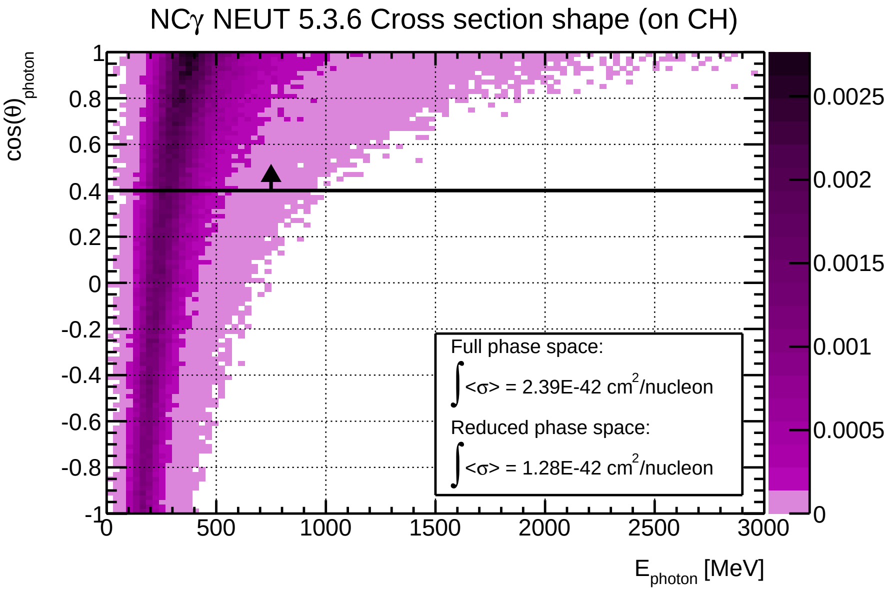

Figure 7.1: NEUT NCγ PDF for photon kinematics $(E_{\gamma}, cos(\theta_{\gamma}))$. The black line and arrow indicates the true phase space cut.

Next, by using the simple extrapolation:

$$\sigma_{\mathrm{NC}\gamma}^{\text{full phase space}} = \sigma_{\mathrm{NC}\gamma}^{\text{reduced } \cos(\theta)} \times \frac{\sigma_{\text{NEUT NC}\gamma}^{\text{full phase space}}}{\sigma_{\text{NEUT NC}\gamma}^{\text{reduced } \cos(\theta)}} \tag{7.2}$$

$$= \sigma_{\mathrm{NC}\gamma}^{\text{reduced } \cos(\theta)} \times \frac{2.386 \times 10^{-42}}{1.028 \times 10^{-42}}, \tag{7.3}$$

one can get the full phase space result:

$$0.1068 \times 10^{-38} \mathrm{cm}^2/\mathrm{nucleon}. \tag{7.4}$$

The corresponding sensitivity limit in the case where no OOFV background is present is: $0.0278 \times 10^{-38}\mathrm{cm}^2/\mathrm{nucleon}$.

7.2 Data result

The number of observed data events is 39 and the expected background is 45.

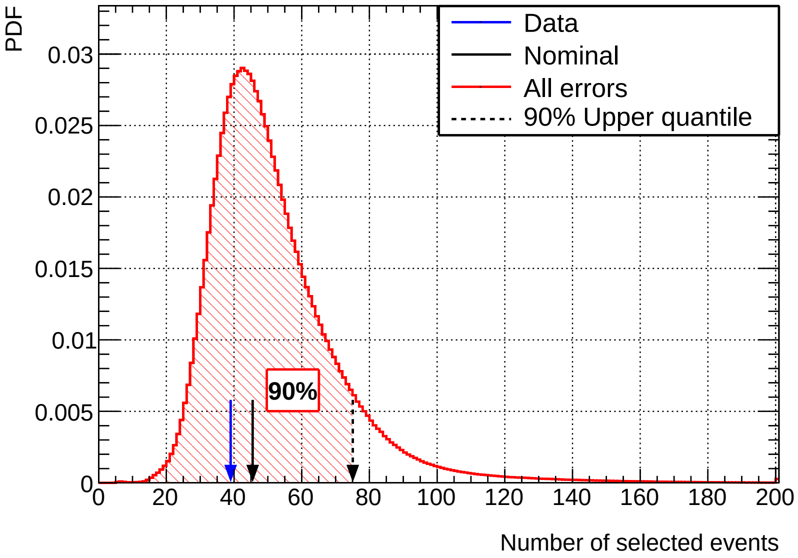

Figure 7.2: Effect of all the uncertainties in the total number of events selected, shown with the upper quantile at 90%. The blue arrow indicates the number of data events, the solid black line is the MC nominal and the dotted black line is the upper 90% CL from data. Note that the statistical error of the efficiency is also included, with the ϕ_{photon} cut.

The limit for NCγ, after propagation of all the errors on the data distribution 7.2 is, for the reduced phase space:

$$\sigma_{NC\gamma} < 0.0389 \times 10^{-38}\text{cm}^2/\text{nucleon}\ |_{90\%CL}\ . \tag{7.5}$$

This can be compared with the result from the previous section:

$$\sigma_{NC\gamma} < 0.0460 \times 10^{-38}\text{cm}^2/\text{nucleon}\ |_{90\%CL}\ , \tag{7.6}$$

which is, as expected from Figure 5.12, higher than the data result.

Again, both these results can be converted to full phase space using the extrapolation in Equation 7.2, which gives, for the data:

$$\sigma_{NC\gamma} < 0.0903 \times 10^{-38}\text{cm}^2/\text{nucleon}\ |_{90\%CL}\ , \tag{7.7}$$

that can be compared to its MC-only equivalent from the previous section:

$$\sigma_{NC\gamma} < 0.1068 \times 10^{-38}\text{cm}^2/\text{nucleon}\,|_{90\%CL}\,. \tag{7.8}$$

This result is then compared with the NOMAD one [114] in Figure 7.3. Note that there was a different phase space cut that was made which brings the sensitivity down as can be seen in Figure 7.3. The cut is made on the "collinearity," (ζ) defined as such:

$$\zeta = E_{\text{photon}} \times (1 - \cos(\theta)_{\text{photon}})\,. \tag{7.9}$$

In the NOMAD analysis, this quantity is required to be less than 0.05.

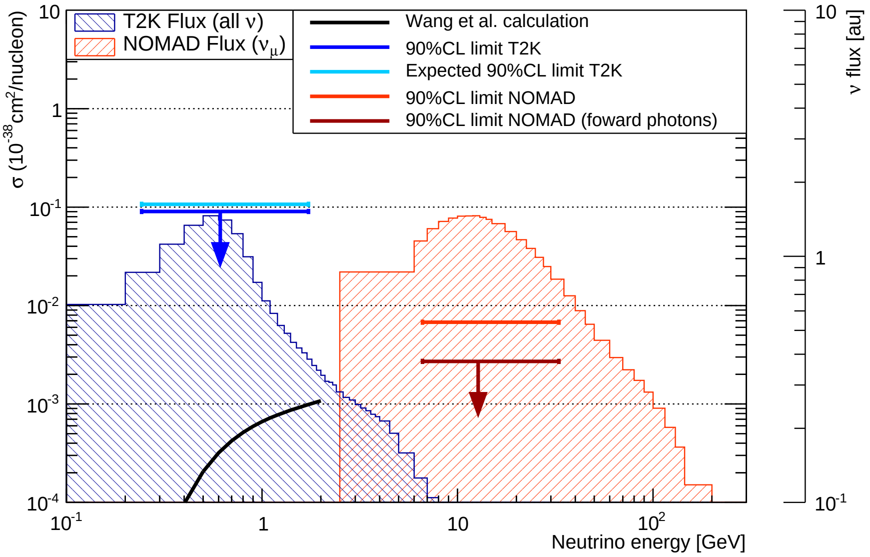

Figure 7.3: T2K limit (dark blue) and expected limit (turquoise) to NCγ (solid dark blue line); NOMAD reduced and complete phase space result (orange solid line); NOMAD reduced phase space result (red solid line) as explained in the text [114]. The flux of T2K and NOMAD are represented by the blue and orange hatched histograms, respectively. The calculation from [139] is also shown in black for the full phase space.

This result is by several orders of magnitude higher than the cross section needed for detection [139]. Two comments have to be made:

- The presence of a high OOFV background which has a large uncertainty, as described in Section 6.3.4. One can imagine that the limit would be significantly much smaller if this background was not present (the achievable limit would be

0.0278×10^{-38}cm^2/nucleon in that case). There is, unfortunately, very little hope that this problem could ever be overcome in the ND280 for such sample without the use of proton and / or vertex activity, which very significantly decreases the robustness of the limit without a NC1π^0 + 1 proton measurement on its own.

- The limited efficiency (0.013) of the selection is also accountable for the high limit. Note the efficiency is inversely proportional to the limit. If one compares with the NOMAD ($\simeq 0.09$) unfortunately there is little hope to have a better efficiency with the current detector.

All the results are summarised in Table 7.2.

Source	Phase space	Cross section [$\times 10^{-38}$cm^2/Nucleon]
NEUT truth	Full	0.000239
NEUT truth	$\cos(\theta_{\text{photon}}) > 0.4$	0.000128
T2K MC	Full	< 0.1068
T2K MC	$\cos(\theta_{\text{photon}}) > 0.4$	< 0.0460
T2K data	Full	< 0.0903
T2K data	$\cos(\theta_{\text{photon}}) > 0.4$	< 0.0389
NOMAD data	Full	< 0.0156
NOMAD data	$\zeta > 0.05$ (Equation 7.9)	< 0.0063

Table 7.2: Summary of all the measurements, sensitivities and published limits from [114]

7.3 Discussion

In a sense, this analysis demonstrates the need for a large active target (like the MINERνA, SciBooNE or NOMAD experiments) to realise this sort of measurements on light nucleus.

Although a large active target seems to have some drawbacks for particle identification, it can be designed and used to provide an acceptable PID for photons (for example, using precise dE/dx measurements in the case of argon or scintillator, with a shower-vertex distance cut). Other advantages are: a better efficiency for photon detection, and critically, this kind of detectors enables the veto of external photons.

There is a significant interest from the LArTPC (liquid argon TPC) community, from the SBN (Short Baseline Neutrino) program, which will probably be able to shed a light on these processes.

This measurement is dominated by the backgrounds and leads to a very weak limit on the cross section. The main uncertainty that drives the analysis are the OOFV systematic error, the RES and the the FSI cross section errors, each of which were checked and assigned sensible values.

When computing the limit for these processes, the result is also hampered by the very low efficiency of the ND280 which comes from its intrinsic directionality and the small size of the FGD1.

The NOMAD measurement that was made spans over neutrino energies that are much higher (23 GeV), where the theoretical predictions are not reliable any more (NEUT can predict NCγ up to 30 GeV). Most of the theoretical calculation go only up to 2 GeV.

Even if this measurement is worse than the NOMAD one, it is still valuable given that there is no other measurement in this energy range.

The T2K limit for NCγ for the reduced phase space is:

$$\sigma_{NC\gamma} < 0.0389 \times 10^{-38}\text{cm}^2/\text{nucleon}\,|_{90\%CL}\,, \tag{7.10}$$

using the true cut: $\cos(\theta_{\text{photon}}) > 0.4$ and the reconstructed cut: $-108° < \phi_{\text{photon}} < -72°$).

This is equivalent to a full phase space limit of:

$$\sigma_{NC\gamma} < 0.0903 \times 10^{-38}\text{cm}^2/\text{nucleon}\,|_{90\%CL}\,, \tag{7.11}$$

using the extrapolation from NEUT.

Chapter 8

Fitting the ND280 samples to constrain oscillation analysis systematic errors with electron samples

8.1 Introduction

In this section, the ND280 inclusive electron (anti-) neutrino samples and the ND280 muon (anti-) neutrino samples in RHC are used in the context of oscillation analysis. This was never realised previously on T2K. This study has three goals, two of which are related to the electron (anti-) neutrino appearance samples at SK in light of the search for CP violation in the neutrino sector. The other goal is related to the muon (anti-) neutrino disappearance measurement at T2K. These goals are:

- The consolidation of the result for CP violation by moving from a theory-driven electron neutrinos cross section uncertainty to an equivalent data-driven uncertainty.
- An overall the reduction of systematic uncertainties related to the electron (anti-) neutrinos appearance samples at SK: as will be shown in this chapter, the data result can be improved simply by collecting more data, as opposed to the theory-driven error.
- Finally, this study can be used for testing the single pion model in the anti-neutrino sector. This has some importance in the oscillation in the atmospheric sector using the anti-neutrino disappearance samples.

In the second section, the oscillation analysis strategy is explained. Then, the framework for characterising the oscillation analyses systematic uncertainties with the ND280 is described, and the samples used in the fit are described. In the subsequent sections, the expected sensitivity and the data result are shown. Finally, the propagation of the sensitivity to the CP violation allowed region is shown.

8.2 The TK oscillation analysis strategy

In this section, the strategy for the oscillation analyses in T2K is explained. There are three main analyses on T2K that produce the oscillation parameter results. Two of them use a semi-frequentist approach and aim to produce confidence intervals on oscillation parameters, and run a fit over them and the nuisance parameters. These two analyses are called “p-theta” and “VaLOR” [177], both of them use a Minuit2 [178] log-likelihood fit. The other one uses a Markov-Chain Monte Carlo (MCMC) to sample over the parameter space; it is called “MaCh3” [179]. It is a fully Bayesian analysis and produces credible intervals on neutrino mixing parameters.

The fact that the oscillation analyses are repeated by different groups allows validation and comparisons of the result.

These analyses use the multiple inputs from different T2K groups. The inputs are listed here:

- The beam group provides the absolute flux histograms (such as the one shown in Figure 2.5), the flux covariance matrix which encloses all the systematic errors on these histograms (see Figure 2.6 and Section 6.1) and the flux tuning which is, as described in Section 2.3, determined from *in situ* measurements of the beam and additional hadron production data from NA61 / SHINE [121–123].
- The neutrino interaction working group (NIWG) provides a parametrisation for the cross section and “prefit” systematic errors on each of the nuisance parameter of interest. These generally rely on the use of external data sets and fit such as the one described in [30], discussions with theorists, and phenomenology work done within T2K.
- The ND280 data, which is used before the main oscillation fit to constrain the flux and cross section systematic uncertainties. Traditionally, the ND280 data that was used for the fits was restricted to the ν_μ and $\bar{\nu}_\mu$ data, however the aim of this analysis is to include samples sensitive to the background ν_e flux (which represent around

1% of the neutrino at the flux peak) to constrain cross section and flux parameters. Fitting these parameters with such samples can introduce anti-correlation between flux and cross section parameters (i.e. at constant number of ν_e in the ND280, if the flux increases, the cross section has to decrease).

- The SK CCQE-like ν_μ, ν_e, $\bar{\nu}_\mu$ and $\bar{\nu}_\mu$ samples, and the ν_e CC1π^+ sample.

Note that the statistical power of the data from the ND280 is much larger than the one from SK. This means that ND280 data uncertainty is largely dominated by systematic uncertainties, whereas the SK data uncertainty is mostly statistical (especially for the appearance samples, the ν_e and $\bar{\nu}_e$ samples), although this is becoming less and less true as T2K data is being collected.

For all the three oscillation analyses, the first step is to fit the ND280 data to constrain flux and cross section parameters. Once an acceptable fit ($p_{\text{value}} > 5\%$) is reached, it is considered that the parametrisation is sufficient for an oscillation fit and the errors are propagated to SK.

There are other mechanisms to check that the parametrisation is sufficient under significant change of cross section model, called fake data, but these are beyond the scope of the analysis that is presented here.

In this section, the focus is on the ND280 fits that are used in oscillation analyses. This step is essential to reduce the systematic uncertainties on the cross section and neutrino flux.

8.3 Beam and Near Detector Fit Framework

The software framework used for this is called BANFF. It performs a Minuit2 [178] fit and minimises the Poisson logarithmic likelihood with extra χ^2 penalty terms for the systematic error. They are defined as follows:

$$
\begin{aligned}
-2\ln(\mathscr{L}) = 2 &\sum_{i=0}^{\text{N bins}} N_i^p(\vec{b},\vec{x},\vec{d}) - N_i^d + N_i^d \ln[N_i^d/N_i^p(\vec{b},\vec{x},\vec{d})] \\
+ &\sum_{k,l=0}^{E_\nu \text{ bins}} \Delta b_k (V_{\text{beam}}^{-1})_{k,l} \Delta b_l \\
+ &\sum_{m,n=0}^{\text{xsec param}} \Delta x_m (V_{\text{xsec}}^{-1})_{m,n} \Delta x_n \\
+ &\sum_{i,j=0}^{\text{N bins}} \Delta d_i (V_{\text{det}}^{-1})_{i,j} \Delta d_j ,
\end{aligned}
\tag{8.1}
$$

where $\mathscr{L}$ is the total likelihood (note that $-2\ln(\mathscr{L})$ can be approximated to a χ^2 function for sufficient statistics), i and j are the bin numbers for the reconstructed quantities p_{lepton} (momentum of the leading lepton) and $\cos(\theta_{\text{lepton}})$ (cosine of the angle between the neutrino direction and the leading lepton). $N_i^p(\vec{b},\vec{x},\vec{d})$ is the number of expected events in the i^{th} bin, which depends on $\vec{b}$, the beam weight, which encloses the action of the flux systematic uncertainties on the events; $\vec{x}$, the cross section weight, which parametrises the effect of the cross section systematic uncertainties and $\vec{d}$, the detector weight, which parametrises the detector uncertainty in each reconstructed bin. N_i^d is the number of events seen in the i^{th} bin.

V_{beam}, V_{xsec} and V_{det} represent the covariance matrices of the flux, cross section and detector systematic uncertainties, respectively. They respectively correlate: the number of neutrinos in each true energy bin in the case of the flux, the cross section parameters, and the number of events in each reconstructed bin. Δb, Δx, Δd, are the variations of the beam, cross section and detector parameters with respect to their nominal values, respectively.

8.4 Samples used

The samples that are used are ND280 “tracker” samples (i.e. they do not include the analyses where the P0D is used as a target). These analyses are divided according to their topology, detector (FGD 1 or 2) and whether the neutrino beam is running in neutrino mode (FHC) or anti-neutrino mode (RHC). Twenty-eight binned samples are used in the fit. The first six samples have not changed compared to previous analyses:

- 3 ν_μ CC selections in FGD1 in FHC: 1 muon + 0 pion; 1 muon + 1 positively charged pion; 1 muon + everything else;

- 3 ν_μ CC selections in FGD2 in FHC: 1 muon + 0 pion; 1 muon + 1 positively charged pion; 1 muon + everything else.

The remaining samples are new selections that have been used for the first time in this fit:

- 3 $\bar{\nu}_\mu$ CC selections in FGD1 in RHC: 1 anti-muon + 0 pion; 1 anti-muon + 1 negatively charged pion; 1 anti-muon + everything else;
- 3 $\bar{\nu}_\mu$ CC selections in FGD2 in RHC: 1 anti-muon + 0 pion; 1 anti-muon + 1 negatively charged pion; 1 anti-muon + everything else;
- 3 ν_μ CC selections in FGD1 in RHC: 1 muon + 0 pion; 1 muon + 1 positively charged pion; 1 muon + everything else;
- 3 ν_μ CC selections in FGD2 in RHC: 1 muon + 0 pion; 1 muon + 1 positively charged pion; 1 muon + everything else;
- Inclusive ν_e CC selection in FGD1 in FHC;
- Inclusive ν_e CC selection in FGD2 in FHC;
- Inclusive $\bar{\nu}_e$ CC selection in FGD1 in RHC;
- Inclusive $\bar{\nu}_e$ CC selection in FGD2 in RHC;
- Inclusive ν_e CC selection in FGD1 in RHC;
- Inclusive ν_e CC selection in FGD2 in RHC;
- Photon sample in FGD1 selection in FHC;
- Photon sample in FGD2 selection in FHC;
- Photon sample in FGD1 selection in RHC;
- Photon sample in FGD2 selection in RHC.

For previous iterations of these fits [180], the RHC were using a different categorisation, and had a split between ν_μ CC with one or several tracks (so-called “CC 1-track” and “CC n-tracks”). The electron samples had never been used in the these fits. However, they are used in NOνA analyses [24]).

The remainder of this section covers the description of the samples used and how they are selected. Firstly, the amount of POT that is used is shown. Then, the selections are broadly described. The binning used is detailed in Appendix D.

8.4.1 Run periods and Proton On Target

The data sets used correspond to the data collected with the ND280 when all the sub-detectors are in place (excluding run 1), up to summer 2017, all the corresponding POT is listed in Table 8.1. Note that the year 2017 data was only partially calibrated (so called “pc1”), which is different from all the rest of the data which was fully calibrated (“rdp,” for real data processing). The ECal run 8 data was not fully calibrated at the time this document was written. This has an impact on the ν_e selections which are using the ECal for PID, as will be explained in the next section, so the run 8 data was not used for the electron neutrino selections. However, this has no impact on the muon neutrinos selections, so this data was used for these selections.

Runs	POT				
	Data	Magnet MC (ratio)		Sand MC (ratio)	
2a (FHC)	3.59×10^{19}	9.24×10^{20}	(0.0389)	3.71×10^{19}	(0.968)
2w (FHC)	4.34×10^{19}	1.2×10^{21}	(0.036)	4×10^{19}	(1.08)
3ba (FHC)	2.17×10^{19}	4.45×10^{20}	(0.0488)	2.35×10^{19}	(0.923)
3ca (FHC)	1.36×10^{20}	2.63×10^{21}	(0.0519)	1.31×10^{20}	(1.04)
4a (FHC)	1.78×10^{20}	3.5×10^{21}	(0.0509)	1.74×10^{20}	(1.02)
4w (FHC)	1.64×10^{20}	1.89×10^{21}	(0.0868)	1.6×10^{20}	(1.03)
5w (RHC)	4.35×10^{19}	2.3×10^{21}	(0.0189)	9.07×10^{19}	(0.479)
6ba (RHC)	1.27×10^{20}	1.42×10^{21}	(0.0898)	3.42×10^{20}	(0.373)
6ca (RHC)	5.08×10^{19}	5.28×10^{20}	(0.0963)	1.05×10^{20}	(0.485)
6da (RHC)	7.75×10^{19}	6.88×10^{20}	(0.113)	1.58×10^{20}	(0.491)
6ea (RHC)	8.51×10^{19}	8.59×10^{20}	(0.0991)	1.75×10^{20}	(0.485)
7w (RHC)	2.44×10^{20}	3.37×10^{21}	(0.0723)	5.04×10^{20}	(0.484)
8a (FHC)	4.15×10^{20}	3.63×10^{21}	(0.114)	4.04×10^{20}	(1.03)
8w (FHC)	1.58×10^{20}	2.64×10^{21}	(0.0598)	1.61×10^{20}	(0.98)
Total FHC	1.15×10^{21}	1.69×10^{22}	(0.0684)	1.13×10^{21}	(1.02)
Total RHC	6.7×10^{20}	9.16×10^{21}	(0.0732)	1.37×10^{21}	(0.487)

Table 8.1: POT and POT ratios (data / MC) used for the BANFF 2018 analysis, note that the run 8 data is only partially calibrated (pc1).

8.4.2 Muon (anti-) neutrino description

All the muon selections rely on the identification of a muon starting in the FGD1 or 2. Based on the topology of the remaining particles, the event is then tagged as “CC 0 pion,” “CC 1 pion” or “CC other,” depending upon the presence of a detected pion in the selection. Note that, other than the reconstructed charge of the particle, the selections are identical in FHC and RHC and for the anti-neutrino equivalent.

- The “CC 0 pion” selections mostly contain CCQE events, but can also have some events where a pion was created inside the nucleus (such as resonant events) and was absorbed by the nucleus through FSI.
- The “CC 1 pion” selections contain events where a positive pion was tagged, in

general, this selection is dominated by RES and COH events, but some CCQE events can enter if the ejected proton from the interaction creates a pion through FSI.

- The "CC other" selections are all the remaining events, which are mostly DIS and SIS events. All the wrong sign TPC pions can also be present.

The event selection and cuts are illustrated in Figure 8.1. Each cut is quickly detailed. For a more complete description, see [151, 152].

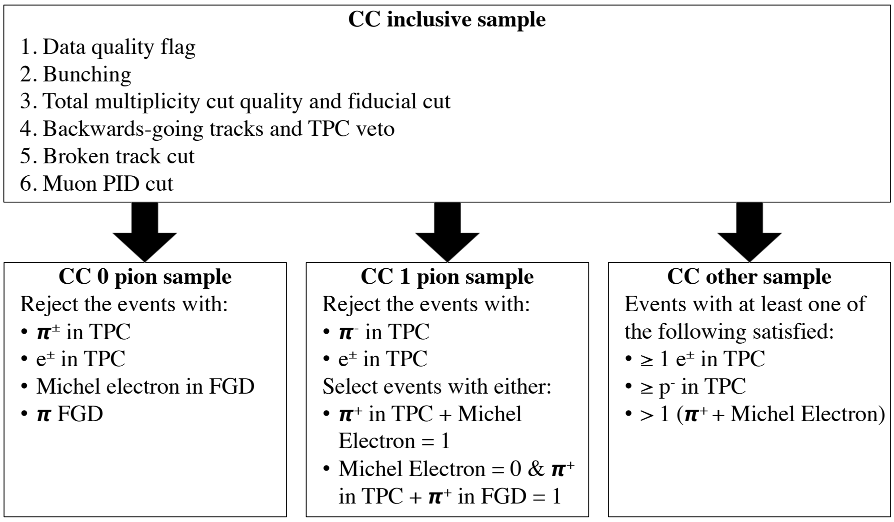

Figure 8.1: The flow chart for the ν_{μ} CC multi-pion selections, from [151].

8.4.2.1 Data quality flag and Bunching

These cuts are identical to the ones given in the description in Section 5.4.

8.4.2.2 Total multiplicity cut quality and fiducial cut

These cuts are the same as the "Cut 1" and "Cut 2" in Section 5.3.1

8.4.2.3 Backwards-going tracks and TPC veto

It happens that tracks starting from the upstream layers of the FGD1 are reconstructed as backward going tracks, especially if the muon undergoes a hard scatter in the FGD1 and is reconstructed as two tracks. To overcome this problem, an upstream TPC veto was designed and if a track starts at less than 150 mm upstream from the main muon track, it is rejected. Additionally, for FGD2 selections, if the track starts or ends in the FGD1, the event is rejected.

8.4.2.4 Broken track cut

This cut was made to remove events where the reconstruction failed and, rather than a single muon reconstructed, a short track is reconstructed in the FGD and another one is reconstructed in the last layers of the FGD and TPC. The cut therefore removes events where a track starts in the last two layers of the FGD in the downstream direction and has another isolated FGD track.

8.4.2.5 Muon Particle Identification

The PID relies on the TPC. If the reconstructed momentum is smaller than 500 MeV, then the track has to satisfy the relation:

$$L_{MIP} = \frac{L_\mu + L_\pi}{1 - L_p} > 0.8. \tag{8.2}$$

Then, to remove proton and pions, all the tracks have to satisfy:

$$L_\mu > 0.05 \tag{8.3}$$

In the above equations, L is the likelihood related to the PID of the particle i by the following equation:

$$L_i = \frac{e^{-\pi_{i,\mathrm{PID}}^2}}{\sum_l e^{-\pi_{l,\mathrm{PID}}^2}}, \tag{8.4}$$

where $\pi_{l,\mathrm{PID}}$ is defined in Equation (5.2) and based on the difference between the expected and the measured dE/dx of the particle. The index l runs over the particles: proton, electron, muon and pion.

8.4.2.6 Pion tag

All the remaining tracks in the events are checked to create a pion tag. They are required to start in the same FGD and bunch. If the track has more than 18 TPC hit[1] and has a

---

[1] i.e. the particle has triggered at least 18 MicroMegas.

positive charge, a TPC PID is realised as such:

$$L_{MIP} = \frac{L_\mu + L_\pi}{1 - L_p} > 0.8 \text{ if } p < 500 \text{ MeV/c}$$
$$L_\pi > 0.3 \text{ for all the tracks.}$$

If a track satisfies this requirement, it is tagged as a TPC pion. The same quantities can be constructed for electron, positron, proton and pion. The events containing TPC tracks are sorted as indicated in the Figure 8.1.

For a track to be tagged as a "Michel electron" (which, within T2K, means a decay electron from a charged pion or charged muon), the requirement is to have a deposition of at least 200 photo-electrons in the FGD, after the end of bunch timing window.

Finally, the FGD PID can be realised on short pion tracks. In that case, the track must be fully contained in the FGD and, using a similar definition of the pull, as in Equation (5.2), based on the dE/dx of the particle and the energy deposited in the FGD, one can make a cut on its value (in this case, $-2 < \pi_{\pi \text{FGD PID}} < 2.5$).

8.4.3 Electron (anti-) neutrino selections

The electron (anti-) neutrino selections are now described. The selections are aimed to select all electron (anti-) neutrino samples and do not depend on the presence of charged pions or additional tracks in the event. For more details on the selections, the reader can refer to [153]. Future development of the selections will probably involve the usage of more advanced event categorisation techniques, and machine learning. However this is still in development within the T2K collaboration as this introduces complex model dependencies, in a context where the neutrino generators have some known deficiencies (which will be covered in the following of this chapter) and sometimes use several models that are theoretically incompatible[1]. The complexity of the selection highlights the difficulty of selecting and measuring the electron neutrino in accelerators neutrino experiments.

8.4.3.1 Data quality flag, Bunching and Fiducial volume cut

This cut is identical to the first cut of the ν_μ selections.

---

[1] This is sometime called the "Frankenmodel" in T2K.

8.4.3.2 Track quality cut

This cut is different from the one that was described before, since the PID cut is more advanced and it uses the ECal. Therefore, if the track does not enter the ECal, the number of TPC nodes should be 36; if it does, this number is 18.

8.4.3.3 Electron PID cut

The electron PID is rather complicated, due to the presence of the proton, from ν_μ interactions. This happens predominantly in the case of the anti-electron neutrino selections because the dE/dx of positron and proton are overlapping (this is visible in the right of Figure 2.11). In Figure 8.2, one can see the flow chart for the electron PID.

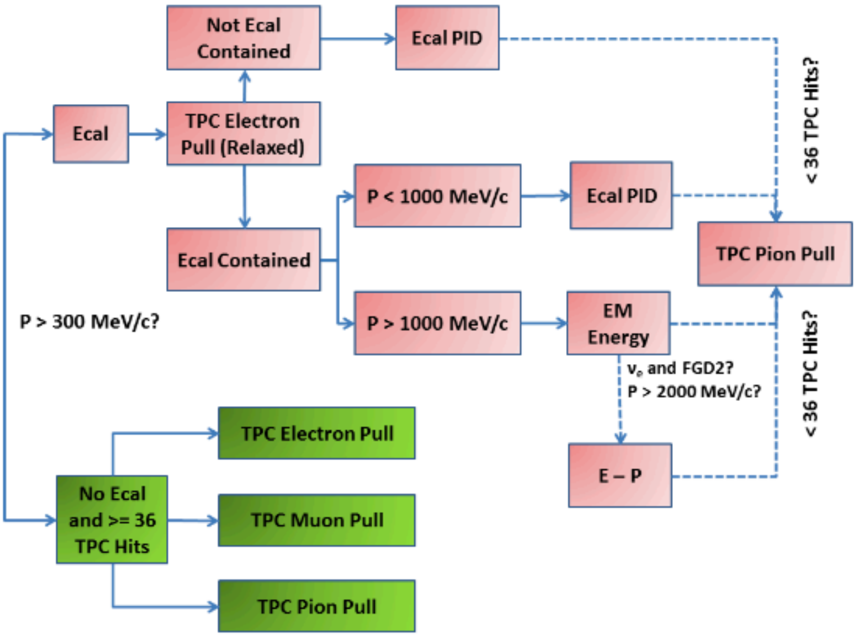

Figure 8.2: The flow chart for the (anti-)ν_e CC inclusive selections PID, from [153].

In Figure 8.2, one can see that if the track does not enter the ECal (green boxes), there are three TPC PID cuts that have been satisfied. They are the following:

- $-1 < \pi_{e,\mathrm{PID}} < 2$,
- $\pi_{\mu,\mathrm{PID}} \notin [-2.5; 2.5]$
- and $\pi_{\pi,\mathrm{PID}} \notin [-2.5; 2.5]$.

In the case where the track enters the ECal, it must have a momentum greater than 300 MeV to be correctly reconstructed in the ECal. Firstly, the track is required to satisfy a relaxed TPC PID ($-2 < \pi_{e,\text{PID}} < 2.5$). Then, according to the momentum of the track, the ECal can be used to provide a PID:

- The track is tagged as an electron if: (1), the track has a momentum greater than 1000 MeV (2), the ECal reconstructed energy is greater than 1100 MeV and (3), the shower is fully contained in the ECal.
- In the case where one of the conditions above is not satisfied, the PID quantity MIPEM[1] has to be greater than 0.

Another special case is when the track was selected in the FGD2. In that case, it was noted that there are still many muons after the selection, therefore another cut was made using a combined variable of TPC and ECal which is defined as $E - p$. This variable has to be greater than -2000 MeV for the event to pass the selection.

8.4.3.4 Second TPC PID

If the track is from FGD1 and propagates until the TPC3, then another PID is realised with it:

- in the case of electron neutrino selection, the requirement is $-2.5 < \pi_{e,\text{PID}} < 2.5$;
- in the case of electron anti-neutrino selection, the requirement is $-3 < \pi_{e,\text{PID}} < 3$, but is only applied in the region where the proton dE/dx overlaps (positron momentum between 600 and 1650 MeV).

8.4.3.5 Proton PID

In the case of electron anti-neutrino selection, there is still a large contamination of protons for track of momentum greater than 600 MeV. Another hybrid TPC / ECal variable is therefore constructed (E/p), and the following requirements are made:

- if $p < 1650$ MeV, $E/p > 0.65$,
- if $p > 1650$ MeV, $E/p > 0.15$,

Then, another ECal PID cut is made on the quantity EMHIP[2]. This variable has to be negative.

---

[1] The MIPEM quantity is an ECal reconstructed variable related to the topology of the particle. It is the discriminator of a boosted decision tree on the ECal object variables. This tree was trained electron and muon particle guns, and therefore aims at differentiating MIP-like object and EM showers.

[2] Similar to MIPEM, this variable is the discriminator variable of a boosted decision the tree on the ECal object variable. This tree was trained on a proton and electrons particle guns and therefore aims at differentiating hadronic-like object and EM showers.

8.4.3.6 TPC veto

This cut is the same as the one described in Section 8.4.2, except the difference in distance is 100 mm rather than 150 mm.

8.4.3.7 Photon veto

One of the problem with these samples is the presence of a large photon background in the first bins of the electron (or positron) momentum, this background has very similar characteristics to the one observed in Chapter 5. This is the reason why a constraint from the photon sample was introduced to reduce the uncertainty on these backgrounds.

If there is a second track of opposite charge, with a number of TPC nodes greater than 18, and a PID satisfying: $-3 < \pi_{e,\mathrm{PID}} < 3$, and if the system's invariant mass (Equation (5.3)) is smaller than 100 MeV, and starts at a distance smaller than 100 mm, the event is rejected.

8.4.3.8 P0D, P0DECal and FGD1 veto

If there is any upstream activity in the P0D or P0DECal, the event is rejected. If the event was in FGD2, any activity in the FGD1 results in the vetoing of the event.

8.4.3.9 ECal veto

The ECal veto aims at rejecting the OOFV events. However, it is applied differently from the one described in Section 5.3.2, due to the complexity of the ECal PID as described before. In this case, only upstream events are vetoed, and the selected event is rejected if an object starts at a distance greater than 100 mm in the upstream direction.

8.4.3.10 FGD2 shower

This cut is only applied to electron anti-neutrino selection which have tracks of momentum greater than 600 MeV. Positrons coming from FGD1 can shower in the FGD2, and produce several tracks in the TPC3.

Note that this cut is realised since there is still a large proton contamination in this sample. Firstly, the track is required to go the FGD2, then, the number of matched tracks from FGD1-TPC2 has to be greater than FGD2-TPC3 matched tracks.

The criteria on the number of FGD2-TPC3 tracks are applied and the event is rejected if:

- There are two or less FGD2-TPC3 tracks in the proton momentum region ($600 < p < 1650$), or one or less FGD2-TPC3 tracks in high energy region ($p > 1650$ MeV), as the high energy tail is less contaminated with the proton background.
- Only applied to tracks where the second TPC PID has not been applied: in the proton momentum region ($600 < p < 1650$), if there is at least one secondary FGD1-TPC2 track and there are three or less FGD2-TPC3 tracks. This cut is applied to reduce reconstruction effects (such as the FGD-TPC matching failures) and deals with secondary tracks showering in FGD2.

8.5 Systematic uncertainties

In this analysis, the errors are the parameters of interest, however this is a Bayesian analysis, therefore they have some prefit values and errors, which enclose the "best guesses" for these values. Each of them is detailed here, starting with the flux, then the cross section and finally the detector systematic uncertainties.

8.5.1 Flux error

The description of this systematic error can be found in Section 6.1.

8.5.2 Cross section error

The cross section systematic errors evaluations are relying on the use of external data sets. In this section, only the parameters related to the CCQE-like events that have not already been used in Section 6.2[1] are described.

8.5.2.1 Long range correlations

The long range correlations refer to the one of the corrections listed in Section 1.2.3, their effects is on the Q^2 quantity: at low Q^2 the cross section is expected to be reduced; whereas it is enhanced at intermediate Q^2 and goes back to unity for $Q^2 \to \infty$. This can be seen in Figure 8.3, which shows the central value and error envelope from [40].

For T2K analysis, the effects are parametrised through a weight which takes Q^2 as a parameter and is called the eRPA (for effective Random Phase Approximation). Since a

---

[1] Two marginal differences ought to be noted, the parameter controlling the Δ resonance mass is not used here, since it is more related to the "hadronic side" or the interaction and the pion momentum distributions; and the NC COH uncertainty is 30% (the CC is still 100%).

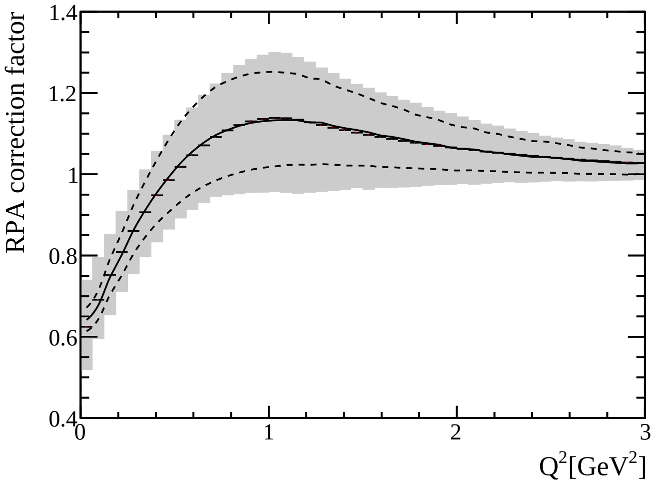

Figure 8.3: The BeRPA corrections and errors, from Nieves et al. [40] (black solid line for the central value and dotted line for the error) and the ones used in T2K (black data points for the central value and grey band for the error, as shown in Table 8.2); from [158].

simple parametrisation via polynomials led to complex correlations between its parameters, the formalism was developed in a Bernstein polynomial basis (and the correction is therefore referred as BeRPA within T2K). The weighting function is defined as:

$$f(Q^2) = \begin{cases} A(1-\frac{Q^2}{U})^3 + 3B(1-\frac{Q^2}{U})^2\left(\frac{Q^2}{U}\right) + 3p_1(1-\frac{Q^2}{U})\left(\frac{Q^2}{U}\right)^2 + C\left(\frac{Q^2}{U}\right)^3, & Q^2 < U \\ 1 + p_2\exp(Q^2 p(-D(Q^2-U)), & Q^2 > U, \end{cases}$$

where A, B, C and p_1 are the normalisation parameters of each Bernstein polynomial. U is the value for which the parametrisation becomes exponential for which D is the damping parameter. Note that continuity between the two parts of this equation leads to a non trivial relation between the parameters:

$$p_1 = C + \frac{UD(C-1)}{3}$$
$$p_2 = C - 1$$

The fit to the RPA corrections from [40] and an *ad hoc* choice of errors are listed in Table 8.2.

Parameter	Nominal value	Uncertainty
A	0.59	20%
B	1.05	20%
C	1.13	15%
D	0.88 GeV^2	40%
U	1.20 GeV^2	fixed

Table 8.2: Nominal values and uncertainties for the five BeRPA parameters. Note that U should not be varied and no uncertainty is provided. All the parameters must be positive and are uncorrelated between them. Reproduced from [158].

8.5.2.2 Multi nucleons error parametrisation

As can be seen in Figure 1.5 (which shows integrated neutrino cross section on carbon as function of energy), multi nucleon processes are expected to have a major impact on oscillation analyses at T2K [31]. The normalisation and shape of the cross section can be changed within the BANFF. The normalisations are changed based on the (anti-) neutrino type (ν_μ, $\bar{\nu}_\mu$, ν_e and $\bar{\nu}_e$) and target (carbon or oxygen).

Since the multi nucleon cross section can be separated into two components, the Delta resonance and the 2p2h contributions, the shape uncertainty is determined by running the code from Nieves et al. [40] with the contributions seperately and adopting a reweighting scheme that takes care of the interferences between them (note that the total cross section is maintained constant to avoid interfering with the other normalisation parameters). The illustration of the shape change is shown in Figure 8.4. The reweighting scheme is done in three dimensions: neutrino energy, momentum and energy transfer (E_ν, q_3 and q_0, respectively).

8.5.2.3 CCQE and multi nucleon errors

The CCQE form factor extracted from bubble chamber data [33–35] does not reproduce T2K data. Similarly this applies to the Fermi momentum in the nucleus and the multi-nucleon errors derived from MiniBooNE [42] and MINERνA [41], experiments. Therefore, there is no prior for these quantities.

8.5.2.4 Final state interaction error

Unlike what is described in Section 6.2.4, the FSI uncertainty is parametrised as continuous parameters, which allows to simply fit them. Note that the FSI parameters are not

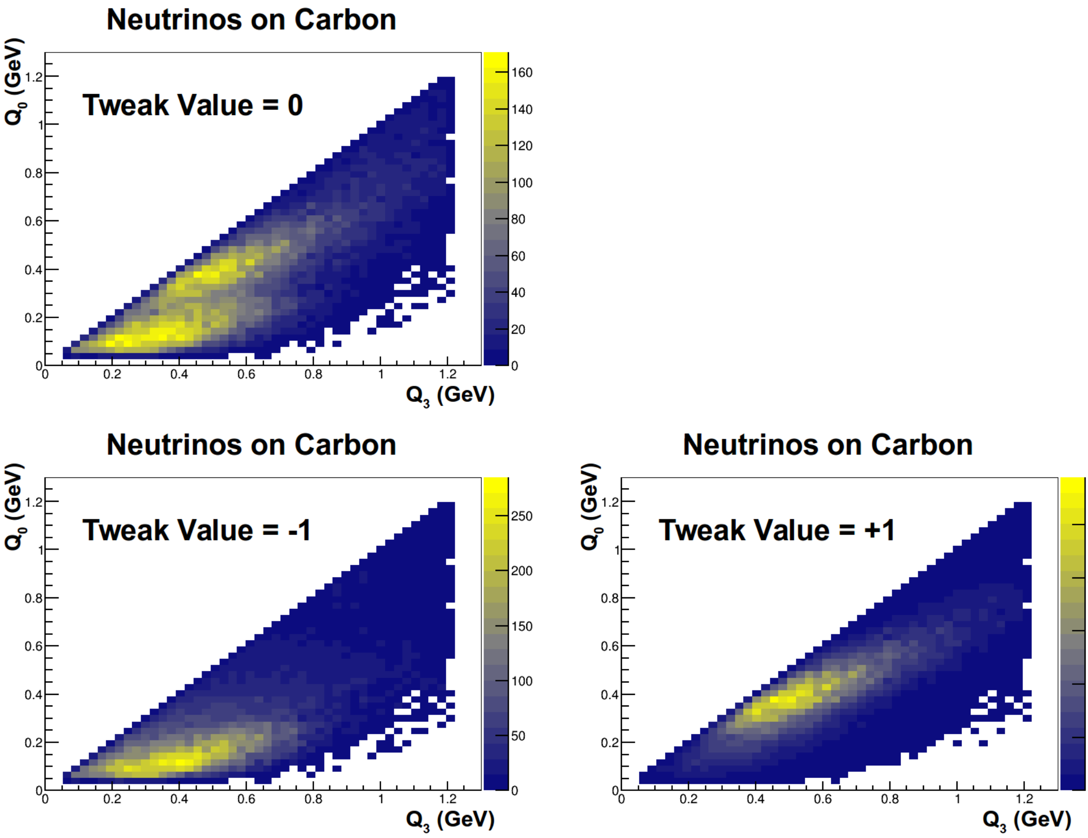

Figure 8.4: Effect of change in the multi nucleon parameters for q_3, q_0, for all the ND280. ***Top:*** Nominal. ***Bottom left:*** -1σ variation. ***Bottom right:*** $+1\sigma$ variation. From [158].

propagated to SK and therefore are purely nuisance parameters. The systematic error are the same as what was described in Section 6.2.4.

8.5.2.5 Electron neutrino error

The error described in Section 6.2.2 is smaller than the errors that are found when measuring the electron neutrino cross sections (let alone the electron anti-neutrinos!). It seems that this theory-driven approach is a fairly dangerous way of estimating the error on the CP violation signal. For this analysis, the errors are inflated to the somewhat arbitrary 140% (and no correlation) which is well beyond the expected sensitivity of the electron neutrino samples. For example, the fact that the electron neutrino has a smaller mass opens different areas of the parameter space in very low Q^2 regions, for example.

8.5.2.6 Prefit correlation matrix

Finally, the prefit correlations are shown in Figure 8.5. This correlation matrix is created "by hand," using *ad hoc* correlations. For example, in the case of 2p2h-shape on carbon and oxygen, the correlation is 50% based on discussions with theorists [181]. Some of the other correlations come from data, namely the resonant parameters correlations come from bubble chamber data analysis, and the FSI parameters ones come from pion scattering data analysis. For the rest of the CCQE parameters, no correlations are assumed, this is because T2K is very sensitive to the these processes and usually produces a bad fit if correlations are included in the prefit matrix. This means that the T2K data is not compatible with the MiniBooNE and MINERνA data within our models.

Note that, as mentioned in the previous section and visible in the Figure 8.5, the correlation between the ν_e/ν_μ and its equivalent in for anti-neutrino has been set to zero.

8.5.3 Detector, Monte Carlo statistics and 1p1h error

As for the FSI, the detector errors are "nuisance" parameters and are not propagated to SK. The error is parametrised using a covariance matrix. This covariance matrix is built by throwing "toy experiments" according to a binning similar to the one used for the fit (which is detailed in Appendix D), but coarser (note that there are 1438 bins in the fit, and if one used of the full matrix, the fit would become unacceptably long, the reduced binning brings the number of bins to 542). The fit is then allowed to change the overall normalisation of a bin in a coherent way according to the detector errors. Most of the systematic uncertainties that are relevant are the same as the one listed in Section 6.3, note that the OOFV normalisation that was described in that section was not applied during the construction of the covariance matrix. Rather, a symmetric, Gaussian uncertainty of 30% was used. In this case, the photon sample acts as a control sample for the ν_e samples and the OOFV error is correlated between the electron samples. The correlations and diagonal errors are shown in Figure 8.6.

Note that all the figures in this section are organised with the order for the samples in Table 8.3, (left to right and down to up in the matrix, with the detector binning from Appendix D, with each momentum bin being inside a cosine bin).

The MC statistical errors should not be propagated to SK, therefore the inverse of square root of the number of entries of the Monte Carlo histograms is added in quadrature to the diagonal of the covariance matrix to take it into account. The MC statistical relative

Horn current	FGD	Topology	Number of bins in the fit (covariance)		
			Momentum	$\cos(\theta)$	Total
FHC	1	ν_μ CC 0 pion	14 (6)	11 (7)	154 (42)
FHC	1	ν_μ CC 1 pion	13 (5)	11 (8)	143 (40)
FHC	1	ν_μ CC other	14 (5)	11 (8)	154 (40)
FHC	2	ν_μ CC 0 pion	14 (6)	11 (7)	154 (42)
FHC	2	ν_μ CC 1 pion	13 (5)	11 (8)	143 (40)
FHC	2	ν_μ CC other	14 (5)	11 (8)	154 (40)
FHC	1	ν_e CC inclusive	6 (6)	3 (1)	18 (6)
FHC	2	ν_e CC inclusive	6 (6)	3 (1)	18 (6)
RHC	1	ν_μ CC 0 pion	6 (4)	7 (7)	42 (28)
RHC	1	ν_μ CC 1 pion	8 (4)	4 (4)	32 (16)
RHC	1	ν_μ CC other	6 (4)	3 (3)	18 (12)
RHC	2	ν_μ CC 0 pion	6 (4)	7 (7)	42 (28)
RHC	2	ν_μ CC 1 pion	8 (8)	4 (4)	32 (32)
RHC	2	ν_μ CC other	6 (4)	3 (3)	18 (12)
RHC	1	$\bar{\nu}_\mu$ CC 0 pion	8 (4)	10 (10)	80 (40)
RHC	1	$\bar{\nu}_\mu$ CC 1 pion	6 (4)	3 (3)	18 (12)
RHC	1	$\bar{\nu}_\mu$ CC other	8 (4)	4 (4)	32 (16)
RHC	2	$\bar{\nu}_\mu$ CC 0 pion	8 (4)	10 (10)	80 (40)
RHC	2	$\bar{\nu}_\mu$ CC 1 pion	6 (6)	3 (3)	18 (18)
RHC	2	$\bar{\nu}_\mu$ CC other	8 (4)	4 (4)	32 (16)
RHC	1	ν_e CC inclusive	6 (6)	2 (1)	12 (6)
RHC	2	ν_e CC inclusive	6 (6)	2 (1)	12 (6)
RHC	1	$\bar{\nu}_e$ CC inclusive	3 (3)	2 (1)	6 (3)
RHC	2	$\bar{\nu}_e$ CC inclusive	3 (3)	2 (1)	6 (3)
FHC	1	photon background	5 (5)	1 (1)	5 (5)
FHC	2	photon background	5 (5)	1 (1)	5 (5)
RHC	1	photon background	5 (5)	1 (1)	5 (5)
RHC	2	photon background	5 (5)	1 (1)	5 (5)

Table 8.3: Sample-wise number of bins and ordering in the covariance matrices.

errors are shown in Figure 8.7.

Finally, some cross section errors have not been fully implemented yet, and the T2K collaboration only has access to differences between the NEUT and the Nieves et al. model [40] for the propagation of the 1p1h error. In this case, since one cannot parametrise properly the difference between the two models, a "fake data" is created and the difference between the two models is added to the covariance matrix, assuming full correlations for the differences of models. This allows to have a smooth transition between the NEUT and Nieves models via the covariance matrix. The fake data relative errors are shown in Figure 8.8.

The addition of the detector, MC statistical and 1p1h fake data errors are shown in Figure 8.9. Note that when the covariance is constructed, the detector systematic uncertainties produce shifts due to their non gaussianity. To take this into account, the normalisation of each bin is shifted according to the mean value of the toys observed in each bin. These "bin shifts" can be found in Figure 8.10.

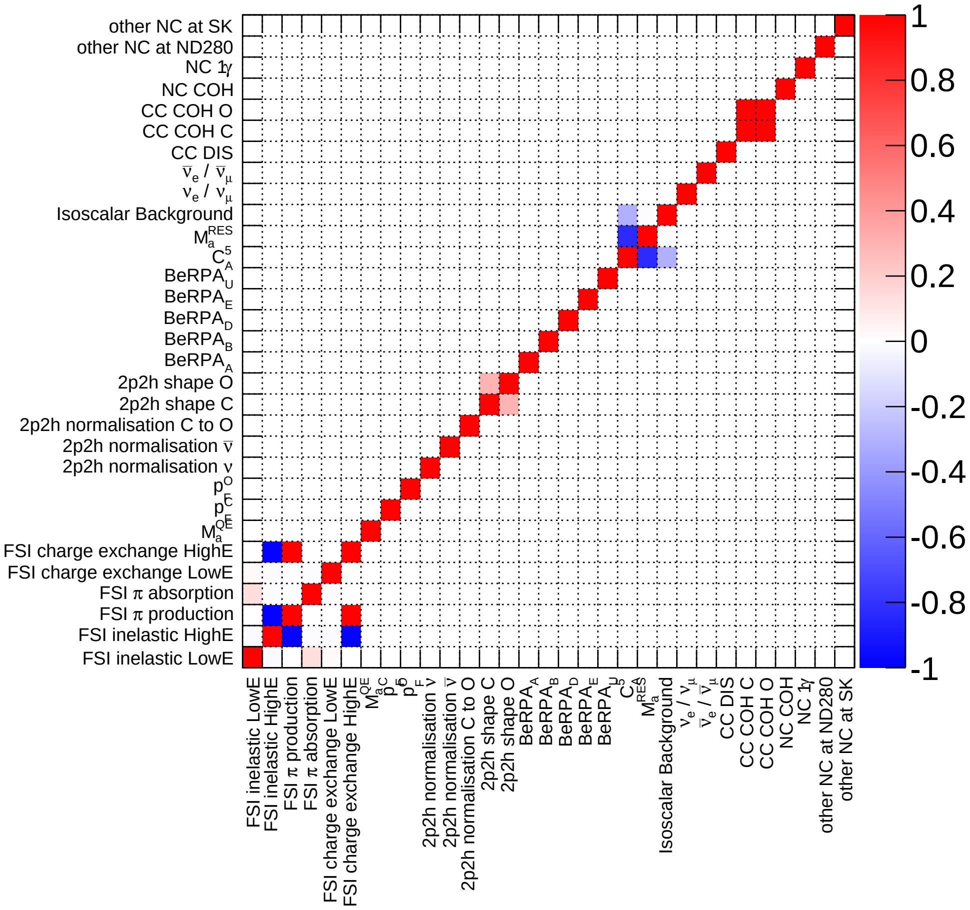

Figure 8.5: The prefit error correlations for the cross section uncertainties.

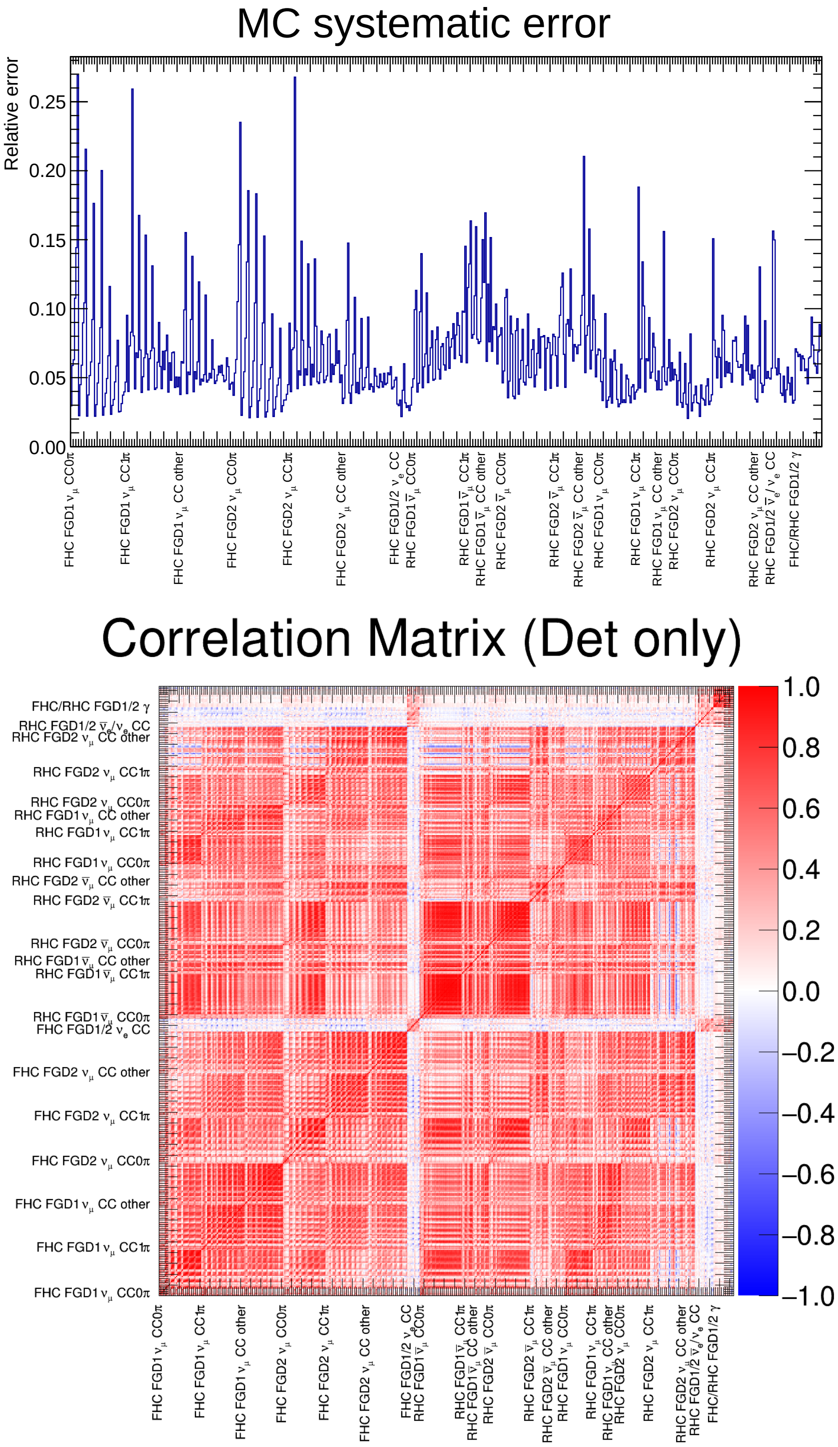

Figure 8.6: ***Top:*** Relative detector uncertainties for each lepton reconstructed bin (square root of the diagonal of the covariance matrix). ***Bottom:*** Correlations between the bins. The samples are organised as mentioned in Table 8.3.

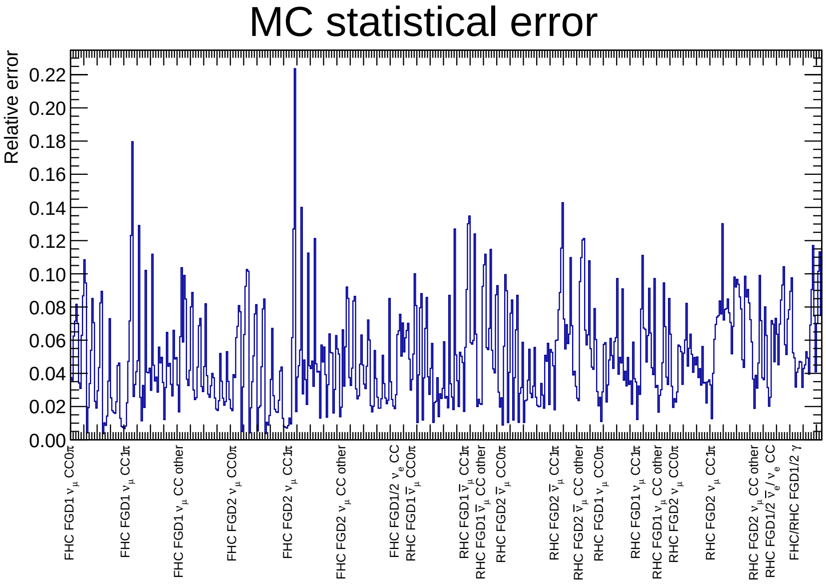

Figure 8.7: Monte Carlo statistical uncertainty for the lepton reconstructed bins. The samples are organised as mentioned in Table 8.3.

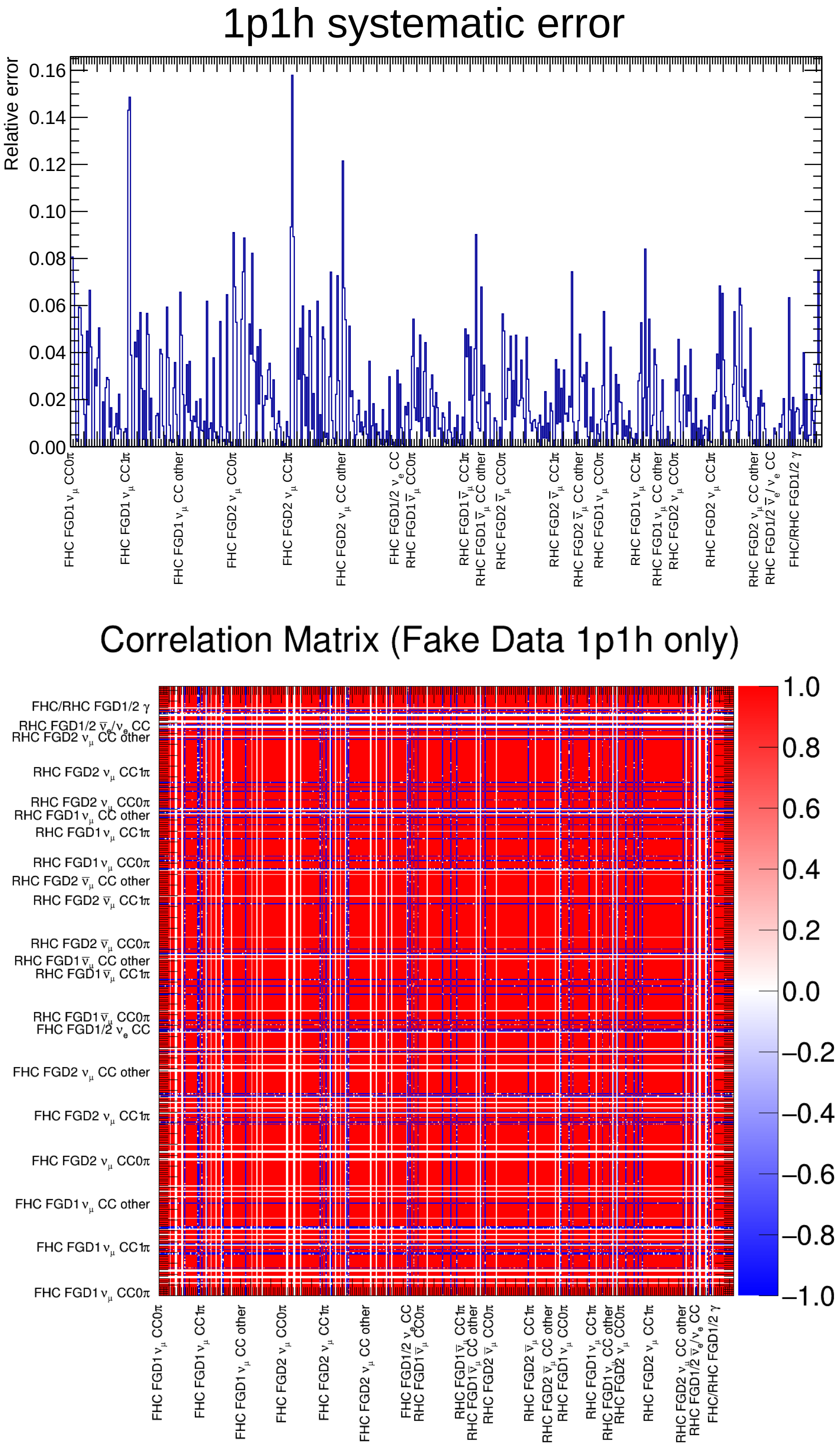

Figure 8.8: Top: 1p1h fake data error for the lepton reconstructed bins. ***Bottom:*** Correlations between the bins (100%, −100% or 0%). The samples are organised as mentioned in Table 8.3.

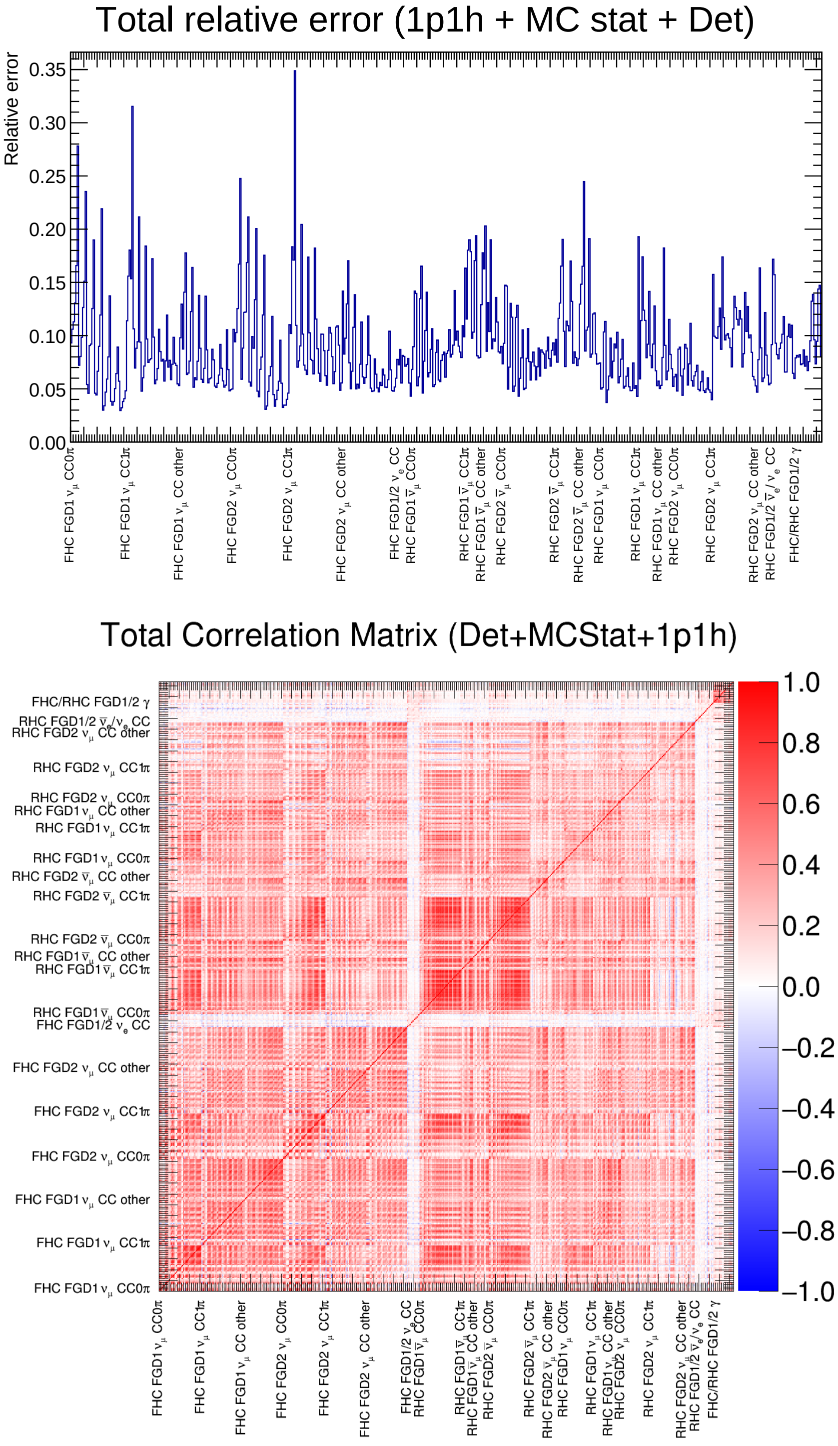

Figure 8.9: ***Top:*** Total error for the lepton reconstructed bins. ***Bottom:*** Correlations between bins. The samples are organised as mentioned in Table 8.3.

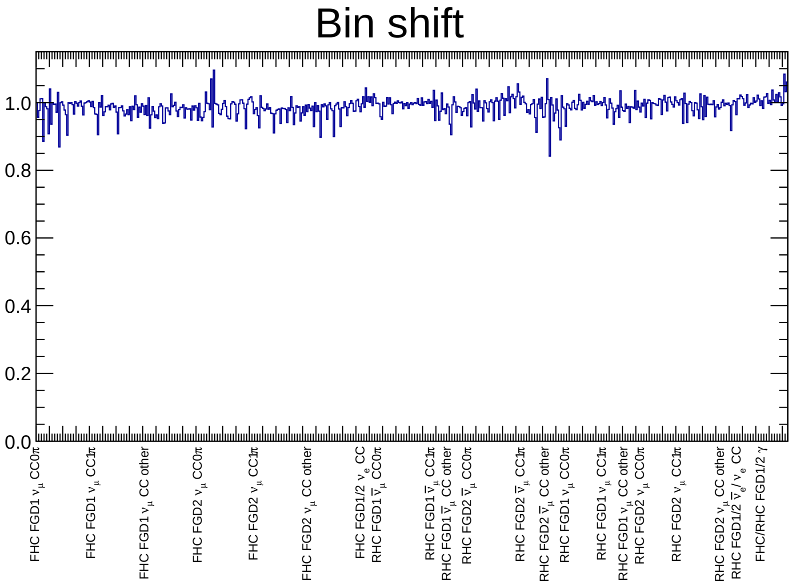

Figure 8.10: Shifts applied to the nominal predictions on the lepton reconstructed bins. The samples are organised as mentioned in Table 8.3.

8.6 Event rates

In this section, the event rates are compared for data and MC. This is done in Tables 8.4 and 8.5, where each correction from the previous section is applied independently to build the so-called Asimov data set [182]. The Asimov data set is the “best guess” MC prediction given all the priors: i.e. this data set is created by setting all the corrections to their most probable value, given all the prior knowledge from other experiments, beam settings and detector parameters.

The statistical weight of the electron neutrino samples is very small compared to that of the muon neutrino samples. This is due to the fact that the electron (anti-) neutrino fluxes are much smaller compared to the muon (anti-) neutrino ones.

Note that around half of the electron / positrons from the ν_e, $\bar{\nu}_e$ and photon samples have momentum below a 200 MeV threshold that was introduced. This was done because at low energy these samples have a very large and dominant photon contamination.

Sample	Data	Raw MC	POT	POT + Flux	POT + XSec	POT + Det	POT + Shift	Prefit
FHC FGD1								
ν_μ CC 0π	33548	459887	31468.27	37255.42	29993.65	30301.11	31094.08	33889.88
ν_μ CC 1π	7755	117199	8057.27	10357.07	7580.53	7686.00	7876.86	9136.50
ν_μ CC other	8052	90341	6208.35	8813.59	6148.81	5902.42	6080.17	8136.08
ν_e CC	297	5865	326.80	421.73	319.35	312.29	329.53	398.38
photon	153	3036	174.13	225.53	173.01	167.42	175.37	217.68
FHC FGD2								
ν_μ CC 0π	33451	460361	31203.39	36941.06	29911.08	30349.04	30628.44	33952.94
ν_μ CC 1π	6133	93215	6295.84	8161.10	5981.79	6114.35	6156.31	7413.34
ν_μ CC other	7640	85621	5821.90	8265.69	5776.64	5679.64	5713.78	7868.08
ν_e CC	342	5909	334.20	430.65	328.70	316.06	336.02	403.72
photon	147	2810	157.09	203.99	155.63	148.12	157.87	191.86

Table 8.4: Event rates at the ND280 for the neutrino mode samples, data (first column). The bare Monte Carlo (Raw MC column) was scaled to the data according to the POT (POT column), the neutrino flux was reweighted according to the NA61 / SHINE thin target measurements [121–123] (POT + Flux column), tuned to external data for the cross section shifts [158] (POT + XSec column), all the detector parameters were changed according to *in situ* measurements of cosmic, sand, and through going muons (POT + Det) and corrected for non gaussianity of the detector throws (POT + Shift). The last column shows the effect of all the corrections on the event rates (Prefit column).

Sample	Data	Raw MC	POT	POT + Flux	POT + XSec	POT + Det	POT + Shift	Prefit
RHC FGD1								
$\bar{\nu}_\mu$ CC 0π	6367	96574	6781.46	7218.22	6229.52	6721.28	6715.31	6497.48
$\bar{\nu}_\mu$ CC 1π	535	9150	640.62	686.50	541.59	624.69	635.00	562.22
$\bar{\nu}_\mu$ CC other	1070	14713	1044.25	1174.19	1001.93	1022.28	1008.39	1076.07
ν_μ CC 0π	2707	34939	2456.68	2866.54	2383.68	2378.80	2448.31	2687.39
ν_μ CC 1π	846	12344	870.87	1046.66	821.61	837.53	854.92	935.32
ν_μ CC other	1012	10859	761.64	965.19	754.44	730.97	748.87	901.59
$\bar{\nu}_e$ CC	79	1223	86.30	86.68	81.56	88.68	87.65	86.73
ν_e CC	141	2010	140.97	152.31	138.88	138.28	140.98	152.79
photon	83	1227	88.18	98.15	88.45	85.79	88.90	96.68
RHC FGD2								
$\bar{\nu}_\mu$ CC 0π	6451	95543	6688.79	7124.82	6170.68	6574.83	6681.16	6450.17
$\bar{\nu}_\mu$ CC 1π	465	8160	568.38	622.08	494.13	552.79	552.55	512.04
$\bar{\nu}_\mu$ CC other	1004	13443	943.85	1064.33	911.63	928.26	896.00	962.03
ν_μ CC 0π	2645	35130	2454.59	2861.12	2393.86	2415.67	2447.32	2742.4
ν_μ CC 1π	693	9686	674.95	813.48	636.64	660.75	666.77	746.58
ν_μ CC other	929	10330	726.14	927.55	719.98	714.40	715.88	892.49
$\bar{\nu}_e$ CC	96	1283	90.81	90.82	85.07	89.48	91.35	84.33
ν_e CC	148	2071	147.74	167.16	146.92	142.79	148.66	162.50
photon	71	1152	80.11	89.49	79.44	76.70	81.24	86.12

Table 8.5: Event rates at the ND280 for the anti-neutrino mode samples, data (first column). The bare Monte Carlo (Raw MC column) was scaled to the data according to the POT (POT column), the neutrino flux was reweighted according to the NA61 / SHINE thin target measurements [121–123] (POT + Flux column), tuned to external data for the cross section shifts [158] (POT + XSec column), all the detector parameters were changed according to *in situ* measurements of cosmic, sand, and through going muons (POT + Det) and corrected for non gaussianity of the detector throws (POT + Shift). The last column shows the effect of all the corrections on the event rates (Prefit column).

8.7 Asimov fit

The Asimov data set [182] is the data set which is the “best guess” for what the data distribution would be. In the present case, the Asimov data set is the MC set reweighted with the POT ratio, with the neutrino flux reweighting according the to the NA61 / SHINE thin target measurement [121–123], with the cross section tuned according to external data [158], with all the detector shifts and corrected to non-gaussianity for detector throws.

The fit of the nominal Monte Carlo (Asimov) is shown in Figure 8.11 for the cross section parameters; Figures 8.12 and 8.13 for the ND280 and SK flux parameters, respectively (shown with the binning of the covariance matrix of the flux, Figure 6.1); and Figures 8.14 and 8.15 for all the detector parameters which control the normalisation of each bin.

The Minuit2 minimisation was run on the PPRC cluster at Queen Mary University using 25 CPU in parallel. It took 113632 steps for the minimiser to converge and the HESS method was then ran to estimate the postfit correlations and errors.

For an Asimov fit, it is important to check that the implementation of all the systematic uncertainties does not create any bias in the final distributions and values of the parameters, which is visible in all the figures mentioned in this section: no parameter is pulled away from its nominal value, indicating that the minimisation has taken place normally.

These figures are also indicative of the power of the ND280 in constraining the oscillation analysis systematic errors. For example, one can easily see that the flux uncertainty is largely decreased at SK after the ND280 fit. Similarly, this is visible for the cross section parameters.

The focus of this analysis is on the ν_e, which for the first time were used in this kind of fits. One can see that the error on the ν_e/ν_μ ratio is still larger than the 3% that is used currently in T2K oscillation analyses. In this case, it is 7.6% for the ν_e and 19.3% for $\bar{\nu}_e$. This means that the theoretical result in [99] can still not be tested with the current data at T2K.

On Figures 8.16, strong anti-correlations between the cross section and flux parameters are visible (blue bands off diagonal). This is expected, since when the flux is increasing, the cross section should be smaller for a constant number of events. A zoom of this region is visible in Figure 8.17. It is interesting to see some correlations appear for the first time between the flux and the cross section parameters related to the ν_e events. This correlation reaches -35.6% for the highest energy bin of the ν_e in FHC and the ν_e/ν_μ error.

Finally, the cross section and flux correlation are visible in Figure 8.18 and 8.19.

Although this is still marginal, some correlation between electron (anti-) neutrino and the other cross section parameters are introduced. The rest of the correlation are due to the muon (anti-) neutrino samples:

- The parameters which acts on the Q^2 distribution, such as M_a and the BeRPA, get correlated.
- The parameters which control the RES events gets correlated (M_a^{RES}, the isoscalar background and C_A^5).
- Some additional correlations between the RES parameters and 2p2h appear due to the RES events present in the CC 0 pion samples.
- Finally, although the FSI parameter get correlated, they are not used in the oscillation analyses fit, they will not be discussed here.

All of the cross section parameter values before and after the Asimov fit are shown in Table 8.6 (note that these are shown with the real data fit result, in the interest of space).

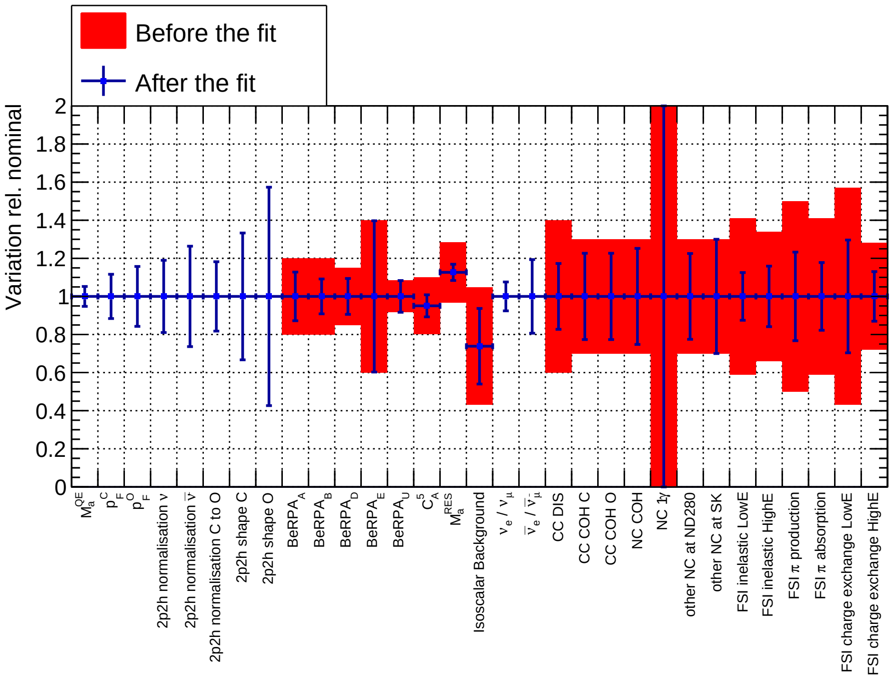

Figure 8.11: Cross section uncertainties before (red) and after (blue) a fit to the Asimov data set of the ND280 selections.

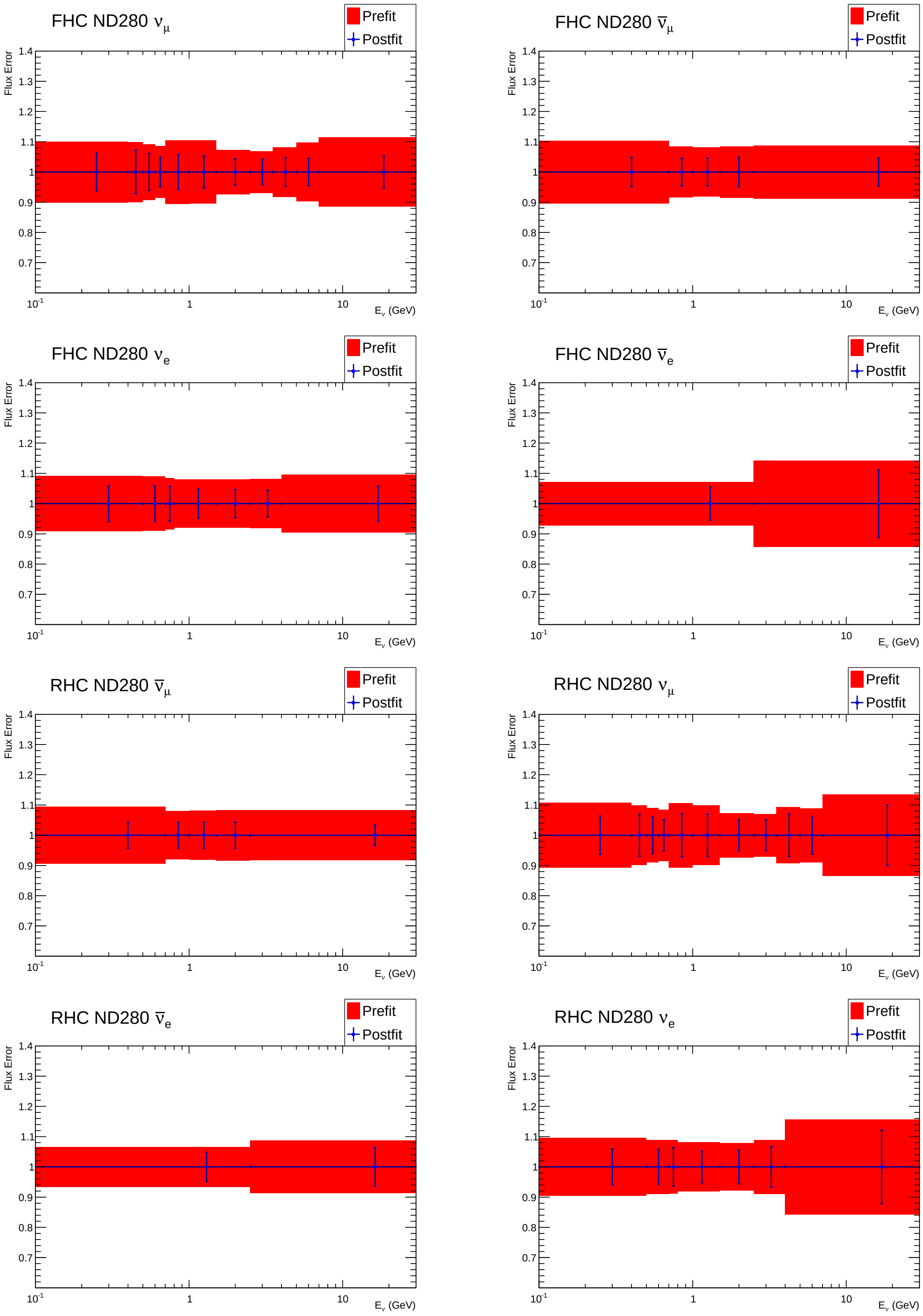

Figure 8.12: ND280 flux uncertainties before (red) and after (blue) a fit to the Asimov data set of the ND280 selections.

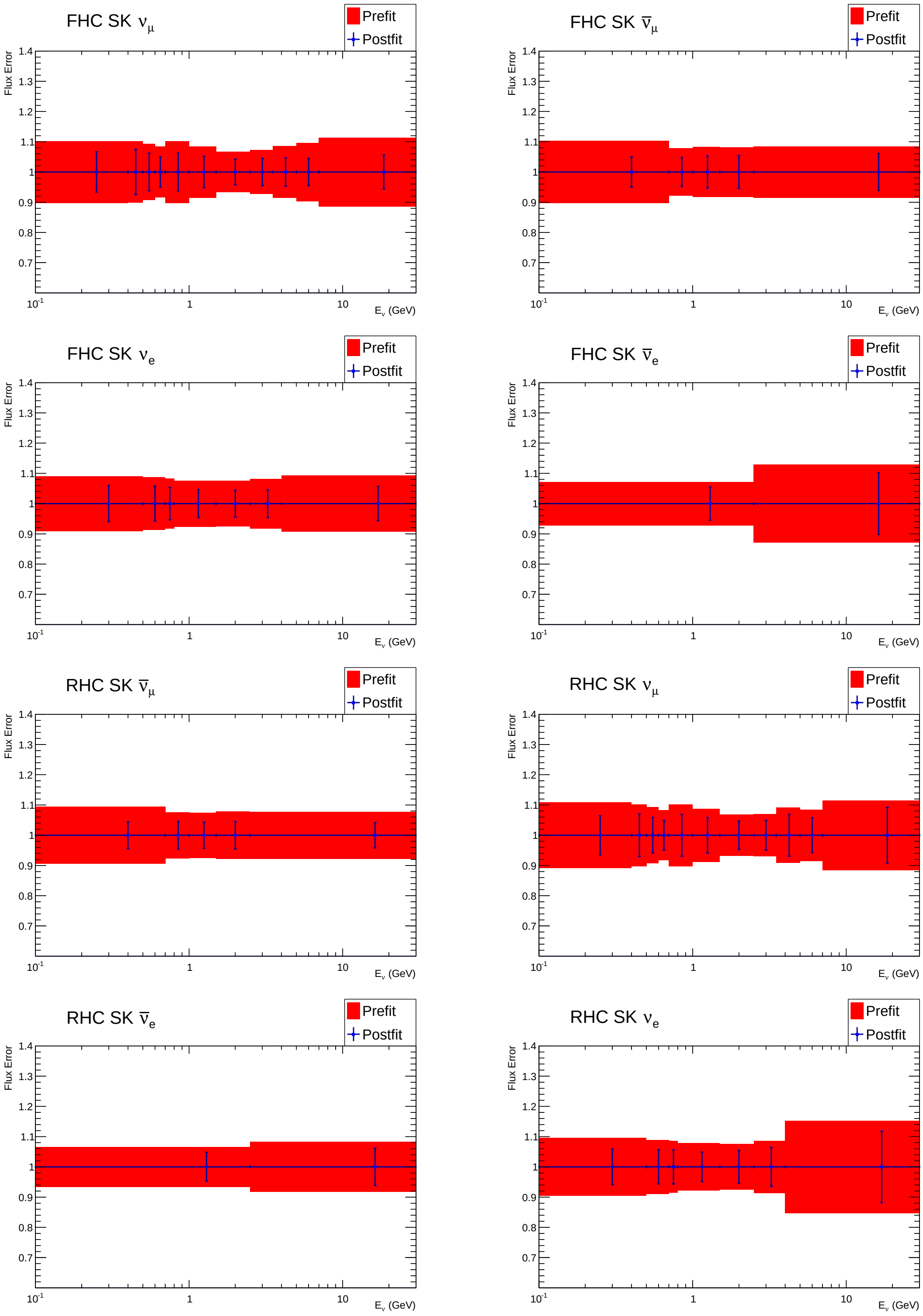

Figure 8.13: SK flux uncertainties before (red) and after (blue) a fit to the Asimov data set of the ND280 selections.

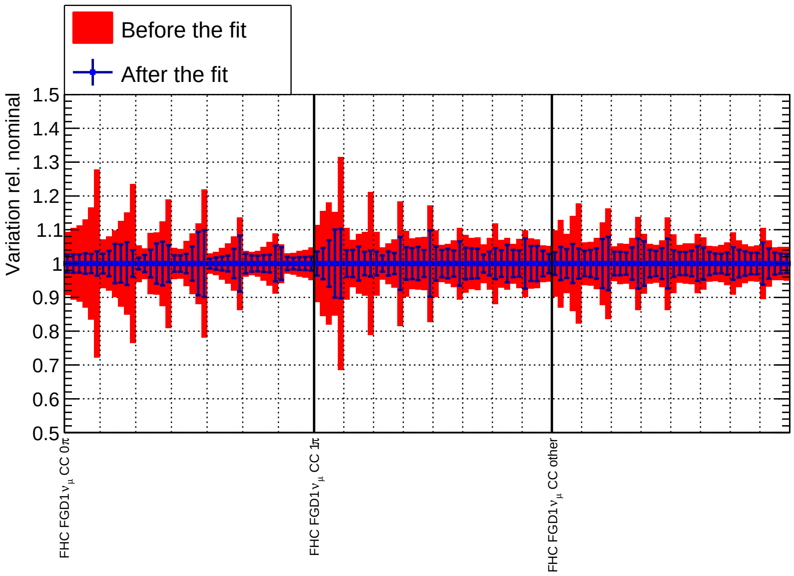

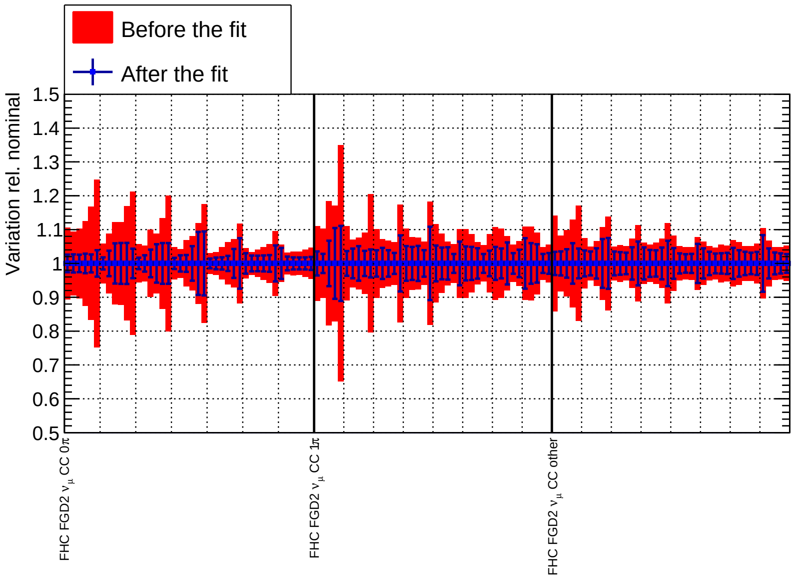

Figure 8.14: ND280 detector and 1p1h uncertainties before (red) and after (blue) a fit over the data from the ND280 selections. The dotted lines are the edges of the $\cos(\theta_{\text{lepton}})$ bins (left to right for increasing $\cos(\theta_{\text{lepton}})$ bins). ***Top:*** FHC FGD1 ν_μ CC selections. ***Bottom:*** FHC FGD2 ν_μ CC selections.

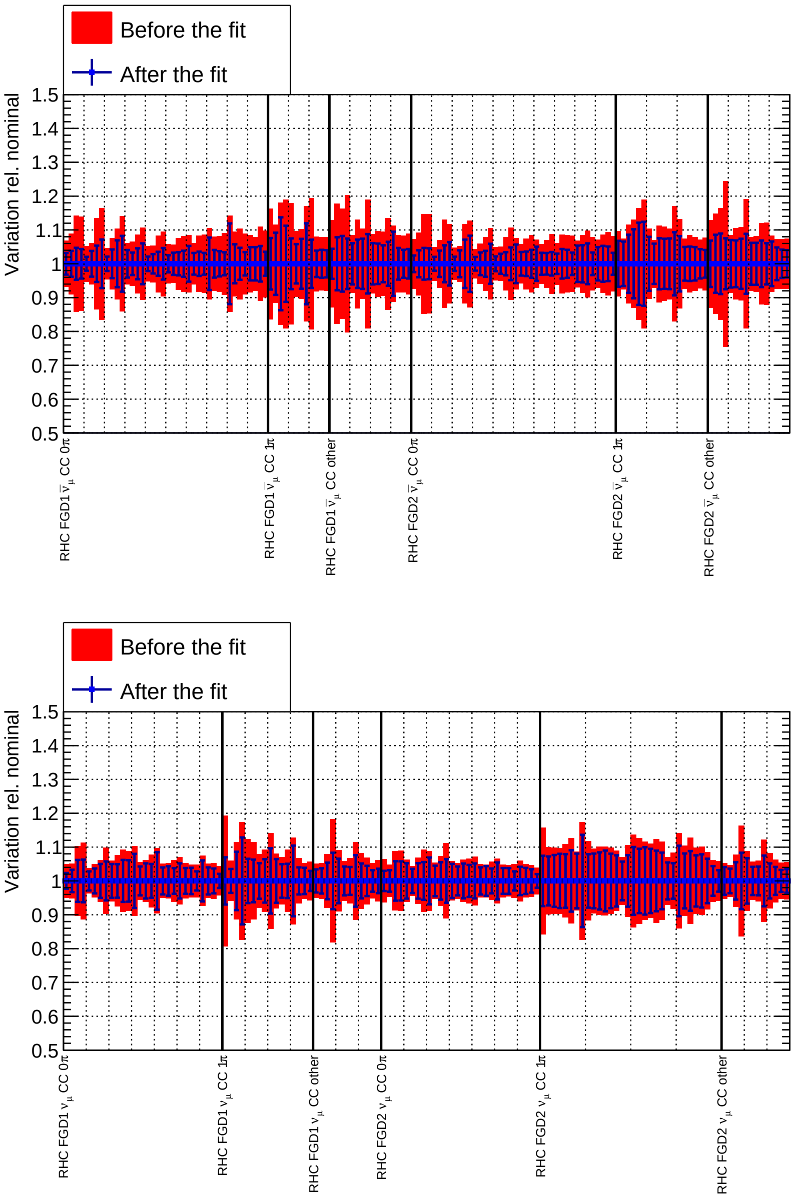

Figure 8.15: ND280 detector and 1p1h uncertainties before (red) and after (blue) a fit over the data from the ND280 selections. The dotted lines are the edges of the $\cos(\theta_{\text{lepton}})$ bins (left to right for increasing $\cos(\theta_{\text{lepton}})$ bins). ***Top:*** RHC FGD1/2 $\bar{\nu}_{\mu}$ CC selections. ***Bottom:*** RHC FGD1/2 ν_{μ} CC selections.

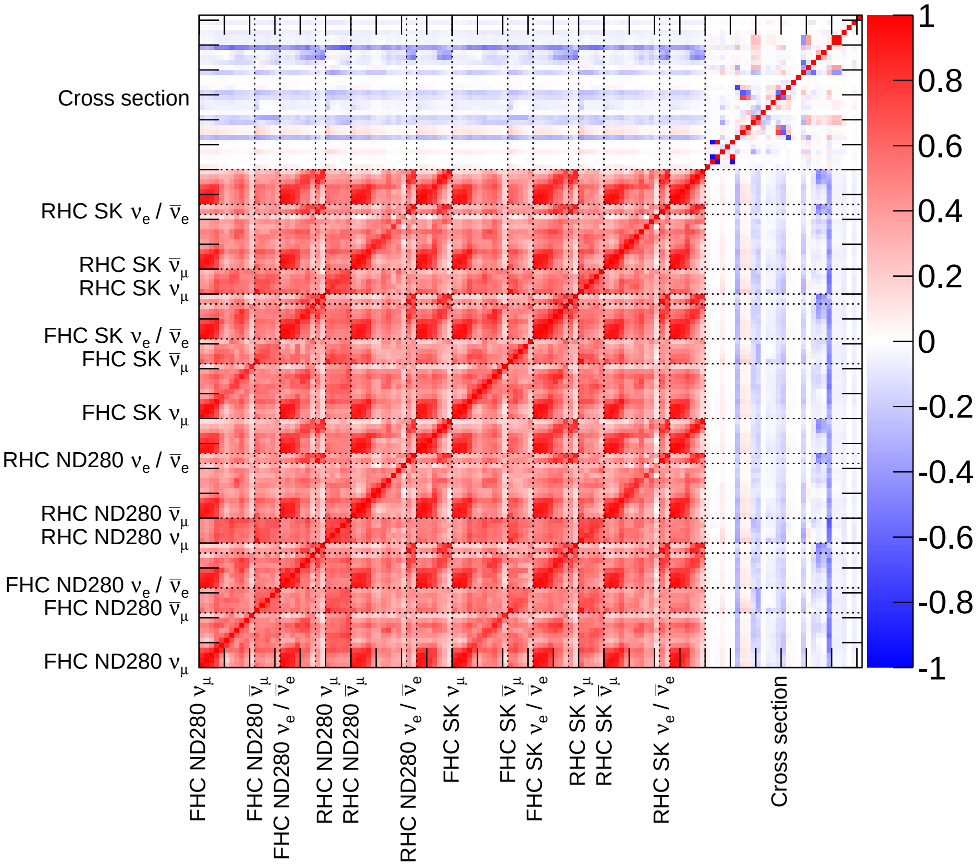

Figure 8.16: Correlations between all the parameters used for oscillation analyses after a fit to the Asimov data set of the ND280 selections.

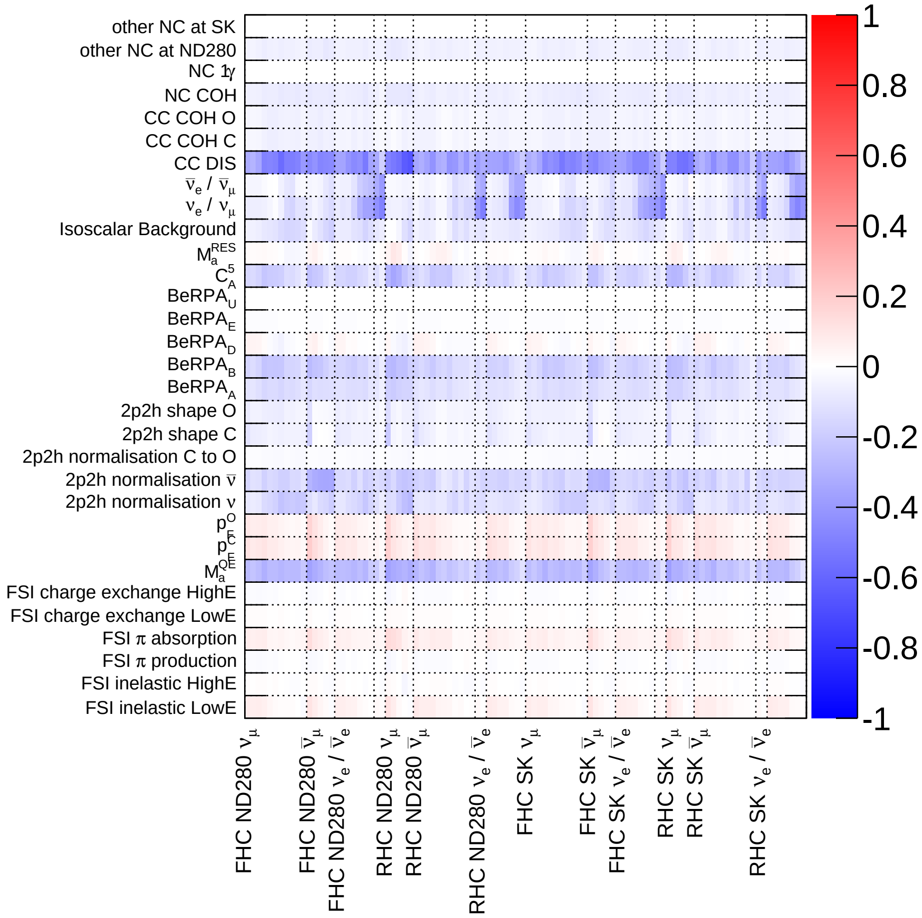

Figure 8.17: Zoom of Figure 8.16, correlations between the flux and cross section parameters used for oscillation analyses after a fit to the Asimov data set of the ND280 selections.

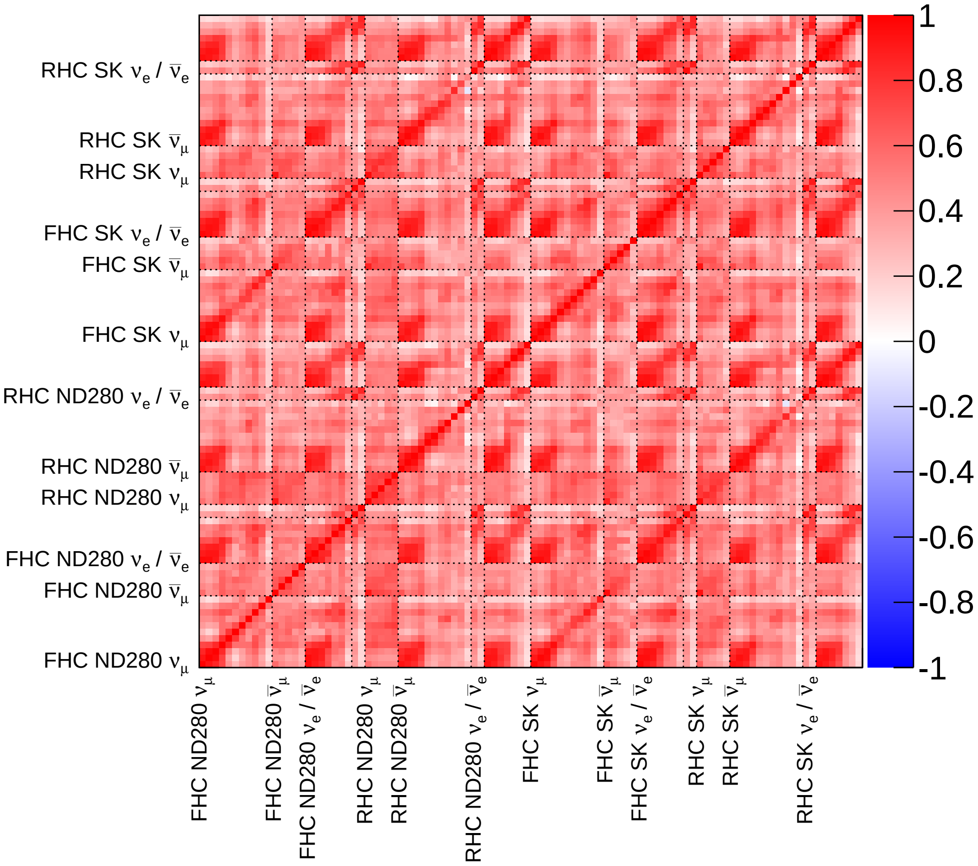

Figure 8.18: Zooms of Figure 8.16, correlation of the flux parameters used for oscillation analyses after a fit to the Asimov data set of the ND280 selection.

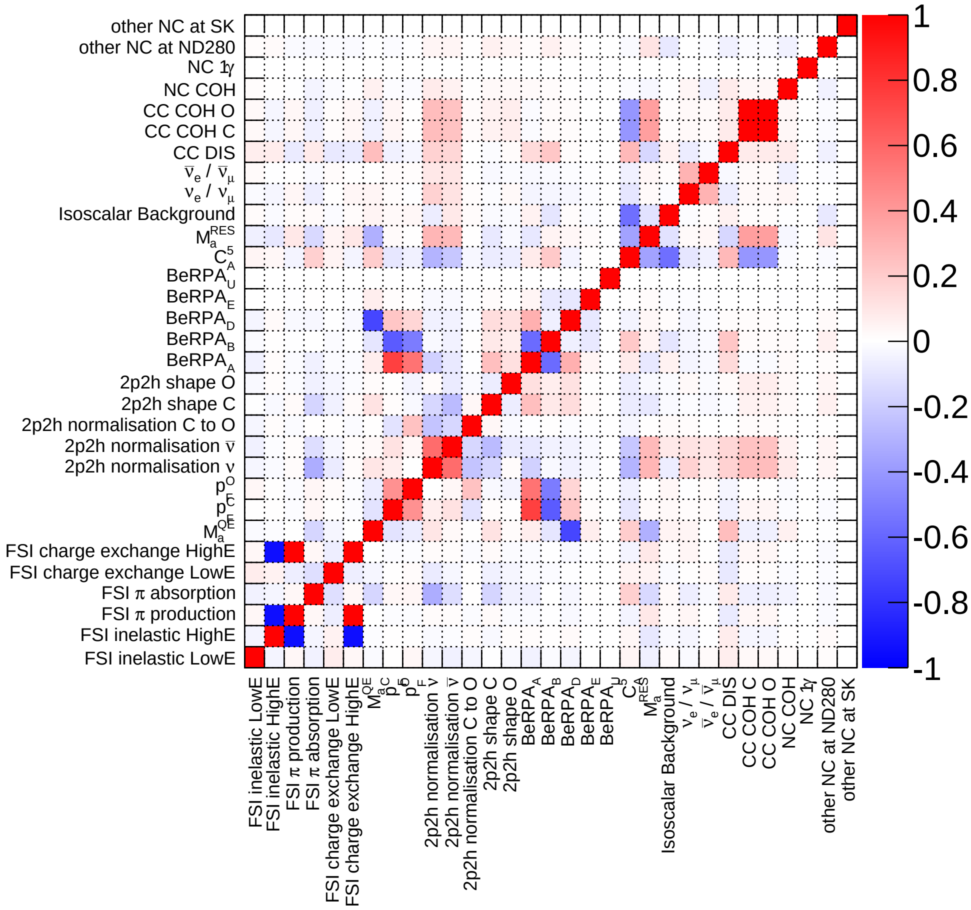

Figure 8.19: Zooms of Figure 8.16, correlation of the cross section parameters used for oscillation analyses after a fit to the Asimov data set of the ND280 selection.

8.8 Data result

In this section, the result of the real data fit is commented. Similarly to what was done for the Asimov fit, the fit was run using the cluster at Queen Mary University and took 246011 steps to finalise the minimisation.

8.8.1 Data comparisons

8.8.1.1 Prefit comparisons

The one-dimensional muon momentum projections of the ν_μ selections are shown before and after the data fit in Figures 8.20 to 8.28. Note that all the corrections listed in the previous sections were applied in the stacked histograms, they are the "Asimov" data sets. On the bottom of the same figures, the data / MC ratios before and after the fit are shown.

Some interesting features are already visible in the prefit distributions:

- In the ν_μ CC 0 pion selections, both in FHC and RHC (Figures in 8.20 and 8.26), the MC distributions are lower than the data for low momentum and this is inverted for high energy. This could be symptomatic of problems in the form factor at low Q^2, since most of the high energy events are also very forward, and sensitive to the relatively low Q^2.
- In the ν_μ CC 1 pion selections, the MC systematically overestimates the data (Figures in 8.21 and 8.24), except in the RHC wrong sign component (ν_μ) selections (Figure 8.27). There are multiple reasons why this could happen. Firstly, the fact that the wrong sign component has a different behaviour can mean that the neutrino flux prediction is wrong. Secondly, on average the neutrinos in RHC have a higher energy. This allow creation of higher mass resonances, for which predictions are more complex than for the Δ resonance.

  The fact that $\bar{\nu}_\mu$ and ν_μ selections (Figures in 8.21 and 8.24) show the same types of disagreements does not mean it comes from the same mismodelling. There are reasons to believe that the RES modelling in anti-neutrino can be significatively wrong, due to the more sparse data. Hence, the behaviour of the isoscalar background could be different for the case of anti-neutrinos. Finally, since the pion is negatively charged for $\bar{\nu}_\mu$ selections, some of the FSI parameters such as the charge exchange parameter could be very different to the positively charged case.
- In the ν_μ CC other case, the data is largely underestimated at around 1 GeV, for all the selections (Figures in 8.22, 8.25 and 8.28). These selections are sensitive to the SIS and DIS, which is probably one of the least well simulated part of the T2K

model due to the absence of reliable models. The fact that the data is not reproduced adequatly in these regions is not surprising.

Next, moving on the ν_e selections, their one-dimensional projections are shown from Figures 8.29 to 8.33. The first observations of the prefit is that the photon samples are over-estimated (Figures in 8.30 and 8.33), this is very similar to what was observed in the neutrino-induced single photons searches (Figure 5.12). It also seems that the high momentum bins of the electron (anti-) neutrino samples are the ones that will be able to constrain the electron neutrino parameters because they are purer (Figure in 8.29, 8.31 and 8.32).

In the FHC ν_e samples (Figures in 8.29), the first momentum bin has a data / MC disagreement in only the FGD1 sample: In FGD1 the MC overpredicts the data, whereas this seems to not be the case for FGD2. This feature is not visible in the photon control sample (Figures in 8.30), whereas this is marginally visible for RHC samples (ν_e and $\bar{\nu}_e$, Figures in 8.32 8.31, respectively). This seem to indicate that there are physical effects which are not present in the MC for one of the FGD selections. Given the fact that this is only visible in the electron (positron) samples and not in the photon sample, such effects are most likely due to the PID which is realised in Section 8.4.3. The difference could be due to:

- A difference in the TPC2 and 3 PID, since the photon sample uses the invariant mass cut, there is much less dependancy to the TPC PID for the photon sample than there is for the ν_e and $\bar{\nu}_e$ samples.
- The electron ECal PID, which is, in the case of the FGD2 uses the DsECal (see cut described in Section 8.4.3.3).
- The second TPC PID cut (see cut described in Section 8.4.3.4).
- The usage of the FGD2 shower cut for FGD1 electron and positron sample (see cut described in Section 8.4.3.10).
- The electron

Finally, the statistics are quite reduced which means that the ND280 is overall not very sensitive to electron neutrinos.

8.8.1.2 Postfit comparisons

The first thing to notice is that all the data / MC ratios get better for all the samples. These are shown in Figures 8.20 to 8.33. The residual differences are:

- In the CC other samples, the data excess still remains (Figures in 8.22, 8.25 and 8.28). This probably means that the DIS parameter has not enough freedom encoded in it to fit the shape of the muon momentum. In fact, the data / MC ratios in these samples almost do not change, even in the ones that have the highest statistical power in neutrino mode.

- The CC 1 pion samples ratios in RHC (Figures in 8.24 and 8.27) almost do not change, indicating that the FHC samples are dominating the fit to the resonant parameters (Figures in 8.21). This is in general true for most of the RHC samples, it seems that the anti-neutrino samples have a reduced impact on the fit due their lower statistics, and therefore some adequat anti-neutrino parameters need to be designed to let more freedom to the MC prediction in these samples.
- The photon sample low energy discrepancy is not absorbed by the fit (Figures in 8.30 and 8.33), which indicates that the photon error has not enough freedom to change the shape of the distributions, this means that central values of the parameters relevant to ν_e and $\bar{\nu}_e$ probably are wrong.

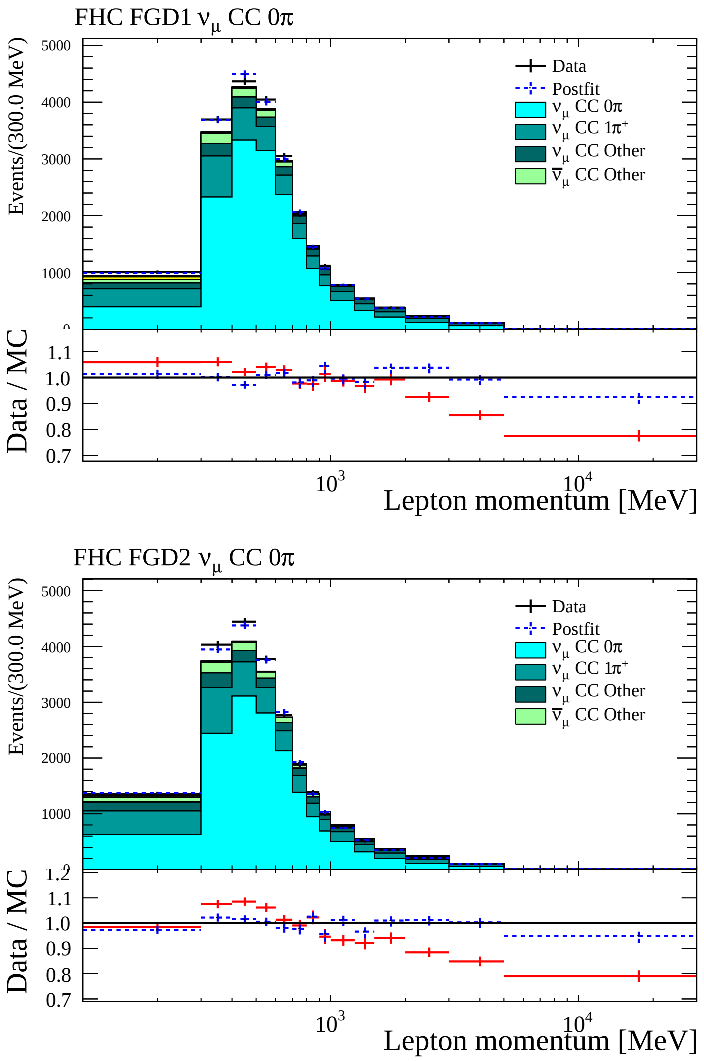

Figure 8.20: One-dimensional projections of the lepton momentum of the FHC ν_μ CC 0 pion FGD1 and 2 samples before (stack) and after (blue dotted) a fit over the data from the ND280 selections. ***Top:*** FGD1. ***Bottom:*** FGD2. The bottom pads on each figure show the data / MC ratio before (red) and after (blue dotted) the data fit.

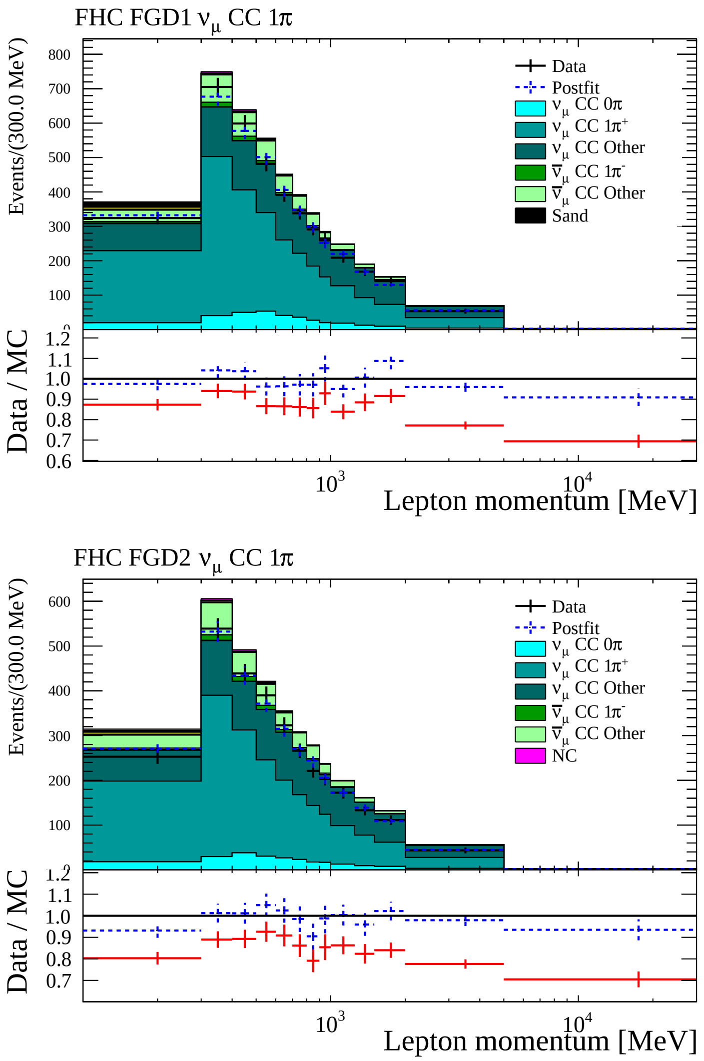

Figure 8.21: One-dimensional projections of the lepton momentum of the FHC ν_μ CC 1 pion FGD1 and 2 samples before (stack) and after (blue dotted) a fit over the data from the ND280 selections. ***Top:*** FGD1. ***Bottom:*** FGD2. The bottom pads on each figure show the data / MC ratio before (red) and after (blue dotted) the data fit.

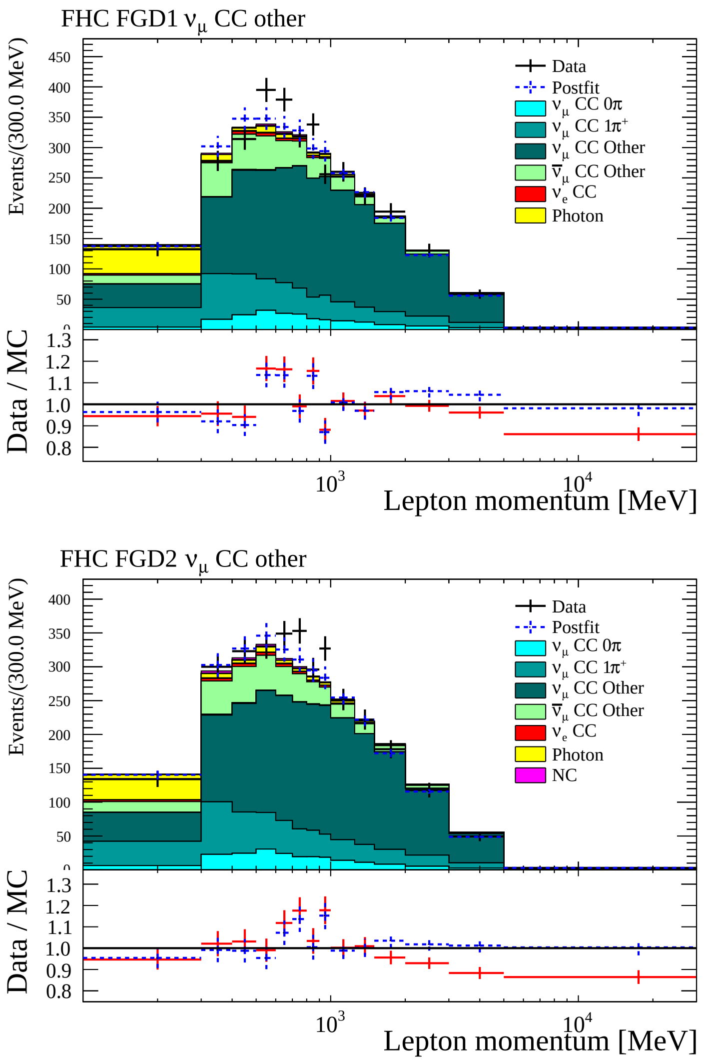

Figure 8.22: One-dimensional projections of the lepton momentum of the FHC ν_μ CC other FGD1 and 2 samples before (stack) and after (blue dotted) a fit over the data from the ND280 selections. ***Top:*** FGD1. ***Bottom:*** FGD2. The bottom pads on each figure show the data / MC ratio before (red) and after (blue dotted) the data fit.

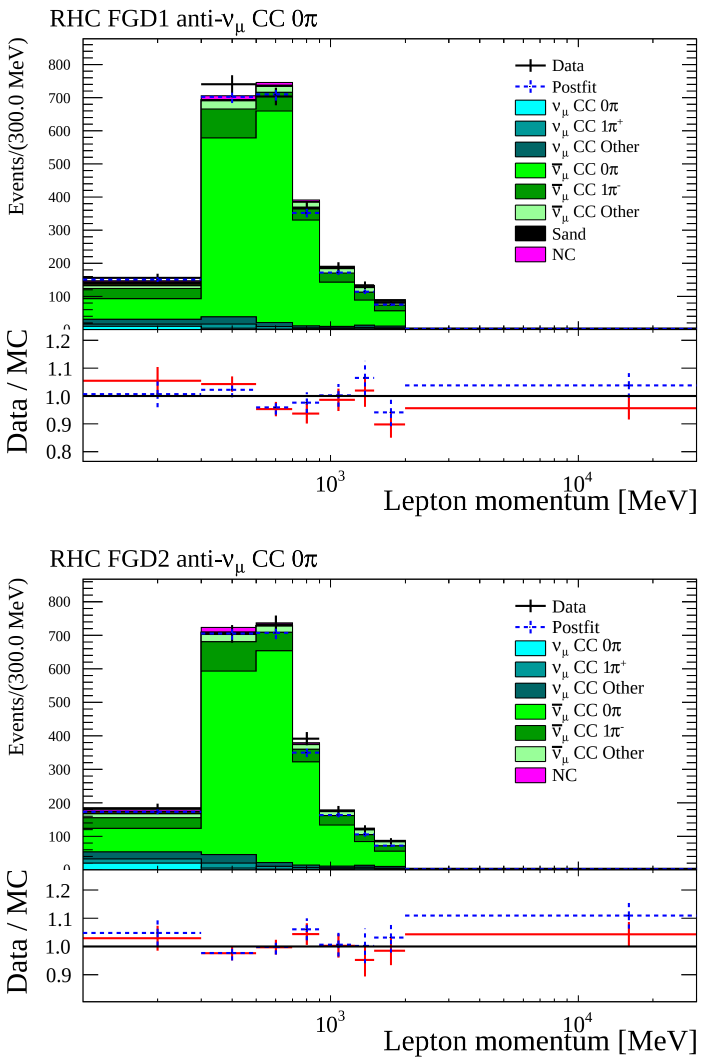

Figure 8.23: One-dimensional projections of the lepton momentum of the RHC $\bar{\nu}_\mu$ CC 0 pion FGD1 and 2 samples before (stack) and after (blue dotted) a fit over the data from the ND280 selections. ***Top:*** FGD1. ***Bottom:*** FGD2. The bottom pads on each figure show the data / MC ratio before (red) and after (blue dotted) the data fit.

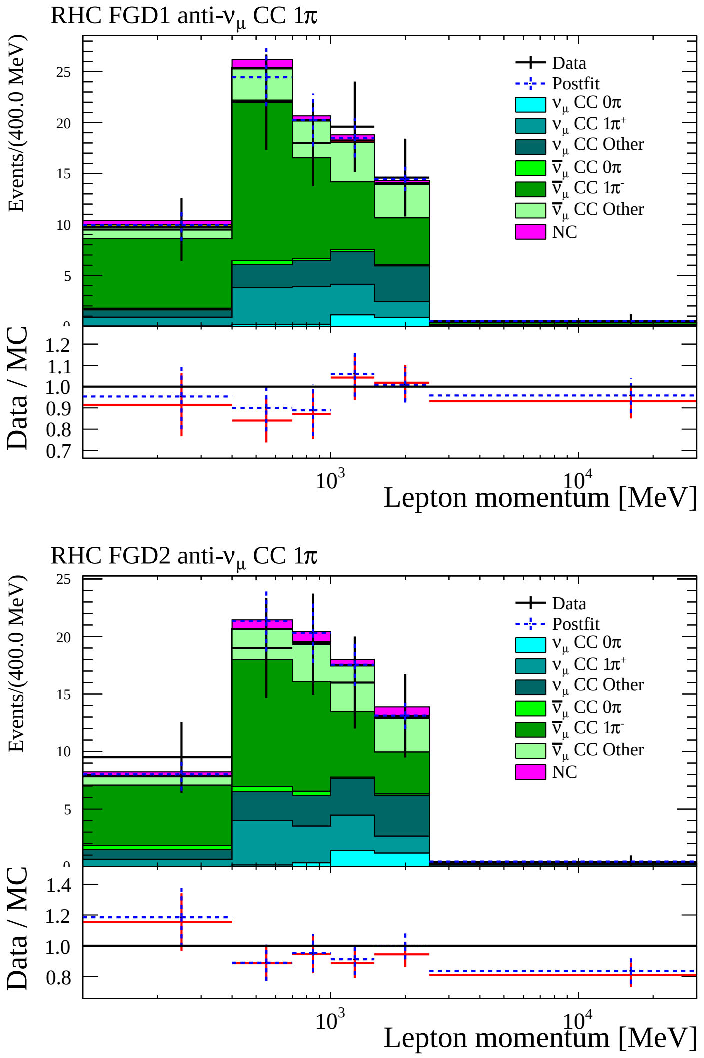

Figure 8.24: One-dimensional projections of the lepton momentum of the RHC $\bar{\nu}_\mu$ CC 1 pion FGD1 and 2 samples before (stack) and after (blue dotted) a fit over the data from the ND280 selections. ***Top:*** FGD1. ***Bottom:*** FGD2. The bottom pads on each figure show the data / MC ratio before (red) and after (blue dotted) the data fit.

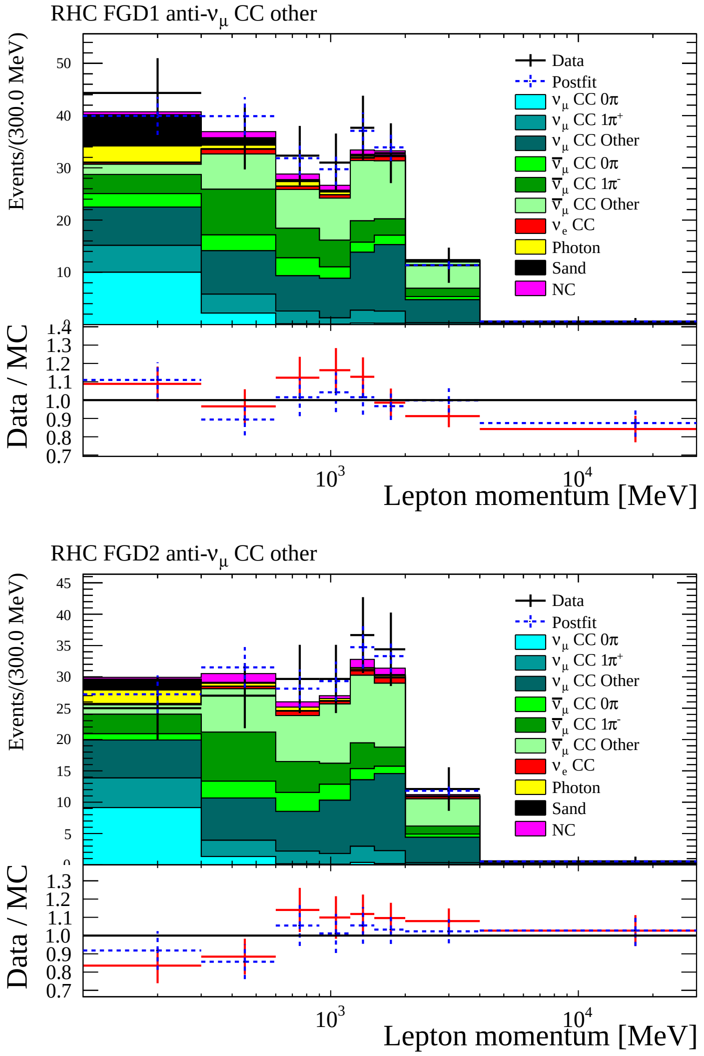

Figure 8.25: One-dimensional projections of the lepton momentum of the RHC $\bar{\nu}_\mu$ CC other FGD1 and 2 samples before (stack) and after (blue dotted) a fit over the data from the ND280 selections. ***Top:*** FGD1. ***Bottom:*** FGD2. The bottom pads on each figure show the data / MC ratio before (red) and after (blue dotted) the data fit.

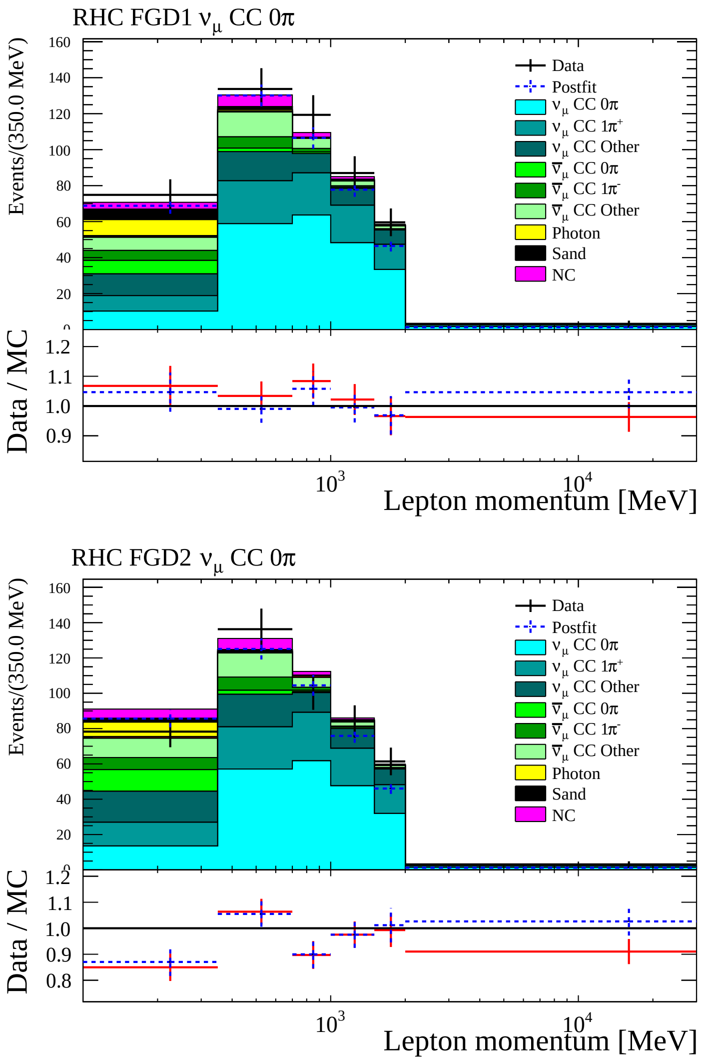

Figure 8.26: One-dimensional projections of the lepton momentum of the RHC ν_μ CC 0 pion FGD1 and 2 samples before (stack) and after (blue dotted) a fit over the data from the ND280 selections. ***Top:*** FGD1. ***Bottom:*** FGD2. The bottom pads on each figure show the data / MC ratio before (red) and after (blue dotted) the data fit.

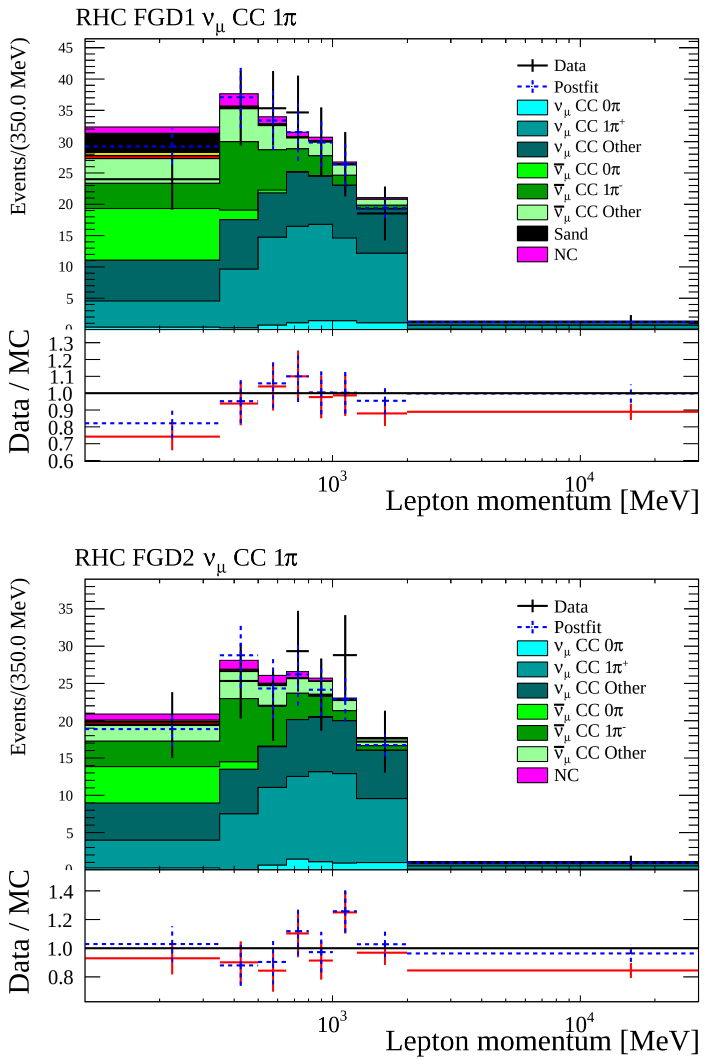

Figure 8.27: One-dimensional projections of the lepton momentum of the RHC ν_μ CC 1 pion FGD1 and 2 samples before (stack) and after (blue dotted) a fit over the data from the ND280 selections. ***Top:*** FGD1. ***Bottom:*** FGD2. The bottom pads on each figure show the data / MC ratio before (red) and after (blue dotted) the data fit.

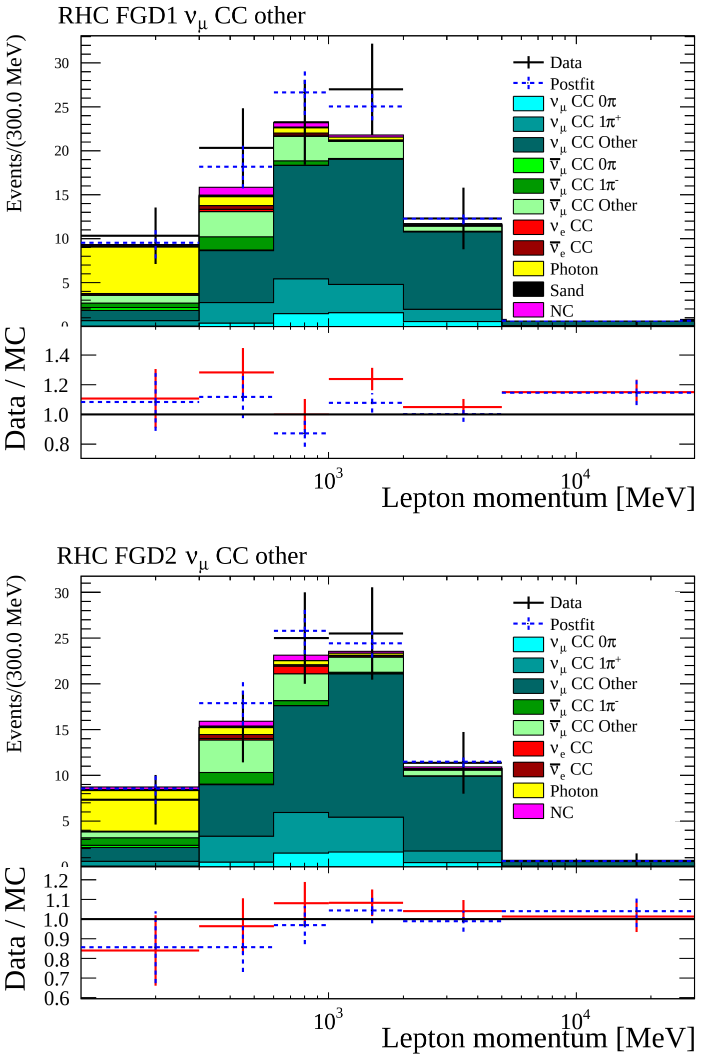

Figure 8.28: One-dimensional projections of the lepton momentum of the RHC ν_μ CC other FGD1 and 2 samples before (stack) and after (blue dotted) a fit over the data from the ND280 selections. ***Top:*** FGD1. ***Bottom:*** FGD2. The bottom pads on each figure show the data / MC ratio before (red) and after (blue dotted) the data fit.

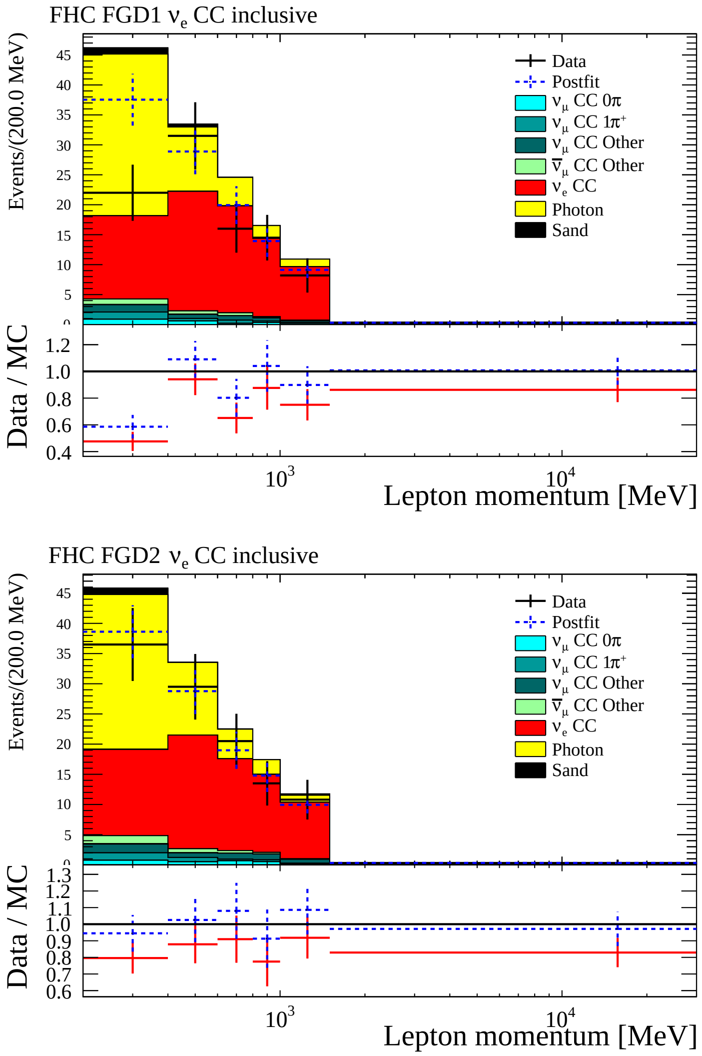

Figure 8.29: One-dimensional projections of the lepton momentum of the FHC ν_e CC inclusive FGD1 and 2 samples before (stack) and after (blue dotted) a fit over the data from the ND280 selections. ***Top:*** FGD1. ***Bottom:*** FGD2. The bottom pads on each figure show the data / MC ratio before (red) and after (blue dotted) the data fit.

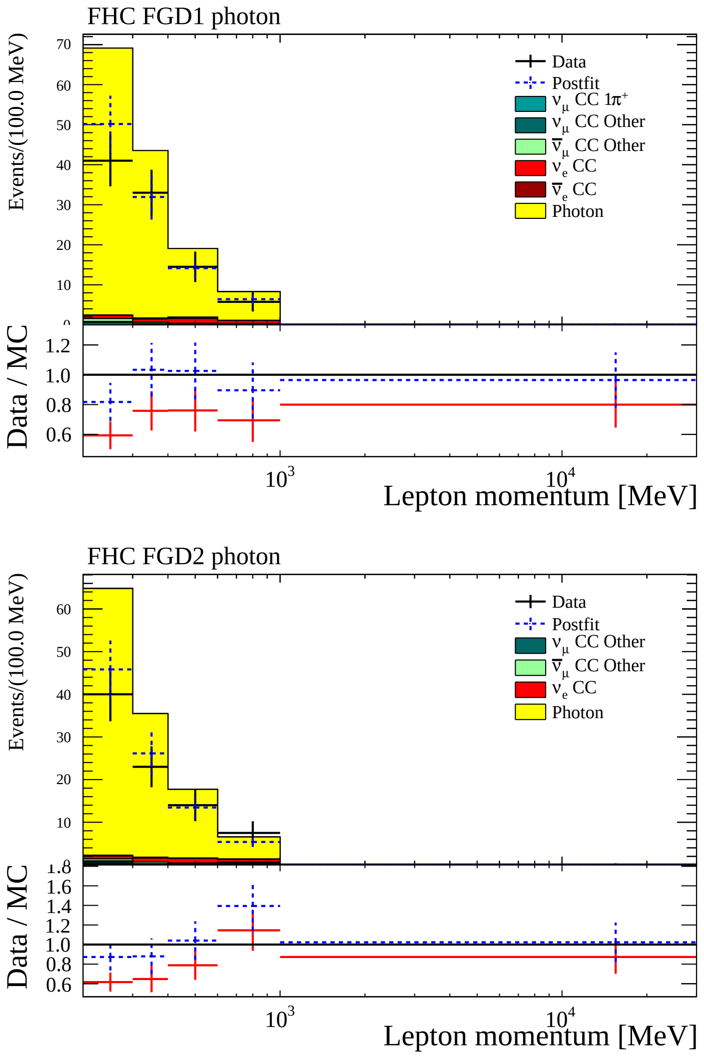

Figure 8.30: One-dimensional projections of the lepton momentum of the FHC photon FGD1 and 2 samples before (stack) and after (blue dotted) a fit over the data from the ND280 selections. ***Top:*** FGD1. ***Bottom:*** FGD2. The bottom pads on each figure show the data / MC ratio before (red) and after (blue dotted) the data fit.

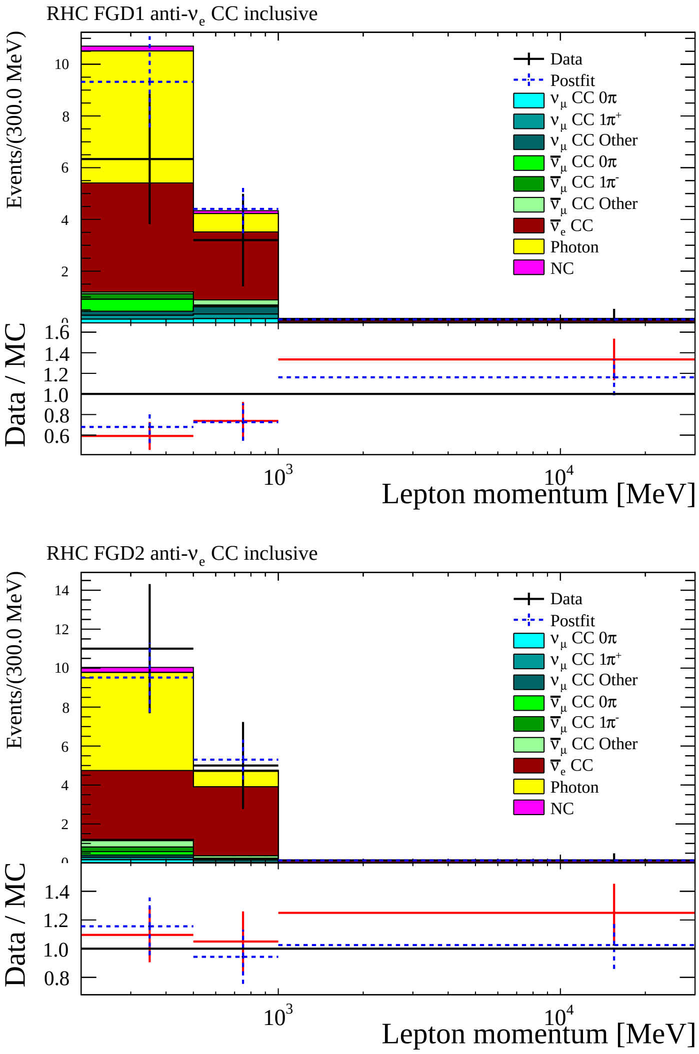

Figure 8.31: One-dimensional projections of the lepton momentum of the RHC $\bar{\nu}_e$ CC inclusive FGD1 and 2 samples before (stack) and after (blue dotted) a fit over the data from the ND280 selections. ***Top:*** FGD1. ***Bottom:*** FGD2. The bottom pads on each figure show the data / MC ratio before (red) and after (blue dotted) the data fit.

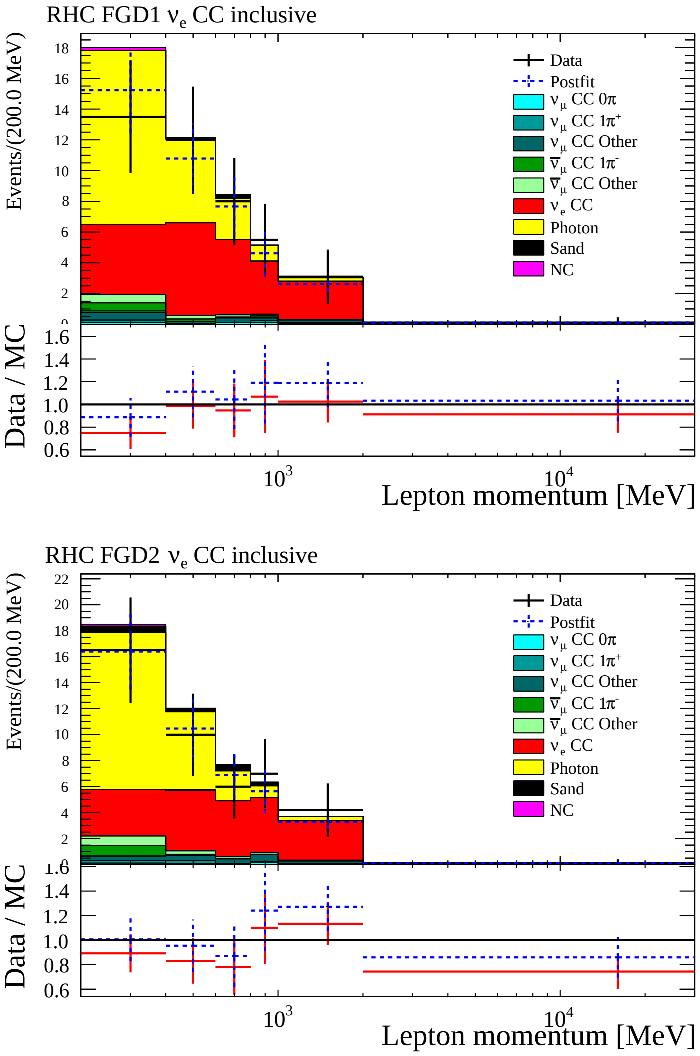

Figure 8.32: One-dimensional projections of the lepton momentum of the RHC ν_e CC inclusive FGD1 and 2 samples before (stack) and after (blue dotted) a fit over the data from the ND280 selections. ***Top:*** FGD1. ***Bottom:*** FGD2. The bottom pads on each figure show the data / MC ratio before (red) and after (blue dotted) the data fit.

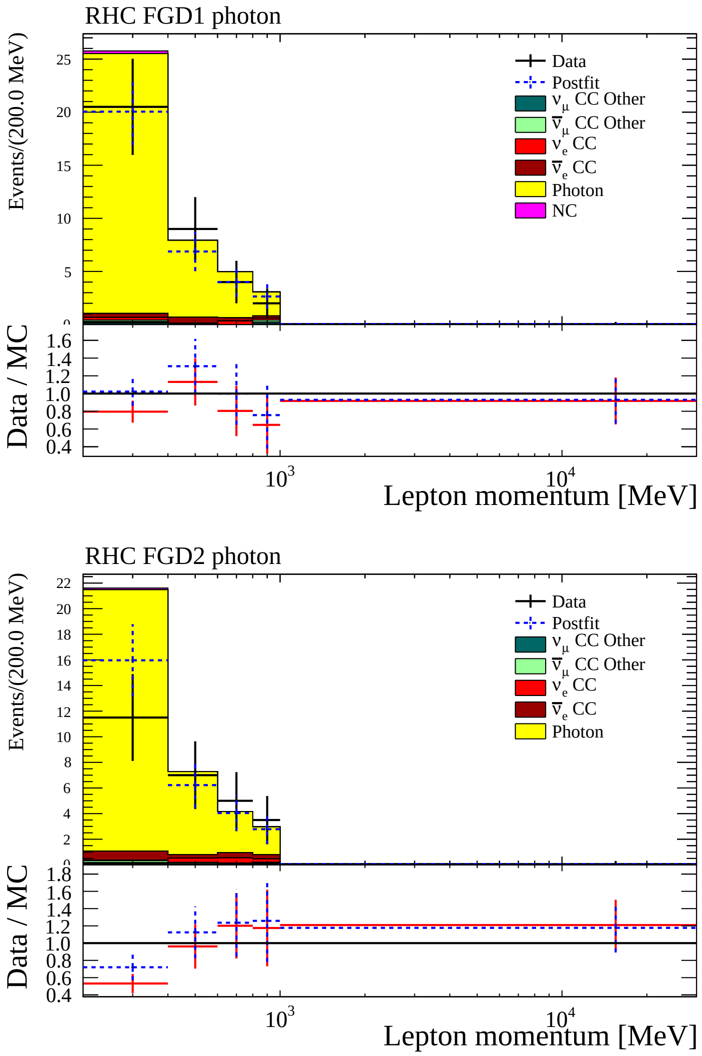

Figure 8.33: One-dimensional projections of the lepton momentum of the RHC photon FGD1 and 2 samples before (stack) and after (blue dotted) a fit over the data from the ND280 selections. ***Top:*** FGD1. ***Bottom:*** FGD2. The bottom pads on each figure show the data / MC ratio before (red) and after (blue dotted) the data fit.

8.8.2 Fitted systematic uncertainties

For the parameters after the data fit, it should be first noted in Figure 8.34 that there is an overall decrease in the flux. The flux is very correlated, therefore it is not very surprising to see group effects of this sort. Note that the high energy $\bar{\nu}_e$ parameter, (the only parameter in Figure 8.34 which is pulled higher than its prefit value), is predominantly governed by the kaon flux, which is somewhat decorrelated from the bulk of the flux (which comes from pion and muon).

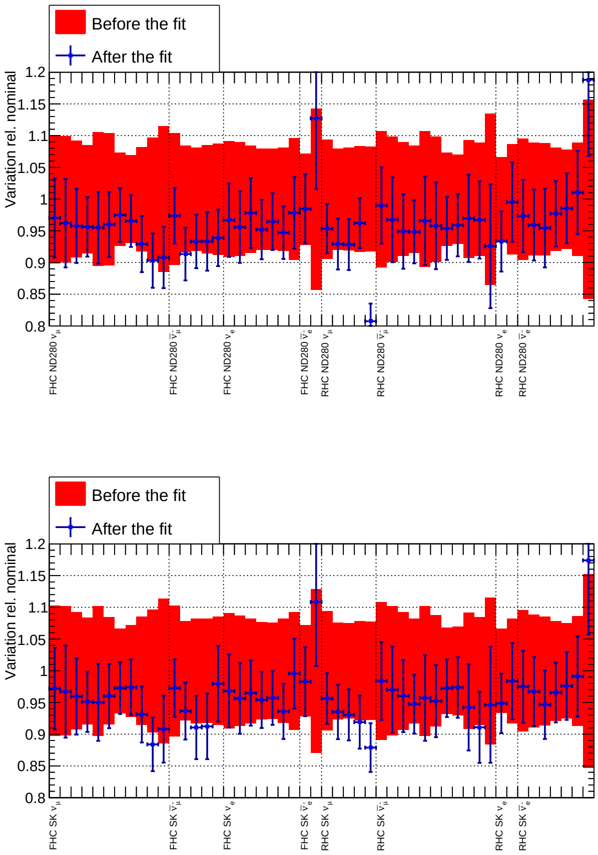

Figure 8.34: Flux uncertainties before (red) and after (blue) a fit over the data from the ND280 selections. ***Top:*** ND280 flux. ***Bottom:*** SK flux.

Other interesting features can be seen in the Figure 8.35 and Table 8.6[1], which show

---

[1] Note that the equivalent table for the flux can be found in Apprendix E

the value of the fitted cross section parameters. The most important is the 2p2h-shape for carbon which reaches the limit of its allowed value (which should be in the range 0 to 2). This is not a new feature [180] and was already observed for previous fits which were not using the ν_e samples and and the multi-track samples in RHC, unlike the previous time this is only visible for the carbon parameter. Previously, this behaviour had been seen for the oxygen counterpart as well. The 2p2h normalisation is also pulled away from its prefit value in the case of anti-neutrino. This considered as acceptable since the ratio of normalisation between 2p2h neutrinos and anti-neutrinos is not well known, which differs between models [45–48].

Although within their acceptable prefit errors, it seems that the Fermi momentum parameters are also reaching their lower limit values (186 MeV and 194 MeV for carbon and oxygen, respectively).

The addition of data corresponding to the run 8 for the ν_μ selections is confirming that there is a major deficiency of our modelling for these cross sections. Similarly, the BeRPA$_B$ gets pulled far away from its prior value. This, again, highlights that the Q^2 parametrisation that is used cannot reproduce the observed data.

The ν_e and $\bar{\nu}_e$ parameters are pulled away from the nominal value, however they have at this stage a too large uncertainty to claim a mismodelling in this sector.

The isoscalar background parameter is also pulled away, which is due to the addition of samples more sensitive to anti-neutrino, however this is also not a new feature of the data [180].

Finally, the only other parameter which is pulled away from its nominal value is the DIS parameter. Again this is not new, but the effect is increased by the fact that the selections are more sensitive than before to a mismodelling in the DIS sector because the RHC selections are now using the multi-pion selections, and the increase in the statistical power due to the addition of the run 8 data.

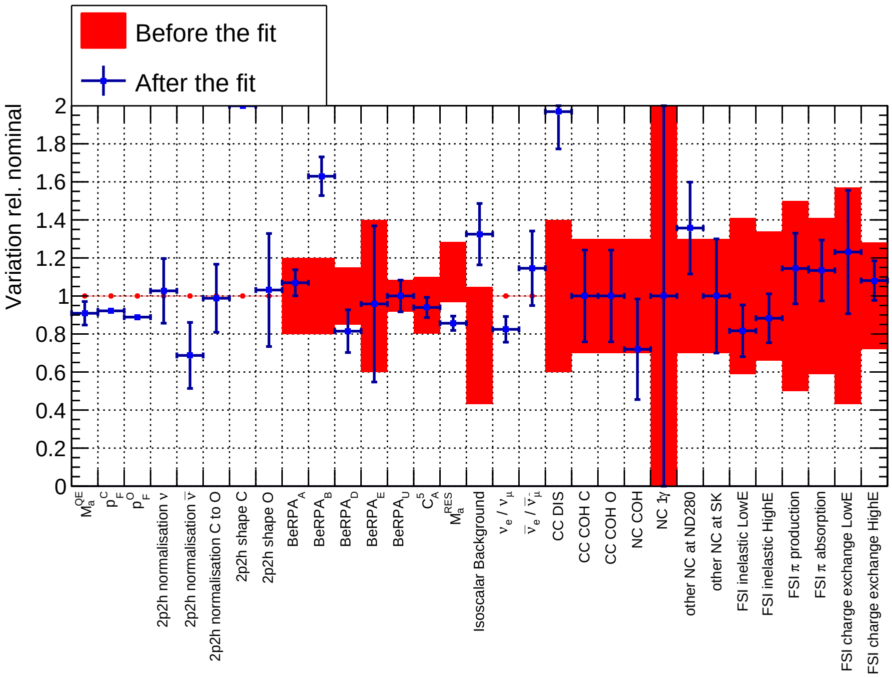

Figure 8.35: Cross section uncertainties before (red) and after (blue) a fit over the data from the ND280 selections.

Parameter	Prefit	Asimov fit	Data fit
$M_a^{\mathrm{QE}}(\mathrm{GeV/c^2})$	1.2	1.2 ± 0.063	1.09 ± 0.07
$p_F^C(\mathrm{MeV/c})$	217.0	217.0 ± 25	200.0 ± 0.02
$p_F^O(\mathrm{MeV/c})$	225.0	225.0 ± 35	200.0 ± 0.04
2p2h normalisation ν	1.0 ± 1.0	1.0 ± 0.19	1.03 ± 0.17
2p2h normalisation $\bar{\nu}$	1.0 ± 1.0	1.0 ± 0.3	0.69 ± 0.17
2p2h normalisation C to O	1.0 ± 0.2	1.0 ± 0.18	0.99 ± 0.18
2p2h shape C	100 ± 300	100 ± 33	200 ± 0.5
2p2h shape O	100 ± 300	100 ± 57	103 ± 29
BeRPA_A	0.59 ± 0.12	0.59 ± 0.08	0.63 ± 0.04
BeRPA_B	1.1 ± 0.2	1.05 ± 0.10	1.71 ± 0.11
BeRPA_D	1.13 ± 0.17	1.13 ± 0.11	0.92 ± 0.13
BeRPA_E	0.9 ± 0.4	0.88 ± 0.35	0.8 ± 0.4
BeRPA_U	1.2 ± 0.1	1.2 ± 0.1	1.2 ± 0.1
C_a^5	0.96 ± 0.15	0.96 ± 0.06	0.95 ± 0.05
$M_a^{\mathrm{RES}}(\mathrm{GeV/c^2})$	1.07 ± 0.15	1.07 ± 0.04	0.81 ± 0.04
Isoscalar Background	0.96 ± 0.4	0.96 ± 0.3	1.7 ± 0.2
ν_e/ν_μ	1.0 ± 1.4	1.0 ± 0.08	0.82 ± 0.07
$\bar{\nu}_e/\bar{\nu}_\mu$	1.0 ± 1.4	1.0 ± 0.19	1.1 ± 0.2
CC DIS	0.0 ± 0.4	0.0 ± 0.17	0.9 ± 0.2
CC COH C	1.0 ± 0.3	1.0 ± 0.2	1.0 ± 0.2
CC COH O	1.0 ± 0.3	1.0 ± 0.2	1.0 ± 0.2
NC COH	1.0 ± 0.3	1.0 ± 0.3	0.7 ± 0.3
NCγ	1.0 ± 1.0	1.0 ± 1.0	1.0 ± 1.0
other NC at ND280	1.0 ± 0.3	1.0 ± 0.2	1.3 ± 0.2
other NC at SK	1.0 ± 0.3	1.0 ± 0.3	1.0 ± 0.3
FSI Inelastic LowE	0.0 ± 0.4	0.0 ± 0.13	-0.18 ± 0.14
FSI Inelastic HighE	0.0 ± 0.3	0.0 ± 0.16	-0.11 ± 0.13
FSI π production	0.0 ± 0.5	0.0 ± 0.23	0.14 ± 0.19
FSI π absorption	0.0 ± 0.4	0.0 ± 0.18	0.13 ± 0.16
FSI Charge exchange LowE	0.0 ± 0.6	0.0 ± 0.3	0.2 ± 0.3
FSI Charge exchange HighE	0.0 ± 0.3	0.0 ± 0.13	0.08 ± 0.10

Table 8.6: Cross section parameters values and uncertainties before and after an Asimov fit and a data fit.

Figures 8.36 and 8.37 shows an interesting feature. At high angle in the CC0 pion sector, the detector and 1p1h parameters are pulled to low value (indicating that the MC was overpredicting the data) and this tendancy is inverted at high momentum. This probably indicates a problem in the 1p1h error, however the fact that these parameters affect directly the bin normalisation of the bin, it is hard to draw any conclusion. However, since this is the part of the model that is not propagated, this is somehow a smaller problem. Similar features have been observed previously [180].

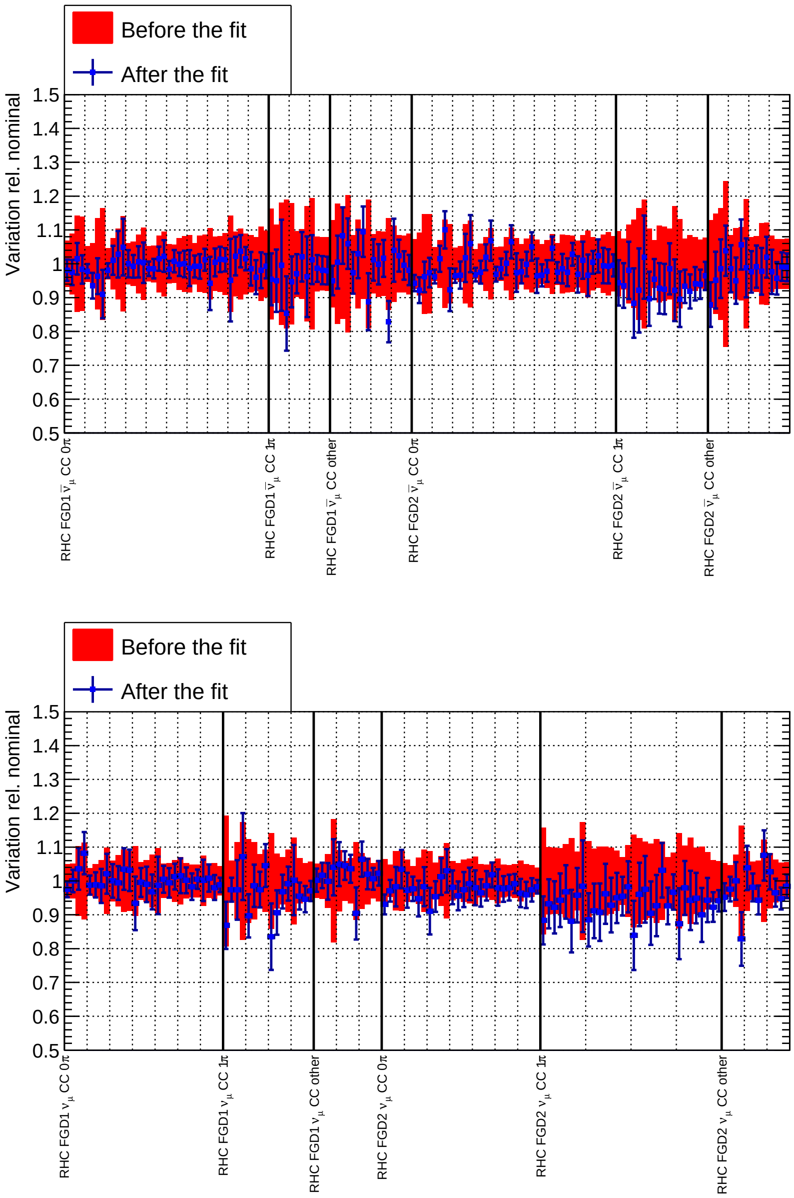

Figure 8.36: ND280 detector and 1p1h uncertainties before (red) and after (blue) a fit over the data from the ND280 selections. The dotted lines are the edges of the $\cos(\theta_{\text{lepton}})$ bins (left to right for increasing $\cos(\theta_{\text{lepton}})$ bins). ***Top:*** FHC FGD1 ν_μ CC selections. ***Bottom:*** FHC FGD2 ν_μ CC selections.

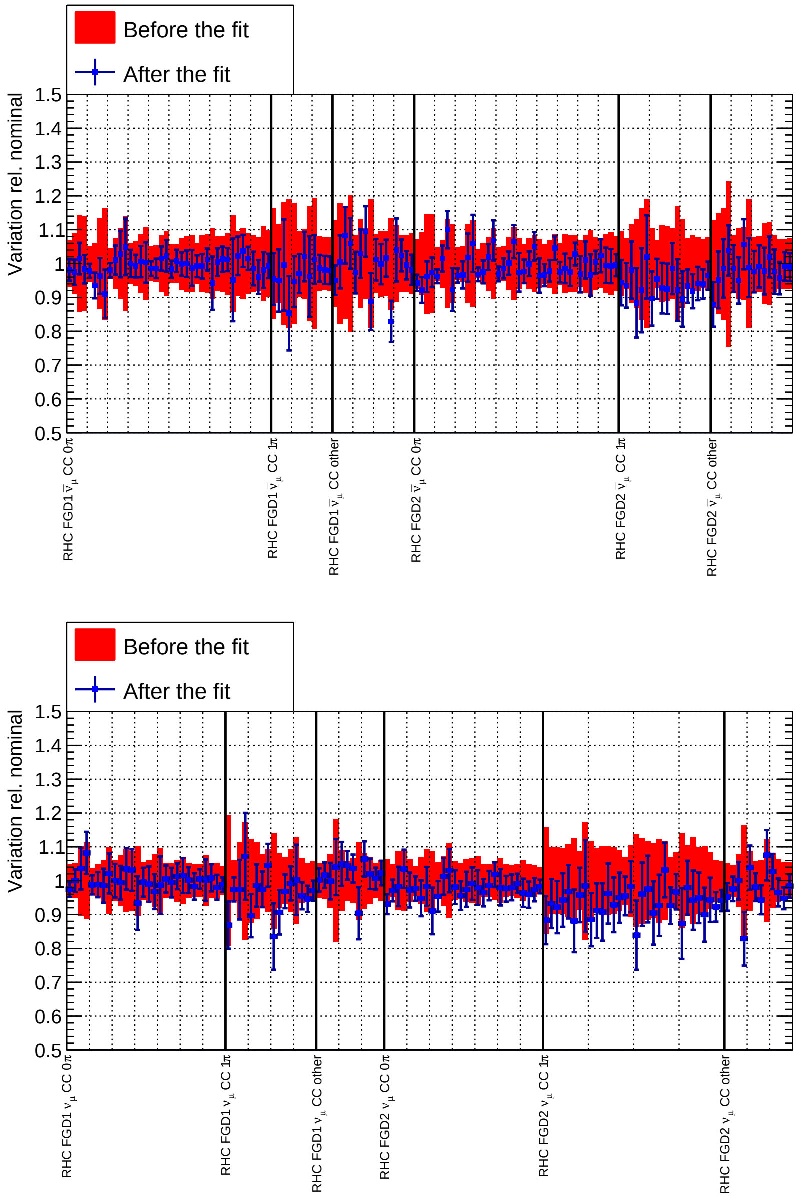

Figure 8.37: ND280 detector and 1p1h uncertainties before (red) and after (blue) a fit over the data from the ND280 selections. The dotted lines are the edges of the $\cos(\theta_{\mathrm{lepton}})$ bins (left to right for increasing $\cos(\theta_{\mathrm{lepton}})$ bins). ***Top:*** RHC FGD1/2 $\bar{\nu}_\mu$ CC selections. ***Bottom:*** RHC FGD1/2 ν_μ CC selections.

The top of Figure 8.39 and the strong anti-correlation between the BeRPA$_D$ parameter and the axial mass (M_a^{QE}) indicate an unexpected behaviour at high Q^2 for the CCQE events. This could either be related to the 2p2h parametrisation (for example if it does not fill some regions of the parameter space, then the BeRPA parameters could be used to fill the missing events), or, alternatively, this could relate to problem in the CCQE form factor (it could be that the dipole parametrisation, in Equation (1.24), is not an appropriate choice).

In any case, it is very likely that a p_{value} calculation (after throwing toy experiments) would be very low, however the fit seems to perform better than the ones used for previous analyses [180], with clearer but localised deficiencies in the models. This is due to the better statistics and to the better discriminating power in RHC with the multi-pion samples.

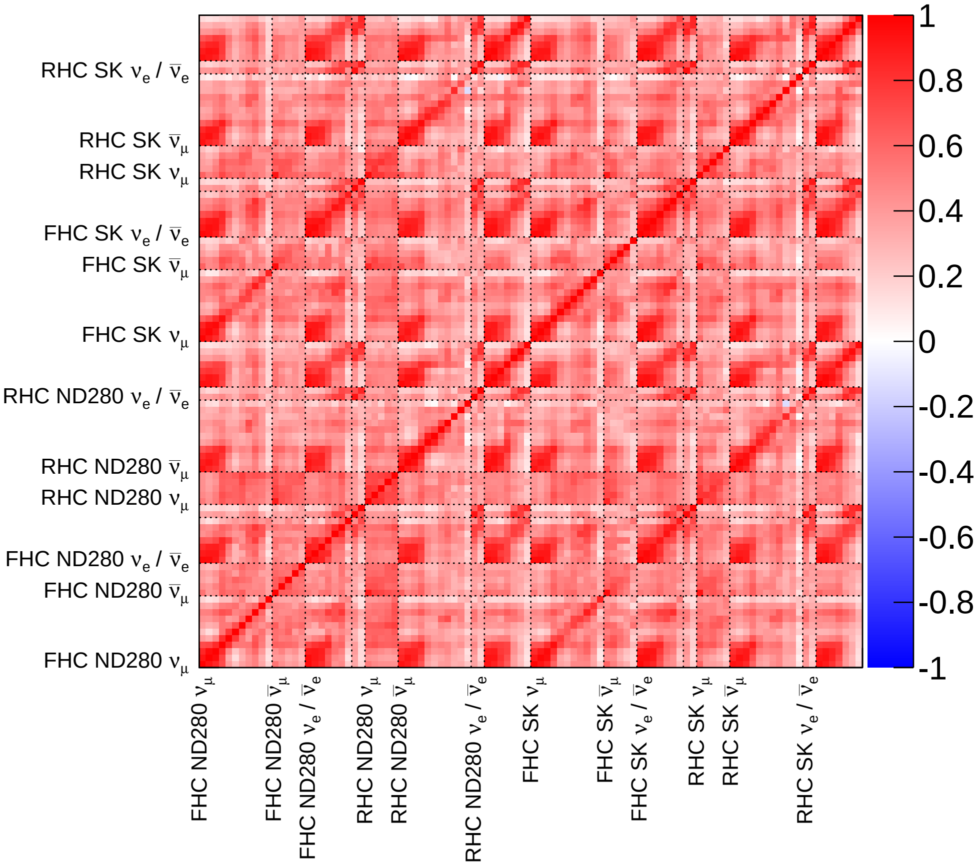

Figure 8.38: Zoom of Figure 8.16, correlation of the flux parameters used for oscillation analyses after a fit to the data of the ND280 selection.

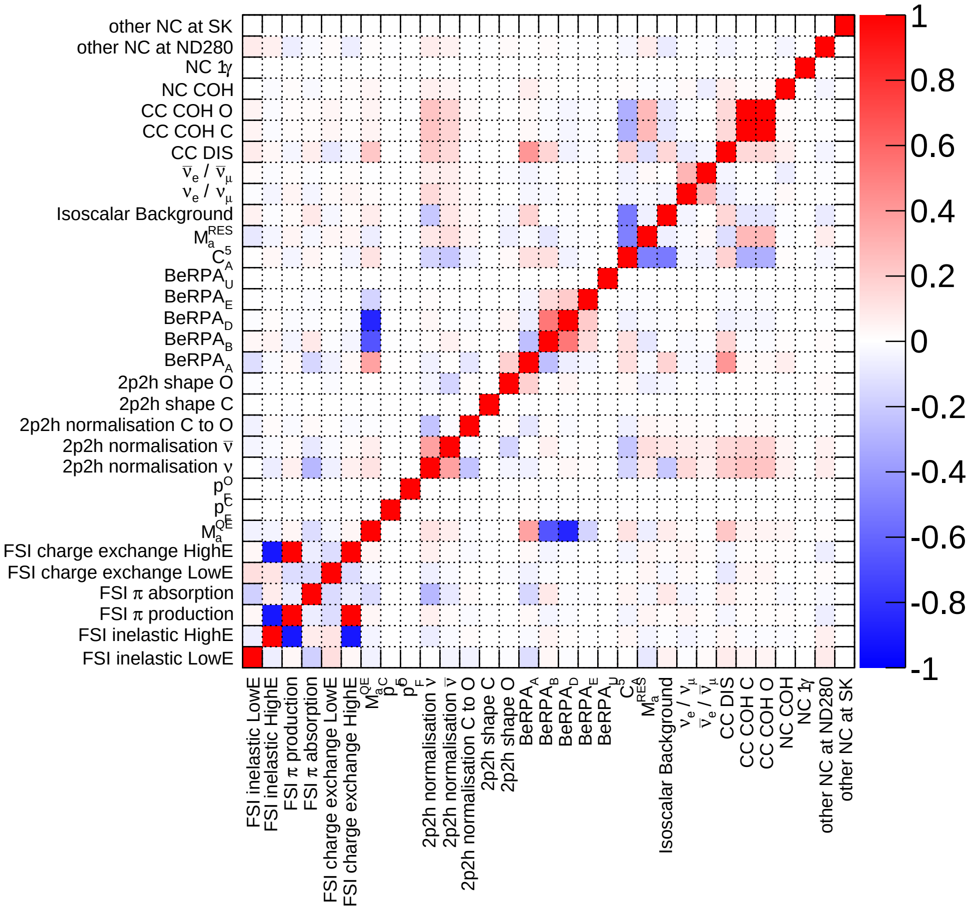

Figure 8.39: Zoom of Figure 8.16, correlation of the cross section parameters used for oscillation analyses after a fit to the data of the ND280 selection.

8.9 Discussion and future

In this section, the errors in the Asimov fit described in Section 8.7 are propagated to the following SK Asimov data set:

- FHC muon one ring,
- RHC muon one ring,
- FHC electron one ring,
- RHC electron one ring,
- RHC electron one ring + one Michel electron.

These samples are sensitive to oscillation parameters, so to construct this Asimov data sets, the values in Table 8.7 were used. These oscillation parameters have values close to the best fit point from T2K: with maximum oscillation in the disappearance sector ($\sin(\theta_{32})$ close to 0.5), CP at $-\pi/2$ and with "the reactor constraint," which means that the Daya Bay, Double Chooz and Reno $\bar{\nu}_e$ disappearance results are used to estimate θ_{13}, to fit the oscillation parameters.

Parameter	Value
$\sin(2\theta_{13})$	0.0857
δ_{CP}	-1.601
Δm^2_{32}	2.509^{-3} eV^2
$\sin(\theta_{23})$	0.528

Table 8.7: Values of the oscillation parameters used for the T2K δ_{CP} sensitivity comparison.

The result of the fit and comparisons with the previous similar fit using the Asimov result of the BANFF are shown in Figure 8.40. The plots show the one and two dimensional $-2\log(\text{likelihood})$ in the appearance sector (δ_{CP} and $\sin(2\theta_{13})$), after marginaling over all the unseen oscillation parameters (which explains why the 68% contour from the top figure does not correspond to the $-2\log(\text{likelihood}) = 1$ at the bottom). Note that these plots were produced by Simon Bienstock.

The major difference here between the red and black curves are the electron neutrino cross section errors. In the case of the black curves, the error relies uniquely on the assumed 3% uncertainty and 50% correlations between neutrinos and anti-neutrinos cross sections as explained in Section 8.5.2; whereas for the red curves, the same error come from the ND280 constraints.

As expected, the combined effect of releasing the ν_e/ν_μ error and using the ND280 to fit them brings the T2K sensitivity down. Note however that the effect is somehow not as drastic as one would have expected. This is probably due to the additionnal prefit (post BANFF) anti-correlations between the background ν_e flux and the cross section errors. Since the ν_e samples error is predominantly statistical it is important to check the same quantities after the run 8 has been calibrated and the ν_e have a smaller statistical error.

Therefore, the electron neutrino samples have a somewhat small impact on the cross section systematic uncertainties compared to the assumed error, and this could have effects in the observed sensitivity to the δ_{CP} sensitivity. It is expected that further improvements on the selections may lead to more stringent constraints on these parameters. Unfortunately, the main problem in constraining the electron neutrino cross section stems from a complex photon background present in the selections.

Similarly, the data fit shows some strange behaviours in the CCQE and 2p2h parameters sector, which highlights some of the deficiencies in the models used.

Note, however, that is still difficult to draw any conclusion without a complete $\Delta\chi^2$ analysis where toys are thrown. This allows a p_{value} calculation.

In a standard T2K analysis, the next step is to perform "fake data studies," which consists in realising fits such as the one described previously in Section 8.7, but changing the Asimov predictions to be a variations of the underlying cross section models. For example, rather than using the baseline Nieves et al. model [40] for 2p2h events, one can use the Martini et al. model [45, 46] and build a fake data to check how the fitted parameters would respond to a change in the model and how robust the parametrisation is.

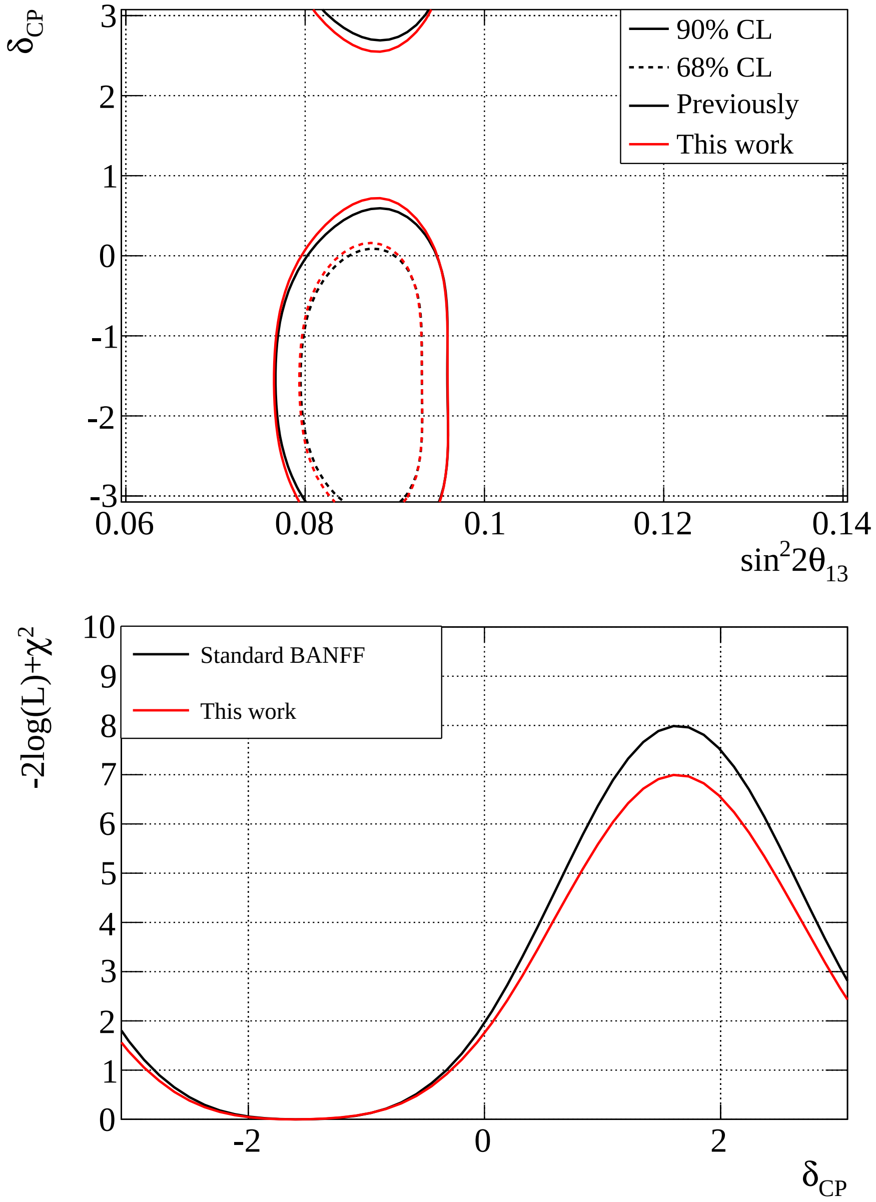

Figure 8.40: Sensitivities comparison for T2K $\delta_{\rm CP}$ and $\sin(2\theta_{13})$ with (red) and without (black) the ND280 electron neutrino samples. ***Top:*** Two-dimensional $-2\log(\text{likelihood})$ ($\delta_{\rm CP}$ and $\sin(2\theta_{13})$). ***Bottom:*** one-dimensional $-2\log(\text{likelihood})$ $\delta_{\rm CP}$. Both figures were made by Simon Bienstock.

8.10 Summary

In this chapter, it was demonstrated that it is possible to better use the ND280 and increase its the sensitivity to the cross section and flux models used in the oscillation analyses at T2K. To achieve this, new samples were used in the BANFF fit to the systematic uncertainties:

- Electron neutrinos in FHC
- Photon background in FHC
- Electron neutrinos in RHC
- Electron anti-neutrinos in RHC
- Photon background in RHC
- Muon anti-neutrinos CC 0 pion in RHC
- Muon anti-neutrinos CC 1 pion in RHC
- Muon anti-neutrinos CC other in RHC
- Muon neutrinos CC 0 pion in RHC
- Muon neutrinos CC 1 pion in RHC
- Muon neutrinos CC other in RHC

These samples use both the FGD1 and 2, and are therefore sensitive to carbon and oxygen interactions.

The outcome is that, compared to the version of the BANFF fit which was not using these samples, one gets a similar sensitivity of T2K to CP violation in the neutrino sector. Additionally, the ND280 BANFF fit is now more sensitive to the flux and cross section models and can better discriminate any mismodelling, and thus would increase the robustness of the result in CP violation. Finally, the inclusion of the electron (anti-) neutrino samples and the accumulation of the ND280 data reduces the statistical uncertainty on these samples. It is the only viable option to decrease the electron (anti-) neutrino cross section uncertainty other than a direct measurement of the electron (anti-) neutrino cross section.

Conclusion

This thesis aimed at addressing some of the challenges that are still at stake for a measurement of the CP violating phase using neutrino oscillations. The NCγ cross section is already one the largest unknown in the measurement of the appearance signal at the far detector.

The search for NCγ leads to a limit of $0.0903 \times 10^{-38}\text{cm}^2/\text{nucleon}$ at 90% CL for these processes on carbon. At the time this conclusion was written, the NCγ was already the biggest cross section error for the electron sample in RHC at SK. Of course, the poor statistical power of this sample and the SK detector uncertainties are still, by far, the main uncertainties, but both of these are expected to improve in the future. Within the current paradigm for the next generation of near detectors, it should be feared that nobody will be able to measure this cross section on a light isoscalar target in time to be able to characterise this process in time for HK, and certainly not using the T2K flux.

Similarly, the electron neutrino cross section is a fundamental input for a CP violation measurement in the neutrino sector. To date, there is no published, exclusive measurement of the anti-electron cross section and the electron neutrino equivalents suffers poor statistics and unexplained (or uncontrolled) backgrounds. There is currently no other constraints used in the T2K oscillation analyses than a flat constrain on the electron (anti-) neutrino, which is still very far from reach experimentally.

Both of these issues described in this thesis are complicated experimental problems. It seems that the way of appropriately dealing with this problem is to use a large homogeneous detector that can efficiently reject external photons and differentiate them from single electrons. This probably requires a large and heavy scintillator target with a small granularity, submerged in a magnetic field and exposed to the T2K off-axis flux.

Appendix A

Out of Fiducial Volume Photon studies

In Section 5.3.2, there is a discussion about photons from OOFV and a description of a set of rather strict vetoes is made. In this appendix, the importance of these vetoes is highlighted by showing the two-dimensional true positions of the neutrino vertices for the true OOFV events before and after the vetoes. This is in Figure A.1 and in Figure A.2, respectively. For help, the same distributions for the true FV FGD1 vertices is shown in Figure A.3.

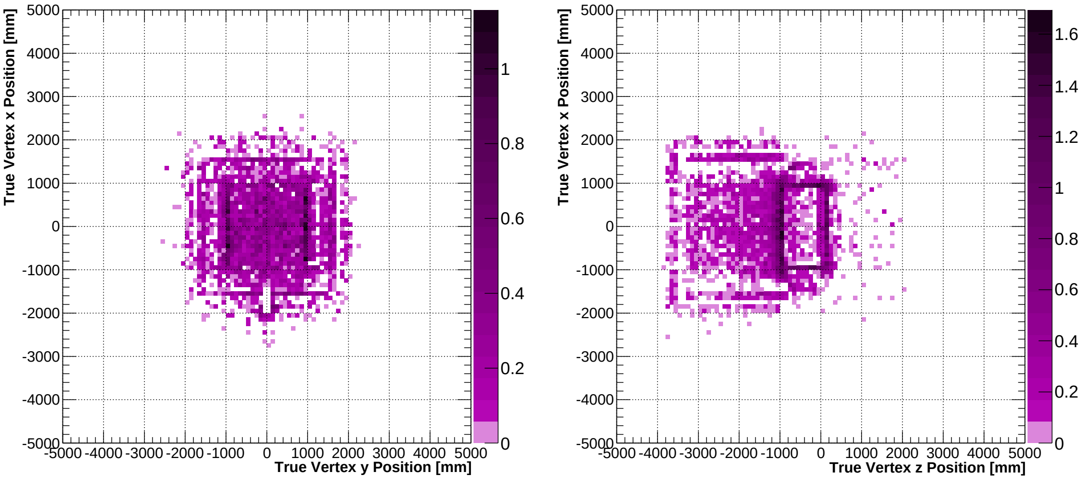

Figure A.1: True positions of the true OOFV events before the vetoes (after the invariant mass cut). ***Left:*** XY projection. ***Right:*** XZ projection.

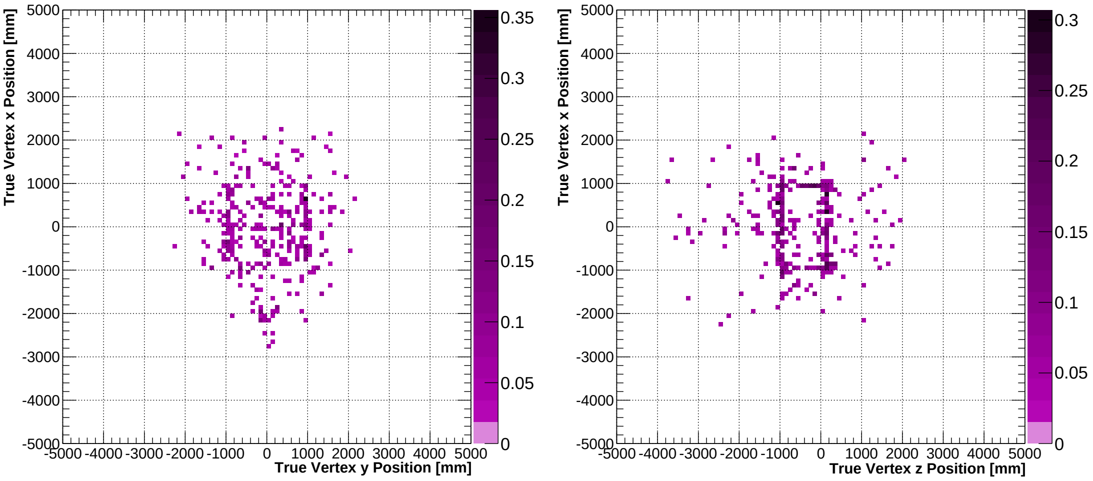

Figure A.2: True positions of the true OOFV events after the vetoes (ECal veto). ***Left:*** XY projection. ***Right:*** XZ projection.

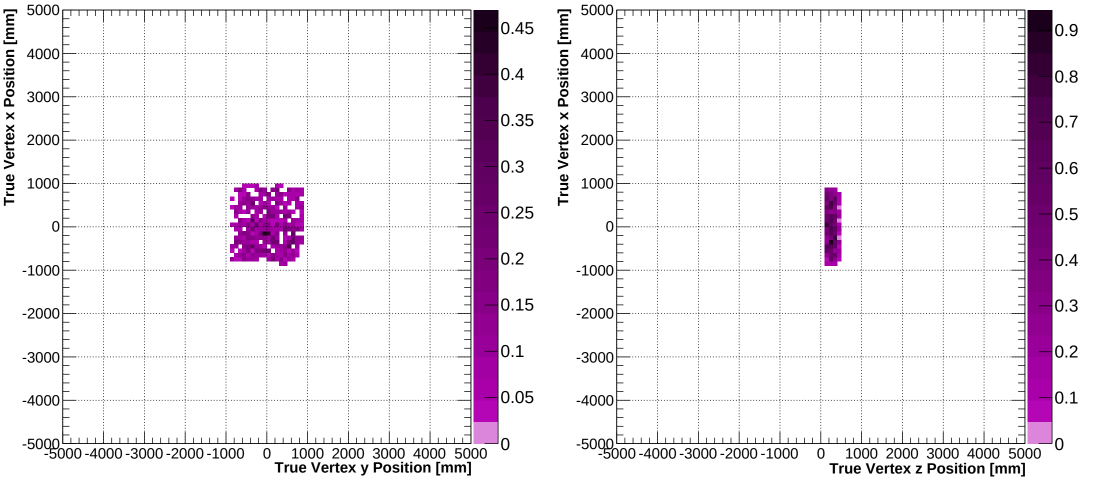

Figure A.3: True positions of the true FGD1 FV events after the vetoes (ECal veto). ***Left:*** XY projection. ***Right:*** XZ projection.

Appendix B

Systematic error on the mass of the detectors

In this appendix, the errors on the mass of each detector is detailed. The P0D, ECal and FGD mass uncertainties are reported, as well as the errors for those events which originates from the other regions of the ND280, that are not the FGDs, ECal and P0D. These regions are later called Out Of All Fiducial Volumes (OOAFV).

All these errors are used in Section 6.3.3.5, where the systematic error for the "out of fiducial volume" photons is explained.

The FGD mass uncertainty

The FGD mass uncertainty is known and is 0.6%, see Section 6.3.3.1.

The P0D mass uncertainty

For the P0D mass uncertainty, the error is directly extracted from [183], where the corrections are summed to the errors reported for simplicity. This leads to the mass uncertainties listed on Table B.1. To get the numbers corresponding to the mass proportions for the two configurations (with and without water), the masses of the components reported in [184] were used.

Component	Mass uncertainty	Proportion with water	Proportion without water
Water	2.16 %	22.25 %	0 %
Brass	17.8 %	8.54 %	10.98 %
Lead	2.3 %	21.84 %	28.08 %
Other	0.95 %	47.37 %	60.93 %

Table B.1: P0D components mass uncertainties.

The ECal mass uncertainty

The errors for the masses of the ECal componenent were retrieved from [136], however, rather than computing the covariance matrix between the different components of the ECal, the uncertainties in the dimensions of the different components of the ECal were simply added in quadrature. The uncertainties in the sizes of the holes for the fibre in the scintillators were neglected since they are very small compared to the overall size of the bars. Similarly, the masses of the fibres were neglected. In Table B.2, the uncertainties and proportions of the various components are shown for the BrECal modules (note that the DsECal is irrelevant for this study, since no photon come from the DsECal in the analysis). The relatively large mass uncertainties comes from the fact that the errors on the widths of the scintillator bars are quite large (this also applies for the lead layers).

Bar type	Size and error $[mm]$	#/layer	$\rho[g/cm^3]$	δ mass	Proportion
Top / bottom modules					
Scintillator	$(3840 \pm 0.1) \times (40 \pm 0.4) \times (10 \pm 0.4)$	38	1	4.12 %	24.96 %
Scintillator	$(1520 \pm 0.1) \times (40 \pm 0.4) \times (10 \pm 0.4)$	96	1	4.12 %	24.96 %
Lead	$(3858 \pm 4) \times (765 \pm 4) \times (1.75 \pm 0.1)$	2	11.34	5.74 %	50.08 %
Total				4.93 %	100 %
Left / right modules					
Scintillator	$(3840 \pm 0.1) \times (40 \pm 0.4) \times (10 \pm 0.4)$	57	1	4.12 %	24.77 %
Scintillator	$(2280 \pm 0.1) \times (40 \pm 0.4) \times (10 \pm 0.4)$	96	1	4.12 %	24.77 %
Lead	$(964.5 \pm 4) \times (2330 \pm 4) \times (1.75 \pm 0.1)$	4	11.34	5.73 %	50.46 %
Total				4.93 %	100 %

Table B.2: BrECal bars masses and uncertainties.

The OOAFV mass uncertainties

Each detector in the ND280 has a mass uncertainty, however it is not trivial to estimate the errors on the masses of the dead materials in the ND280. For that, a control sample was constructed with the aim of uncovering possible errors in mass modelling at the ND280.

A CC inclusive selection was performed on the edges of the FGD1. The selection is briefly described below:

- The track is required to have more than 18 nodes in the TPC and to start in the FGD1 detector (note that this does not necessarily have to be in its FV).
- The events were vetoed when activity (one or more reconstructed tracks) was seen in the BrECal, in the P0D and more importantly in the TPC1. The aim of these vetoes is to remove the sand muons and the ECal interactions.
- Next, the events were classified according to whether they would come from the edges of the FGD1 (which are the "signal regions") or inside the fiducial volume of the FGD1 (later used as side-band region).

That way, the selection is dominated by interactions occurring on the edges of the scintillator of FGD1 and in the dead material surrounding it, as illustrated in Figures B.1 and B.2.

Next, the FGD1 FV events were used to reweight the simulation for the events outside the fiducial volume (OOFV). One can then assign the data / MC differences to be due to a mass mis-modelling and assign uncertainties on each component from these differences. This assumes that it is possible to extrapolate the cross sections on elements that are in the support structure from the FGD1 data. [185] shows that the neutrino CCQE cross section implemented in the NEUT generator is not necessarily reproducing well all the nuclear data observed at MINERνA [186]. However this study is beyond the scope of this thesis, so it was assumed that the uncertainties in ratio of the neutrino cross sections between different targets are under control.

Since this is a geometrical effect, the contributions were categorised according to their positions with respect to the FGD1. The categories are bottom, top, back, left and right of the FGD1.

Note that this selection is extremely sensitive to the so-called sand interactions. These events happen outside the ND280, in the sand surrounding it. The reason sand events enter the selection is because the vetoes do not work well for events next to the edges of the FGD1: sand muons come in between the P0DECal and the P0D and do not produce a visible signal in the TPC1.

The results of this study and the mass uncertainties are given in Table B.3. Note the great uncertainty of the $-y$ region: this is because there is a gap in the isolation between the bottom left and right BrECal modules (which is used for cabling). This is probably is not modelled well, therefore one can expect some disagreements here.

Region	Mass uncertainty
$+x$	6.6506 %
$-x$	6.0402 %
$+y$	5.5572 %
$-y$	38.2304 %
$-z$	6.5380 %

Table B.3: The FGD1 surroundings (OOAFV) mass uncertainties.

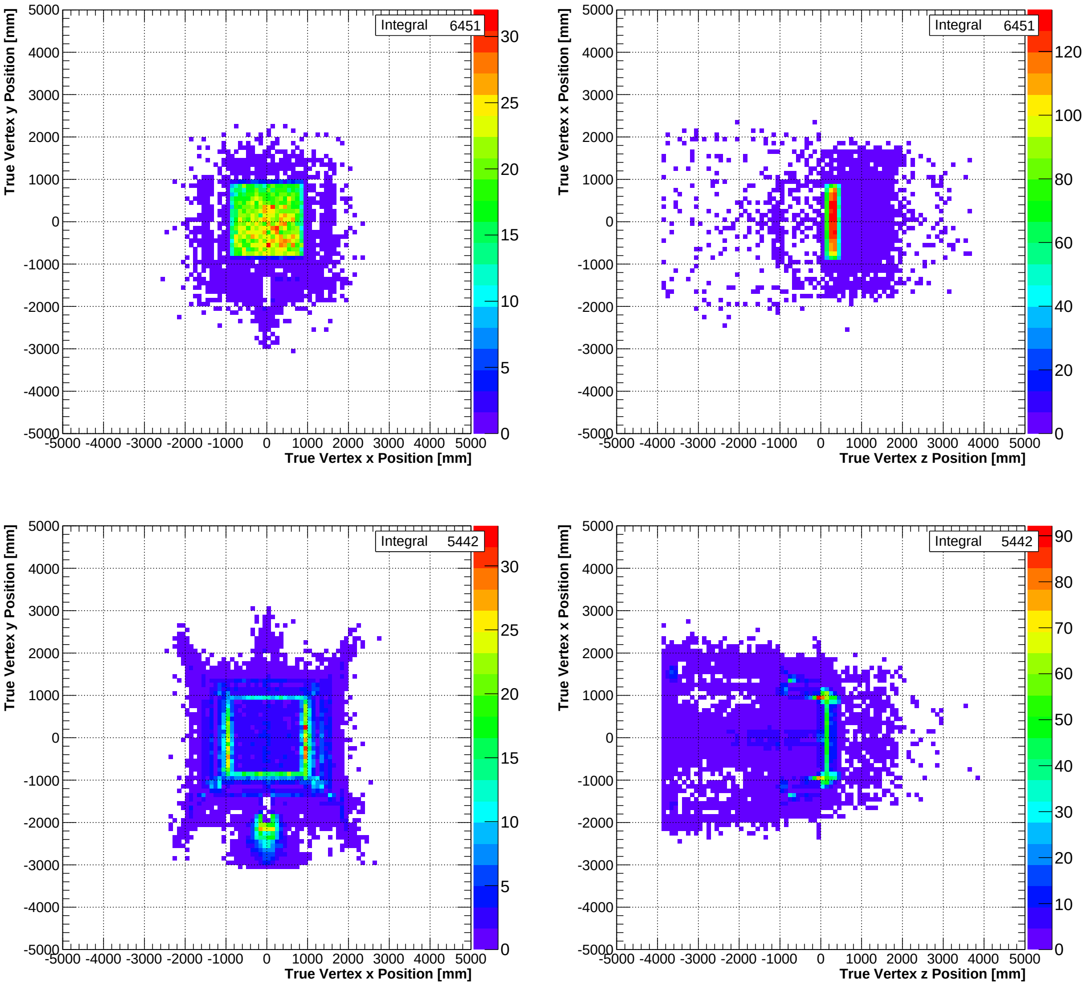

Figure B.1: True positions of vertices for the events selected for the estimation of the OOAFV error. ***Top left:*** Inside the FGD1 FV, XY plane projection. ***Top right:*** Inside the FGD1 FV, XZ plane projection. ***Bottom left:*** Outside the FGD1 FV, XY plane projection. ***Bottom right:*** Outside the FGD1 FV, XZ plane projection.

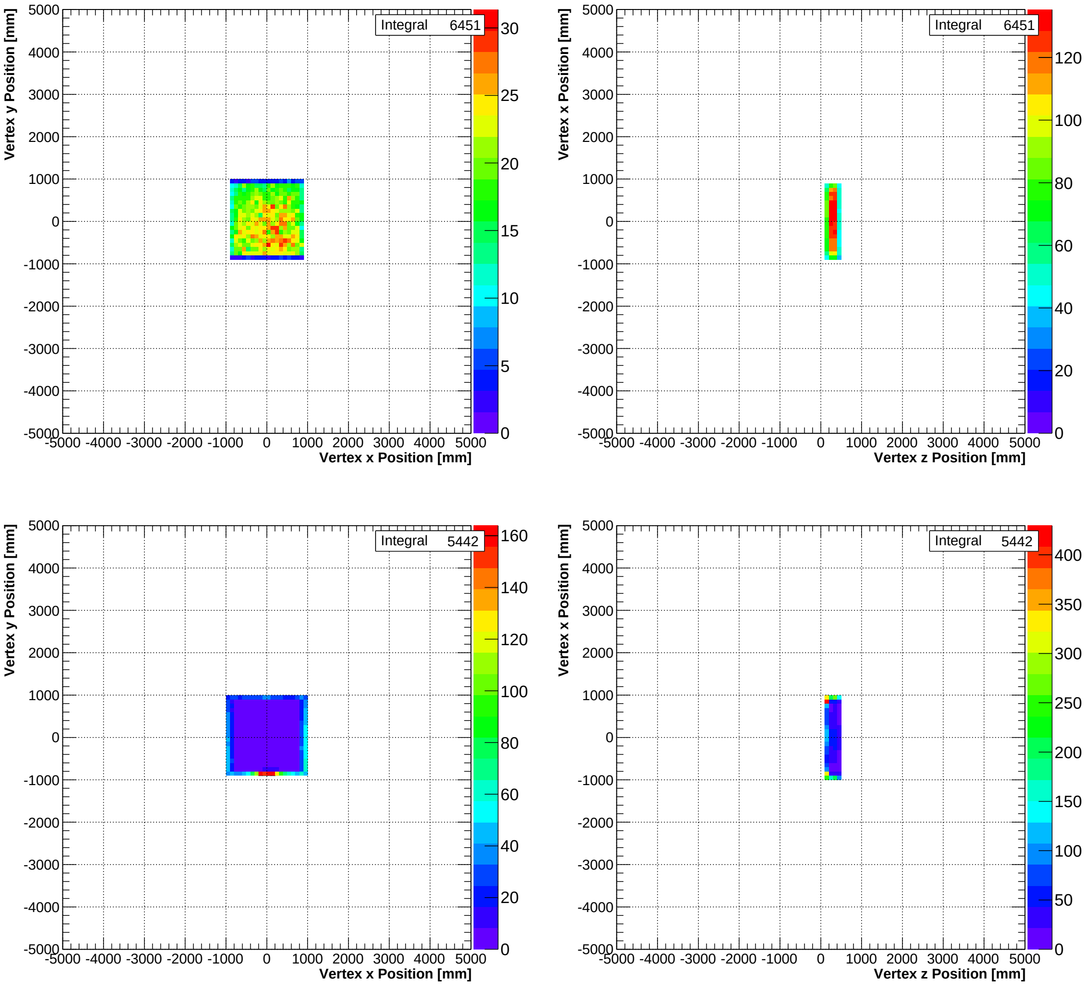

Figure B.2: Same as Figure B.1 for the reconstructed positions of the vertices.

Appendix C

Photon reconstruction capabilities

Although there is no real motivation specific to the NCγ analysis to compute the resolutions, the use of the analysis could go beyond a standard cross section analysis. Namely, computing resolutions allows forward folding, when combined with the efficiency. This would allow folding some more exotic models. In Figure C.1, the electrons / positrons reconstruction capabilities are shown (after the PID cut) for one-dimensional distributions (momentum and $\cos(\theta)$).

Note the bias towards small reconstructed momentum which probably comes from the Bremsstrahlung losses.

Next, the same quantities are computed for photons after the invariant mass cut, in Figure C.2.

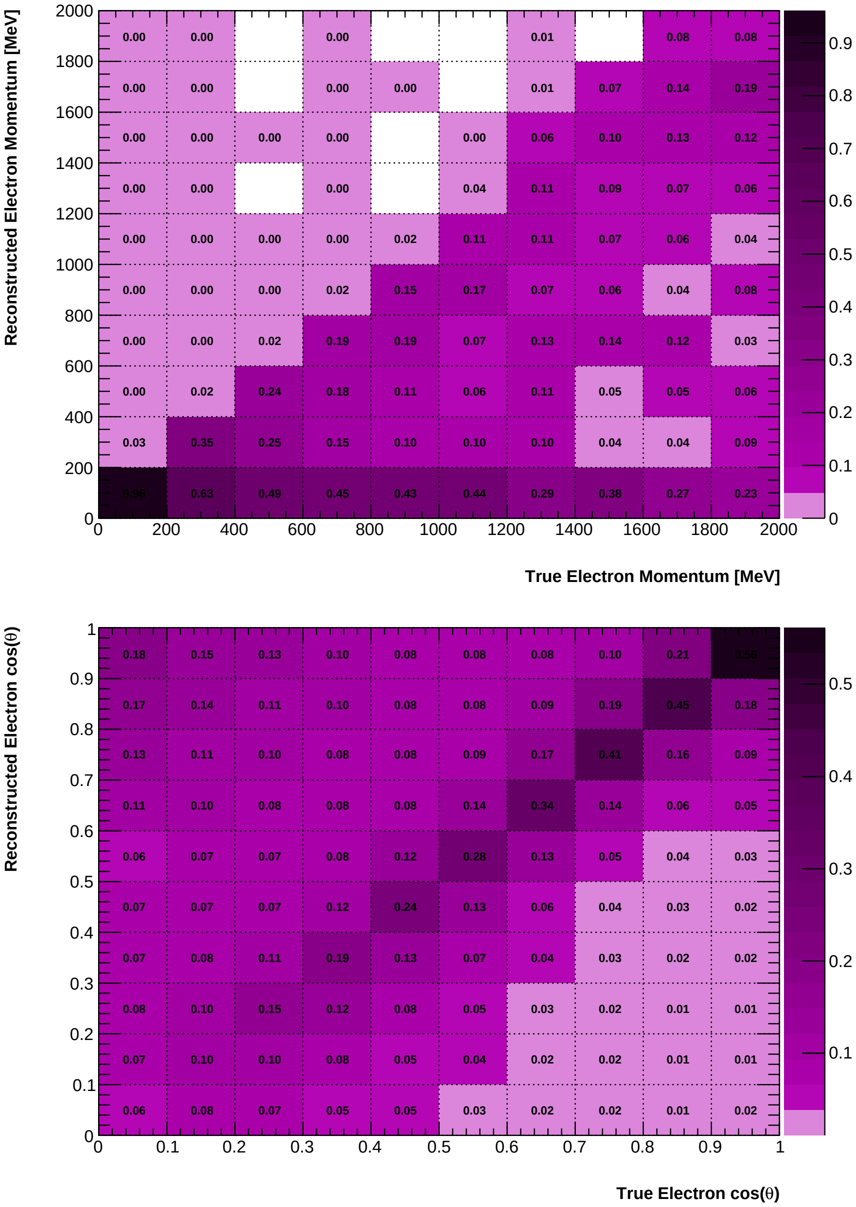

Figure C.1: Electrons / positrons resolutions. ***Top:*** Momentum resolution. ***Bottom:*** Angular resolution.

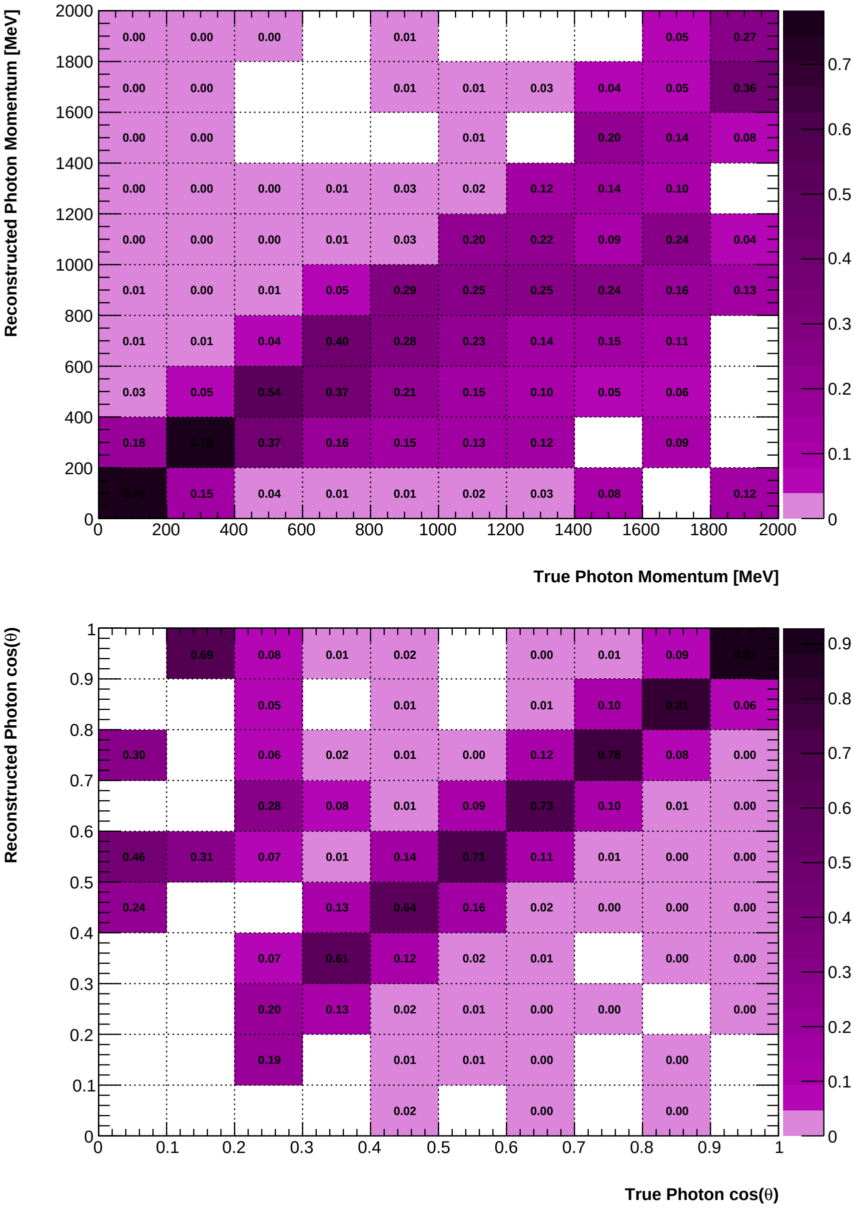

Figure C.2: Same as Figure C.1 for photons.

Appendix D

BANFF binning

In Chapter 8, fits are performed over several samples from the ND280; these samples are binned in two dimensions according to the lepton momentum (p_l, in MeV) and to the cosine of the angle between the directions of the neutrino and the lepton ($\cos(\theta_l)$) . The binnings of the samples are given here in details.

Firstly, the binning used in the fit for the construction of the likelihood is:

- FHC ν_μ CC 0π (FGD1 and 2):
    - p_μ: 14 bins, {0, 300, 400, 500, 600, 700, 800, 900, 1000, 1250, 1500, 2000, 3000, 5000, 30000}
    - $\cos(\theta_\mu)$: 11 bins, {-1, 0.6, 0.7, 0.8, 0.85, 0.9, 0.92, 0.94, 0.96, 0.98, 0.99, 1}
- FHC ν_μ CC 1π (FGD1 and 2):
    - p_μ: 13 bins, {0, 300, 400, 500, 600, 700, 800, 900, 1000, 1250, 1500, 2000, 5000, 30000}
    - $\cos(\theta_\mu)$: 11 bins, {-1, 0.6, 0.7, 0.8, 0.85, 0.9, 0.92, 0.94, 0.96, 0.98, 0.99, 1}
- FHC ν_μ CC other (FGD1 and 2):
    - p_μ: 14 bins, {0, 300, 400, 500, 600, 700, 800, 900, 1000, 1250, 1500, 2000, 3000, 5000, 30000}
    - $\cos(\theta_\mu)$: 11 bins, {-1, 0.6, 0.7, 0.8, 0.85, 0.90, 0.92, 0.94, 0.96, 0.98, 0.99, 1}
- RHC $\bar{\nu}_\mu$ CC 0π (FGD1 and 2):
    - p_μ: 8 bins, {0, 300, 500, 700, 900, 1250, 1500, 2000, 30000}

  - $\cos(\theta_\mu)$: 10 bins, $\{-1, 0.7, 0.8, 0.85, 0.9, 0.94, 0.96, 0.98, 0.99, 0.995, 1\}$

- RHC $\bar{\nu}_\mu$ CC 1π (FGD1 and 2):
  - p_μ: 6 bins, $\{0, 400, 700, 1000, 1500, 2500, 30000\}$
  - $\cos(\theta_\mu)$: 3 bins, $\{-1, 0.8, 0.9, 1\}$

- RHC $\bar{\nu}_\mu$ CC other (FGD1 and 2):
  - p_μ: 8 bins, $\{0, 300, 600, 900, 1200, 1500, 2000, 4000, 30000\}$
  - $\cos(\theta_\mu)$: 4 bins, $\{-1, 0.8, 0.9, 0.95, 1\}$

- RHC ν_μ CC 0π (FGD1 and 2):
  - p_μ: 6 bins, $\{0, 350, 700, 1000, 1500, 2000, 30000\}$
  - $\cos(\theta_\mu)$: 7 bins, $\{-1, 0.85, 0.9, 0.92, 0.94, 0.96, 0.98, 1\}$

- RHC ν_μ CC 1π (FGD1 and 2):
  - p_μ: 8 bins, $\{0, 350, 500, 650, 800, 1000, 1250, 2000, 30000\}$
  - $\cos(\theta_\mu)$: 4 bins, $\{-1, 0.8, 0.9, 0.95, 1\}$

- RHC ν_μ CC other (FGD1 and 2):
  - p_μ: 6 bins, $\{0, 300, 600, 1000, 2000, 5000, 30000\}$
  - $\cos(\theta_\mu)$: 3 bins, $\{-1., 0.9, 0.95, 1\}$

- FHC ν_e CC inclusive (FGD1 and 2):
  - p_μ: 6 bins, $\{200, 400, 600, 800, 1000, 1500, 30000\}$
  - $\cos(\theta_\mu)$: 3 bins, $\{-1, 0.9, 0.95, 1\}$

- FHC photon (FGD1 and 2):
  - p_μ: 5 bins, $\{200, 300, 400, 600, 1000, 30000\}$
  - $\cos(\theta_\mu)$: 1 bin, $\{-1, 1\}$

- RHC $\bar{\nu}_e$ CC inclusive (FGD1 and 2):
  - p_μ: 3 bins, $\{200, 500, 1000, 30000\}$
  - $\cos(\theta_\mu)$: 2 bins, $\{-1, 0.9, 1\}$

- RHC ν_e CC inclusive (FGD1 and 2):
  - p_μ: 6 bins, $\{200, 400, 600, 800, 1000, 2000, 30000\}$
  - $\cos(\theta_\mu)$: 2 bins, $\{-1, 0.9, 1\}$
- RHC photon (FGD1 and 2):
  - p_μ: 5 bins, $\{200, 400, 600, 800, 1000, 30000\}$
  - $\cos(\theta_\mu)$: 1 bin, $\{-1, 1\}$.

Therefore, the likelihood runs over 1438 bins. Next, the binning for the covariance is detailed:

- FHC ν_μ CC 0π (FGD1 and 2):
  - p_μ: 6 bins, $\{0, 1000, 1250, 2000, 3000, 5000, 30000\}$
  - $\cos(\theta_\mu)$: 7 bins, $\{-1, 0.6, 0.7, 0.8, 0.85, 0.94, 0.96, 1\}$
- FHC ν_μ CC 1π (FGD1 and 2):
  - p_μ: 5 bins, $\{0, 300, 1250, 1500, 5000, 30000\}$
  - $\cos(\theta_\mu)$: 8 bins, $\{-1, 0.7, 0.85, 0.9, 0.92, 0.96, 0.98, 0.99, 1\}$
- FHC ν_μ CC other (FGD1 and 2):
  - p_μ: 5 bins, $\{0, 1500, 2000, 3000, 5000, 30000\}$
  - $\cos(\theta_\mu)$: 8 bins, $\{-1, 0.8, 0.85, 0.9, 0.92, 0.96, 0.98, 0.99, 1\}$
- RHC $\bar{\nu}_\mu$ CC 0π (FGD1 and 2):
  - p_μ: 4 bins, $\{0, 900, 1250, 2000, 30000\}$
  - $\cos(\theta_\mu)$: 10 bins, $\{-1, 0.7, 0.8, 0.85, 0.9, 0.94, 0.96, 0.98, 0.99, 0.995, 1\}$
- RHC $\bar{\nu}_\mu$ CC 1π FGD1, FGD2 is the same as the likelihood binning:
  - p_μ: 4 bins, $\{0, 400, 1500, 2500, 30000\}$
  - $\cos(\theta_\mu)$: 3 bins, $\{-1, 0.8, 0.9, 1\}$
- RHC $\bar{\nu}_\mu$ CC other (FGD1 and 2):
  - p_μ: 4 bins, $\{0, 1500, 2000, 4000, 30000\}$
  - $\cos(\theta_\mu)$: 4 bins, $\{-1, 0.8, 0.9, 0.95, 1\}$

- RHC ν_μ CC 0π (FGD1 and 2):
  - p_μ: 4 bins, {0, 1000, 1500, 2000, 30000}
  - $\cos(\theta_\mu)$: 7 bins, $\{-1, 0.85, 0.9, 0.92, 0.94, 0.96, 0.98, 1\}$
- RHC ν_μ CC 1π FGD1, FGD2 is the same as the likelihood binning :
  - p_μ: 4 bins, {0, 350, 1250, 2000, 30000}
  - $\cos(\theta_\mu)$: 4 bins, $\{-1, 0.8, 0.9, 0.95, 1\}$
- RHC ν_μ CC other (FGD1 and 2):
  - p_μ: 4 bins, {0, 1000, 2000, 5000, 30000}
  - $\cos(\theta_\mu)$: 3 bins, $\{-1, 0.9, 0.95, 1\}$
- FHC ν_e CC inclusive (FGD1 and 2):
  - p_μ: 6 bins, {200, 400, 600, 800, 1000, 1500, 30000}
  - $\cos(\theta_\mu)$: 1 bin, $\{-1, 1\}$
- FHC photon (FGD1 and 2):
  - p_μ: 5 bins, {200, 300, 400, 600, 1000, 30000}
  - $\cos(\theta_\mu)$: 1 bin, $\{-1, 1\}$
- RHC ν_e CC inclusive (FGD1 and 2):
  - p_μ: 6 bins, {200, 400, 600, 800, 1000, 2000, 30000}
  - $\cos(\theta_\mu)$: 1 bin, $\{-1, 1\}$
- RHC $\bar{\nu}_e$ CC inclusive (FGD1 and 2):
  - p_μ: 3 bins, {200, 500, 1000, 30000}
  - $\cos(\theta_\mu)$: 1 bin, $\{-1, 1\}$
- RHC photon (FGD1 and 2):
  - p_μ: 5 bins, {200, 400, 600, 800, 1000, 30000}
  - $\cos(\theta_\mu)$: 1 bin, $\{-1, 1\}$,

all of which add up to 542 bins (the size of the detector covariance matrix).

Appendix E

BANFF postfit flux parameters

In this appendix, the flux parameters are shown before and after fits to the Asimov and the real data sets of the ND280.

Parameter	Prefit	Asimov fit	Data fit
ND280 FHC ν_μ 0	1.0 ± 0.10	1.0 ± 0.06	0.97 ± 0.06
ND280 FHC ν_μ 1	1.0 ± 0.10	1.0 ± 0.07	0.96 ± 0.07
ND280 FHC ν_μ 2	1.0 ± 0.09	1.0 ± 0.06	0.96 ± 0.06
ND280 FHC ν_μ 3	1.0 ± 0.09	1.0 ± 0.05	0.96 ± 0.05
ND280 FHC ν_μ 4	1.0 ± 0.11	1.0 ± 0.06	0.95 ± 0.06
ND280 FHC ν_μ 5	1.0 ± 0.10	1.0 ± 0.05	0.96 ± 0.05
ND280 FHC ν_μ 6	1.0 ± 0.07	1.0 ± 0.04	0.97 ± 0.04
ND280 FHC ν_μ 7	1.0 ± 0.07	1.0 ± 0.04	0.96 ± 0.04
ND280 FHC ν_μ 8	1.0 ± 0.08	1.0 ± 0.05	0.93 ± 0.04
ND280 FHC ν_μ 9	1.0 ± 0.10	1.0 ± 0.05	0.90 ± 0.04
ND280 FHC ν_μ 10	1.0 ± 0.11	1.0 ± 0.05	0.91 ± 0.05
ND280 FHC $\bar{\nu}_\mu$ 0	1.0 ± 0.10	1.0 ± 0.05	0.97 ± 0.04
ND280 FHC $\bar{\nu}_\mu$ 1	1.0 ± 0.08	1.0 ± 0.05	0.91 ± 0.04
ND280 FHC $\bar{\nu}_\mu$ 2	1.0 ± 0.08	1.0 ± 0.05	0.93 ± 0.04
ND280 FHC $\bar{\nu}_\mu$ 3	1.0 ± 0.09	1.0 ± 0.05	0.93 ± 0.05
ND280 FHC $\bar{\nu}_\mu$ 4	1.0 ± 0.09	1.0 ± 0.05	0.94 ± 0.04
ND280 FHC ν_e 0	1.0 ± 0.09	1.0 ± 0.06	0.97 ± 0.06
ND280 FHC ν_e 1	1.0 ± 0.09	1.0 ± 0.06	0.96 ± 0.06
ND280 FHC ν_e 2	1.0 ± 0.08	1.0 ± 0.06	0.98 ± 0.06
ND280 FHC ν_e 3	1.0 ± 0.08	1.0 ± 0.05	0.95 ± 0.05
ND280 FHC ν_e 4	1.0 ± 0.08	1.0 ± 0.05	0.96 ± 0.04
ND280 FHC ν_e 5	1.0 ± 0.08	1.0 ± 0.04	0.95 ± 0.04
ND280 FHC ν_e 6	1.0 ± 0.10	1.0 ± 0.06	0.98 ± 0.06
ND280 FHC $\bar{\nu}_e$ 0	1.0 ± 0.07	1.0 ± 0.05	0.98 ± 0.05
ND280 FHC $\bar{\nu}_e$ 1	1.0 ± 0.14	1.0 ± 0.11	1.13 ± 0.11

Table E.1: ND280 FHC flux parameters values and uncertainties before and after an Asimov fit and a data fit.

Parameter	Prefit	Asimov fit	Data fit
ND280 RHC ν_μ 0	1.0 ± 0.09	1.0 ± 0.04	0.95 ± 0.04
ND280 RHC ν_μ 1	1.0 ± 0.08	1.0 ± 0.04	0.93 ± 0.04
ND280 RHC ν_μ 2	1.0 ± 0.08	1.0 ± 0.04	0.93 ± 0.04
ND280 RHC ν_μ 3	1.0 ± 0.08	1.0 ± 0.04	0.96 ± 0.04
ND280 RHC ν_μ 4	1.0 ± 0.08	1.0 ± 0.03	0.81 ± 0.03
ND280 RHC $\bar{\nu}_\mu$ 0	1.0 ± 0.11	1.0 ± 0.06	0.99 ± 0.06
ND280 RHC $\bar{\nu}_\mu$ 1	1.0 ± 0.10	1.0 ± 0.07	0.97 ± 0.07
ND280 RHC $\bar{\nu}_\mu$ 2	1.0 ± 0.09	1.0 ± 0.06	0.95 ± 0.06
ND280 RHC $\bar{\nu}_\mu$ 3	1.0 ± 0.08	1.0 ± 0.05	0.95 ± 0.05
ND280 RHC $\bar{\nu}_\mu$ 4	1.0 ± 0.11	1.0 ± 0.07	0.97 ± 0.07
ND280 RHC $\bar{\nu}_\mu$ 5	1.0 ± 0.10	1.0 ± 0.07	0.96 ± 0.07
ND280 RHC $\bar{\nu}_\mu$ 6	1.0 ± 0.07	1.0 ± 0.05	0.95 ± 0.05
ND280 RHC $\bar{\nu}_\mu$ 7	1.0 ± 0.07	1.0 ± 0.05	0.96 ± 0.05
ND280 RHC $\bar{\nu}_\mu$ 8	1.0 ± 0.09	1.0 ± 0.07	0.97 ± 0.07
ND280 RHC $\bar{\nu}_\mu$ 9	1.0 ± 0.09	1.0 ± 0.06	0.97 ± 0.06
ND280 RHC $\bar{\nu}_\mu$ 10	1.0 ± 0.13	1.0 ± 0.10	0.93 ± 0.10
ND280 RHC ν_e 0	1.0 ± 0.07	1.0 ± 0.05	0.93 ± 0.05
ND280 RHC ν_e 1	1.0 ± 0.09	1.0 ± 0.06	0.99 ± 0.06
ND280 RHC $\bar{\nu}_e$ 0	1.0 ± 0.10	1.0 ± 0.06	0.97 ± 0.06
ND280 RHC $\bar{\nu}_e$ 1	1.0 ± 0.09	1.0 ± 0.06	0.96 ± 0.06
ND280 RHC $\bar{\nu}_e$ 2	1.0 ± 0.09	1.0 ± 0.06	0.95 ± 0.06
ND280 RHC $\bar{\nu}_e$ 3	1.0 ± 0.08	1.0 ± 0.05	0.98 ± 0.05
ND280 RHC $\bar{\nu}_e$ 4	1.0 ± 0.08	1.0 ± 0.06	0.99 ± 0.06
ND280 RHC $\bar{\nu}_e$ 5	1.0 ± 0.09	1.0 ± 0.07	1.01 ± 0.07
ND280 RHC $\bar{\nu}_e$ 6	1.0 ± 0.16	1.0 ± 0.12	1.19 ± 0.12

Table E.2: ND280 RHC flux parameters values and uncertainties before and after an Asimov fit and a data fit.

Parameter	Prefit	Asimov fit	Data fit
SK FHC ν_μ 0	1.0 ± 0.10	1.0 ± 0.07	0.97 ± 0.06
SK FHC ν_μ 1	1.0 ± 0.10	1.0 ± 0.07	0.97 ± 0.07
SK FHC ν_μ 2	1.0 ± 0.09	1.0 ± 0.06	0.96 ± 0.06
SK FHC ν_μ 3	1.0 ± 0.08	1.0 ± 0.05	0.95 ± 0.05
SK FHC ν_μ 4	1.0 ± 0.10	1.0 ± 0.06	0.95 ± 0.06
SK FHC ν_μ 5	1.0 ± 0.08	1.0 ± 0.05	0.96 ± 0.05
SK FHC ν_μ 6	1.0 ± 0.07	1.0 ± 0.04	0.97 ± 0.04
SK FHC ν_μ 7	1.0 ± 0.07	1.0 ± 0.05	0.97 ± 0.04
SK FHC ν_μ 8	1.0 ± 0.09	1.0 ± 0.05	0.93 ± 0.04
SK FHC ν_μ 9	1.0 ± 0.10	1.0 ± 0.04	0.88 ± 0.04
SK FHC ν_μ 10	1.0 ± 0.11	1.0 ± 0.06	0.91 ± 0.05
SK FHC $\bar{\nu}_\mu$ 0	1.0 ± 0.10	1.0 ± 0.05	0.97 ± 0.05
SK FHC $\bar{\nu}_\mu$ 1	1.0 ± 0.08	1.0 ± 0.05	0.94 ± 0.04
SK FHC $\bar{\nu}_\mu$ 2	1.0 ± 0.08	1.0 ± 0.05	0.91 ± 0.05
SK FHC $\bar{\nu}_\mu$ 3	1.0 ± 0.08	1.0 ± 0.05	0.91 ± 0.05
SK FHC $\bar{\nu}_\mu$ 4	1.0 ± 0.09	1.0 ± 0.06	0.98 ± 0.06
SK FHC ν_e 0	1.0 ± 0.09	1.0 ± 0.06	0.97 ± 0.06
SK FHC ν_e 1	1.0 ± 0.09	1.0 ± 0.06	0.96 ± 0.06
SK FHC ν_e 2	1.0 ± 0.08	1.0 ± 0.05	0.96 ± 0.05
SK FHC ν_e 3	1.0 ± 0.08	1.0 ± 0.05	0.95 ± 0.04
SK FHC ν_e 4	1.0 ± 0.08	1.0 ± 0.04	0.96 ± 0.04
SK FHC ν_e 5	1.0 ± 0.08	1.0 ± 0.05	0.94 ± 0.04
SK FHC ν_e 6	1.0 ± 0.09	1.0 ± 0.06	1.00 ± 0.06
SK FHC $\bar{\nu}_e$ 0	1.0 ± 0.07	1.0 ± 0.06	0.98 ± 0.05
SK FHC $\bar{\nu}_e$ 1	1.0 ± 0.13	1.0 ± 0.10	1.11 ± 0.10

Table E.3: SK FHC flux parameters values and uncertainties before and after an Asimov fit and a data fit.

Parameter	Prefit	Asimov fit	Data fit
SK RHC ν_μ 0	1.0 ± 0.09	1.0 ± 0.04	0.96 ± 0.04
SK RHC ν_μ 1	1.0 ± 0.08	1.0 ± 0.05	0.94 ± 0.04
SK RHC ν_μ 2	1.0 ± 0.07	1.0 ± 0.04	0.93 ± 0.04
SK RHC ν_μ 3	1.0 ± 0.08	1.0 ± 0.05	0.92 ± 0.04
SK RHC ν_μ 4	1.0 ± 0.08	1.0 ± 0.04	0.88 ± 0.04
SK RHC $\bar{\nu}_\mu$ 0	1.0 ± 0.11	1.0 ± 0.06	0.98 ± 0.06
SK RHC $\bar{\nu}_\mu$ 1	1.0 ± 0.10	1.0 ± 0.07	0.97 ± 0.07
SK RHC $\bar{\nu}_\mu$ 2	1.0 ± 0.09	1.0 ± 0.06	0.96 ± 0.06
SK RHC $\bar{\nu}_\mu$ 3	1.0 ± 0.08	1.0 ± 0.05	0.95 ± 0.05
SK RHC $\bar{\nu}_\mu$ 4	1.0 ± 0.10	1.0 ± 0.07	0.96 ± 0.07
SK RHC $\bar{\nu}_\mu$ 5	1.0 ± 0.09	1.0 ± 0.06	0.95 ± 0.06
SK RHC $\bar{\nu}_\mu$ 6	1.0 ± 0.07	1.0 ± 0.05	0.97 ± 0.05
SK RHC $\bar{\nu}_\mu$ 7	1.0 ± 0.07	1.0 ± 0.05	0.97 ± 0.05
SK RHC $\bar{\nu}_\mu$ 8	1.0 ± 0.09	1.0 ± 0.07	0.94 ± 0.07
SK RHC $\bar{\nu}_\mu$ 9	1.0 ± 0.08	1.0 ± 0.06	0.91 ± 0.06
SK RHC $\bar{\nu}_\mu$ 10	1.0 ± 0.11	1.0 ± 0.09	0.95 ± 0.09
SK RHC ν_e 0	1.0 ± 0.07	1.0 ± 0.05	0.95 ± 0.05
SK RHC ν_e 1	1.0 ± 0.08	1.0 ± 0.06	0.98 ± 0.06
SK RHC $\bar{\nu}_e$ 0	1.0 ± 0.10	1.0 ± 0.06	0.97 ± 0.06
SK RHC $\bar{\nu}_e$ 1	1.0 ± 0.09	1.0 ± 0.06	0.97 ± 0.05
SK RHC $\bar{\nu}_e$ 2	1.0 ± 0.09	1.0 ± 0.06	0.95 ± 0.05
SK RHC $\bar{\nu}_e$ 3	1.0 ± 0.08	1.0 ± 0.05	0.97 ± 0.05
SK RHC $\bar{\nu}_e$ 4	1.0 ± 0.08	1.0 ± 0.05	0.98 ± 0.05
SK RHC $\bar{\nu}_e$ 5	1.0 ± 0.09	1.0 ± 0.06	0.99 ± 0.06
SK RHC $\bar{\nu}_e$ 6	1.0 ± 0.15	1.0 ± 0.12	1.17 ± 0.12

Table E.4: SK RHC flux parameters values and uncertainties before and after an Asimov fit and a data fit.

Bibliography

[1] W. Pauli. Dear Radioactive Ladies and Gentlemen. *Phys. Today*, 31N9:27, 1978. URL `http://inspirehep.net/record/45177/files/meitner_0393.pdf`.

[2] F. Reines et al. Detection of the Free Neutrino. *Phys. Rev.*, 92:830–831, Nov 1953, doi:10.1103/PhysRev.92.830.

[3] K. Abe et al. The T2K Experiment. *Nucl. Instrum. Meth.*, A659:106–135, 2011, doi:10.1016/J.NIMA.2011.06.067. arXiv:1106.1238 [physics.ins-det].

[4] Y. Fukuda et al. The Super-Kamiokande Detector. *Nucl. Instrum. Meth.*, A501:418–462, 2003, doi:10.1016/S0168-9002(03)00425-X.

[5] J. Boger et al. The Sudbury Neutrino Observatory. *Nucl. Instrum. Meth.*, 449(1):172 – 207, 2000, doi:10.1016/S0168-9002(99)01469-2. arXiv:nucl-ex/9910016 [nucl-ex].

[6] F. An et al. The Detector System of The Daya Bay Reactor Neutrino Experiment. *Nucl. Instrum. Meth.*, A811:133–161, 2016, doi:10.1016/J.NIMA.2015.11.144. arXiv:1508.03943 [physics.ins-det].

[7] B. Pontecorvo. Inverse β Processes and Nonconservation of Lepton Charge. *Zhur. Eksptl'. i Teoret. Fiz.*, 34, 1958.

[8] Z. Maki et al. Remarks on the unified model of elementary particles. *Prog. Theor. Phys.*, 28:870–880, 1962, doi:10.1143/PTP.28.870.

[9] Y. Fukuda et al. Evidence for Oscillation of Atmospheric Neutrinos. *Phys. Rev. Lett.*, 81:1562–1567, Aug 1998, doi:10.1103/PhysRevLett.81.1562. arXiv:hep-ex/9807003 [physics.ins-det].

[10] Q. Ahmad et al. Direct Evidence for Neutrino Flavor Transformation from Neutral-Current Interactions in the Sudbury Neutrino Observatory. *Phys. Rev. Lett.*,

89:011301, Jun 2002, doi:10.1103/PhysRevLett.89.011301. arXiv:nucl-ex/0204008 [physics.ins-det].

[11] T. Kajita and A. McDonald. The Nobel Prize in Physics for the discovery of neutrino oscillations, which shows that neutrinos have mass, 2015. URL `http://nobelprize.org/nobel_prizes/physics/laureates/2015/index.html`.

[12] E. Akhmedov et al. Neutrino Oscillations: Quantum Mechanics vs. Quantum Field Theory. *Journal of High Energy Physics*, 2010(4):8, Apr 2010, doi:10.1007/JHEP04(2010)008. arXiv:1001.4815 [hep-ph].

[13] B. Kayser. Neutrino Physics. *eConf*, C040802:L004, 2004. URL `https://www.slac.stanford.edu/econf/C040802/papers/L004.PDF`. arXiv:hep-ph/0506165 [hep-ph].

[14] V. Aseev et al. Upper Limit on the Electron Antineutrino Mass from the Troitsk Experiment. *Phys. Rev.*, D84:112003, Dec 2011, doi:10.1103/PhysRevD.84.112003. arXiv:1108.5034 [hep-ex].

[15] W. Hampel et al. GALLEX Solar Neutrino Observations: Results for GALLEX IV. *Phys. Lett.*, B447(1):127 – 133, 1999, doi:10.1016/S0370-2693(98)01579-2.

[16] B. Pontecorvo. Neutrino Experiments and the Problem of Conservation of Leptonic Charge. *Sov. Phys. JETP*, 26:984–988, 1968. [Zh. Eksp. Teor. Fiz.53,1717(1967)].

[17] B. Pontecorvo. Mesonium and Anti-Mesonium. *Sov. Phys. JETP*, 6:429, 1957. [Zh. Eksp. Teor. Fiz.33,549(1957)].

[18] S. Bilenky et al. Lepton Mixing and Neutrino Oscillations. *Phys. Rept.*, 41:225–261, 1978, doi:10.1016/0370-1573(78)90095-9.

[19] W. H. Furry. On transition probabilities in double beta-disintegration. *Phys. Rev.*, 56:1184–1193, Dec 1939, doi:10.1103/PhysRev.56.1184.

[20] A. Cervera et al. Golden Measurements at a Neutrino Factory. *Nucl. Phys.*, B579:17–55, 2000, doi:10.1016/S0550-3213(00)00606-4. arXiv:hep-ph/0002108 [hep-ph]. [Erratum: Nucl. Phys.B593,731(2001)].

[21] R. Wendell. Prob3++ Software for Computing Three Flavor Neutrino Oscillation Probabilities. 2012. URL `http://webhome.phy.duke.edu/~raw22/public/Prob3++/`.

[22] M. Wurm. Mass ordering illustration, website consulted on the 5th february 2018. URL `http://www.staff.uni-mainz.de/wurmm/wurm-home/mass-hierarchy.png`.

[23] F. Capozzi et al. Global Constraints on Absolute Neutrino Masses and their Ordering. *Phys. Rev.*, D95:096014, May 2017, doi:10.1103/PhysRevD.95.096014. arXiv:1703.04471 [hep-ex].

[24] P. Adamson et al. Constraints on Oscillation Parameters from ν_e Appearance and ν_μ Disappearance in NOvA. *Phys. Rev. Lett.*, 118:231801, Jun 2017, doi:10.1103/PhysRevLett.118.231801. arXiv:1703.03328 [hep-ex].

[25] C. Andreopoulos et al. The GENIE Neutrino Monte Carlo Generator. *Nucl. Instrum. Meth.*, A614:87–104, 2010, doi:10.1016/J.NIMA.2009.12.009. arXiv:0905.2517 [hep-ph].

[26] C. Andreopoulos et al. The GENIE Neutrino Monte Carlo Generator: Physics and User Manual. 2015. arXiv:1510.05494 [hep-ph].

[27] Y. Hayato. A Neutrino Interaction Simulation Program Library NEUT. *Acta Phys. Polon.*, B40:2477–2489, 2009. URL `http://www.actaphys.uj.edu.pl/fulltext?series=Reg&vol=40&page=2477`.

[28] O. Benhar et al. Spectral Function of Finite Nuclei and Scattering of GeV Electrons. *Nucl. Phys.*, A579(3):493 – 517, 1994, doi:10.1016/0375-9474(94)90920-2.

[29] N. Rocco. Unified Description of Electron-Nucleus Scattering within the Spectral Function Formalism. *JPS Conf. Proc.*, 12:010029, 2016, doi:10.7566/JPSCP.12.010029.

[30] C. Wilkinson et al. Testing Charged Current Quasi-Elastic and Multinucleon Interaction Models in the NEUT Neutrino Interaction Generator with Published Datasets from the MiniBooNE and MINERνA Experiments. *Phys. Rev.*, D93:072010, Apr 2016, doi:10.1103/PhysRevD.93.072010. arXiv:1601.05592 [hep-ex].

[31] M. Martini et al. Neutrino Energy Reconstruction Problems and Neutrino Oscillations. *Phys. Rev.*, D85:093012, 2012, doi:10.1103/PhysRevD.85.093012. arXiv:1202.4745 [hep-ph].

[32] L. Smith et al. Neutrino Reactions at Accelerator Energies. *Phys. Rep.*, 3:261–379, 1972. URL `http://cds.cern.ch/record/396544`.

[33] S. Barish et al. Study of Neutrino Interactions in Hydrogen and Deuterium. 1. Description of the Experiment and Study of the Reaction Neutrino $d \to \mu^- pp(s)$. *Phys. Rev.*, D16:3103, 1977, doi:10.1103/PhysRevD.16.3103.

[34] T. Kitagaki et al. High-Energy Quasielastic $\nu_\mu n \to \mu^- p$ Scattering in Deuterium. *Phys. Rev.*, D28:436–442, Aug 1983, doi:10.1103/PhysRevD.28.436.

[35] D. Allasia et al. Investigation of Exclusive Channels in $\nu/\bar{\nu}$-Deuteron Charged Current Interactions. *Nucl. Phys.*, B343(2):285 – 309, 1990, doi:10.1016/0550-3213(90)90472-P.

[36] A. Meyer et al. Deuterium Target Data for Precision Neutrino-Nucleus Cross Sections. *Phys. Rev.*, D93:113015, Jun 2016, doi:10.1103/PhysRevD.93.113015. arXiv:1603.03048 [hep-ph].

[37] B. Bhattacharya et al. Model-Independent Determination of the Axial Mass Parameter in Quasielastic Antineutrino-Nucleon Scattering. *Phys. Rev.*, D92:113011, Dec 2015, doi:10.1103/PhysRevD.92.113011. arXiv:1510.05652 [hep-ph].

[38] S. Singh. The Effect of Final Ftate Interactions and Deuteron Binding in $\nu d \to \mu pp$. *Nucl. Phys.*, B36(2):419 – 435, 1972, doi:10.1016/0550-3213(72)90227-1.

[39] R. Smith et al. Neutrino Reaction on Nuclear Targets. *Nucl. Phys.*, B43:605, 1972, doi:10.1016/0550-3213(75)90612-4. [Erratum: Nucl. Phys.B101,547(1975)].

[40] J. Nieves et al. Inclusive Charged-Current Neutrino-Nucleus Reactions. *Phys. Rev.*, C83:045501, Apr 2011, doi:10.1103/PhysRevC.83.045501. arXiv:1102.2777 [hep-ph].

[41] G. Fiorentini et al. Measurement of Muon Neutrino Quasielastic Scattering on a Hydrocarbon Target at $E_\nu \sim 3.5$ GeV. *Phys. Rev. Lett.*, 111:022502, Jul 2013, doi:10.1103/PhysRevLett.111.022502. arXiv:1305.2243 [hep-ex].

[42] A. Aguilar-Arevalo et al. First Measurement of the Muon Neutrino Charged Current Quasielastic Double Differential Cross Section. *Phys. Rev.*, D81:092005, May 2010, doi:10.1103/PhysRevD.81.092005. arXiv:1002.2680 [hep-ex].

[43] K. Abe et al. Measurement of the ν_μ Charged Current Quasielastic Cross Section on Carbon with the T2K On-Axis Neutrino Beam. *Phys. Rev.*, D91:112002, Jun 2015, doi:10.1103/PhysRevD.91.112002. arXiv:1503.07452 [hep-ex].

[44] R. Gran et al. Measurement of the Quasielastic Axial Vector Mass in Neutrino Interactions on Oxygen. *Phys. Rev.*, D74:052002, Sep 2006, doi:10.1103/PhysRevD.74.052002. arXiv:hep-ex/0603034 [hep-ex].

[45] M. Martini et al. Neutrino and Antineutrino Quasielastic Interactions with Nuclei. *Phys. Rev.*, C81:045502, 2010, doi:10.1103/PhysRevC.81.045502. arXiv:1002.4538 [hep-ph].

[46] M. Martini et al. Neutrino Quasielastic Interaction and Nuclear Dynamics. *Phys. Rev.*, C84:055502, 2011, doi:10.1103/PhysRevC.84.055502. arXiv:1110.0221 [nucl-th].

[47] J. Nieves et al. Inclusive Charged-Current Neutrino-Nucleus Reactions. *Phys. Rev.*, C83:045501, 2011, doi:10.1103/PhysRevC.83.045501. arXiv:1102.2777 [hep-ph].

[48] J. Nieves et al. Two Particle-Hole Excitations in Charged Current Quasielastic Antineutrino-Nucleus Scattering. *Phys. Lett.*, B721:90–93, 2013, doi:10.1016/j.physletb.2013.03.002. arXiv:1302.0703 [hep-ph].

[49] G. Megias et al. Meson-Exchange Currents and Quasielastic Predictions for Charged-Current Neutrino-^{12}C Scattering in the Superscaling Approach. *Phys. Rev.*, D91(7):073004, 2015, doi:10.1103/PhysRevD.91.073004. arXiv:1412.1822 [nucl-th].

[50] J. Amaro et al. Meson-Exchange Currents and Quasielastic Antineutrino Cross Sections in the SuperScaling Approximation. *Phys. Rev. Lett.*, 108:152501, 2012, doi:10.1103/PhysRevLett.108.152501. arXiv:1112.2123 [nucl-th].

[51] A. Aguilar-Arevalo et al. First Measurement of the Muon Antineutrino Double-Differential Charged-Current Quasielastic Cross Section. *Phys. Rev.*, D88:032001, Aug 2013, doi:10.1103/PhysRevD.88.032001. arXiv:1301.7067 [hep-ex].

[52] P. Rodrigues et al. Identification of Nuclear Effects in Neutrino-Carbon Interactions at Low Three-Momentum Transfer. *Phys. Rev. Lett.*, 116:071802, 2016, doi:10.1103/PhysRevLett.116.071802. arXiv:1511.05944 [hep-ex].

[53] M. Antonello et al. A Proposal for a Three Detector Short-Baseline Neutrino Oscillation Program in the Fermilab Booster Neutrino Beam. 2015. arXiv:1503.01520 [physics.ins-det].

[54] R. Acciarri et al. Design and Construction of the MicroBooNE Detector. *JINST*, 12(02):P02017, 2017, doi:10.1088/1748-0221/12/02/P02017. arXiv:1612.05824 [physics.ins-det].

[55] T. Van Cuyck et al. Influence of Short-Range Correlations in Neutrino-Nucleus Scattering. *Phys. Rev.*, C94(2):024611, 2016, doi:10.1103/PhysRevC.94.024611. arXiv:1606.00273 [nucl-th].

[56] D. Rein et al. Neutrino Excitation of Baryon Resonances and Single Pion Production. *Annals Phys.*, 133:79–153, 1981, doi:10.1016/0003-4916(81)90242-6.

[57] D. Rein. Angular Distribution in Neutrino Induced Single Pion Production Processes. *Z. Phys.*, C35:43–64, 1987, doi:10.1007/BF01561054.

[58] E. Oset et al. Delta Self-Energy in Nuclear Matter. *Nucl. Phys.*, A468(3):631 – 652, 1987, doi:10.1016/0375-9474(87)90185-0.

[59] S. Singh et al. Nuclear Effects in Neutrino Production of Δ at Intermediate Energies. *Phys. Lett.*, B416(1–2):23 – 28, 1998, doi:10.1016/S0370-2693(97)01325-7.

[60] N. Baker et al. Study of the Isospin Structure of Single-Pion Production in Charged-Current Neutrino Interactions. *Phys. Rev.*, D23:2495–2498, Jun 1981, doi:10.1103/PhysRevD.23.2495.

[61] M. Kabirnezhad. Single pion production in neutrino-nucleon Interactions. *Phys. Rev.*, D97(1):013002, 2018, doi:10.1103/PhysRevD.97.013002. arXiv:1711.02403 [hep-ph].

[62] G. Radecky et al. Study of Single Pion Production by Weak Charged Currents in Low-Energy Neutrino d Interactions. *Phys. Rev.*, D25:1161–1173, 1982, doi:10.1103/PhysRevD.25.1161. [Erratum: Phys.Rev.D26,3297(1982)].

[63] M. Derrick et al. Study of Single-Pion Production by Weak Neutral Currents in Low-Energy νd Interactions. *Phys. Rev.*, D23:569–575, Feb 1981, doi:10.1103/PhysRevD.23.569.

[64] T. Kitagaki et al. Charged-Current Exclusive Pion Production in Neutrino-Deuterium Interactions. *Phys. Rev.*, D34:2554–2565, Nov 1986, doi:10.1103/PhysRevD.34.2554.

[65] C. Wilkinson, P. Rodrigues, S. Cartwright, L. Thompson, and K. McFarland. Reanalysis of bubble chamber measurements of muon-neutrino induced single pion production. *Phys. Rev.*, D90(11):112017, 2014, doi:10.1103/PhysRevD.90.112017. arXiv:1411.4482 [hep-ex].

[66] B. Eberly et al. Charged pion production in ν_μ interactions on hydrocarbon at $\langle E_\nu \rangle = 4.0$ GeV. *Phys. Rev.*, D92(9):092008, 2015, doi:10.1103/PhysRevD.92.092008. arXiv:1406.6415 [hep-ex].

[67] A. Aguilar-Arevalo et al. Measurement of Neutrino-Induced Charged-Current Charged Pion Production Cross Sections on Mineral Oil at $E_\nu \sim 1$ GeV. *Phys. Rev.*, D83:052007, Mar 2011, doi:10.1103/PhysRevD.83.052007. arXiv:1011.3572 [hep-ex].

[68] A. Aguilar-Arevalo et al. Measurement of ν_μ-Induced Charged-Current Neutral Pion Production Cross Sections on Mineral Oil at $E_\nu \in 0.5 - 2.0$ GeV. *Phys. Rev.*, D83:052009, 2011, doi:10.1103/PhysRevD.83.052009. arXiv:1010.3264 [hep-ex].

[69] A. Aguilar-Arevalo et al. Measurement of ν_μ and $\bar{\nu}_\mu$ Induced Neutral Current Single π^0 Production Cross Sections on Mineral Oil at $E_\nu \sim \mathcal{O}(1\text{GeV})$. *Phys. Rev.*, D81:013005, 2010, doi:10.1103/PhysRevD.81.013005. arXiv:0911.2063 [hep-ex].

[70] A. Rodriguez et al. Measurement of Single Charged Pion Production in the Charged-Current Interactions of Neutrinos in a 1.3-GeV Wide Band Beam. *Phys. Rev.*, D78:032003, 2008, doi:10.1103/PhysRevD.78.032003. arXiv:0805.0186 [hep-ex].

[71] Y. Dokshitzer. Calculation of the Structure Functions for Deep Inelastic Scattering and e+ e- Annihilation by Perturbation Theory in Quantum Chromodynamics. *Sov. Phys. JETP*, 46:641–653, 1977. [Zh. Eksp. Teor. Fiz.73,1216(1977)].

[72] V. Gribov et al. Deep Inelastic e p Scattering in Perturbation Theory. *Sov. J. Nucl. Phys.*, 15:438–450, 1972. [Yad. Fiz.15,781(1972)].

[73] V. N. Gribov et al. e+ e- Pair Annihilation and Deep Inelastic e p Sxcattering in Perturbation Theory. *Sov. J. Nucl. Phys.*, 15:675–684, 1972. [Yad. Fiz.15,1218(1972)].

[74] G. Altarelli et al. Asymptotic Freedom in Parton Language. *Nucl. Phys.*, B126:298–318, 1977, doi:10.1016/0550-3213(77)90384-4.

[75] M. Tzanov et al. Precise Measurement of Neutrino and Anti-Neutrino Differential Cross Sections. *Phys. Rev.*, D74:012008, 2006, doi:10.1103/PhysRevD.74.012008. arXiv:hep-ex/0509010 [hep-ex].

[76] G. Onengut et al. Measurement of Nucleon Structure Functions in Neutrino Scattering. *Phys. Lett.*, B632:65–75, 2006, doi:10.1016/J.PhysLetB.2005.10.062.

[77] J. Berge et al. A Measurement of Differential Cross-Sections and Nucleon Structure Functions in Charged Current Neutrino Interactions on Iron. *Z. Phys.*, C49:187–224, 1991, doi:10.1007/BF01555493.

[78] J. Mousseau et al. Measurement of Partonic Nuclear Effects in Deep-Inelastic Neutrino Scattering using MINERvA. *Phys. Rev.*, D93(7):071101, 2016, doi:10.1103/PhysRevD.93.071101. arXiv:1601.06313 [hep-ex].

[79] A. Airapetian et al. Multiplicities of Charged Pions and Kaons from Semi-Inclusive Deep-Inelastic Scattering by the Proton and the Deuteron. *Phys. Rev.*, D87:074029, Apr 2013, doi:10.1103/PhysRevD.87.074029. arXiv:1212.5407 [hep-ex].

[80] T. Katori et al. PYTHIA Hadronization Process Tuning in the GENIE Neutrino Interaction Generator. *J. Phys.*, G42(11):115004, 2015, doi:10.1088/0954-3899/42/11/115004. arXiv:1412.4301 [hep-ex].

[81] R. Acciarri et al. Long-Baseline Neutrino Facility (LBNF) and Deep Underground Neutrino Experiment (DUNE) : Conceptual Design Report, Volume 1: The LBNF and DUNE Projects. 2016. URL `http://lss.fnal.gov/archive/design/fermilab-design-2016-01.pdf`. arXiv:1601.05471 [physics.ins-det].

[82] R. Acciarri et al. Long-Baseline Neutrino Facility (LBNF) and Deep Underground Neutrino Experiment (DUNE) : Conceptual Design Report, Volume 2: The Physics Program for DUNE at LBNF. 2015. URL `http://lss.fnal.gov/archive/design/fermilab-design-2016-02.pdf`. arXiv:1512.06148 [physics.ins-det].

[83] J. Strait et al. Long-Baseline Neutrino Facility (LBNF) and Deep Underground Neutrino Experiment (DUNE) : Conceptual Design Report, Volume 3: Long-Baseline Neutrino Facility for DUNE. 2016. URL `http://lss.fnal.gov/archive/design/fermilab-design-2016-03.pdf`. arXiv:1601.05823 [physics.ins-det].

[84] R. Acciarri et al. Long-Baseline Neutrino Facility (LBNF) and Deep Underground Neutrino Experiment (DUNE) : Conceptual Design Report, Volume 4: The

DUNE Detectors at LBNF. 2016. URL `http://lss.fnal.gov/archive/design/fermilab-design-2016-04.pdf`. arXiv:1601.02984 [physics.ins-det].

[85] D. Ayres et al. The NOvA Technical Design Report. 2007. URL `http://lss.fnal.gov/archive/design/fermilab-design-2007-01.pdf`.

[86] M. Aartsen et al. Letter of Intent: The Precision IceCube Next Generation Upgrade (PINGU). 2014. arXiv:1401.2046 [physics.ins-det].

[87] E. Hernandez et al. Neutrino Induced Threshold Production of Two Pions and N*(1440) Electroweak Form Factors. *Phys. Rev.*, D77:053009, 2008, doi:10.1103/PhysRevD.77.053009. arXiv:0710.3562 [hep-ph].

[88] D. Rein et al. PCAC and the Deficit of Forward Muons in pi+ Production by Neutrinos. *Phys. Lett.*, B657:207–209, 2007, doi:10.1016/J.PhysLetB.2007.10.025. arXiv:hep-ph/0606185 [hep-ph].

[89] C. Berger et al. PCAC and Coherent Pion Production by Low Energy Neutrinos. *Phys. Rev.*, D79:053003, 2009, doi:10.1103/PhysRevD.79.053003. arXiv:0812.2653 [hep-ph].

[90] H. Grabosch et al. Coherent Pion Production in Neutrino and Anti-Neutrino Interactions on Nuclei of Heavy Freon Molecules. *Z. Phys.*, C31:203, 1986, doi:10.1007/BF01479528.

[91] P. Allport et al. Coherent Production of π^+ Mesons in Neutrino - Neon Interactions. *Z. Phys.*, C43:523–526, 1989, doi:10.1007/BF01550929.

[92] P. Vilain et al. Coherent Single Charged Pion Production by Neutrinos. *Phys. Lett.*, B313:267–275, 1993, doi:10.1016/0370-2693(93)91223-A.

[93] M. Aderholz et al. Coherent Production of $\pi^+\pi^-$ Mesons by Charged Current Interactions of Neutrinos and Anti-neutrinos on Neon Nuclei at the Tevatron. *Phys. Rev. Lett.*, 63:2349, 1989, doi:10.1103/PhysRevLett.63.2349.

[94] M. Hasegawa et al. Search for Coherent Charged Pion Production in Neutrino-Carbon Interactions. *Phys. Rev. Lett.*, 95:252301, 2005, doi:10.1103/PhysRevLett.95.252301. arXiv:hep-ex/0506008 [hep-ex].

[95] K. Hiraide et al. Search for Charged Current Coherent Pion Production on Carbon in a few-GeV Neutrino Beam. *Phys. Rev. D*, 78:112004, Dec 2008, doi:10.1103/PhysRevD.78.112004.

[96] A. Higuera et al. Measurement of Coherent Production of $\pi^{\pm}$ in Neutrino and Antineutrino Beams on Carbon from E_{ν} of 1.5 to 20 GeV. *Phys. Rev. Lett.*, 113(26):261802, 2014, doi:10.1103/PhysRevLett.113.261802. arXiv:1409.3835 [hep-ex].

[97] K. Abe et al. Measurement of Coherent π^{+} Production in Low Energy Neutrino-Carbon Scattering. *Phys. Rev. Lett.*, 117(19):192501, 2016, doi:10.1103/PhysRevLett.117.192501. arXiv:1604.04406 [hep-ex].

[98] R. Acciarri et al. First Measurement of Neutrino and Antineutrino Coherent Charged Pion Production on Argon. *Phys. Rev. Lett.*, 113(26):261801, 2014, doi:10.1103/PhysRevLett.113.261801. arXiv:1408.0598 [hep-ex]. [Erratum: Phys. Rev. Lett.114,no.3,039901(2015)].

[99] M. Day et al. Differences in Quasi-Elastic Cross-Sections of Muon and Electron Neutrinos. *Phys. Rev.*, D86:053003, 2012, doi:10.1103/PhysRevD.86.053003. arXiv:1206.6745 [hep-ph].

[100] J. Blietschau et al. Total Cross-Sections for electron-neutrino and anti-electron-neutrino Interactions and Search for Neutrino Oscillations and Decay. *Nucl. Phys.*, B133:205–219, 1978, doi:10.1016/0550-3213(78)90299-7.

[101] K. Abe et al. Measurement of the Inclusive Electron Neutrino Charged Current Cross Section on Carbon with the T2K Near Detector. *Phys. Rev. Lett.*, 113(24):241803, 2014, doi:10.1103/PhysRevLett.113.241803. arXiv:1407.7389 [hep-ex].

[102] J. Wolcott et al. Measurement of Electron Neutrino Quasielastic and Quasielasticlike Scattering on Hydrocarbon at $\langle E_{\nu} \rangle = 3.6$ GeV. *Phys. Rev. Lett.*, 116(8):081802, 2016, doi:10.1103/PhysRevLett.116.081802. arXiv:1509.05729 [hep-ex].

[103] A. Aguilar-Arevalo et al. First Measurement of the Muon Antineutrino Double-Differential Charged-Current Quasielastic Cross Section. *Phys. Rev.*, D88(3):032001, 2013, doi:10.1103/PhysRevD.88.032001. arXiv:1301.7067 [hep-ex].

[104] L. Fields et al. Measurement of Muon Antineutrino Quasielastic Scattering on a Hydrocarbon Target at $E_{\nu} \sim 3.5$ GeV. *Phys. Rev. Lett.*, 111(2):022501, 2013, doi:10.1103/PhysRevLett.111.022501. arXiv:1305.2234 [hep-ex].

[105] T. Le et al. Single Neutral Pion Production by Charged-Current $\bar{\nu}_{\mu}$ Interactions on Hydrocarbon at $\langle E_{\nu} \rangle = 3.6$ GeV. *Phys. Lett.*, B749:130–136, 2015, doi:10.1016/J.PhysLetB.2015.07.039. arXiv:1503.02107 [hep-ex].

[106] L. Ahrens et al. Measurement of Neutrino - Proton and anti-neutrino - Proton Elastic Scattering. *Phys. Rev.*, D35:785, 1987, doi:10.1103/PhysRevD.35.785.

[107] G. Garvey et al. Determination of Proton Strange Form-Factors from Neutrino p Elastic Scattering. *Phys. Rev.*, C48:761–765, 1993, doi:10.1103/PhysRevC.48.761.

[108] W. Alberico et al. Strange Form-Factors of the Proton: A New Analysis of the Neutrino (Anti-Neutrino) Data of the BNL-734 Experiment. *Nucl. Phys.*, A651:277–286, 1999, doi:10.1016/S0375-9474(99)00142-6. arXiv:hep-ph/9812388 [hep-ph].

[109] K. Olive et al. Review of Particle Physics. *Chin. Phys.*, C38:090001, 2014, doi:10.1088/1674-1137/38/9/090001.

[110] S. Nakayama et al. Measurement of Single π^0 Production in Neutral Current Neutrino Interactions with Water by a 1.3-GeV Wide Band Muon Neutrino Beam. *Phys. Lett.*, B619:255–262, 2005, doi:10.1016/J.PhysLetB.2005.05.044. arXiv:hep-ex/0408134 [hep-ex].

[111] A. Aguilar-Arevalo et al. Measurement of ν_μ and $\bar{\nu}_\mu$ Induced Neutral Current Single π^0 Production Cross Sections on Mineral Oil at $E_\nu \sim \mathcal{O}(1\text{GeV})$. *Phys. Rev.*, D81:013005, 2010, doi:10.1103/PhysRevD.81.013005. arXiv:0911.2063 [hep-ex].

[112] A. Aguilar-Arevalo et al. First Observation of Coherent π^0 Production in Neutrino Nucleus Interactions with $E_\nu < 2$ GeV. *Phys. Lett.*, B664:41–46, 2008, doi:10.1016/J.PhysLetB.2008.05.006. arXiv:0803.3423 [hep-ex].

[113] C. Kullenberg et al. A Measurement of Coherent Neutral Pion Production in Neutrino Neutral Current Interactions in the NOMAD Experiment. *Phys. Lett.*, B682(2):177 – 184, 2009, doi:10.1016/J.PhysLetB.2009.10.083. arXiv:0910.0062 [physics.ins-det].

[114] C. Kullenberg et al. A Search for Single Photon Events in Neutrino Interactions. *Phys. Lett.*, B706:268–275, 2012, doi:10.1016/J.PhysLetB.2011.11.049. arXiv:1111.3713 [hep-ex].

[115] J. Wolcott et al. Evidence for Neutral-Current Diffractive π^0 Production from Hydrogen in Neutrino Interactions on Hydrocarbon. *Phys. Rev. Lett.*, 117(11):111801, 2016, doi:10.1103/PhysRevLett.117.111801. arXiv:1604.01728 [hep-ex].

[116] K. Abe et al. Measurement of Neutrino and Antineutrino Oscillations by the T2K Experiment Including a New Additional Sample of ν_e Interactions at the

Far Detector. *Phys. Rev.*, D96:092006, Nov 2017, doi:10.1103/PhysRevD.96.092006. arXiv:1707.01048 [hep-ex].

[117] K. Abe et al. T2K Neutrino Flux Prediction. *Phys. Rev.*, D87:012001, Jan 2013, doi:10.1103/PhysRevD.87.012001.

[118] A. Mann et al. Long Baseline Neutrino Oscillation Experiment at the AGS: Proposal. 1993.

[119] M. Hartz. Commissioning of the T2K Beamline. 1222:327–331, Mar. 2010, doi:10.1063/1.3399335.

[120] T. Vladisavljevic. Flux Release Runs 1-7 New Release Using Tuning Code 13av2+ Run 8 Release, April 2017. URL `http://www.t2k.org/beam/NuFlux/FluxRelease/13arelease/13av2-tuned-fluxes-for-runs-1-8-slides`. Presentation at the beam meeting.

[121] N. Abgrall et al. Measurements of Cross Sections and Charged Pion Spectra in Proton-Carbon Interactions at 31 GeV/c. *Phys. Rev.*, C84:034604, 2011, doi:10.1103/PhysRevC.84.034604. arXiv:1102.0983 [hep-ex].

[122] N. Abgrall et al. Measurement of Production Properties of Positively Charged Kaons in Proton-Carbon Interactions at 31 GeV/c. *Phys. Rev.*, C85:035210, 2012, doi:10.1103/PhysRevC.85.035210. arXiv:1112.0150 [hep-ex].

[123] N. Abgrall et al. Measurements of $\pi^{\pm}$, $K^{\pm}$, K^0_S , $\mathit{\Lambda}$ and proton production in proton–carbon interactions at 31 GeV/c with the NA61/SHINE spectrometer at the CERN SPS. *Eur. Phys. J.*, C76(2):84, 2016, doi:10.1140/epjc/s10052-016-3898-y. arXiv:1510.02703 [hep-ex].

[124] M. Hartz. Flux Uncertainty Update for 13av2 and Run 8, April 2017. URL `http://www.t2k.org/beam/NuFlux/FluxRelease/13arelease/13av2-flux-uncertainty`. Presentation at the beam meeting.

[125] M. Yokoyama et al. Application of Hamamatsu MPPCs to T2K neutrino detectors. *Nucl. Instrum. Meth.*, 610(1):128 – 130, 2009, doi:10.1016/J.NIMA.2009.05.077. arXiv:0807.3145 [physics.ins-det]. New Developments In Photodetection NDIP08.

[126] S. Aoki et al. The T2K Side Muon Range Detector (SMRD). *Nucl. Instrum. Meth.*, A698:135–146, 2013, doi:10.1016/J.NIMA.2012.10.001. arXiv:1206.3553 [physics.ins-det].

[127] S. Assylbekov et al. The T2K ND280 Off-Axis Pi-Zero Detector. *Nucl. Instrum. Meth.*, A686:48–63, 2012, doi:10.1016/J.NIMA.2012.05.028. arXiv:1111.5030 [physics.ins-det].

[128] N. Abgrall et al. Time Projection Chambers for the T2K Near Detectors. *Nucl. Instrum. Meth.*, A637:25–46, 2011, doi:10.1016/J.NIMA.2011.02.036. arXiv:1012.0865 [physics.ins-det].

[129] P. Amaudruz et al. The T2K Fine-Grained Detectors. *Nucl. Instrum. Meth.*, A696:1–31, 2012, doi:10.1016/J.NIMA.2012.08.020. arXiv:1204.3666 [physics.ins-det].

[130] D. Allan et al. The Electromagnetic Calorimeter for the T2K Near Detector ND280. *JINST*, 8:P10019, 2013, doi:10.1088/1748-0221/8/10/P10019. arXiv:1308.3445 [physics.ins-det].

[131] H. Kume et al. 20-Inch Diameter Photomultiplier. *Nucl. Instrum. Meth.*, 205:443–449, 1983, doi:10.1016/0167-5087(83)90007-8.

[132] M. Hartz. The 50th KEK colloquium: T2K neutrino oscillation results with data up to 2017 summer. 2017. URL `https://kds.kek.jp/indico/event/25337/`.

[133] T. N. C. Group. Calibration of the ND280 Scintillator Detectors. 2012. URL `https://www.t2k.org/docs/technotes/037`. T2K-TN-037, only accessible to T2K collaborators.

[134] A. Garcia and F. Sanchez. Measurement of the flux integrated ν_μ inclusive charge current cross section in FGD1. 2017. URL `https://www.t2k.org/docs/technotes/310`. T2K-TN-310-V1.0, only accessible to T2K collaborators.

[135] R. Berner. 4π coverage event selection for $\bar{\nu}_\mu$ CC inclusive interaction in FGD1. 2018. URL `https://www.t2k.org/docs/technotes/348`. T2K-TN-348, only accessible to T2K collaborators.

[136] D. Brailsford. *Measurement of the Charged Current Inclusive Muon Neutrino Interaction Cross-Section on Lead Using the T2K ND280 Electromagnetic Calorimeters.* PhD thesis, Imperial College, Dec 2015. URL `http://www.t2k.org/docs/thesis/066`.

[137] A. Aguilar-Arevalo et al. Unexplained Excess of Electron-like Events from a 1-GeV Neutrino Beam. *Phys. Rev. Lett.*, 102:101802, Mar 2009, doi:10.1103/PhysRevLett.102.101802.

[138] A. Aguilar-Arevalo et al. Improved Search for $\overline{\nu}_\mu \rightarrow \overline{\nu}_e$ Oscillations in the MiniBooNE Experiment. *Phys. Rev. Lett.*, 110:161801, Apr 2013, doi:10.1103/PhysRevLett.110.161801.

[139] E. Wang et al. Photon Emission in Neutral-Current Interactions at Intermediate Energies. *Phys. Rev.*, C89:015503, Jan 2014, doi:10.1103/PhysRevC.89.015503. arXiv:1311.2151 [hep-ex].

[140] J. Harvey et al. Anomaly Mediated Neutrino-Photon Interactions at Finite Baryon Density. *Phys. Rev. Lett.*, 99:261601, Dec 2007, doi:10.1103/PhysRevLett.99.261601. arXiv:0708.1281 [hep-ph].

[141] J. Rosner. Low-Energy Photon Production in Neutrino Neutral-Current Interactions. *Phys. Rev.*, D91:093001, May 2015, doi:10.1103/PhysRevD.91.093001. arXiv:1502.01704 [hep-ph].

[142] B. Serot et al. Neutrino-Production of Photons and Pions from Nucleons in a Chiral Effective Field Theory for Nuclei. *Phys. Rev.*, C86:015501, Jul 2012, doi:10.1103/PhysRevC.86.015501. arXiv:1208.1553 [nucl-th].

[143] J. Jenkins et al. Some radiative corrections to neutrino scattering: Neutral currents. *Phys. Rev.*, D80:053005, Sep 2009, doi:10.1103/PhysRevD.80.053005. arXiv:0906.0984 [hep-ph].

[144] D. Rein et al. Coherent Production of Photons by Neutrinos. *Phys. Lett.*, 104B:394–398, 1981, doi:10.1016/0370-2693(81)90706-1. [Erratum: Phys. Lett.106B,513(1981)].

[145] D. Casper. The NUANCE Neutrino Physics Simulation, and the Future. *Nucl. Phys. B - Proceedings Supplements*, 112(1):161 – 170, 2002, doi:10.1016/S0920-5632(02)01756-5. arXiv:hep-ph/0208030 [hep-ex].

[146] G. T. Garvey, D. A. Harris, H. A. Tanaka, R. Tayloe, and G. P. Zeller. Recent Advances and Open Questions in Neutrino-induced Quasi-elastic Scattering and Single Photon Production. *Phys. Rept.*, 580:1–45, 2015, doi:10.1016/J.PhysRep.2015.04.001. arXiv:1412.4294 [hep-ex].

[147] E. Wang et al. Photon Emission in Neutral Current Interactions at the T2K Experiment. *Phys. Rev.*, D92:053005, Sep 2015, doi:10.1103/PhysRevD.92.053005. arXiv:1507.02446 [hep-ph].

[148] A. Hillaret et al. ND280 Reconstruction. 2011. URL `https://www.t2k.org/docs/technotes/072`. T2K-TN-072-v1.0, only accessible to T2K collaborators.

[149] A. Izmaylov. HighLAND Tutorial, Jun 2017. URL `http://www.t2k.org/nd280/physics/xsec/meetings/2017/workshop/talks/highland/view`.

[150] K. Kowalik. The simulation of beam neutrinos interactions outside the ND280 detector. 2012. URL `https://www.t2k.org/docs/technotes/077`. T2K-TN-077-v2, only accessible to T2K collaborators.

[151] C. Bojechko et al. CC-Multiple-Pion ν_μ Event Selections in the ND280 Tracker Using Run 1+2+3+4 Data. 2013. URL `https://www.t2k.org/docs/technotes/152`. T2K-TN-152-v4.2, only accessible to T2K collaborators.

[152] P. Bartet et al. ν_μ Event Selections in the ND280 Tracker Using Run 2+3+4 Data. 2015. URL `https://www.t2k.org/docs/technotes/212`. T2K-TN-212-v0.9, only accessible to T2K collaborators.

[153] G. Christodoulou et al. Selection of ν_e and $\overline{\nu_e}$ in the ND280 Tracker Using Anti-Neutrino Beam Data from Run5 and Run6. 2016. URL `https://www.t2k.org/docs/technotes/282`. T2K-TN-282-v0.5, only accessible to T2K collaborators.

[154] S. Short. *Study of Neutrino-Induced Neutral Current Neutral Pion Production in the T2K Near Detector*. PhD thesis, Imperial College, Jun 2013. URL `http://www.t2k.org/docs/thesis/031`.

[155] K. Mahn. T2KReWeight Tutorial, Sep 2011. URL `https://www.t2k.org/nd280/software/meetings/2011/sept_soft_tutorial/t2kreweightv2/view`.

[156] M. Scott. *Measuring Charged Current Neutrino Interactions in the Electromagnetic Calorimeters of the ND280 Detector*. PhD thesis, Aug 2013. URL `http://www.t2k.org/docs/thesis/036`.

[157] K. Graczyk et al. Form Factors in the Quark Resonance Model. *Phys. Rev.*, D77:053001, Mar 2008, doi:10.1103/PhysRevD.77.053001. arXiv:0707.3561 [hep-ph].

[158] S. Bolognesi et al. NIWG Model and Uncertainties for 2017 Oscillation Analysis. 2017. URL `https://www.t2k.org/docs/technotes/315`. T2K-TN-315-v5.0, only accessible to T2K collaborators.

[159] K. Abe et al. Measurements of Neutrino Oscillation in Appearance and Disappearance Channels by the T2K Experiment with 6.6×10^{20} Protons on Target. *Phys. Rev.*, D91(7):072010, 2015, doi:10.1103/PhysRevD.91.072010. arXiv:1502.01550 [hep-ex].

[160] P. Stowell et al. NUISANCE: a Neutrino Cross-Section Generator Tuning and Comparison Framework. *JINST*, 12:P01016, 2017, doi:10.1088/1748-0221/12/01/P01016. arXiv:1612.07393 [physics.ins-det].

[161] A. Bercellie et al. Implementation of Additional NIWG Cross Section Parameterizations for 2014 Analyses. 2014. URL `https://www.t2k.org/docs/technotes/193`. T2K-TN-193-v1.1, only accessible to T2K collaborators.

[162] R. Acciarri et al. Measurement of ν_μ and $\bar{\nu}_\mu$ neutral current $\pi^0 \rightarrow \gamma\gamma$ production in the ArgoNeuT detector. *Phys. Rev.*, D96(1):012006, 2017, doi:10.1103/PhysRevD.96.012006. arXiv:1511.00941 [hep-ex].

[163] L. Alvarez-Ruso et al. NuSTEC White Paper: Status and Challenges of Neutrino-Nucleus Scattering. 2017. URL `http://lss.fnal.gov/archive/2017/pub/fermilab-pub-17-195-nd-t.pdf`. arXiv:1706.03621 [hep-ph].

[164] P. Adamson et al. Neutrino and Antineutrino Inclusive Charged-current Cross Section Measurements with the MINOS Near Detector. *Phys. Rev.*, D81:072002, 2010, doi:10.1103/PhysRevD.81.072002. arXiv:0910.2201 [hep-ex].

[165] P. De Perio et al. Cross Section Parameters for the 2012a Oscillation Analysis. 2012. URL `https://www.t2k.org/docs/technotes/108`. T2K-TN-108-v1.5, only accessible to T2K collaborators.

[166] E. Pinzon. FSI on Heavy Targets, Jun 2016. URL `http://www.t2k.org/asg/xsec/meetings/2016/niwg-24june2016-meeting/Current-FSI-Heavy_Targets/view`. Presentation at the NIWG meeting.

[167] P. De Perio et al. NEUT Nuclear Effects (FSI). 2012. URL `https://www.t2k.org/docs/technotes/033`. T2K-TN-033-v2.0, only accessible to T2K collaborators.

[168] D. Brailsford et al. Study of the tracker ECal systematic uncertainties. 2017. URL `https://www.t2k.org/docs/technotes/279`. T2K-TN-279-v2, only accessible to T2K collaborators.

[169] D. Wright et al. The Geant4 Bertini Cascade. *Nucl. Instrum. Meth.*, 804(Supplement C):175 – 188, 2015, doi:10.1016/J.NIMA.2015.09.058.

[170] J. Myslic. Determination of Pion Secondary Interaction Systematics for the ND280 Tracker ν_μ Analysis. 2013. URL `https://www.t2k.org/docs/technotes/125`. T2K-TN-125-v1.0, only accessible to T2K collaborators.

[171] T. Feusels et al. Tuning of the NEUT Cascade Model Using $\pi^\pm - A$ Scattering External Data to Improve Final State Interaction and Secondary Interaction Systematic Uncertainties. 2017. URL `https://www.t2k.org/docs/technotes/325`. T2K-TN-325-v0.0, only accessible to T2K collaborators.

[172] D. Ashery et al. True Absorption and Scattering of Pions on Nuclei. *Phys. Rev.*, C23:2173–2185, 1981, doi:10.1103/PhysRevC.23.2173.

[173] F. Dufour et al. Systematics on Out-of-Fiducial-Volume Backgrounds in the ND280 Tracker. 2015. URL `https://www.t2k.org/docs/technotes/098`. T2K-TN-098-v1.1, only accessible to T2K collaborators.

[174] S. Oser. Elemental Composition of the FGD XY Modules. 2010. URL `https://www.t2k.org/docs/technotes/091`. T2K-TN-091-v1.2, only accessible to T2K collaborators.

[175] F. Di Lodovico et al. T2K Cross Section Measurement Best Practice. 2016. URL `https://www.t2k.org/docs/technotes/263`. T2K-TN-263-v1, only accessible to T2K collaborators.

[176] M. Ravonel. Measurement of the Flux Averaged Muon Neutrino Inclusive Charged Current Cross-Section at the Near tector. 2012. URL `https://www.t2k.org/docs/technotes/117`. T2K-TN-117-v2.4, only accessible to T2K collaborators.

[177] C. Andreopoulos et al. The VALOR Neutrino Fit Group. 2010. URL `https://valor.pp.rl.ac.uk/`.

[178] F. James et al. Minuit: A System for Function Minimization and Analysis of the Parameter Errors and Correlations. *Comput. Phys. Commun.*, 10:343–367, 1975, doi:10.1016/0010-4655(75)90039-9.

[179] R. Calland. *A 3 Flavour Joint Near and Far Detector Neutrino Oscillation Analysis at T2K*. PhD thesis, University of Liverpool, 9 2014. URL `https://www.t2k.org/docs/thesis/059`.

[180] S. Bienstock et al. Constraining the Flux and Cross Section Models with Data from the ND280 Detector using FGD1 and FGD2 for the 2017 Joint Oscillation Analysis.

2017. URL `https://www.t2k.org/docs/technotes/324`. T2K-TN-324-v3, only accessible to T2K collaborators.

[181] Conversation with J. Nieves.

[182] G. Cowan, K. Cranmer, E. Gross, and O. Vitells. Asymptotic formulae for likelihood-based tests of new physics. *Eur. Phys. J.*, C71:1554, 2011, doi:10.1140/EPJC/s10052-011-1554-0. arXiv:1007.1727 [physics.data-an]. [Erratum: Eur. Phys. J.C73,2501(2013)].

[183] T. Yuan et al. A Double Differential Measurement of the Flux Averaged $\nu_\mu CC0\pi$ Cross Section on Water. 2016. URL `https://www.t2k.org/docs/technotes/258`. T2K-TN-258-v4.6.1, only accessible to T2K collaborators.

[184] S. Assylbekov et al. The T2K ND280 Off-Axis Pi-Zero Detector. *Nucl. Instrum. Meth.*, A686:48–63, 2012, doi:10.1016/J.NIMA.2012.05.028. arXiv:1111.5030 [physics.ins-det].

[185] C. Wilkinson. MINERvA Heavy Target Ratios. Presentation at the NIWG meeting, 24th Jun 2016, URL `http://www.t2k.org/asg/xsec/meetings/2016/niwg-24june2016-meeting/heavy-target-ratios`.

[186] B. Tice et al. Measurement of Ratios of ν_μ Charged-Current Cross Sections on C, Fe, and Pb to CH at Neutrino Energies 2-20 GeV. *Phys. Rev. Lett.*, 112(23):231801, 2014, doi:10.1103/PhysRevLett.112.231801. arXiv:1403.2103 [hep-ex].